The University of Nottingham

AXISYMMETRIC CENTRIFUGE MODELLING OF DEEP PENETRATION IN SAND

Weiwei Liu

Thesis submitted to The University of Nottingham for the degree of Doctor of Philosophy

Sep 2010

This thesis is dedicated

to the two greatest people in my life:

my parents

AFFIRMATION

The following publication is published on the work presented in this thesis:

Liu, W., Ellis, E. A., Cox, C. M. & Reddish, D. J. (2010). The soil displacement field in centrifuge modelling of a cylindrical penetrometer, *7th International Conference on Physical Modelling in Geotechnics*, Zurich.

ABSTRACT

The advancement of a slender object into soil (to depths of 10s of metres) is of fundamental interest to Geotechnical Engineers. Considerable advances have recently been made in beginning to understand some detailed aspects of the fundamental behaviour for penetration in sand using physical models.

In this project, a 180^{o} axisymmetric model is developed, which allows viewing of soil movement as a circular penetrometer advances into the soil. The model was tested in a geotechnical centrifuge with digital photographic techniques used to track soil movement.

A series of 10 centrifuge tests is reported. The soil displacement during pile installation was measured. The soil strain paths during installation were also calculated from the measured soil displacements. The stress along the pile shaft was also measured by strain gauges during the pile installation. The displacements show reasonable correspondence with circular (cylindrical) cavity expansion. The amount of displacement generally increases with penetration. After about 8 to 10 diameters of penetration, the amount of movement does not vary significantly with depth. After the probe passes there is little systematic movement. The magnitude of displacements drops quickly as the radial position increases.

The influence of re-driving, soil density, gravity levels and probe tip shape was examined. Results reveal that displacements are much less in the re-driving test. The centrifuge acceleration has some influence on the displacement and strains. It is found that there is no significant deviation in displacement and strains for different soil density and probe tip shape.

ACKNOWLEDGEMENTS

First and foremost, I would like to show the greatest appreciation to Dr Ed Ellis for his excellent guidance and patience throughout the research. I have been extremely fortunate to have had a supervisor, with vast knowledge and endless enthusiasm to teach and research. He arranged very frequent meetings and help me solve problems during my research. He even squeezes out time from his busy schedule on my research and thesis after he went to University of Plymouth. Again I'm sincerely grateful for the honour of working with him, and without him I would not have made so much progress.

Secondly, I wish to acknowledge the support provided by Dr David Reddish for his guidance, enthusiasm and help on my research and PhD thesis.

I would also like to thank Professor Hai-Sui Yu. He gave me a lot of advice on my PhD life and future career.

I wish to highlight my acknowledgements to all technicians of the School of Civil Engineering, in particular Craig Cox and Mike Langford, who provide the enthusiastic technical contributions in geotechnical centrifuge modelling.

I'm greatly indebted to the EPSRC, the School of Civil Engineering and the University of Nottingham for their financial support.

Finally, my special thanks to my parents for their endless and wonderful love and encouragement in my life.

TABLE OF CONTENTS

CHAPTER 3 CENTRIFUGE MODELLING

CHAPTER 4 PROBE CENTRIFUGE TESTS AT 50g IN DENSE SAND

CHAPTER 5 RE-DRIVEN TEST RESULTS

CHAPTER 6 EFFECT OF DENSITY

CHAPTER 7 EFFECT OF CENTRIFUGE ACCELERATION

CHAPTER 8 BLUNT PROBE TEST RESULTS

CHAPTER 9 AXISYMMETRIC MODEL COMPARED WITH PLANE STRAIN MODEL

LIST OF FIGURES

LIST OF TABLES

NOTATIONS

English letter

d_{50}: average particle size

g: Earth gravity

h: vertical distance above probe tip

h_p: depth in 'prototype'

h_m: depth in model

k_c: factor relating pile end-bearing to the cone resistance q_c

p_{lim}: limit pressure

r_u: maximum under-stress to the prototype stress

r_o: maximum over-stress to the prototype stress

q_b: end bearing capacity

q_c: CPT bearing capacity

x/R:horizontal position relative to R

y : distance from bottom of the container

z : depth in the model

A: cross area of probe

D: dimension of probe

G_s: specific gravity

I_d: relative density of sand

N: scaling factor or gravity level

N_q: bearing capacity factor

Q: load long probe

R: radius of probe

R_e: effective radius

R_t: radius of the top of the soil.

Greek letter

α: angle of the rigid zone

Δx : radial displacement

Δy: vertical displacement

ε_h: horizontal strain

ε_v: vertical strain

μ : displacement

v: Poisson's ratio

ρ: dry density of soil in model (g / mm3)

σ_h': in-situ effective horizontal stress

σ_v': in-situ effective vertical stress

φ: friction angle

ω : angular rotational speed of the centrifuge

Abbreviations

CPT: Cone Penetration Test

DAS: Data Acquisition System

LHS: Left Hand Side

PIV: Particle Image Velocimetry

RHS: Right Hand Side

SPM: Strain Path Method

CHAPTER 1 - INTRODUCTION

1.1 Background

The advancement of a slender object into soil (to depths of 10s of metres) is of fundamental interest to Geotechnical Engineers. A displacement pile is an example of such an object, which may be more than a metre in diameter. At the other extreme the Cone Penetration Test (CPT) is used to characterise soils in situ, and is only a few centimetres in diameter. Unsurprisingly the CPT finds particular application in the design of displacement piles (eg. Randolph, 2003), although there is still considerable debate regarding (for instance) whether or how the differing size of the object affects the resistance to penetration (eg. Jardine & Chow, 1996 and White, 2005).

Many problems in geotechnical engineering are relatively well-suited to numerical modelling (provided the constitutive behaviour of the soil can be described adequately). However, the rigorous numerical modelling of deep penetration is unusually difficult because the problem involves large deformations and highly nonlinear material and interface behaviour (Yu et al, 2000).

Recent advances have been made in the use of digital image analysis to 'track' zones of soil as they move (eg. due to an advancing penetrometer). However, this technique has yet to be used in conjunction with an advancing penetrometer in a geotechnical centrifuge model or calibration chamber test. More particularly, it has not been used with a cylindrical penetrometer (as a pile or CPT would be). Instead a 'plane strain' idealisation in a calibration chamber test has been used, which effectively assumes that the extent of the penetrometer is infinite in one of the horizontal directions (White & Bolton, 2004).

The main emphasis of this research is to develop a (half) cylindrical penetrometer and soil physical model which will allow the associated movement to be observed during

driving. This technique is then used in a geotechnical centrifuge, utilising digital image analysis techniques to track movements of the soil.

The results provide fundamental comparison with the ‘plane strain’ idealisation which has previously been used to observe soil movement. Effects such as centrifuge acceleration, soil density, and the nature of the probe tip are considered through a series of centrifuge tests.

1.2 Thesis outline

This thesis consists of twelve chapters.

Chapter 2 contains a literature review, introducing the various analysis methods for pile capacity ranging from wholly empirical methods to theoretical analyses. Also, previous studies on penetration behaviour using geotechnical centrifuges are presented.

Chapter 3 provides the details of the centrifuge and testing system. The development of the half penetrometer is presented. The details of the model components such as container, actuator, probe, and cameras are introduced. The test programme including soil model preparation is also presented in this chapter.

Chapter 4 is the first of the results chapters, and presents results for 50g tests in dense sand, which is considered as a standard test to compare with the other tests. The displacement measurements from two cameras are reported and analysed here. The summaries of the displacements and strains for different radial position are presented to investigate the general trends in that data

Chapter 5 investigates the effect of 're-driving' the probe in the same sand sample as used in Chapter 4.

Chapter 6 shows the effect of different densities of sand. Results from loose sand and loose over dense sand are presented. The soil displacement and strains with different densities are compared.

Chapter 7 reports the effect of different g-levels. Results from experiments undertaken at 1g and 100g are compared with the previous tests at 50g.

Chapter 8 investigates a ‘blunt’ probe test result compared to the conical tip (standard test). Images obtained when the probe was stopped at different depths are reported. The displacements and strains are also compared with the standard test.

Chapter 9 summaries all the tests and compares the results with previous plane strain tests reported by White & Bolton (2004).

Chapter 10 presents data from the probe load cells. The variations of the load with depth of the probe shoulder are presented. The results are compared to the other researchers in terms of the tip stress.

Chapter 11 compares and discusses the test results with three theories. The implication of the research is also given in this Chapter.

Finally the thesis ends with Chapter 12 presenting the conclusions. Recommendations for future work are also made in this Chapter.

Appendix A shows photos of the probe from the various tests.

Appendix B considers the effect of refraction on the optical measurement system.

CHAPTER 2 - LITERATURE REVIEW

2.1 Introduction

Pile resistance results from two components: the shear stress generated by shaft friction, and the vertical (axial) component of normal stress generated at the base of the pile ('bearing'). The relative magnitude of the shaft and base capacity depend on the pile geometry and the soil profiles. For a typical pile in granular soil the total capacity is generally relatively evenly divided between the shaft and base (or the base may dominate), while in cohesive soils the shaft friction may be 80~90% of the total capacity (Yu, 2000).

There are a number of approaches for predicting the base resistance of piles in sands. Berezantzev et al (1961) tried to use slip planes and bearing capacity theory to link friction angle and base resistance, but failed to capture the trends observed in the field. Researchers then tried alternative methods ranging from wholly empirical to theoretical.

This chapter gives an overview of these various common analysis methods for pile capacity. Some of the previous visual analysis (observation) methods of pile installation are also reviewed. Also, previous studies on penetration behaviour using centrifuge modelling are presented.

2.2 Theoretical methods for estimation of base resistance

2.2.1 Bearing capacity methods

The results of plane strain bearing capacity calculations were often modified empirically in the past for application to the axially symmetric problem. Two kinds of analytical approaches, limit equilibrium and slip-line analysis, are used to determine the cone resistance (bearing capacity).

The limit equilibrium method considers the failure mechanisms first and then analyses the global equilibrium of the soil mass to determine the failure load. Figure 2.1 shows two of the failure mechanisms used in cohesionless soils.

For the slip-line method, a yield criterion (such as Mohr-Coulomb or Tresca) is combined with equations of equilibrium to give the differential equations of equilibrium of the soil mass. From these equations, a slip-line such as shown in Figure 2.2 can be constructed and the collapse load determined.

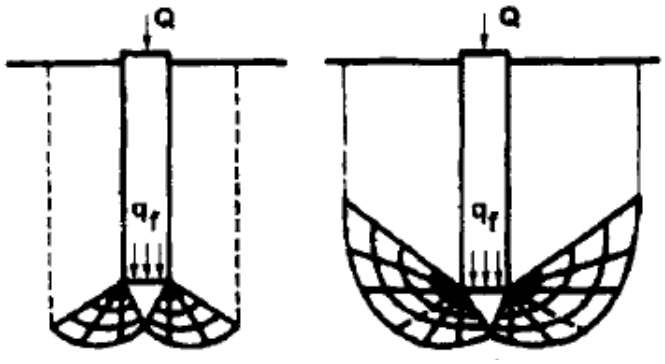

Figure 2.1: Assumed failure mechanisms for cohesionless soil (Durgunoglu & Mitchell, 1975)

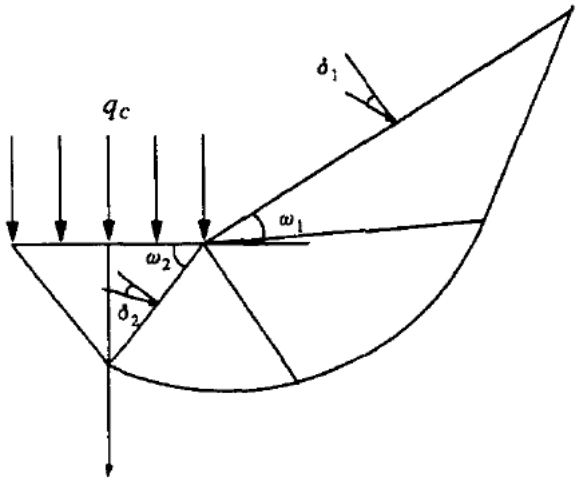

Figure 2.2: Slip-line network of wedge and cone penetration analysis (Yu & Mitchell, 1998).

A major advantage of this approach is its relative simplicity. However, Teh & Houlsby (1991) argued that the conventional approaches for the bearing capacity of shallow objects are inappropriate for deep penetration problems, due to the different mechanisms of shallow and deep failure. During shallow failure, the failure mechanism extends to the surface of the soil whereas during deep failure, the soil is displaced horizontally and the volume of the cone (at the front of the mechanism) is accommodated by the elastic deformation of the soil.

2.2.2 Cavity expansion methods

Gibson (1950) pioneered a model to use the analogy between spherical cavity expansion and bearing failure at the tip of a pile. He assumed a rigid soil cone beneath the pile tip and outside this zone is a soil zone which is under isotropic stress equal to the limit pressure for spherical cavity expansion (Figure 2.3). From this assumption, it is found that

$$q_b = p_{\lim}(1 + \tan\phi' \tan\alpha) \tag{2.1}$$

Where

q_b is the end bearing pressure,

$p_{\lim}$ is the limit pressure,

ϕ' is the friction angle,

α is the angle of the rigid zone.

This equation can also be used for the cone (CPT) resistance q_c by taking α as 60° (the cone angle), and ϕ' as δ, the interface friction angle between cone and soil.

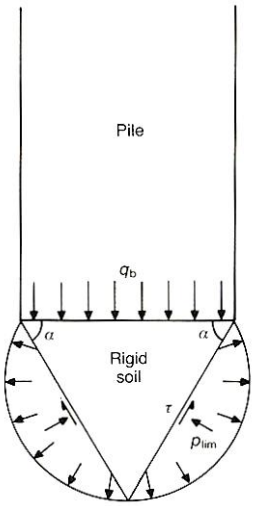

Figure 2.3: Relation of cavity expansion limit pressure and end-bearing capacity (Randolph et al, 1994)

Significant progress has been made by using more realistic soil stress-strain models to develop accurate cavity expansion solutions (e.g. Vesic, 1972; Carter et al., 1986; Yu & Houslby, 1991; Salgado, 1993). Table 2.1 and Figure 2.4 present some of these relationships for cohesionless soils.

Authors	Methods assumptions	Main conclusions
Ladanyi & Johnson (1974)	The normal stress on the cone face is assumed to be equal to that required to expand a spherical cavity from zero radius (Figure2.4(a))	$N_q = \frac{(1+2K_0)A}{3}[1+\sqrt{3}\tan(\lambda\phi')]$ where N_q is a bearing capacity factor, $N_q = q_b / \sigma_v'$, σ_v' is the in-situ effective overburden stress
Vesic(1972); Chen & Juang (1996)	The cone resistance is related to the spherical cavity limit pressure by a failure mechanism (Figure 2.4(b))	$N_q = \frac{(1+2K_0)A}{(3-\sin\phi')}\exp[\pi/2-\phi')\tan\phi']$ $\times\tan^2(\pi/4+\phi/2')(I_{rr})^n$
Salgado(1993); Salgado et al. (1997)	The cone resistance is related to the cylindrical cavity limit pressure by approximate slip line analysis (Figure2.4(c))	The cone resistance can't be expressed analytically
Yasufuku & Hyde (1995)	The cone resistance is related to the spherical cavity limit pressure by a simple failure mechanism (Figure 2.4(d))	$N_q = \frac{(1+2K_0)A}{3(1-\sin\phi')}$

Table 2.1: Summary of cavity expansion solutions for cohesionless soils (Yu & Mitchell, 1998)

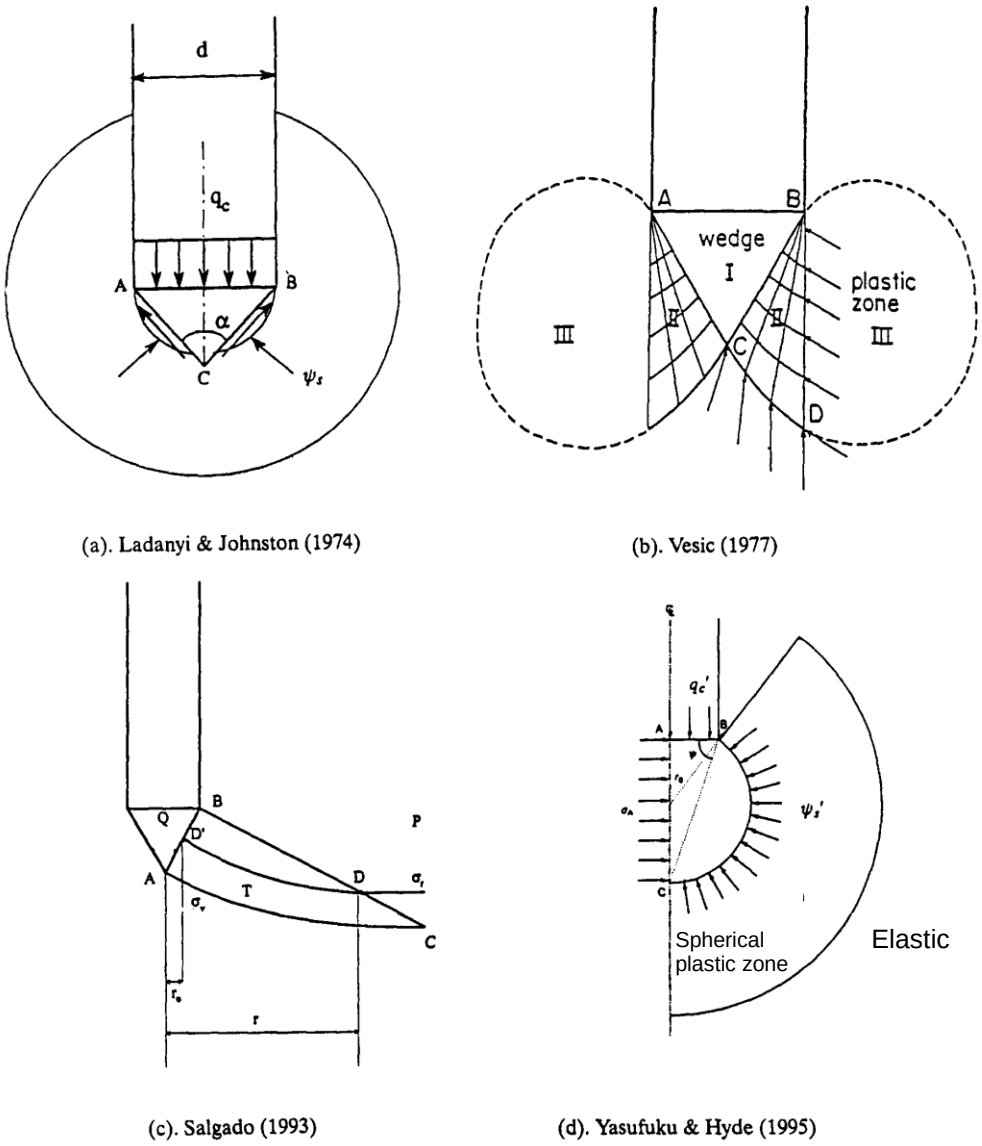

(a). Ladanyi & Johnston (1974)

(b). Vesic (1977)

(c). Salgado (1993)

(d). Yasufuku & Hyde (1995)

Figure 2.4: Assumed relationships between cone resistance and cavity limit pressure (Yu & Mitchell, 1998)

2.2.3 Strain path methods

Baligh (1985) first proposed this method to conduct steady state analysis of cone penetration in soil. The penetration process is considered as a steady flow of soil past a fixed penetrometer. The assumption is that the deformation and strains caused by the penetration are independent of the soil strength and stiffness. Soil is treated as a viscous fluid and a flow field is established from a potential function.

In general, the mean stress cannot simultaneously satisfy all equilibrium equations and the discrepancy reflects the error in the initial flow field. This is because the soil deformation can not be completely decoupled from the soil strength (Yu, 2000).

2.2.4 Finite-element methods

De Borst & Vermeer (1982) conducted small strain analyses of the cone penetration problem for cohesive soils with a smooth penetrometer shaft. The cone is introduced into a pre-bored hole, and the in situ-stress state of the surrounding soil is not disturbed. It is assumed that the collapse load is equal to the cone resistance. However, during the cone penetration high lateral stress tends to develop next to the shaft of the cone. As expected, this would lead to higher cone resistance than predicted by a small strain analysis.

A large strain model is required to include the effect of cone penetration on initial stress conditions, since the cone must be pushed into the soil with a large vertical displacement. Such a large penetration is required to model the stress increases induced around the cone shaft. Cividini & Gioda (1988) give an example of large strain analysis for sand. They use zero-thickness elements to model the frictional interface between the cone and soil. Van den Berg (1994) developed a more comprehensive large strain analysis of the cone penetration problem by using a Eulerean formulation. The finite-element mesh is fixed in space, while the material streams through it. The author suggests that a steady state is normally achieved when the penetration is about three times of the cone diameter. Recently, the Arbitrary Lagrangian-Eulerian (ALE) approach has been developed based on Berg's previous work. In this approach, the grid is not fixed to the material or in space, and the material flows independently of the grid.

It is acknowledged that there are some problems when the finite element method is used to analyse incompressible solids, and this is particularly true for axisymmetric loading conditions. The accuracy of the stresses calculated from the finite-element

model reduces dramatically as the compressibility approaches zero. This phenomena is known as locking, and has been reported by many researchers.

2.2.5 Summary of theoretical method

Table 2.2 gives a summary of three theoretical methods

	Assumption	Advantage	Disadvantage
Bearing capacity method	Various failure mechanism assumptions	Simple	Does not work well for deep penetration problems
Cavity expansion	A rigid soil cone beneath the pile tip is under isotropic stress equal to the limit pressure	Considers both elastic and plastic deformation	Does not consider the cone tip geometry Does not consider the roughness of the cone and shaft
Strain path method	The penetration process is considered as a steady flow of soil past a fixed penetrometer.	Works well for undrained clay	Difficult to use in frictional soils
Finite-element method	Soil is continuous Steady –state assumption	Equilibrium equations are fully accounted.	Problems when analysing incompressible solids 'Locking' phenomena

Table 2.2: Summary of three theoretical methods

2.3 Cone penetration test (CPT)

The cone penetration test (CPT) is an in-situ testing method used to determine the geotechnical engineering properties of soils and to delineate soil stratigraphy. Today, the CPT is one of the most widely used in-situ test methods for obtaining soil profiles worldwide.

Without significantly disturbing the ground, it provides information about the soil type and its geotechnical parameters, such as shear strength, density, elastic modulus, rates of consolidation and other environmental properties. Furthermore, as it can be seen as a small-scale test pile, it is often regarded as the best and most cost effective device to design piled foundations and sheet piles.

The test method consists of pushing an instrumented cone tip into the ground at a controlled rate (usually 20 mm/s). The resolution of the CPT in delineating stratigraphic layers is related to the size of the cone tip, with typical cone tips having a cross-sectional area of either 100 or 150 mm^2, corresponding to diameters of 36 and 44 mm. During the penetration, the forces on the cone and the friction sleeve (the shaft immediately behind the tip) are measured. The measurements are normally carried out using electronic transfer and data logging, with a measurement frequency that can secure detailed information about the soil conditions. Figure 2.5 shows an electrical cone penetration tip.

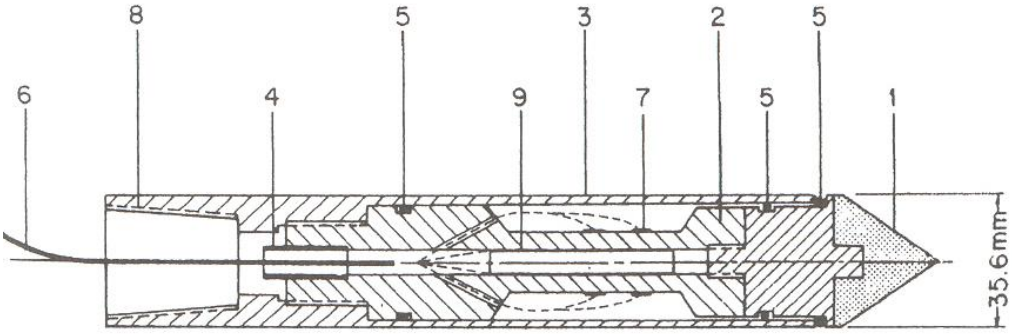

1 Conical point (10 cm^2)
2 Load cell
3 Protective mantle
4 Waterproof bushing
5 O-rings
6 Cable
7 Strain gages
8 Connection with rods

Figure 2.5: Electrical cone penetration tip (Reese et al, 2006)

2.4 Empirical methods based on the CPT test

By eliminating the need to assume a penetration mechanism, design methods using cone penetration test (CPT) data instead of derived soil properties can give improved reliability in the field.

The API (American Petroleum Institute) guideline for the construction of fixed offshore platforms is one of the most widely used design methods for offshore piles. The ultimate end-bearing resistance of a pile is generally expressed as

$$q_b = N_q \sigma_v' \text{ or } q_b = k_c q_c$$

Where N_q is a bearing capacity factor, σ_v' is the in-situ effective overburden stress and k_c is the factor relating pile end-bearing to the cone resistance q_c (API, 2000).

Jardine & Chow (1996) proposed new design methods for offshore piles, referred to as the MTD (Marine Technology Directorate) method. The MTD method, linking base resistance q_b to CPT resistance q_c , is claimed to have a higher reliability in prediction of base resistance in silica sand than the API method (White & Bolton, 2004). This higher reliability is achieved by introducing a scale effect and q_c is factored down by the ratio [1-0.5log (D/D_{cpt})] (D is the diameter of the pile, D_{cpt} is the CPT diameter (normally 0.036m)). Thus base resistance for piles is reduced (as diameter increases) compared to the small diameter CPT resistance. This empirical relationship is based on back analysis of pile test data for various pile diameters. The mechanistic origin of this scale effect is not clear, and researchers have suggested a number of alternative reduction factors to convert q_c to q_b , based on different mechanistic hypotheses (Winterkorn & Fang, 1975; Tejchman & Gwizdala, 1979; Kraft, 1990; Lee & Salgado, 1999; Borghi et al., 2001; White & Bolton, 2004). These reduction factors can be linked to:

(a) Partial embedment of the pile in a stronger layer

(b) Local inhomogeneity

(c) Partial mobilisation of base resistance in a stronger layer during a pile test

(d) The effect of residual stresses (see Section 2.4.3) when interpreting pile test data.

Factors (a) and (b) above are related to the observation that a CPT will 'respond' over a shorter depth of penetration into a different (stronger) layer, due to its much smaller diameter (than a pile). Thus the maximum resistance in a stronger layer will be observed at smaller penetration, or in a thinner layer. Since the CPT is continually advancing, there are no issues with mobilisation of base capacity or residual stresses, which may affect interpretation of pile test data.

White & Bolton (2005) reviewed these factors and reassembled Chow's (1997) database of load tests on closed–ended piles in sand. They proposed that the apparent reduction in base capacity with increasing pile diameter (which they argue has no theoretical basis) is due to effects (a), (c) and (d) above. Thus they re-evaluated the data, accounting for partial embedment and residual stresses. They also excluded data where it is not possible to establish a fully mobilised base capacity or where CPT data was not actually available for comparison with the pile test (and had been estimated from standard penetration test data from Jardine & Chow (1996)). Following this revaluation the resulting values of q_b / q_c (bearing capacity of test pile/ CPT bearing capacity) had a mean value of 0.90 and showed no trend for reduction with increasing pile diameter.

2.4.1 Partial embedment (L/D)

As a pile has a greater diameter than a CPT cone, it needs a deeper embedment into a hard layer to mobilise the full strength of that layer. Prior to sufficient penetration, q_b will be less than q_c , as the previous layer will still be 'felt' by the pile tip. Laboratory tests have shown that this effect can extend to an embedment of several pile diameters, and can be accounted for using a correction of the form illustrated in Figure 2.6.

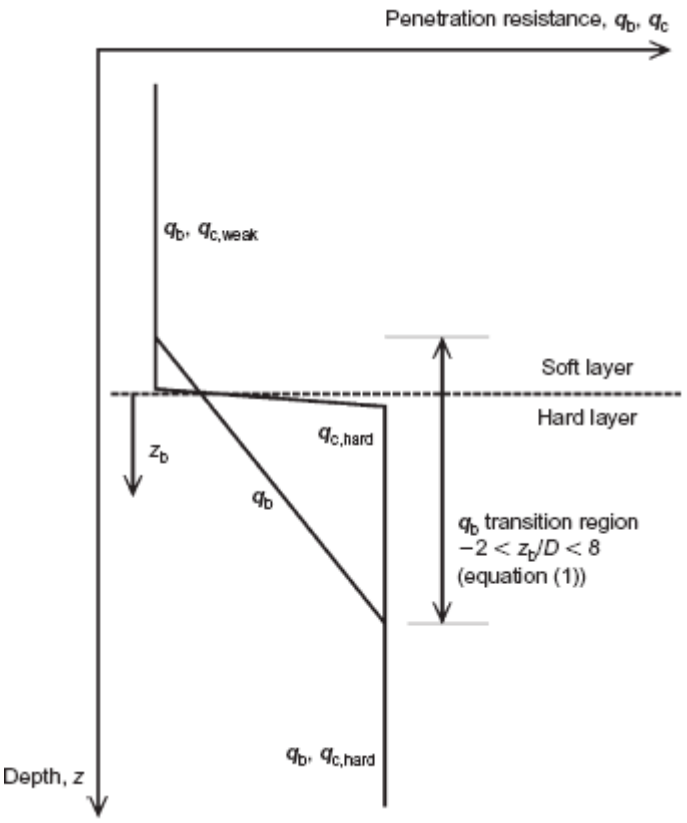

Figure 2.6: Partial embedment reduction factor on base resistance (White & Bolton, 2005).

2.4.2 Partial mobilisation

Randolph (2003) found that when a new loading event occurs on a pile, steady-state conditions are reached after large displacement (4–10 diameters) for zero residual stress (i.e. zero load 'locked-in' at the base following the previous event, such as pile driving). At more limited displacements (such as 10% of the pile diameter, which is often taken as the practical definition of 'ultimate' capacity), the end-bearing resistance will be significantly lower than the cone resistance, and will also depend strongly on residual stress (see Section 2.4.3).

Lee & Salgado (1999) also present reduction factors on CPT resistance to account for partial mobilisation of q_b by noting that the definition of q_b normally relates to a given settlement, rather than to the 'plunging' load required for continued penetration (which is observed in the CPT test).

However, White & Bolton (2005) found that plunging capacity was reached prior to a settlement of D/10 for only 60% of the piles. For a D/10 failure criterion, pile tests show a mean q_b / q_c of 0.75, which rises to 0.89 for a 'true' plunging failure criterion. When assessing pile capacity according to the D/10 displacement failure criterion, the value is also influenced by pile stiffness for this subset of 40% of the piles (since displacement at the toe will be less than at the head, where it is generally measured). For the remaining 60% of the database, the pile stiffness is sufficiently high to have no influence. Partial mobilisation can be accounted for by defining q_b as the plunging capacity.

2.4.3 Residual load

For driven and jacked piles, it is found that there is significant 'residual load' which is 'locked in' at the pile base following installation. At the end of installation, when the load at the head used for installation is removed, the shaft friction on the upper part of the pile is reversed as the pile head rebounds upwards. As the shaft response is stiffer than the base response, the base does not become fully unloaded. As a result, the base load is equilibrated by 'negative' shear stresses along the pile shaft, as if the pile was loaded in tension (Yetginer et al, 2006), Figure 2.7. If a high residual load is present, the ultimate capacity is reached at a smaller settlement. This will lead to a stiffer overall pile response in compression, and significantly higher end-bearing stresses mobilised at small displacement (Randolph, 2003), since some of the base capacity is already mobilised at zero displacement. Reversal of the shaft load requires little displacement, and hence the overall response is stiff.

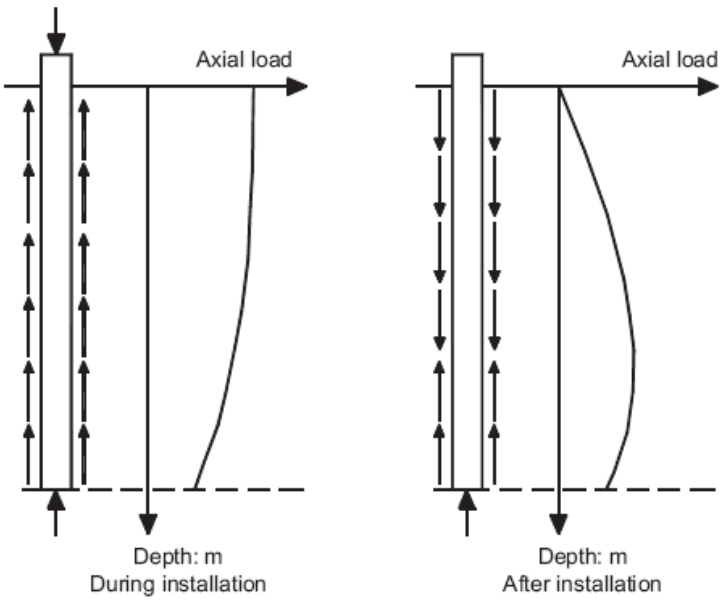

Figure 2.7: Residual load during and after installation (Yetginer et al, 2006)

The residual load depends on the relative magnitude of base and shaft capacity and installation methods. The residual stress could be as high as 75% of the ultimate base capacity for jacked or driven closed ended piles (Maiorano et al, 1996), but not exceeding 70~80% of the shaft capacity (Poulos, 1987).

Open-ended piles give a lower residual load unless they become fully plugged during driving (Randolph, 2003). Residual load does not occur in bored piles, where there is initially approximately zero base pressure following installation (e.g. due to the pressure from wet concrete during pile construction).

2.5 Shaft friction degradation ('friction fatigue')

It has been widely observed that the local shaft friction at a given horizon (vertical location) decreases as the pile penetrates further, and this effect has been referred to as 'friction fatigue' (Heerema, 1980).

White & Lehane (2004) recently proposed that the physical basis for friction degradation is the gradual densification of a thin band of soil adjacent to the pile shaft under the cyclic shearing action of installation (for a driven pile).

White & Bolton (2004) proposed that soil is crushed at the pile tip, and this material 'coats' the shaft as it penetrates. Densification of soil close to the pile shaft results in reduced radial effective stress outside the thin band, as the soil 'relaxes' and undergoes incremental tensile horizontal strain. This in turn, leads to reduction of the shear stress acting on the shaft $\tau = \sigma'_h \tan\delta$.

White & Bolton (2004) used a spring analogy to explain this mechanism (Figure 2.8). High horizontal stress is created as soil is compressed laterally along streamline XY. As the soil continues along streamline YZ, the interface zone immediately adjacent to the pile (zone B in Fig. 2.9) contracts with continued shearing at the pile–soil interface. The stiff unloading response of the heavily overconsolidated soil in the far field is represented by a stiff spring (zone A). This spring is fixed in the far field and exerts horizontal stress on the pile shaft. As *h* (where *h* is the vertical distance of a soil element above the pile tip) increases, zone B contracts and the spring unloads, reducing the shaft friction on the pile.

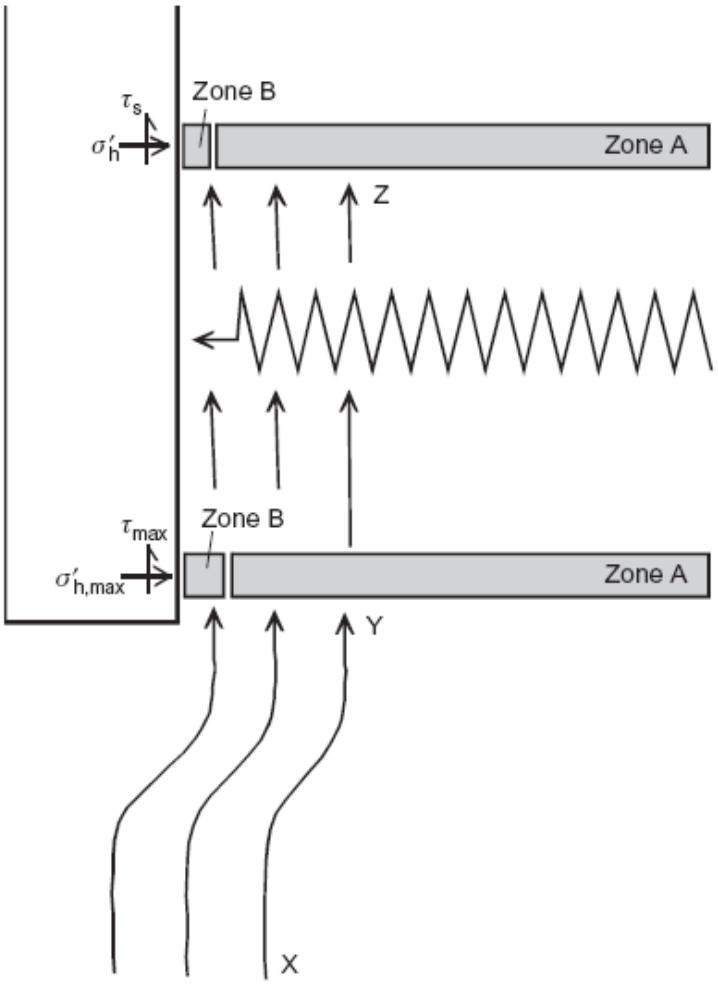

Figure 2.8: Kinematics of friction fatigue close to the pile tip (White & Bolton, 2004)

White & Bolton (2004) found a 2-3mm thick zone of fine broken particles adjacent to the shaft of model piles which enhanced the densification process by gradually migrating though the matrix of uncrushed material.

White & Lehane (2004) argue that the mechanism of friction fatigue following interface contraction will be more significant under cyclic loading than monotonic loading. It is also widely reported that cycles of shear displacement lead to greater volume contraction than monotonic shearing (Al-Douri & Poulos, 1991; DeJong et al, 2003). Poulos et al (1988) found that the mean shaft friction measured in a small-scale model decreased with increasing cyclic amplitude. White & Lehane (2004) found that two-way cycling leads to a greater degradation than one-way cycling during both

installation and load testing (two way cycling refers to both tensile and compressive load at the pile head in one cycle whereas one-way cycling is varying magnitude of compressive load).

Yang et al (2006) found that jacked piles tend to show a higher local shaft resistance than driven piles due to reduction of the fatigue mechanism, an effect which is also predicted by White & Bolton (2002). However, the precise reasons for this correspondence was questioned by Fellenius (2007), since the effect of residual loads were not included in the analysis by Yang et al (2006).

2.6 Set-up

Here ‘set-up’ refers to a time-related increase in shaft capacity, which has been reported by many researchers studying the behaviour of piles in the field over long periods of time.

Chow et al (1997) considered the possible explanations for this time-dependent process. They believed that the dominant process is gain in the radial effective stresses acting on the pile shaft resulting from the relaxation, through creep, of circumferential arching established around the pile shaft during installation. The circumferential arch initially forms outside zone A (Figure 2.8), allowing reduction of stress inside the annular ‘arch’ during driving. If the arch later relaxes the stress inside the annulus (and on the pile) increases again in the long term – see Figure 2.9. Additionally, increases in sand shear strength and stiffness with time (ageing) involving the reorientation of sand grains and possible cementing or micro-interlocking processes are also potential contributing factors resulting in enhanced interface dilation and possibly also enhanced interface friction angles.

White & Bolton (2004) proposed a detailed explanation for this relaxation. They proposed that the mechanism of interface contraction provides the initial conditions for set-up of displacement piles in sand. Immediately after passing the pile tip, the distribution of radial stress (σ_r) with radius from the pile (r) is as shown by the curve OA in Figure. 2.9, created as the soil is pushed outward during flow around the pile tip. As the interface zone contracts, cylindrical cavity collapse of the stiff overconsolidated soil close to the pile shaft then leads to a sharp reduction in radial stress from the high value created during soil flow around the pile tip. As a result, the radial stress acting on the pile shaft (point B in Figure 2.9) is lower than beyond the zone influenced by the cavity collapse. Over time, the high gradients in the stress field around the pile relax, creating the radial stress distribution shown as curve OC, which shows an increase in the radial stress acting on the pile shaft and hence set-up.

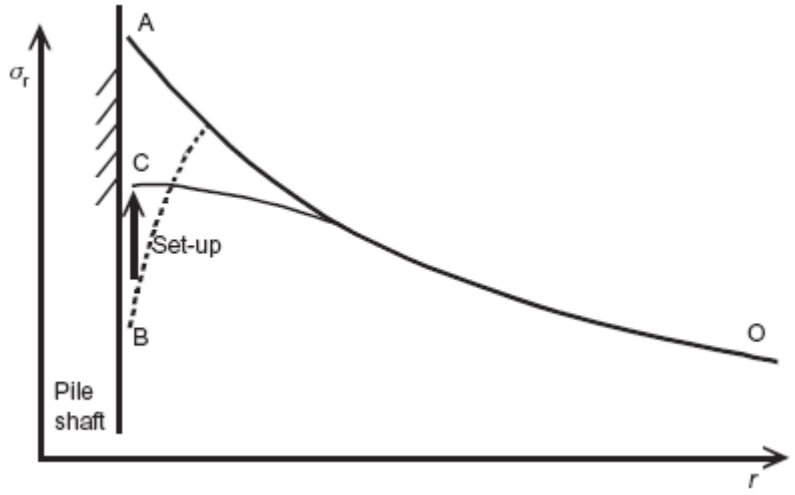

Figure 2.9: Radial stress distribution due to interface contraction (White & Bolton, 2004)

Research by Axelsson (2000) reported large increases with time in the horizontal effective stresses measured (in the field) on the sides of a 235 mm square concrete pile. Bullock et al. (2005) pointed out that the time-related increases in pile capacity are due either to a more dilatant response to loading, or to gains in interface friction angle. Bowman (2002) suggested that the creep volume changes (initiated by the intense shearing imposed during installation) are initially contraction as the soil grains rearrange themselves to redistribute stresses. However, Bowman argues that the creep straining gradually changes to become dilatant, both microscopically and macroscopically. As the kinematic restraint provided by the pile would inhibit expansion of the soil, any such tendency for dilation would lead to increased radial stress.

Jardine et al (2006) reported findings from a programme of first-time loading and retest experiments performed in dense sand at Dunkirk, northern France. The tests demonstrated more marked shaft capacity growth with time than expected. Shaft capacities rose over eight months to more than double those seen in load tests conducted a few days after driving. The aged piles also showed surprisingly brittle failure modes. Prior testing to failure both degraded capacity and modified the ageing

processes, leading to non-monotonic shaft capacity–time traces that fell far below the ‘intact’ ageing characteristic defined by tests on fresh, previously unfailed piles.

2.7 Effect of in situ state of sand

Coop et al (2005) carried out a series of pile load tests in a centrifuge model, investigating the influence of the in-situ volume–stress state on the load–deflection behaviour. A good correlation was found between the load–deflection behaviour and the in-situ state quantified by the distance of the initial state from the critical state line in the v–ln p' plane. How the soil arrived at its initial state, whether by compaction or overconsolidation, did not have a significant impact on the load–deflection behaviour. It was also found that the correlation was influenced strongly by the loading history prior to conducting the load test, with tests taken into a full-tensile condition before loading giving a much softer response than when the pile was held at a zero head load. However, repeated loading with a zero head load condition maintained between each cycle was not found to significantly influence the capacity or stiffness of response.

2.8 Visual analysis of pile installation

Many researchers have attempted to visualise and quantify the penetration mechanism around a pile tip, and the response of the interface layer adjacent to the shaft. Various image techniques have historically been used for observation of failure mechanisms and preceding displacements.

2.8.1 Radiography technique

Robinsky & Morrison (1964) used a Cobalt-60 source to illuminate lead shot around a model pile. The lead shot was arranged in a vertical plane through the centre of a test box, which was then filled with sand. Radiographs were obtained of the lead shot in the sand, before and after penetration in the model. The displacement of the image of the lead shot on the radiograph indicates actual sand movement. Figure 2.10 is a radiograph of a typical pile point (tip) showing the displacement pattern of sand in its immediate vicinity. A zone approximating the shape of a cone is found beneath the pile extending downwards and outwards from the edge of the pile. At the zone limits, vertical compression ceases and vertical expansion begins to take place.

Kobayashi & Fukagawa (2003) also used an X-ray CT imaging technique in combination with image processing to quantify the displacement (Figure 2.11). Three model penetrometers with different tip angles were used in the test. It was found that the tip form does not have significant effect on soil deformation.

The X-ray technique requires specific equipment and safety measures, and may not suitable for large displacement pile testing.

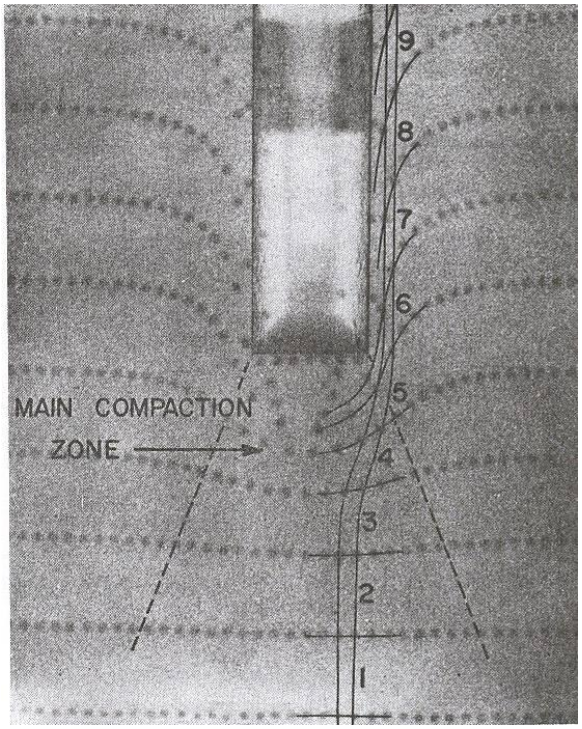

Figure 2.10: Radiograph of a typical pile point showing main compaction zone (Robinsky & Morrison, 1964)

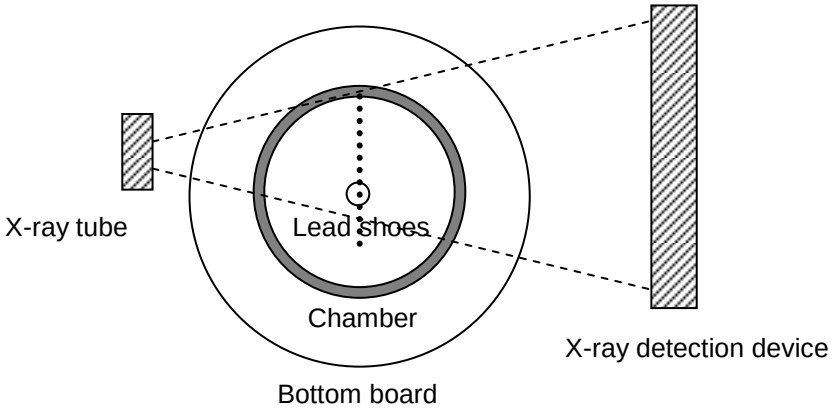

Figure 2.11: X-ray test apparatus (Kobayashi & Fukagawa, 2003)

2.8.2 Colored layers /bead-grid

Yasafuku & Hyde (1995) used different colored layers of sand to examine the displacement around a pile in a plane strain model. They found that the deformation 'bulb' beneath the pile tip strongly resembles that for a spherical cavity expansion in an infinite medium (Figure 2.12). Based on this observation, the authors propose that spherical cavity expansion theory is a suitable analytical method to predict the end-bearing capacities of piles in sand. An assumption is that the pressure exerted at the boundaries of the bulb of soil beneath the pile tip is equal to the limit pressure p_u required to expand a spherical cavity (see Figure 2.4 d).

Ohtomo & Tan (2001) used a bead-grid to measure the vertical and horizontal soil deformation. Fourteen rows of bead-grid were embedded in the soil. The soil container was a split cylinder, which could be dismantled into two halves. After the test, the cylindrical container was then turned into a horizontal position. The upper half container and soil was then removed to allow the final deformation of the bead-grid to be measured.

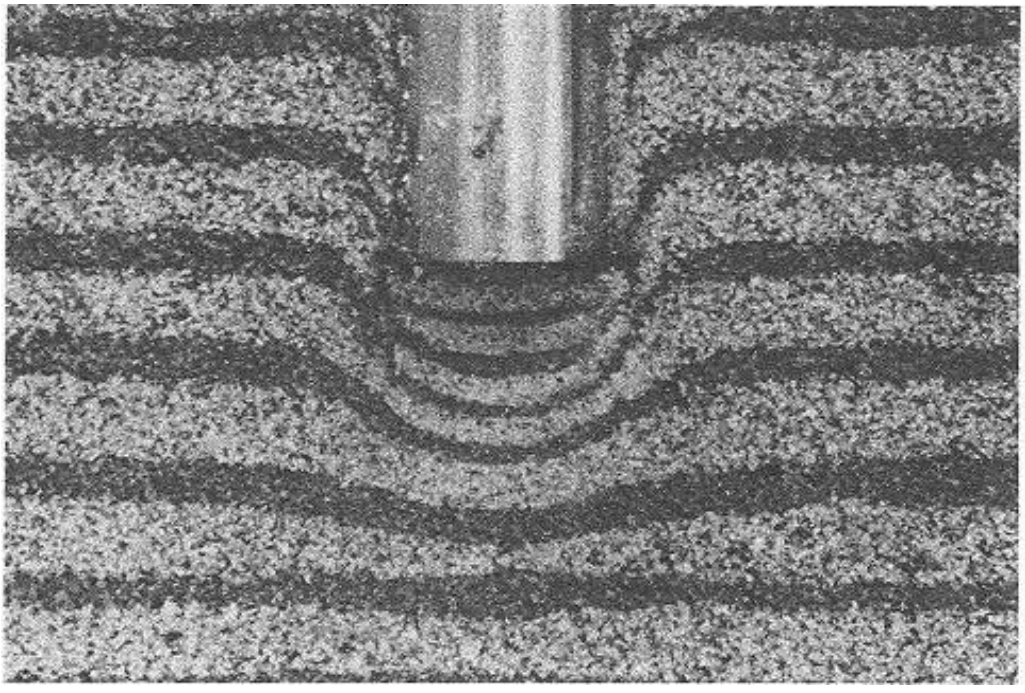

Figure 2.12: Pile tip failure mechanism observed by Yasafuku & Hyde (1995).

2.8.3 Stereo-photogrammetric method

Butterfield et al (1970) developed a stereo-photogrammetric method for measuring displacement fields. The height of the image at any point could be measured with a moving reference mark. If a soil element moves at one point, the height would be changed on the stereo-image, which is proportional to the soil element displacement. By taking a series of these photos, the soil displacement at one point can be measured during the test. The accuracy of standard photogrammetric plotting is about 0.01 mm on the scale of the photographic plate. Moreover, embedded markers or coatings are not required. In this method, it was assumed that the ratio between the image-space to object-space is constant across the field of view.

2.8.4 Laser speckle interferometry technique

De Pater & Nieuwenhuis (1986) used a laser speckle interferometry technique to investigate the displacement around a pile. Double-exposure photographs were made on high resolution film. By directing a laser beam through the negative, the sand displacement was measured with the aid of the interference pattern.

2.8.5 Photoelastically sensitive glass particles

Dijkstra et al (2006) used photoelastically sensitive glass particles to represented soil, which allows optical measurement of stresses. The displacements around the pile are measured using digital image correlation. It was found that there are also some upward movements and movement toward the shaft except for a wedge shape in a medium dense assembly. Both stress state change and stress rotations occur during pile installation. However, the ratio between pile diameter and particle size is only 5 which is much lower than the real field situation. The use of an artificial material rather than actual soil also leads to some question of the relevance to an actual soil.

2.8.6 PIV technique

Most of the techniques referred above rely on targets (lead shot or beads) within the deforming soil, or use of an artificial material to represent the soil. A dense grid of markers would influence the soil behavior, while a widely spaced grid of markers can't provide enough information (White et al, 2003).

White et al (2003) attempted to overcome these problems by using a novel image-based deformation measurement system based on particle image velocimetry (PIV) and close-range photogrammetry. This technique will also be used in the work described here. Tests were conducted in a plane-strain calibration chamber with windows to observe the soil deformation around the pile (which was actually a 'wedge' in the plane strain section). A stress of 50 kN/m^2 was applied to the surface of the sand to give soil behaviour more representative of conditions for a full-scale pile in the field. The following measurements were deduced from the captured images (White & Bolton, 2004):

(a) soil displacement during pile installation

(b) soil strain paths during pile installation

(c) streamlines of soil flow

(d) soil strain post-installation (i.e. as would be the case prior to loading of pile)

(e) soil movement adjacent to the pile shaft.

In fact some aspects of this work have already been referred to above, where it has contributed directly to the understanding of phenomena such as friction fatigue.

Two kinds of sands were used in the tests: Dog's Bay carbonate sand (DBS) and Leighton Buzzard silica sand (LBS). During DBS tests, an approximately constant value of q_b was reached which showed that a steady-state penetration mechanism was reached. This steady-state value of base resistance allowed the influence of initial soil state to be examined. They found that q_b increased as the initial relative

density increased. During LBS tests, a constant value of q_b was not reached, but significantly higher base resistance was observed than for the DBS. At a pile tip depth of 100 mm (3 diameters) the base resistance in tests of comparable relative density differs by a factor of 6-8 (White & Bolton, 2004). This distinction can be attributed mainly to the much more significant tendency for crushing of particles in the carbonate DBS.

Displacement paths during pile installation

The most straightforward illustration of the penetration mechanism is the displacement field around the pile tip. Figure 2.13 shows the displacement field observed in one of White & Bolton's (2004) tests. It was found that the deformation consists primarily of downward movement below the pile, moreover, horizontal displacement of 25 μm are detected in the far field, at an offset of 160 mm (5 times the pile diameter) from the pile centerline. The displacement vectors radiate from the pile tip downwards and to the side, a mechanism which is more comparable to cavity expansion rather than a bearing capacity type mechanism. However, although the contours of displacement follow a circumferential path immediately below the pile, these contours return to the pile shoulder, which is in contrast to a cavity expansion model.

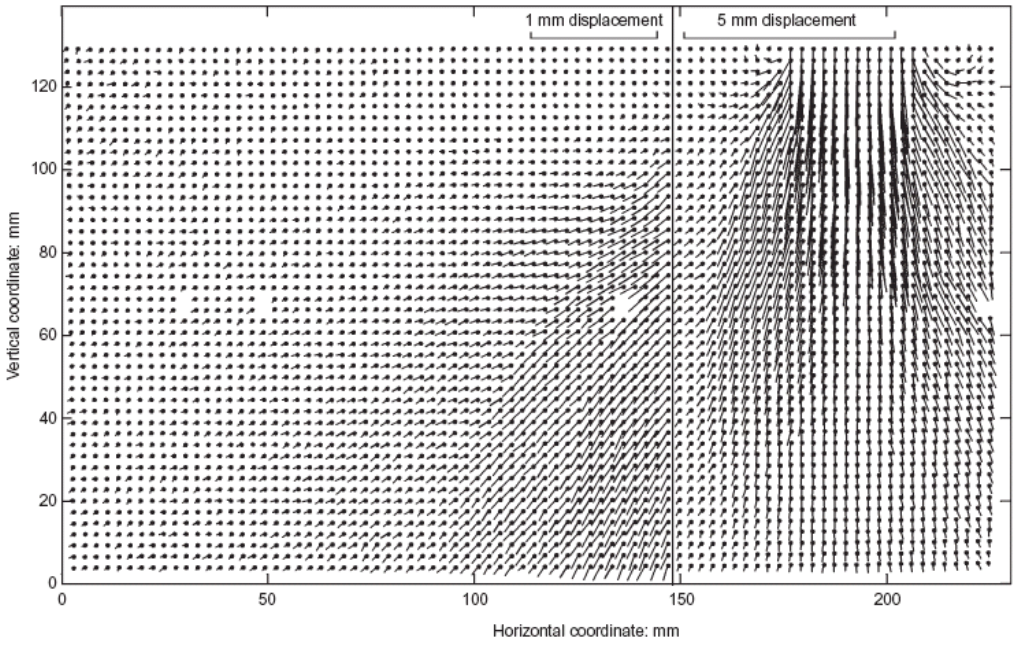

Figure 2.13: Displacement field around pile tip (White & Bolton, 2004)

The authors tracked the full displacement trajectories of two soil elements. Figure 2.14 shows an example observed from a LBS test. The coordinate origin is located on the centreline of the pile and level with the pile tip at the end of installation. As the pile approaches, the movement is generally downwards, with the soil element trajectory curving towards the horizontal as the pile passes. The final part of the element trajectory is upwards, although the net movement is downwards, in contrast to a bearing capacity mechanism. After the pile tip has passed the soil element (i.e. $h > 0$, where h is the vertical distance of a soil element above the pile tip), the soil relaxes back towards the pile shaft. The 'tail' of the trajectories recorded this movement and revealed the behaviour of the soil flow adjacent to pile shaft. The 'tail' shown in close-up on the right of Figure 2.14 for $h > 0$ represents the behaviour from Y to Z in Figure 2.8.

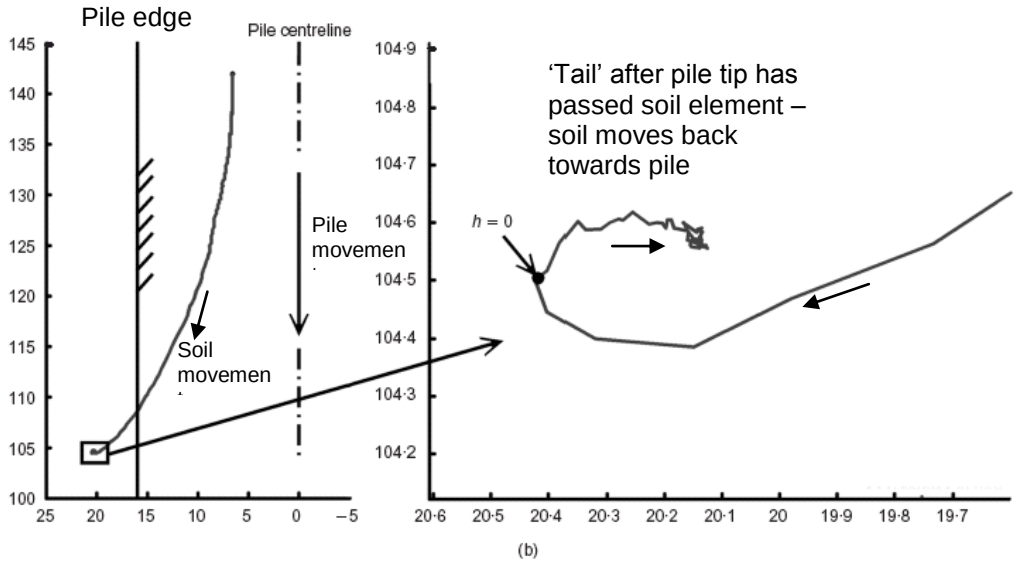

Figure 2.14: Soil element trajectories during pile installation (coordinates in mm) (White & Bolton, 2004)

The authors also found that the displacement trajectories for a given value of h are the same, independent of the original depth of the soil element. Therefore all trajectories from a single column of soil elements can be combined to provide the deformation pattern over a greater vertical extent below the pile tip than is visible at any given instant. This finding may be specific to the calibration chamber where there is virtually

constant in situ stress with depth (and hence constant plunging capacity was observed at the tip).

It was also found that the zone of downward displacement is concentrated closely around the pile shaft, whereas the horizontal displacement decays slowly with offset distance. Furthermore, the strain level adjacent to the pile is lower than below it.

Soil crushing immediately below pile

White & Bolton (2004) observed a region of highly crushed soil referred to as the 'nose cone' below the pile tip during tests (Figure 2.15(a)). This was observed even in the LBS, which has high crushing strength. Discrete slips of soil were observed to slide out from the nose cone and flow around the shaft of the pile ('coating' it as it penetrates). A central core of the nose cone is stationary relative to the pile tip, but the shoulders of the zone are not (Figure 2.15 (b))

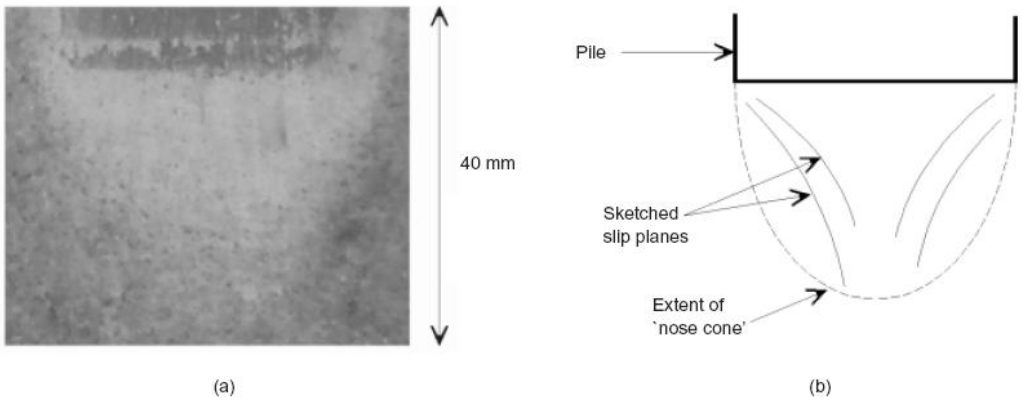

Figure 2.15: Soil below pile tip (White & Bolton, 2004): (a) 'nose cone' of soil beneath pile tip (b) slip planes observed within nose cone

Soil that flows through the nose cone and forms the interface layer adjacent to the pile shaft follows streamline ABC (Figure 2.16). Along streamline AB, very high stress and very high shear strain are encountered, leading to volumetric compression and significant particle breakage. This volume loss is irrecoverable due to the particle

breakage; therefore, as soil flows along the streamline BC, significant volume compression continues, creating a net increase in density. Also, the fines may 'migrate' into the surrounding soil causing further contraction of the zone of crushed soil immediately adjacent to the pile.

Soil in the near field follows streamline DEF. High stress and high shear strains are encountered along streamline DE, resulting in compaction and some particle breakage. On leaving the zone of high stress, the soil is heavily overconsolidated. Critical state theory predicts that this overconsolidated soil will dilate when in shear along streamline EF.

The volumetric strain at the end of streamline ABC and DEF reveals the variation of density with offset from the pile shaft, which is shown in Figure 2.16. Adjacent to the pile shaft, the soil has become denser, following irrecoverable volume change in the nose cone. In LBS, the dilation close to the pile shoulder caused a local loose zone.

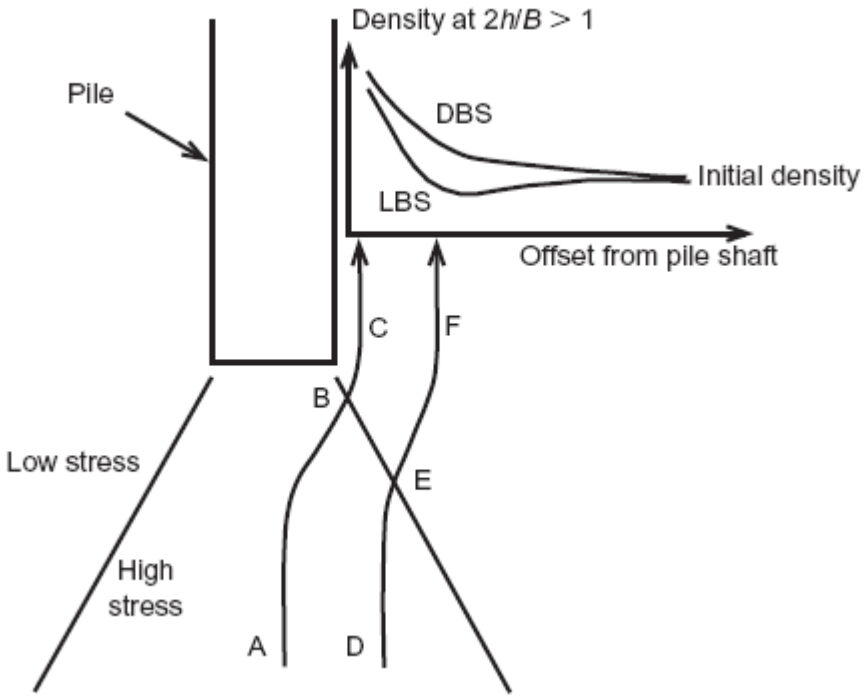

Figure 2.16: Volumetric behavior close to pile tip (White & Bolton, 2004)

2.9 Chapter Summary

The Cone penetration test (CPT) is widely used in geotechnical engineering practice. A large number of correlations between cone resistance and the engineering properties of soil have been developed ranging from wholly empirical to theoretical.

There are four main theoretical approaches for estimation of base resistance: (1) bearing capacity theory; (2) cavity expansion theory; (3) steady state deformation; (4) finite-element analysis.

Based on the CPT test, several empirical methods have also developed. Jardine & Chow (1996) proposed new design methods for offshore piles, referred to as the MTD method. In the MTD method base resistance for piles is reduced (as diameter increases) compared to the CPT resistance. This empirical relationship is based on back analysis of pile test data for various pile diameters. The mechanistic origin of this scale effect is not clear, and researchers have suggested a number of alternative reduction factors to convert q_c to q_b , based on different mechanistic hypotheses. White & Bolton (2005) argue that these reduction factors can be linked to: (a) partial embedment of the pile in a stronger layer; (b) local inhomogeneity; (c) partial mobilisation of base resistance in a stronger layer during a pile test; (d) the effect of residual stresses when interpreting pile test data.

Many researchers have attempted to visualise and quantify the penetration mechanism around an advancing pile, using methods such as: radiography technique, embedding colour layers or bead-grid, stereo-photogrammetry, and laser speckle interferometry. Dijkstra et al (2006) used photoelastically sensitive glass particles to represent soil, which allows for optical measurement of stresses. However, most of these techniques rely on artificial targets (lead shot or beads) within the deforming soil, or use the artificial material to represent the soil. These measurements may be poor representations of a real pile in soil.

White & Bolton (2004) attempted to overcome these problems by using a novel image-based deformation measurement system based on particle image velocimetry (PIV) and close-range photogrammetry (White et al, 2003). A zone of highly compacted soil was observed immediately below the pile tip and along the pile shaft. Crushed soil grains were observed with continued penetration of the pile. A mechanism was proposed to link this kinematic observation to the distribution of shaft friction close to the tip of displacement piles.

CHAPTER 3 - CENTRIFUGE MODELLING

3.1 Introduction

The use of geotechnical centrifuges in physical modelling provides many benefits to academic researches in the field of soil-structure interaction as well as practical design of geotechnical structures. This chapter introduces the basic concept of physical modelling by means of a geotechnical centrifuge and gives a general description of the Nottingham Centre for Geomechanics (NCG) Geotechnical Centrifuge. The details of the model reported in this thesis are also given.

The fundamental principles and limitations of geotechnical centrifuge modelling are given in section 3.2. The general description of NCG Geotechnical Centrifuge recently installed at Nottingham University is presented in section 3.3. Section 3.4 introduces the details of the model components such as container, actuator, probe, and cameras.

3.2 Centrifuge modelling

Centrifuge model testing represents a major tool available to the geotechnical engineer, particularly for research purposes. Soil models are placed at the end of a centrifuge arm and subjected to acceleration many times larger than the Earth's gravity. Soil held in a model container has a free unstressed upper surface and within the soil body the stress increases with depth at a rate related to the soil density and the magnitude of the acceleration field.

3.2.1 Scaling laws for quasi-static models

For a centrifuge model subjected to an inertial acceleration field of *N* times Earth's gravity, the vertical stress at depth h_m will be identical to that in the corresponding 'prototype' at depth h_p where $h_p = N h_m$.

This is the basic scaling law of centrifuge modelling - that stress similarity is achieved at points by acceleration of a model of scale (1/*N*) to *N* times Earth's gravity. Table 3.1 summaries the scale factors relevant to common geotechnical applications of centrifuge modelling.

Table 3.1: Scale factors for centrifuge modelling

Quantity	Units	Scaling factor (prototype/model)
Acceleration	m/s^2	1/N
Density	kg/m^3	1
Unit weight	N/m^3	1/N
Linear dimension	m	N
Area	m^2	N^2
Volume	m^3	N^3
Stress	N/ m^2	1
Strain	Dimensionless	1
Force	N	N^2
Force/unit width	N/m	N

3.2.2 Particle size effects

According to the scaling law, it would seem that the soil particle size should be reduced by a factor of *N*. For instance, if the particle size is 0.2 mm in the prototype, according to the scaling law, the sand particle size should be 0.002 mm for a 100g centrifuge test. Thus clay used in a centrifuge test might be considered as representing fine sand at equivalent prototype scale. However, clay has very different stress-strain behaviour compared to fine sand. Therefore, rather than scaling particle size it is common to use the same (or at least similar) size of soil particles in a centrifuge test as in the prototype, so that stress-strain behaviour is realistic. However, it is then necessary to assume that the soil behaves as a continuum in the centrifuge.

Ovensen (1979) developed simple guidelines on the critical ratio of a major dimension in the model to the average grain size through a series of centrifuge tests on circular

foundations on sand for different model sizes. It was suggested that the ratio between the major model dimension and the average grain size diameter should be greater than 15. However it should be noted that this guideline contains inadequate information to completely assess the particle size effects because the interaction between soil and structure occurred due to the mechanism of localisation of the deformation in shear bands. Foray et al. (1998) showed that the thickness of the shear bands is mainly related to the average size of grains, and hence there are likely to be issues regarding scaling of this effect in centrifuge tests where relevant. In a paper on the subject of shaft resistance of non-displacement piles in sand, Loukidis & Salgado (2008) note that the ratio of grain size to pile diameter is unusually large in laboratory studies, which may affect the shaft resistance.

Gui et al (1998) report cone penetration tests in sand in centrifuge models, considering a variety of effects including the ratio of the probe diameter to the average grain size d_{50} for the sand. As this ratio falls below about 20 there is some evidence of effect on the tip resistance, with significant effect observed when the ratio drops to about 10.

3.2.3 Non-uniform centrifugal acceleration

It is often assumed that a gravitational acceleration field is uniform and acts vertically. However, an inertial 'gravitational' acceleration field in a centrifuge deviates slightly from this. This is because the inertial acceleration field is given by $r\omega^2$ where ω is the angular rotational speed of the centrifuge and r is the radius to any element in the soil model. The nominal distribution of vertical stress in the model is shown in Figure.3.1.

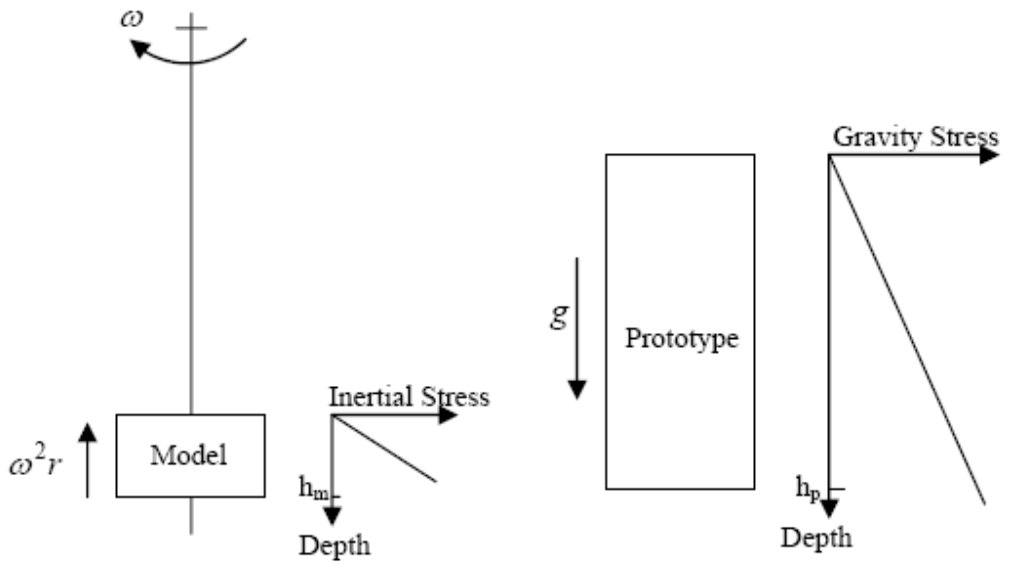

Figure 3.1: Stress distributions with depth for prototype and centrifuge model (Schofield, 1980)

It is therefore necessary to assess the stress error caused by non-uniformity of centrifugal acceleration for a particular model geometry. The ratio of the 'height' of the model to the effective centrifuge radius for the model determines the maximum 'under' and 'over-stress' (Taylor, 1995). The vertical stress in the prototype at depth $h_p = Nh_m$ is given by: $\sigma_{vp} = \rho g h_p = \rho g N h_m$, while the stress at depth z in the model can be determined as: $\sigma_{vm} = \rho \omega^2 z(R_t + z/2)$, where R_t is the radius of the top of the soil.

If gravity is 'correct' at 1/3 depth in the model then the maximum under-stress occurs at this depth:

$$z = \frac{1}{3} h_m$$ (where h_m is the thickness of the soil in the model)

The ratio r_u of maximum under-stress (error in stress) to the nominal stress at this depth is given by

$$r_u = \frac{h_m}{6R_e}$$ (where R_e is the radius at which gravity is correct $= R_t + h_m/3$)

The maximum over-stress occurs at depth

$z = h_m$ (the base of the model)

and the ratio of the error to the nominal stress (r_o) is again $(h_m / 6R_e)$

The vertical stress in the model and prototype are identical at depth

$$z = \frac{2}{3} h_m$$

In this project for the 50g tests, the top of the model is at R_t = 1.63 m, the effective radius is R_e = 1.75 m, the base is 2.00 m, $h_m = 0.37$ m, and γ = 17 kN/m^3 at 1g for the test soil. The two ratios r_u and r_o of maximum under-stress and over-stress to the prototype stress are given by $r_u = r_o = \frac{h_m}{6R_e} = \frac{0.37}{6 \times 1.75} = 0.035$, which is not significant. The result is illustrated in Figure 3.2.

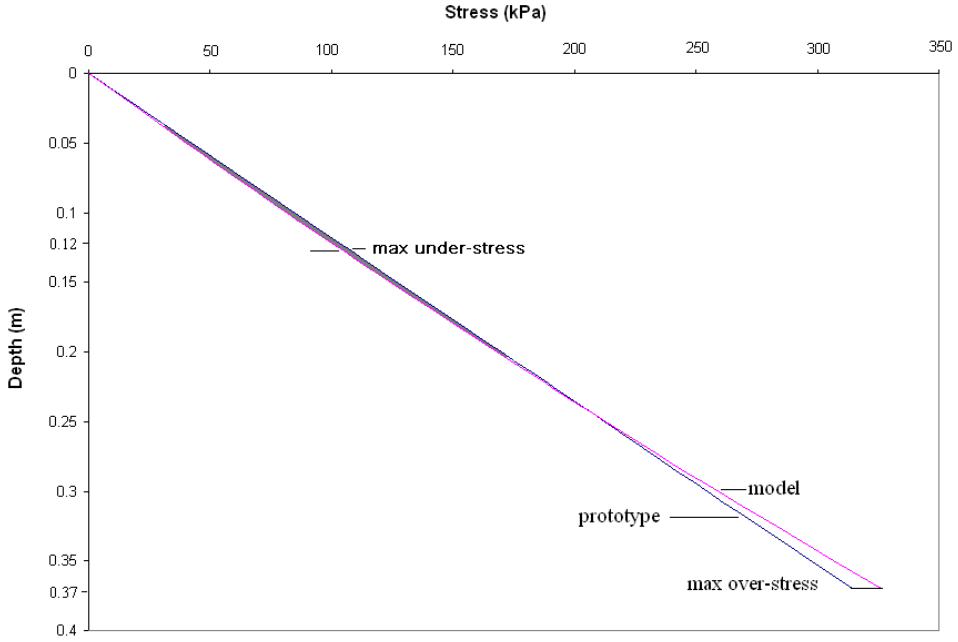

Figure 3.2: Comparison of stress variation with depth in the centrifuge model and the corresponding prototype (50g)

A further difference between a centrifuge model and actual gravitational acceleration is that the acceleration field is radial in a centrifuge. The 'vertical' direction is normally

radial at the centre of a centrifuge model, but the 'vertical' sides of the box will not be exactly radial (in one plane at least), and thus the acceleration will also have a horizontal component in the model. This effect increases with the tangential separation of the sides compared to the radius in the model.

In the work reported here, at a nominal radius of 1.75 m, at a distance of 100 mm from the centre of the model the deviation of the acceleration from 'vertical' is 3.3^{o}, increasing to 8.1^{o} at the edge of the model (a distance of 250 mm from the centre).

Zeng & Lim (2002) presented numerical simulations of this effect and concluded that error in the horizontal stress distribution is more significant than that in vertical stress distribution regardless of the radius of the centrifuge and the size of the model container (for a practical range of values).

Despite the non-uniform stress distribution within centrifuge models, experimental results from the centrifuge will be similar to results for the equivalent prototype. This is because important events which are of a major interest in centrifuge modelling normally occur around the middle of the container where there is least effect from non-uniformity of the acceleration field. As indicated by the equations above the effects are inherently reduced when the model is small compared to the effective radius.

The stress field generated by non-uniform centrifugal acceleration also leads to the effects of Coriolis acceleration which are developed when there is free movement of the particles within the model during flight. However, this effect will not be of significance in the context of the work considered here.

3.2.4 Boundary effects

Due to the finite space in a geotechnical centrifuge, it is necessary to construct the model within the finite boundaries of a model container. It is widely recognised that these boundaries lead to slightly inaccurate simulation of field situations that are of

‘infinite’ lateral extent (however, in reality field situations do not extend to infinity with uniform ground conditions). In practice it is desirable that the boundaries should be ‘sufficiently remote’ that they do not have significant impact on behaviour at the point of interest in the model.

Gui et al (1998) report that the ratio of circular container diameter to penetrometer diameter is required to be more than about 20 to minimise the effect of the boundaries on penetration resistance.

‘Plane strain’ models effectively have infinite extent in a direction normal to the plane considered. However, this does require that the boundary is frictionless – a situation which cannot be completely achieved in the model. This also applies to any boundaries which are not remote, but are a geometrical line of symmetry in the situation considered. The research considered here will examine the novel use of such a boundary in axisymmetry (a ‘window’ through the middle of a circular container). The potential effect of friction at this boundary will be discussed in due course.

3.3 NCG Geotechnical Centrifuge facilities

3.3.1 NCG Geotechnical Centrifuge

The Nottingham Centre for Geomechanics (NCG) Geotechnical Centrifuge broadly consists of the following components:

(1) Geotechnical beam centrifuge

(2) Centrifuge chamber

(3) Data acquisition system (DAS)

The NCG Geotechnical Centrifuge, manufactured by Broadbent G-max, is a typical medium-size beam centrifuge with one swinging platform, and a payload capacity of 500 kg at up to 100g at a nominal radius of 1.70 m (the platform radius is 2.0 m). The maximum acceleration is 150g, with reduced payload. Table 3.2 gives further information.

Table 3.2: Centrifuge specification.

Platform radius	2.0 m
Assumed effective	1.7 m
Max. size of payload	0.8 m wide (vertical in flight)
	0.6 m wide (circumferential in flight)
	0.9 m high (radial in flight)
Max. payload	850 kgm (500 kg at 1.7 m) up to 100g
Max. acceleration	150g (at 1.7 m)
In-flight balancing	+/- 50 kgm
Motor	75 kW 3 phase induction motor

The swinging platform is primarily balanced by a counterweight of fixed mass whose position is manually adjustable to discrete locations, for payload masses between 200 and 500 kg. A secondary automatic ‘in-flight’ balancing system monitors any ‘out of balance’ force, and pumps oil in the centrifuge arms from one side to the other to correct the imbalance (where this can be achieved with the mass of oil). The centrifuge automatically shuts down when the tolerable out-of-balance load of +/– 30 kN is exceeded.

Several power slip rings are linked to the top of the DAS cabinet for AC power distribution and DC supplies on the model. Two hydraulic slip rings allow both air and water to be supplied to the model. Data from transducers is digitised and transmitted via a 'fibre optic rotary joint'. The Acqlipse™ data acquisition programme logs up to 256 channels adjustable at various logging rates from 0.01 to 10 Hz.

For the work described in this thesis a rack mounted PC was added to the DAS cabinet to provide local control of the cameras via the PC's USB (Universal Serial Bus) connections. The inclusion of a PC local to the model significantly reduces the USB cable length required to connect the cameras to a controlling PC. Moreover, it avoids the need to transmit the USB signals through the slip rings, which can be problematic as noise is introduced which can cause the camera connection to fail. The rack mounted PC was controlled from the control room using an ethernet remote desktop connection via the fibre optic rotary joint.

Figure 3.3 shows the main components of the centrifuge.

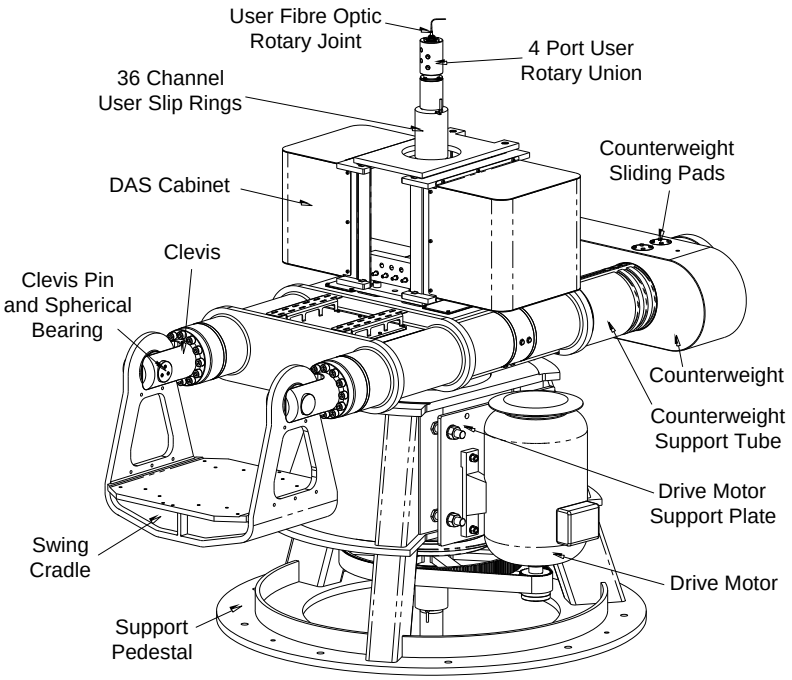

Figure 3.3: Schematic diagram of the NCG Geotechnical centrifuge apparatus (Ellis et al, 2006)

3.3.2 Image data

Various image techniques have historically been used for observation of failure mechanisms and preceding displacements in a centrifuge model, for example

(1) Markers implanted in the soil adjacent to a front window, or at the soil surface,

(2) Lines of coloured sand on the front of a model,

(3) Coloured thin spaghetti,

(4) Threads of lead within the soil body, later located using x-ray images.

In cases 1-3 it is necessary to monitor deformation using video or still images 'in flight' as the test proceeds, or more simply before and after the test.

More recently, the application of digital image analysis to geotechnical centrifuge models has enabled large amounts of movement data to be obtained during tests. White et al. (2003) developed this digital processing system based on digital photography, particle image velocimetry (PIV) and close-range photogrammetry for deformation measurement of geotechnical models (both at 1g and in centrifuge models). The visual 'texture' of 'patches' of soil is tracked without the need for embedded markers. Using the GeoPIV system this technique has been employed on the NCG Geotechnical Centrifuge using digital cameras mounted within the model package to gather in-flight images.

Figure 3.4 summarizes the principle of GeoPIV analysis. The first image was divided into a grid of test patches as shown in Figure 3.5. Considering a patch located at (x_{1m}, y_{1m}) on image 1 ($t = t_1$), to find the displacement between images 1 and 2, a slightly larger search patch is used in the second image ($t = t_2$). The cross-correlation of the original patch and searcher path is evaluated and normalised. The highest correlation of the new and original patches indicates the displacement vector of the test patch. The location of the correlation peak can be established to sub-pixel precision by bicubic interpolation. GeoPIV provides the movement of the patches in pixels from one image to another. These movements in the image space then converted into soil displacement using the colinearity equations (Cox, 2005). The effect of the refractive

index of the Perspex window will discussed further below.

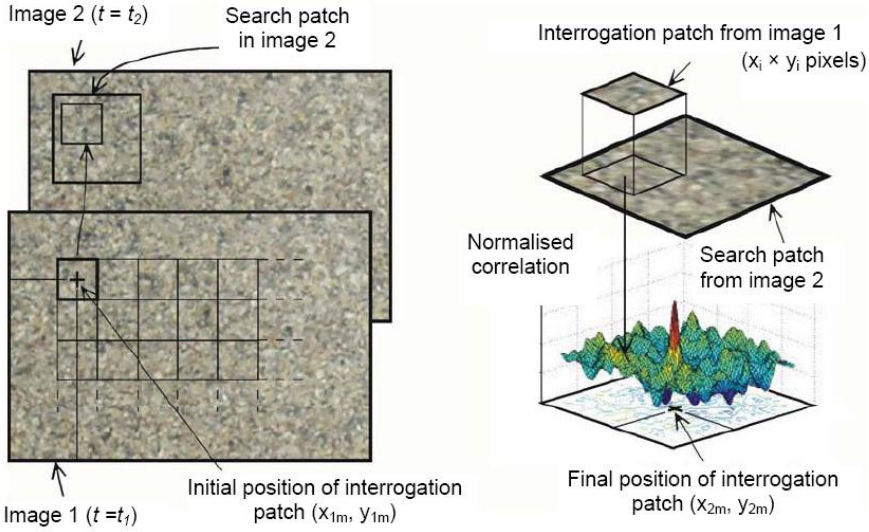

Figure 3.4: Image manipulation during PIV analysis (White et al, 2003)

PIV analysis procedure

Digital image processing based on GeoPIV was carried out by the following steps:

1. A sequence of digital images was taken during a test.

2. A mesh of test patches, of size 75×75 pixels, was created for the first image in the sequence (Figure 3.5).

3. A 'template launch file' was created which included the images to be analysed, analysis parameters to be used, and the location of the initial mesh of patches.

4. The GeoPIV software was then used to track displacements of test patches for each consecutive image pair in the sequence. The displacements (in pixels) were then stored as text files.

5. Anomalous 'wild' (erratic or erroneous) displacement vectors were eliminated.

6. Control point positions (known locations in the model object space) were defined from the first image (Figure 3.7) and used to determine the position, attitude and any in-test movement of the camera relative to the model object space.

7. The displacement vectors in image space (pixel coordinates) were then converted into model object space (XYZ coordinates) by solving the collinearity equations; using

the camera position, attitude and focal length (again, the effect of the Perspex window is considered below).

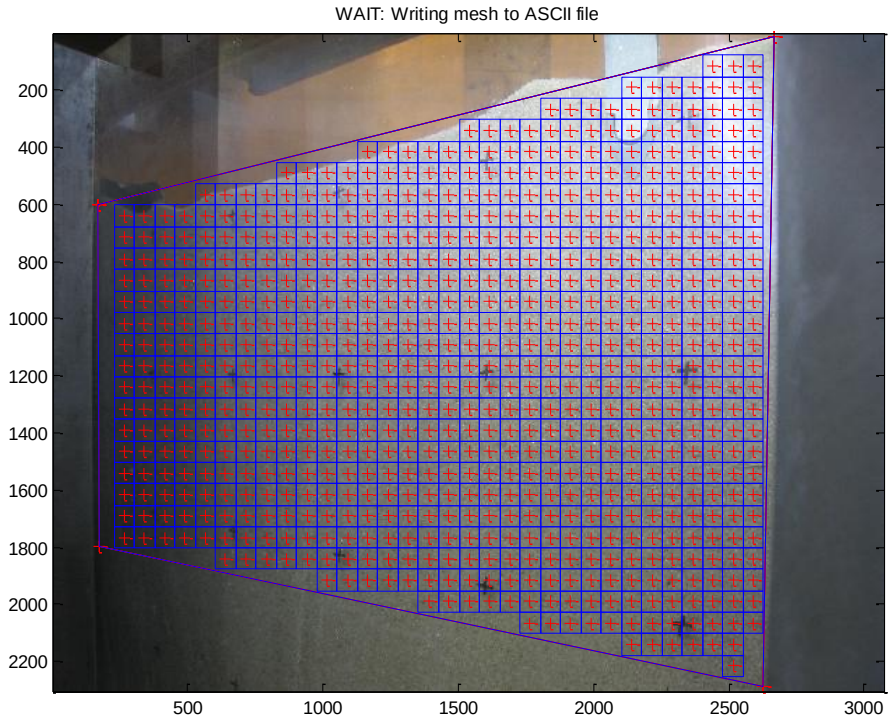

Figure 3.5: Initial test mesh (75 × 75 pixels)

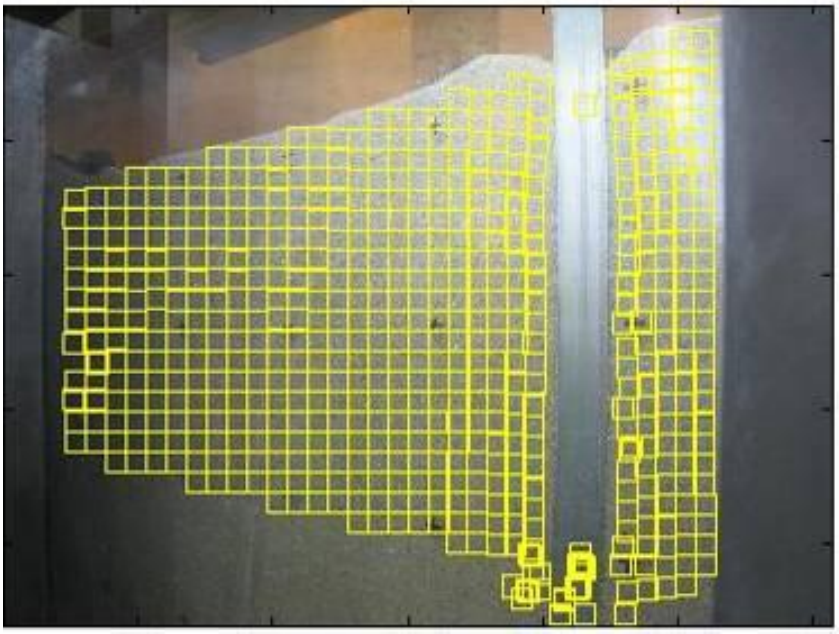

Figure 3.6: Distorted mesh after GeoPIV analysis at the end of the test.

Figure 3.7: Control points

3.3.3 Refraction at window

The 3D camera location and orientation was established from the control points via the colinearity equations. This process was then reversed to establish the model location of PIV patches, which were known to lie in a vertical plane against the window, and hence images from one camera were sufficient to do this. The effect of refraction by the window was not explicitly considered in either direction of this process. Hence the camera position and orientation were 'artificial', with the camera appearing to be closer to the window than it actually was (Figure 3.8), but this was largely compensated by the neglect of refraction.

Sensitivity calculations accounting for refraction (see Appendix B) indicated that the error in determination of position would be up to about 1 mm (primarily because the cameras did not point directly at the window). This value was confirmed by the accuracy with which the location of control points throughout an image could be 'matched' by optimising the camera location and orientation in the associated software. Furthermore it also reflects the accuracy of physically positioning the control points in the model. Determination of movement (rather than absolute position) of a soil 'patch' would have been subject to a much smaller error from the effects of refraction, and thus the approach was considered acceptable.

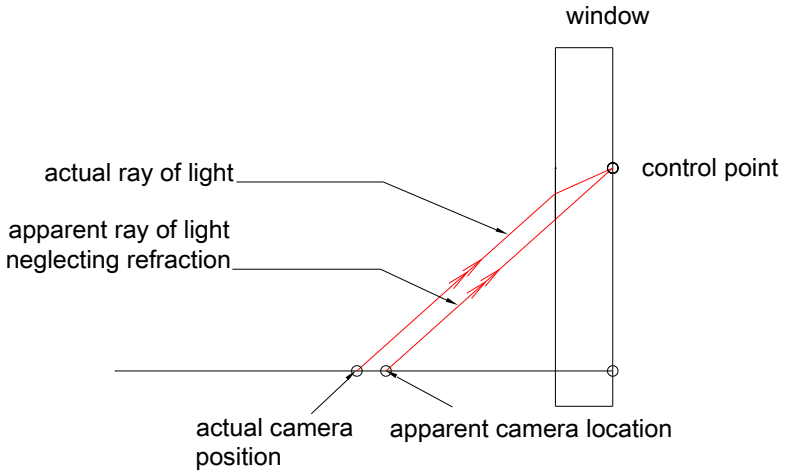

Figure 3.8: Schematic illustration showing artificial apparent camera position neglecting the effect of refraction.

3.4 Apparatus

3.4.1 Tub and window

The project used an 180^o axisymmetric section, which allowed movement of the soil to be observed whilst maintaining axisymmetric conditions. The concept for the 180^o axisymmetric technique is shown in Figures 3.9 and 3.10. Figure 3.11 shows a general view of the actual apparatus. The actuator and reaction frame for the penetrometer were mounted on top of the tub (see below).

The window was mounted across the centre of an existing 500 mm diameter (and 500 mm deep) centrifuge modelling 'tub', retaining the soil model on one side and leaving room for cameras to be mounted (using gantries) on the other side. The window carried load from the soil it retained, and also provided a reaction to the half probe which slid down it. To minimise deformation of the window it was braced against these loads along all four edges, and also along a vertical line near the half width (but not actually down the mid point since this would have obscured the view of the probe).

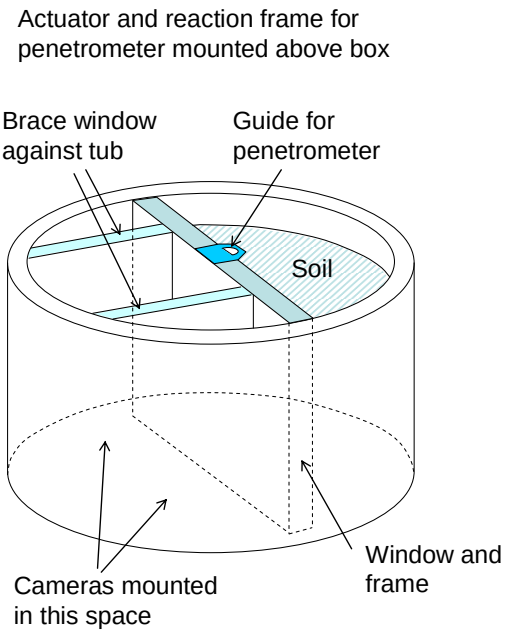

Figure 3.9: Window forming 180^o section in 500 mm diameter axisymmetric tub

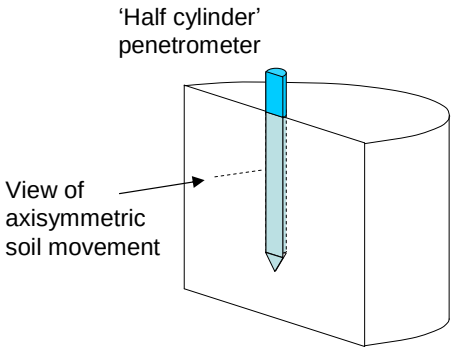

Figure 3.10: View of the penetrometer and soil

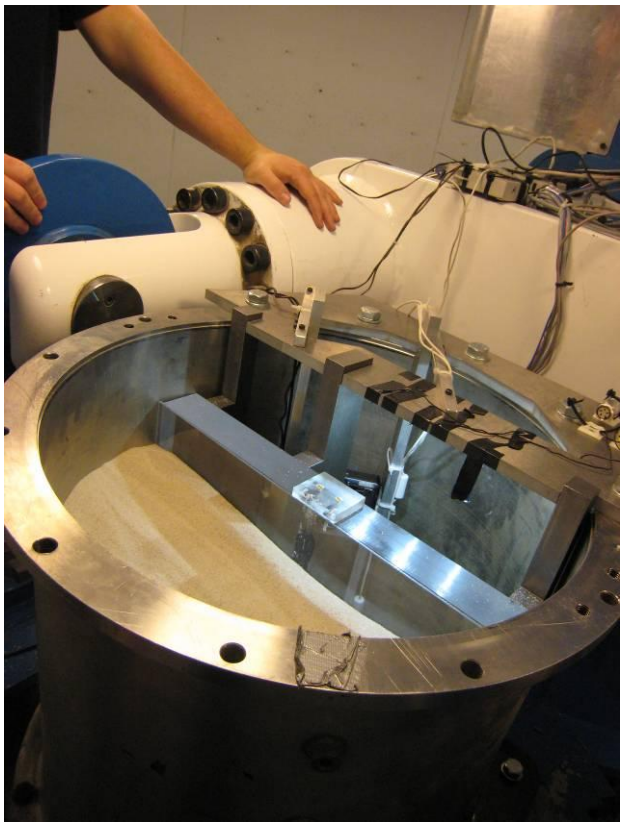

Figure 3.11: Photo of the tub mounted on the centrifuge

3.4.2 Actuator

The actuator and reaction system were mounted above the tub, and drove the probe into the soil at a rate of approximately 1 mm/s up to a maximum load of 10 kN.

The system (Figure 3.12) was based on an electro-mechanical linear actuator. The probe was pushed into the sand by means of the motor acting through a gearbox and lead screw. The design attempted to reduce the eccentricity of the probe from the lead screw, since this would generate a corresponding moment. Nevertheless, some eccentricity was inevitable unless the probe and screw were 'in line', but there was not sufficient height to do this. The moment was ultimately resisted by the 50 mm diameter steel 'reaction bar', whilst the probe/reaction bar connector slides up and down the bar on linear bearings which supply the necessary normal reactions for a couple.

3.4.3 Actuator control system

The motion of the actuator, and hence the probe, was controlled using the centrifuge's rack mounted control unit and a Labview program written for this purpose. The 'front panel view' of the control algorithm which the operator would use is shown in Figure 3.13 A potentiometer was fitted to the probe/ reaction bar connector to measure position, from which speed was also derived. A basic control algorithm was developed to supply a control voltage to the motor control electronics, mounted on the beam, which then generated a Pulse Width Modulated (PWM) drive signal to give the desired constant rate of penetration. Micro-switches were also fitted to the gantry and monitored by the software to detect when the probe had reached its limits of travel. Hard-wired limit switches to cut off the signal to the motor were also used in case the micro-switches should fail.

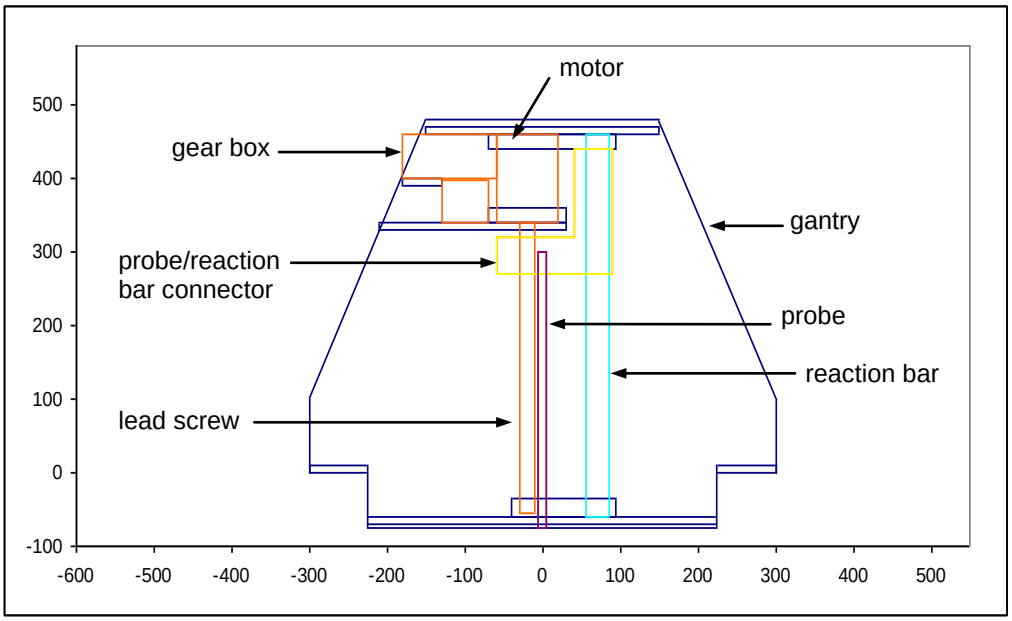

Figure 3.12: Actuator drive system and gantry

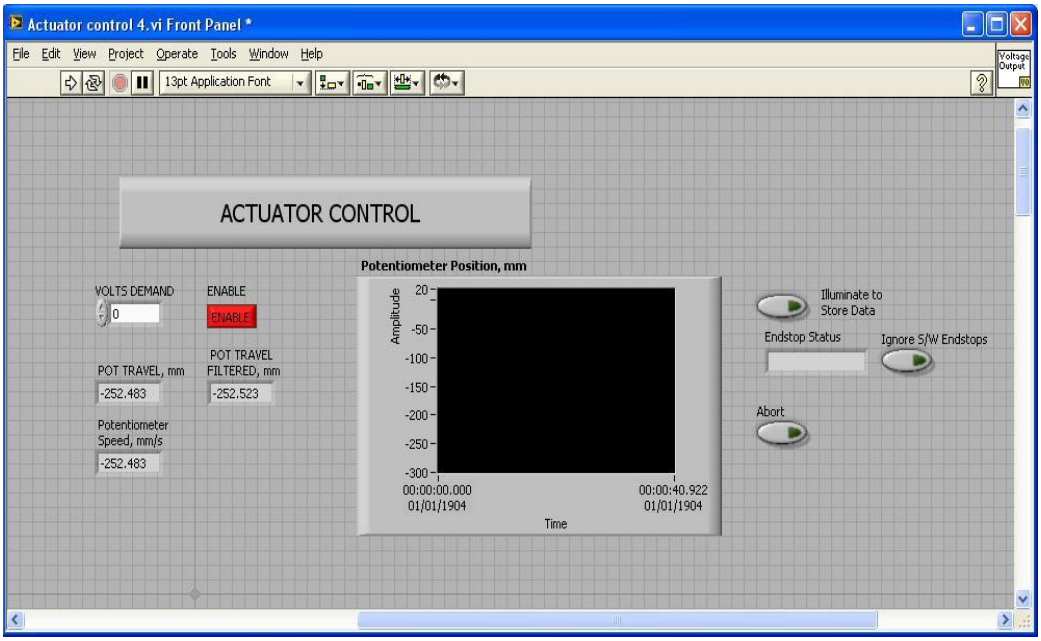

Figure 3.13: Actuator control system user interface and display

3.4.4 Probe and instrumentation

A probe with 12 mm diameter and 300 mm length was manufactured from a solid steel bar (Figure 3.14). The bar was machined to a half section, and had a slot machined along it to accommodate strain gauges and wires. A 60^{o} cone was machined at the tip. Evolution of the probe design and further details are discussed below.

A 12 mm diameter cone was selected for two reasons. Firstly, the ratio of the tub to penetrometer diameter is 500/12 = 42, which implies that boundary effects should be minimal (Gui et al, 1998). Secondly, using Leighton Buzzard Fraction C sand, the ratio of the probe diameter to the d_{50} size is 12/0.5 = 24, which should be sufficient to minimise any effects associated with particle size (Gui et al, 1998).

At a typical acceleration of 50*g* in the centrifuge the probe will correspond to a pile of 0.6 m diameter and 15 m length, which is comparable with the typical size of full-scale driven piles.

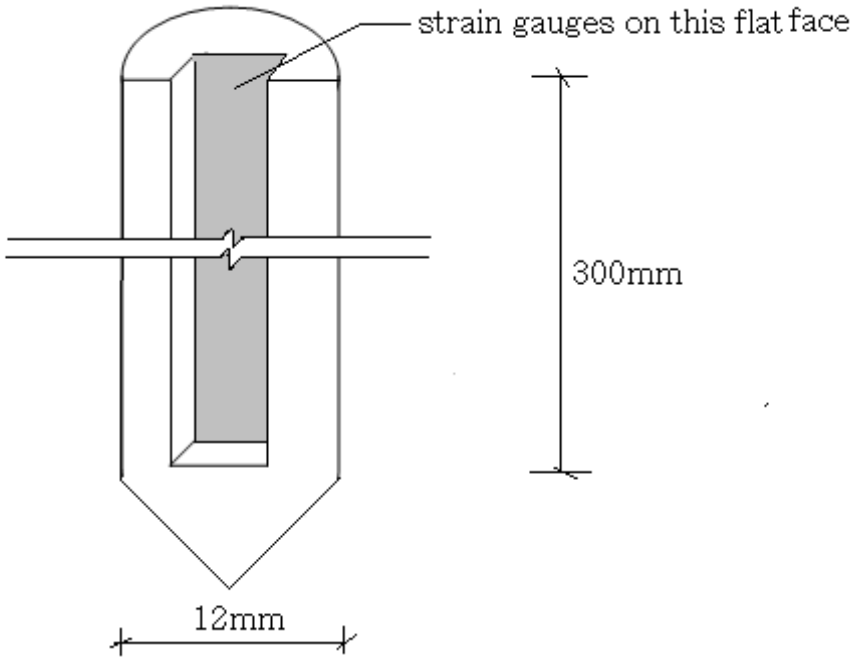

Figure 3.14: Schematic of 180^{o} probe

Evolution of the probe design

The most fundamental issue was to maintain contact between the penetrometer and the window as it advanced, and to prevent sand becoming trapped between the two. The rigidity and compressibility of the penetrometer were found to be key factors in this respect.

A suitable compressible material can be used to fill any small gap between the window and the penetrometer. The first attempt was to stick compressible foam on the probe (Figure 3.15(a)). A number of different types of foam were tried at this stage in an attempt to find a suitable compressibility. However, sand entered the gap at the tip of the probe no matter which type of foam was used.

To improve the strength of the tip, the foam on the tip was replaced by a steel plate (Figure 3.15(b)). This modification resulted in the tip maintaining contact with the glass window, but the stresses at the steel tip caused the adhesive between the tip and probe to fail and the tip to move slightly, and sand would then ingress along the shaft of the probe. In order to overcome these problems, it was decided to machine a new type of probe with a raised tip (thus eliminating the need to stick the tip with adhesive).

To improve the strength of the shaft part of the probe behind the tip, 1 mm aluminium plate was added here to 'sandwich' the foam (Figure 3.15(c)). This 'sandwich' probe behaved better than the previous attempt. However, sand would gather at the interface between the tip and the aluminium plate and push the probe away from the window. Figure 3.16 shows a detail where the foam at the foam-tip interface is confined by the shape of the raised tip. The new design also has a tip with a smaller surface area, therefore, friction between the glass and the tip is minimised.

The final design of the probe (Figure 3.16 and 3.17) used a 300 mm long 12.0 mm diameter solid steel bar as its starting point. A conical tip was then machined at one

end. The bar was then annealed and machined down to half it's diameter to give a semi-circular cross section. The bar was left at the full diameter and threaded over a length of 10 mm at the 'top' end where it screwed into the probe/ reaction bar connection (Figure 3.12), which was restrained against rotation. Thus the probe was effectively clamped against rotation at the point of connection to the actuator (but flexurally not that stiff over its cantilevered length below this).

The shaft of the probe (but not the tip) was then machined down by a further 2.0 mm, and a further channel with width 5.0 mm and depth 2.0 mm was also machined out to accommodate strain gauges and associated wires (Figure 3.17). The strain gauge instrumentation is discussed further below.

The 1.0 mm thick and 12.0 mm wide aluminium strip was used on the face of the shaft, with the remaining nominal 1.0 mm thickness occupied by a strip of foam. This foam provided the compressible element of the shaft. When uncompressed it's thickness was approximately 3 mm, but this reduced to a minimum value of about 0.5 mm under the application of moderate pressure.

The step size and compressibility of the foam were both varied in initial experiments. If the step was too small or the foam was too stiff, the tip tended to 'lift' from the window, presumably because there was significant stress between the shaft and window at some point. On the other hand, if the step was too big, or the foam was too compressible, sand could become trapped between the aluminium strip and window. Of these two situations it was considered more problematic when the tip lifted from the window, since this normally ultimately resulted in the probe separating over the full length. Thus it was considered acceptable if some sand became locally trapped on the shaft provided the tip remained in contact, and this resulted in the choice of step size and foam which were ultimately used.

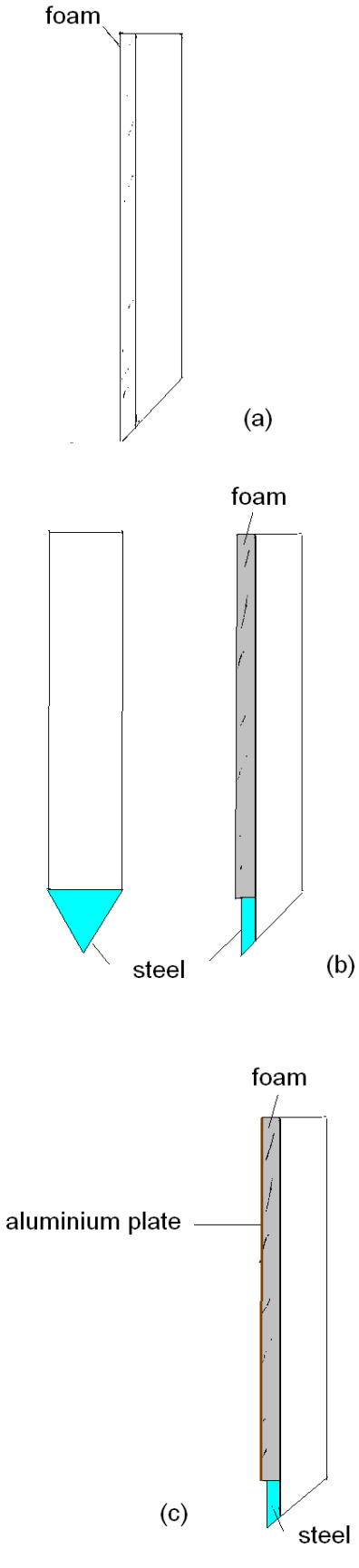

Figure 3.15 Evolution of the pile design

(a) Front view (b) Left view

Figure 3.16: Photos of final pentrometer design

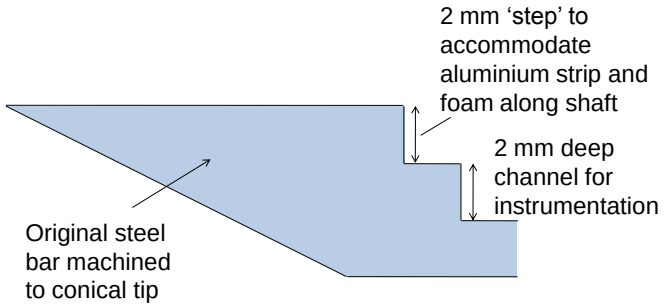

(a) Section through center of probe at tip

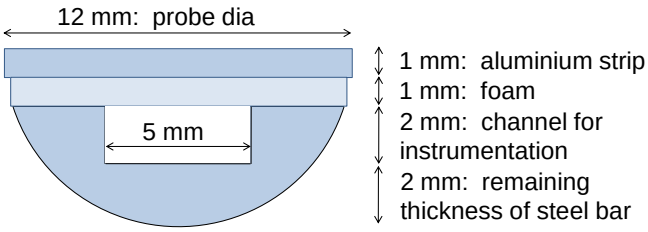

(b) Section normal to axis of probe showing detail on shaft

Figure 3.17: Details of probe at tip and along shaft.

Strain gauges

The probe was instrumented to measure axial load at 6 locations at 25 mm intervals from the tip. The strain gauges were located in the channel shown in Figure 3.17. The strain generated in the pile is transmitted to the foil strain gauge where contraction (or extension) occurs; consequently the gauge experiences a variation in resistance which is proportional to the strain. Each gauge is arranged into a Wheatstone quarter-bridge circuit; where the active gauge only forms one of the four resistors in the circuit. The strains and the change in resistance are very small, and consequently the signal is amplified before being digitised for logging. Quarter bridges were used due to the limited space available in the channel, which had to accommodate the strain gauges and wires.

The depth of the channel was also chosen so that the strain gauges would be close to the neutral axis of the probe. The probe was prone to bending along the shaft where the foam was intended to reduce contact pressure with the window (so that the tip did not lift). However, this would also potentially cause bending which would affect measurement of axial load.

The probe was calibrated by applying axial load in a loading frame, with external support to prevent bending.

Setting up the probe before the test

Setting up the probe prior to a test proved to be an important factor in keeping the probe against the window.

First the threaded top of the probe was screwed into the probe/ reaction bar connector with the actuator. The actuator was then lowered on to the top of the model container. A ‘guide’ was then fixed at the top of the window to hold the tip of the probe in the correct position and orientation against the window (Figure 3.9). This might also require slight movement of the gantry. A piece of paper was used to check for any

small gap between the tip and window. If paper could get into the gap, then crushed sand would also get in during the test as the paper thickness is similar to the crushed sand grain size.

3.4.5 Cameras

Two digital cameras (Canon powershot S70) were mounted in the tub to obtain soil movement data, mounted one above the other. The position of the cameras, as shown in Figure 3.18 (a) ensured that at least half the full window area could be observed. This should sufficiently reflect the whole soil behaviour due to the model symmetry. The Figure 3.18 (b) showed that the two cameras could view 200mm probe penetration.

The cameras were controlled independently by the rack-mounted PC using a Matlab program which captured images at approximately 5 second intervals. During the test, images were stored on the camera's 1 GB memory card as it was impractical to transfer the images to the PC at the rate that the images were taken. The centrifuge rack PC was controlled remotely from the control room using Windows Remote Desktop. After a test, images were transferred from the camera's memory card via the rack PC to the centrifuge PC network for analysis.

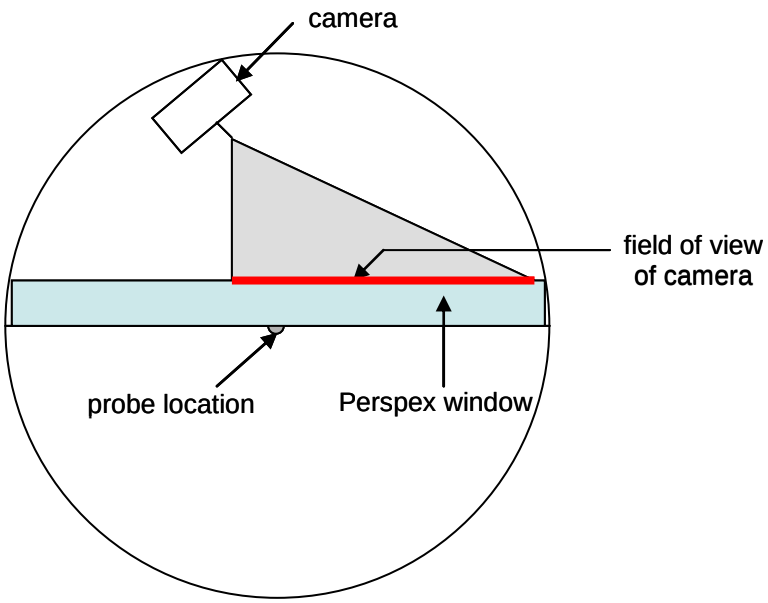

(a) Postion of cameras (plan view)

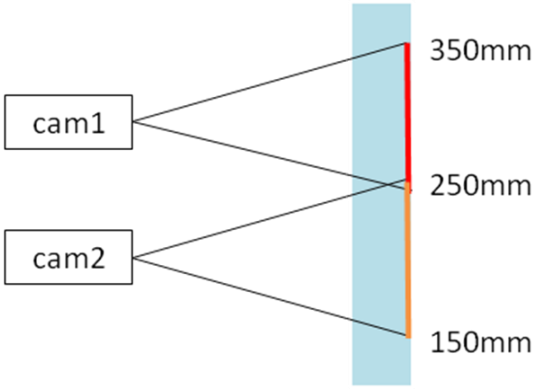

(b) Position of cameras (elevation view)

Figure 3.18: Position of cameras

To observe the progress of the penetrometer or the actuator, a USB web-camera was fitted in one of two locations: either inside the gantry or on the camera mount. When installed on the camera mount, the webcam could be used to check the progress of the probe during a test, specifically to check whether the probe had come away from the glass and become invisible. When installed on the gantry, the webcam showed

the movement of the actuator mechanics allowing the operator to determine if there had been any mechanical failure or to check the position of the probe should the potentiometer or limit switches fail.

3.5 Test programme

3.5.1 Soil model preparation

In this project, the test sand was Leighton Buzzard Fraction C sand with d_{50} approximately 0.5 mm, d_{min} = 0.3 mm and d_{max} = 0.6 mm. Leighton Buzzard sand has been widely used in geotechnical testing in the UK, and is appropriate for this application (having been used by both Klotz & Coop, 2001 and White & Bolton, 2004). The minimum particle size of 0.3 mm means that the sand can be more easily excluded from specific areas (e.g. between the probe and window) than finer sand.

Leighton Buzzard sand is relatively uncrushable (e.g. White & Bolton, 2004). Such sands are characterised by a relatively small variation in angle of friction with stress level and very high volumetric stiffness. Significant dilation occurs during shearing of dense samples. However, when taken to high stress (e.g. during pile installation), even sands that are not normally considered that crushable can exhibit similar patterns of behavior to more crushable soil, and White & Bolton (2004) observed significant crushing of Leighton Buzzard sand.

A 'line' type sand pouring hopper was used to make the centrifuge models in this project (Figure 3.19). This hopper constructed the soil in a uniform and repeatable manner by means of air pluviation. This technique has been verified by Takemura (1998) by cooperative experimental work undertaken in several institutes. The report indicated that almost identical dry densities of sand were achieved by spot or line type hoppers. The advantages of this technique are high dry density, less effect of segregation, no particle crushing, and better repeatability.

Figure 3.19: Line type sand hopper

A range of density can be achieved by varying the rate and height of pluvation. According to Yoon (2008), the density of the resulting model soil reduces as the rate of pluviation (mass/time) increases. Increasing the height of free fall from the hopper to the surface (*h*) increases density up to the point where the particles reach their terminal velocity during free-fall.

The model tub was positioned under the line hopper (Figure 3.20), which was 'blocked' at the left hand side to suit the width of the tub. The drop height was approximately 1.1m at which terminal velocity was probably reached. By reducing the height of the hopper, loose density was achieved.

Figure 3.20: Sand pouring

Details of model construction can be summarised as follows:

1. Control points are marked on the surface of the 3 mm thick glass window for use in determining the camera position and attitude relative to the model. The glass window is then inserted in front of the 50 mm thick Perspex window to form a low friction interface with the soil.

2. The soil model is constructed by air pluviation of sand to a 330 mm thickness from a constant drop height. The hopper is moved at approximately constant velocity by swinging it from the gantry.

3. The model is loaded onto the centrifuge swinging platform.

4. The probe and gantry are then mounted on the top of the tub and the probe is driven down to a height of 350 mm (above the bottom of the soil). The contact between the probe tip and glass window is then checked at this point.

5. A further 30 mm of soil is added by hand to embed the probe tip. The initial horizontal stress at the tip caused by the initial small embedment is thought to help keep the probe tip against the window.

3.5.2 Summary of tests

Ten tests were conducted to assess the effect of soil density, 're-driving' a probe, 'scale' (by varying centrifuge acceleration), and a 'blunt' probe. Table 3.3 summaries the final test series. The relative densities are based on e_{min} = 0.552 and e_{max} = 0.802.

Table 3.3– Final test series

Test (series)	Probe tip	Window at soil interface	Soil profile	g-level	Comments
1	Cone	**Perspex**	Dense (I_d = 85%)	50	
2A-2C	Cone	Glass	Dense (I_d = 90% for 2A) (I_d = 86% for 2B) (I_d = 84% for 2C)	50	
2D	Cone	Glass	Dense (I_d = 84%)	50	Re-drive
3A	Cone	Glass	**Loose** (I_d = 49%)	50	
3B	Cone	Glass	**Loose** (I_d = 53%) **over Dense** (I_d = 89%)	50	
4	Cone	Glass	Dense (I_d = 90%)	**100**	
5	Blunt	Glass	Dense (I_d = 77%)	50	
6	Cone	Glass	Dense (I_d = 86%)	**1**	

3.6 Chapter Summary

An 180^{o} axisymmetric model was developed, which allowed viewing of soil movement as a semi-circular penetrometer advances into the soil. The 'half probe' has a solid tip, but foam was incorporated along the shaft to give some compressibility and hence reduce the tendency for the tip to lift from the window.

The sand was poured (using the pluviation technique) using a line hopper to obtain a uniform high density in most tests. Some loose samples were also used. This method showed good consistency for the density throughout the tests.

Two digital cameras (Canon powershot S70) were mounted in the tub to obtain soil movements. The cameras were controlled in real-time by the the centrifuge rack PC, which was itself remotely operated from the control room. A USB web-camera was fitted to observe the progress of the penetrometer or the actuator.

Photos were taken to assess the soil movement during the penetrometer installation. The movement of 'patches' of soil were tracked using GeoPIV software and other Matlab routines to translate from image coordinates to model object coordinates.

Strain gauges were instrumented along the probe shaft to measure axial load at 6 locations at 25 mm intervals from the tip.

CHAPTER 4 - PROBE CENTRIFUGE TESTS AT 50g IN DENSE SAND

4.1 Introduction

The tests reported in this chapter were undertaken at 50g, with a dense sand sample. The displacement measurements from the two cameras are reported and analysed here. Section 4.2.1 introduces the pattern of displacement to the left side of the probe as it passes. Section 4.2.2 discusses displacement from patches on both left and right to show the axisymmetry of the test. Section 4.2.3 considers the variation of displacement with radial position. Section 4.2.4 summarises the displacement and strains for different radial positions to investigate the general trends in that data.

4.2 Soil displacement patterns

4.2.1 Displacement pattern close to the probe

The displacement field around the probe is the most straightforward illustration of the penetration mechanism. Figure 4.1 shows the displacement field around the probe for an image captured after about 80 mm of penetration. The mesh grid near the pile is approximately 0.4 by 0.4mm, and reduce as the distance away from probe.

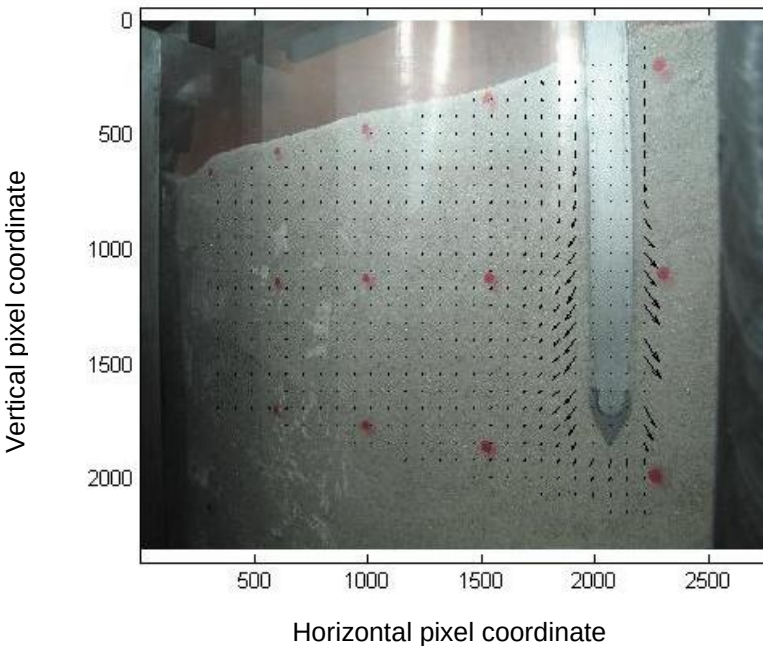

Figure 4.1: Displacement field around the penetrometer (actual image)

One can initially consider a 'column' of soil PIV patches near the probe, whose initial location is a horizontal (radial) distance 1.5*R* (*R* = probe radius) from the centreline of the probe (on the left), and whose vertical y-location (relative to the bottom of the soil model) varies. Figure 4.2 shows results from camera 1 (top camera, see Figure 3.18) with y-location approximately in the range 250 to 350 mm with the soil surface at y = 360 mm. The initial probe shoulder location is y = 350 mm, so that the tip is 'buried' to a depth of 20 mm (tip to shoulder being 10 mm). The final shoulder location at the end of the test is y = 160 mm. The vertical position of the patches can also be

referred to in terms of *h*, the position relative to the shoulder of the moving probe (Figure 4.2.(f)).

Figure 4.2(a) shows the trajectory of a patch during installation of the probe. The red cross ('+') shows the point where $h \approx 0$, i.e. where the shoulder of the probe passes the patch. Note that since images (and hence data) are taken at approximately 5 mm intervals of *h*, there is potentially a small location error on the cross in the range ±2.5 mm. This is potentially reflected in the red crosses not always being located precisely at the obvious change in curve shape. A black cross, ('x'), shows the patch position at the end of the test. Tests start at the graph origin and follow a broad curve with the horizontal displacement increasing approximately in proportion to vertical displacement (although displacement is initially more downward and later more outward). They then turn sharply around near $h = 0$ as the probe passes.

Figure 4.2(b) shows a detail of the trajectory for $h > 0$, representing movement after the probe passes the point. The movement is predominantly downward, with relatively little horizontal movement. The soil appears to be 'dragged' behind the probe after it has passed.

Figure 4.2(c) shows the *x* (radial) and *y* (vertical) displacement at $h = 0$ as profiles with depth. The general trend is that displacement increases steadily with depth except close to the surface, where data from the highest two patches appears somewhat anomalous.

Figure 4.2(d) shows the *x* and *y* displacement for $h > 0$ as profiles with depth. It reveals that the amount of vertical movement after the probe has passed tends to reduce with depth. There is little horizontal movement.

Figure 4.2(e) shows variation of the *x* and *y* displacement with *h*. It confirms that the majority of movement occurs as the probe approaches the patch ($h < 0$). The initial value of *h* is in the range -100 to 0 mm, reflecting the range of *y* values for camera 1 (250 to 350 mm for the data analysed) compared to the initial shoulder location (350 mm). The final value of *h* is in the range +90 to +190 mm, again reflecting the range of *y* values for camera 1 compared to the final shoulder location (160 mm). The length of each line is 190 mm, representing the distance of penetration. The patch located at the top of the image shows *h* from 0 to +190, whilst the patch at the bottom shows *h* from -100 to +90.

The two highest patches again show somewhat anomalous responses. For the highest patches *x* and *y* displacements begin almost immediately as the probe advances and *h* increases, but for the lower patches the movement begins more gradually, and is ultimately larger. It is evident from plots (c) and (e) that movement increases with depth at least in part because the lower patches experience some movement while the probe is still quite remote, whilst this situation never exists for the higher patches since the probe's initial location is already relatively close to them.

The earliest x-displacement starts when $h \approx -50$ mm, or about 4 probe diameters. The earliest y-displacement starts when $h \approx -70$ mm, or about 6 diameters. As noted previously there is little systematic variation of *x* displacement for $h > 0$. For the highest patches (nearest the surface of the soil) there is some sign of upward movement (heave) just as the probe passes, which seems reasonable (see also subplot (a)). There is initially little increase of (negative) *y* displacement when $h > 0$, although this does tend to increase as *h* reaches higher positive values for the highest patches. As *h* increases the gradient of the line approaches a value of about 0.03 for downward movement, so that as the probe advances 1 mm the highest patch is dragged down about 0.03 mm.

Summary

1. There is some limited anomalous behaviour but in general the results seem rational and reasonable.

2. Movement is initially downwards tending to become outwards as the probe arrives and *h* reaches zero, ultimately giving similar vertical and horizontal movement. For the deeper patches significant vertical movement begins when the probe shoulder approaches at a distance of about 6 diameters, with significant horizontal movement starting later at about 4 diameters.

3. The amount of movement generally increases with depth.

4. After the probe passes there is little systematic movement, although the highest patches initially heave upwards and are later dragged down as the probe advances.

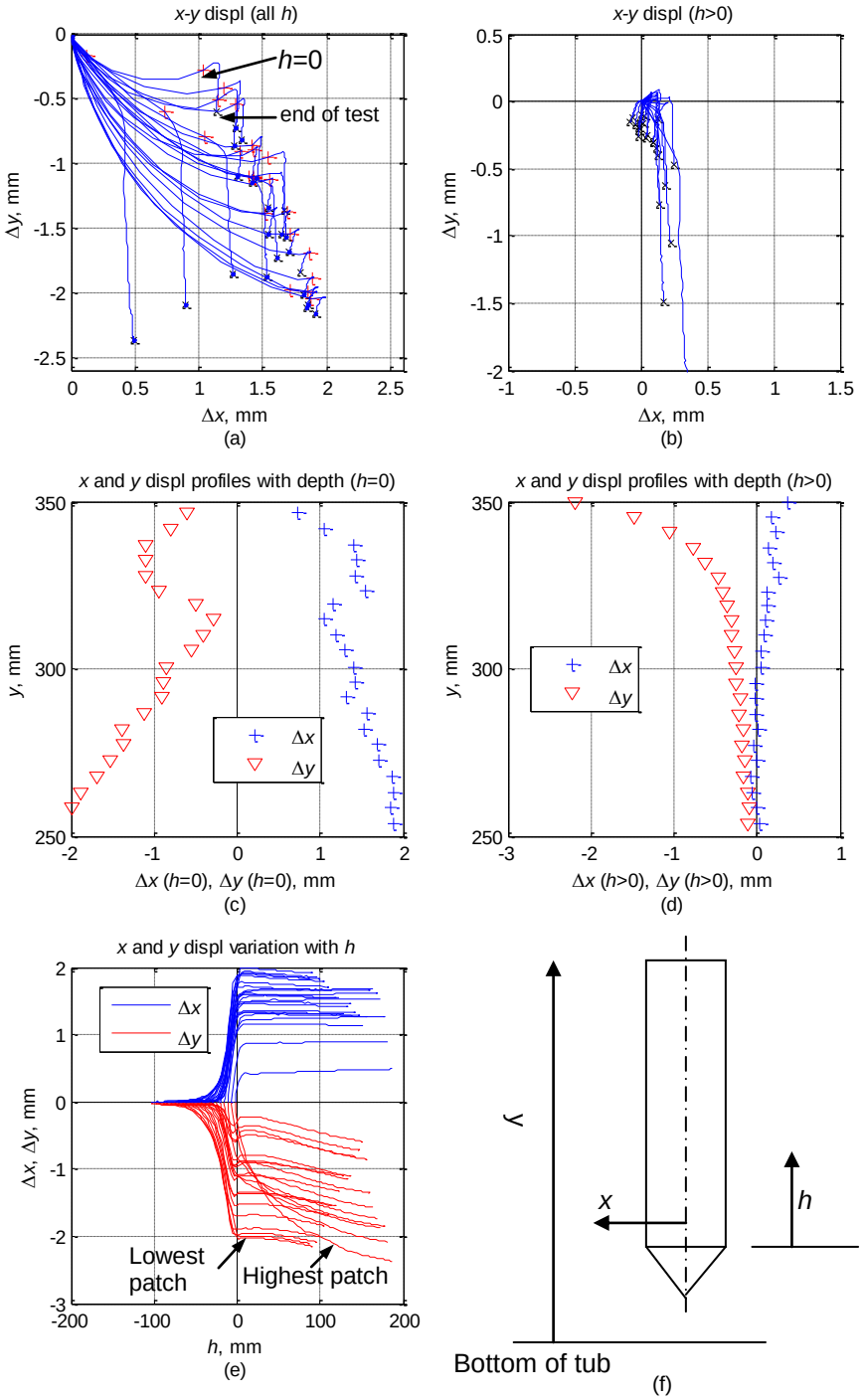

Figure 4.2: Displacement at *x/R*=1.5 in camera 1 (y=250 to 350mm), test 2C.

Data in Figure 4.3 is from camera 2 (see Figure 3.18) with *y*-locations approximately in the range 150 to 250 mm (between 110 and 210 mm depth in the soil). The same 'column' of patches near the probe is chosen, whose initial location is a horizontal distance 1.5*R* from the centreline of the probe (on the left), and whose y-location varies.

As shown in subplot (a), movement is again predominantly initially downward and then outward during the test. In contrast to camera 1, the movement is quite similar for nearly all patches, implying little variation with depth. Final horizontal and vertical movements are again approximately equal. These observations are confirmed in subplot (c).

Subplots (b) and (d) illustrate that there is little movement after the probe passes, and the displacements are very small compared with the size of the individual sand particles (about $1/10^{th}$ the magnitude). It suggests some strain reversal, as shown in White et al (2004).

Since the patch locations are about 100 mm lower than those from camera 1, the range of *h* observed during the test is also about 100 mm lower, and for the bottom patch analyses (at $y \approx 175$ mm), the probe has only just passed this point at the end of the test when the shoulder is at 160 mm and $h = 15$ mm. Results are shown in subplot (e). Significant vertical movement is observed at about 8 diameters, whereas significant horizontal movement again begins at about 4 diameters. As previously noted there is little movement after the probe passes.

Subplot (f) shows the data from subplot (c) for cameras 1 and 2 as profiles with depth. The data shows reasonable consistency for the lowest data from camera 1 and the highest data for camera 2. The plot shows that there is no significant further increase

in displacement with depth (at h = 0) below the interface of the images from the two cameras, which corresponds to an embedment of about 8 or 10 diameters.

Summary

1 The results seem reasonable, and there is reasonable consistency between results from the two cameras.

2 Movement is again initially downwards tending to become outwards as h reaches zero, ultimately giving similar vertical and horizontal movement. Significant vertical movement begins when the probe shoulder is at a distance of about 8 diameters, with significant horizontal movement at about 4 diameters.

3 After about 8 to 10 diameters penetration the amount of movement does not vary with depth.

4 After the probe passes there is very little systematic movement.

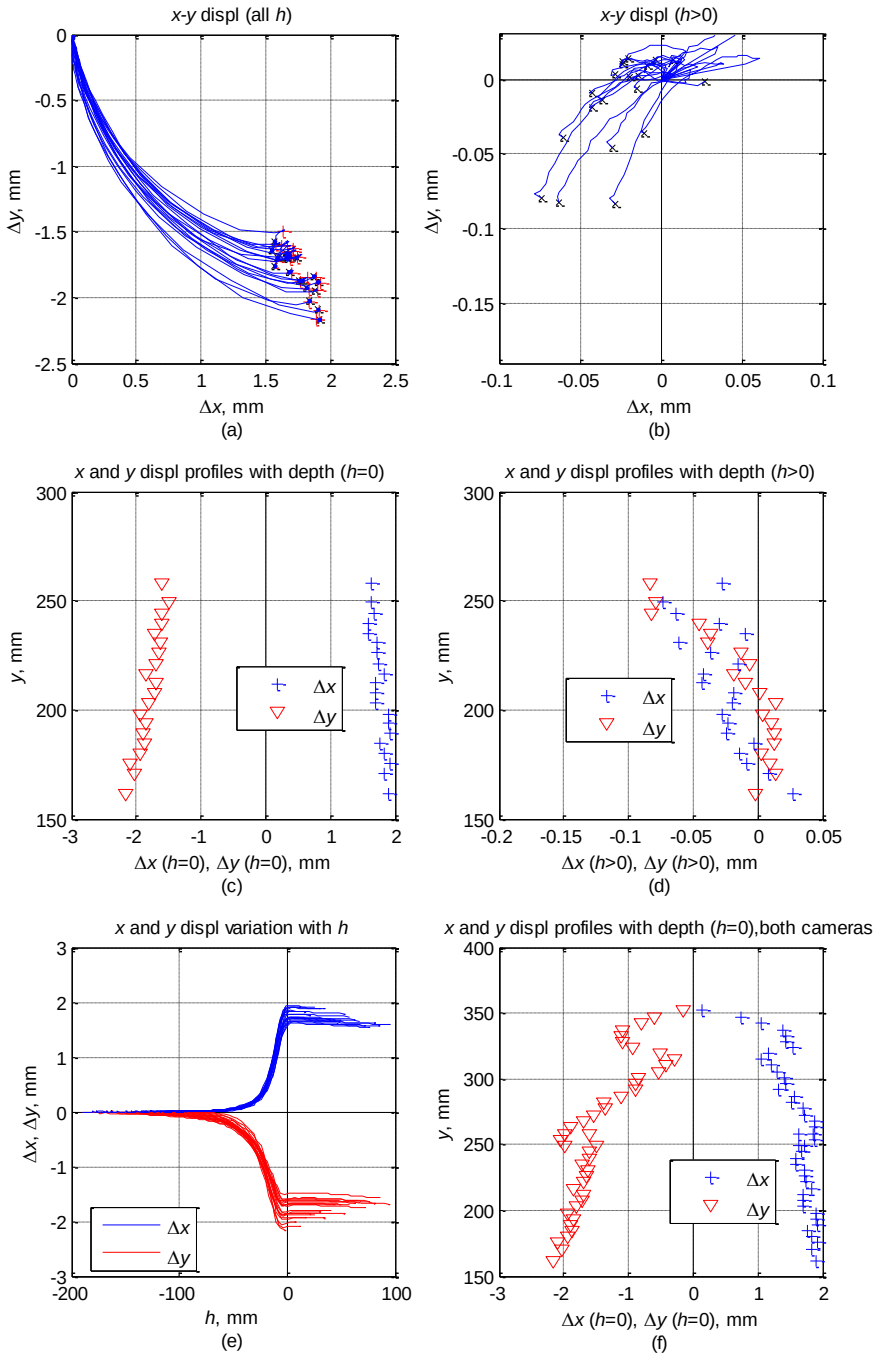

Figure 4.3: Displacement at *x/R*=1.5 in camera 2 (y=150 to 250mm)), test 2C.

4.2.2 Axisymmetry of displacement

Data from points on the left of the test probe need to be compared with that on right so that the degree of symmetry in the tests can be assessed. A 'column' of patches near the probe on the right hand side (RHS), whose initial location is a horizontal distance 1.5*R* from the centreline of the probe is analysed and compared with patches at 1.5*R* on the left hand side (LHS). Figure 4.4 shows the comparison from camera 1 and Figure 4.5 for camera 2.

As can be seen from subplot (a) for both cameras, movement is again predominantly initially downward and then outward during the test. The displacement magnitude is again quite similar for the majority of patches on both sides of the probe, although here are some anomalous results in both cameras (most noticeably on the RHS). Final horizontal and vertical movements are again approximately equal.

As shown in subplot (b) of Figure 4.4, the soil appears to be dragged behind the probe after it has passed in camera 1 as is the case for patches on the left, and movement is large for two patches on the RHS. There is little movement on either side of the probe after it passes in camera 2 (subplot (b) of Figure 4.5).

Except for some anomalous results, subplot (c) of Figure 4.4 shows that the displacements on both sides of the probe (at $h = 0$) increases with depth in camera 1. Again, in subplot (c) of Figure 4.5, the displacement at $h = 0$ varies little in camera 2 (except for some anomalous results on the RHS of the probe close to the interface of the cameras).

The amount of vertical movement after the probe has passed tends to reduce with depth for both cameras 1 and 2 (subplot (d)). This can be related to the reduction in

the magnitude of the positive value of *h* at the end of the test with increasing depth in the soil. There is little evidence of horizontal movement in these plots.

As can be seen from subplot (e) of both figures, significant vertical and horizontal movements appear at approximately the same *h* for patches on both sides (again there are some anomalous results on the RHS).

Figure 4.5 subplot (f) shows final displacements are approximately equal on both sides of the probe with the exception of some anomalous results on the RHS. With the exception of some anomalous results near the interface on the RHS, the data shows reasonable consistency for the lowest data from camera 1 and the highest data for camera 2.

Summary

1 There are some anomalous results in both cameras, but particularly on the RHS.

2 Movement is again initially downwards tending to become outwards as *h* reaches zero, ultimately giving similar vertical and horizontal movement.

3 After about 8 to 10 diameters penetration the amount of movement does not vary with depth, which is similar to the patches at *x/R*=1.5 on the left of the probe.

4 The magnitude and direction of displacement is approximately the same as that at *x/R*=1.5 on the left side of the probe.

5 The general similarity in results for both sides of the probe at *x/R*=1.5 confirms that the displacement of the observable left half side of the model reflects reasonable agreement with that of the right hand side (which is not visible at larger values of *x*).

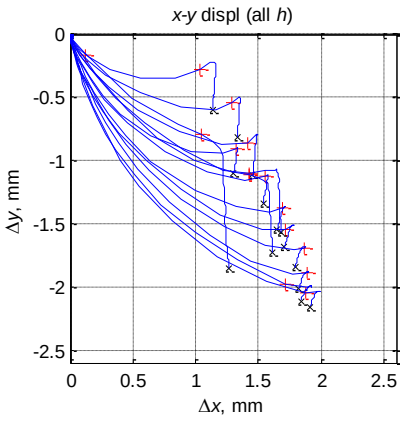

(a) LHS

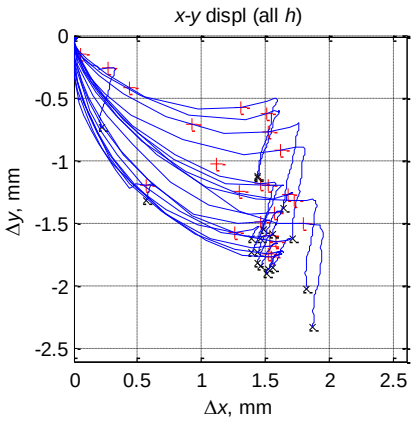

RHS

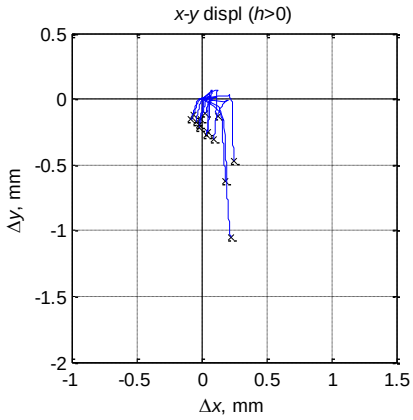

(b) LHS

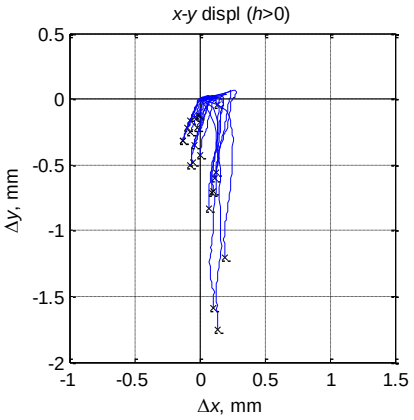

RHS

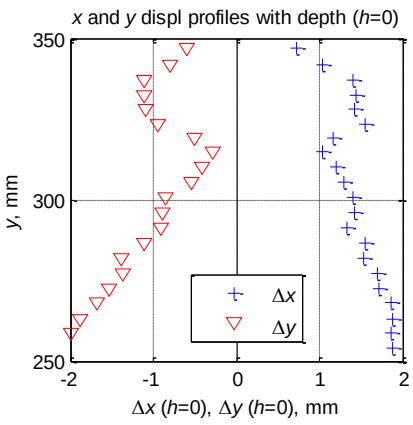

(c) LHS

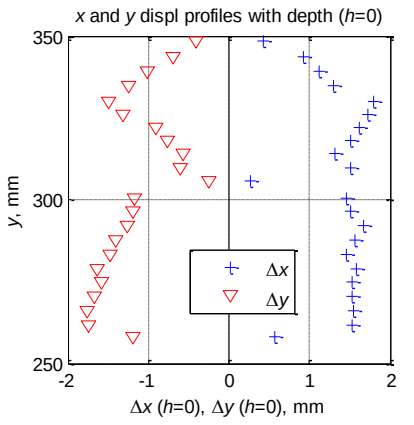

RHS

(Figure 4.4 cont' on next page)

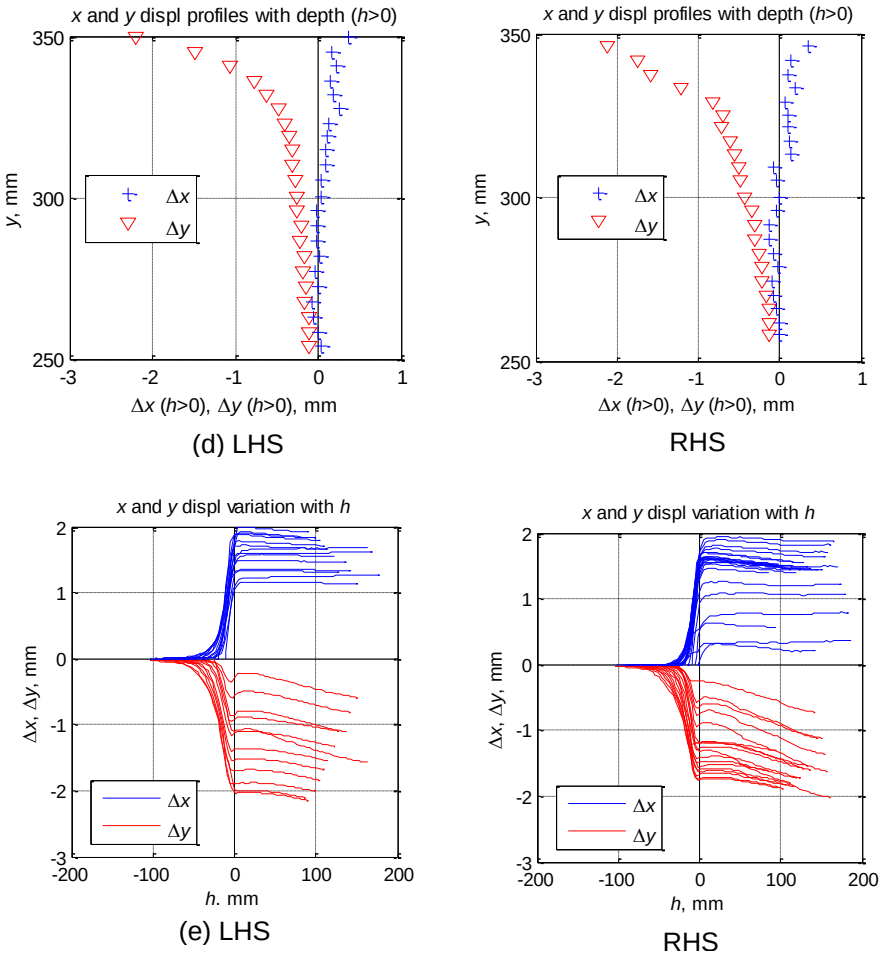

Figure 4.4: Comparison of data from left hand side (LHS) and right hand side (RHS) of probe in camera 1, test 2C.

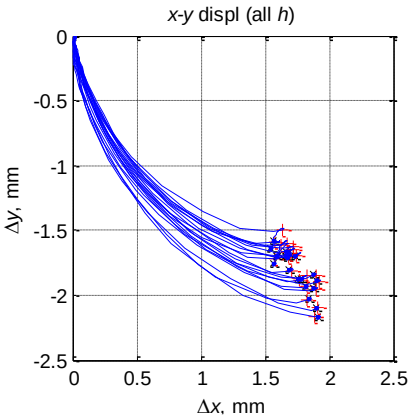

(a) LHS

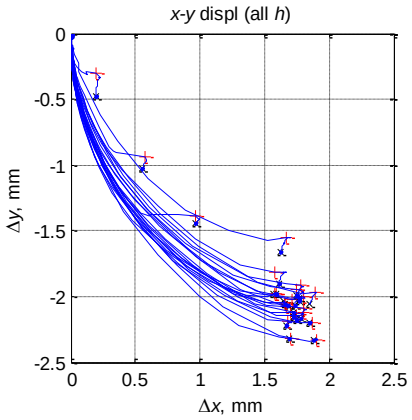

RHS

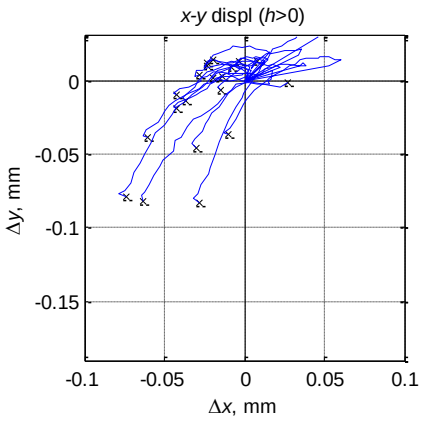

(b) LHS

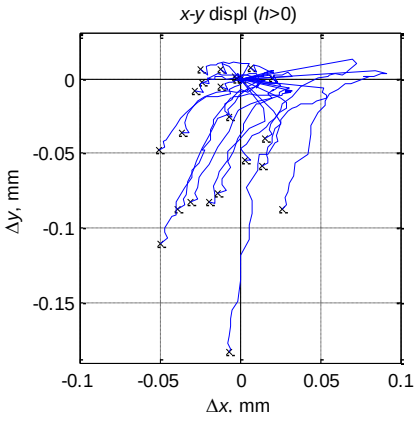

RHS

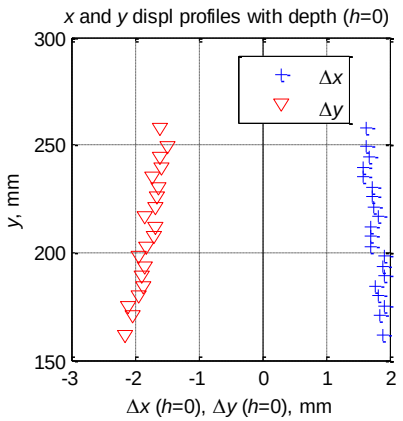

(c) LHS

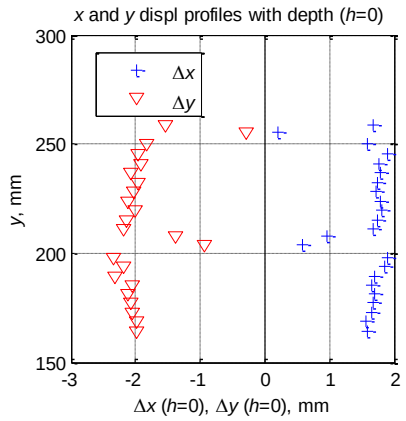

RHS

(Figure 4.5 cont' on next page)

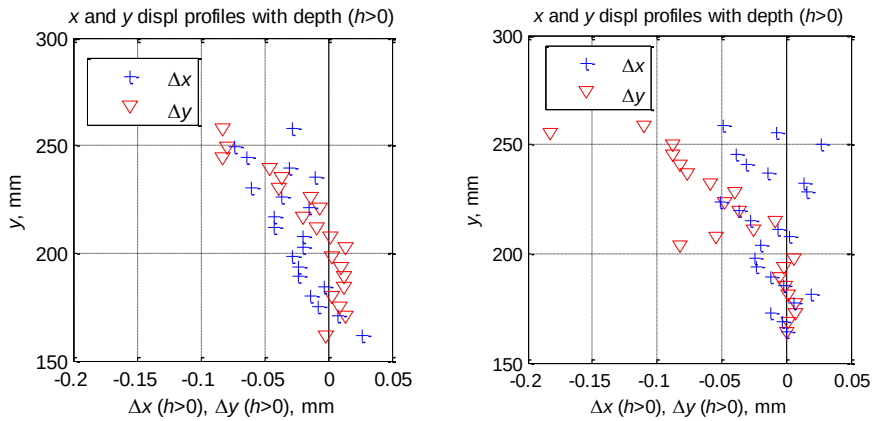

(d) LHS RHS

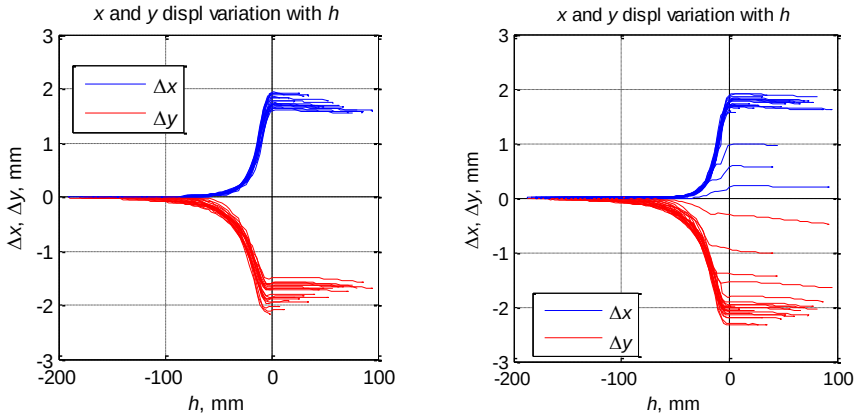

(e) LHS RHS

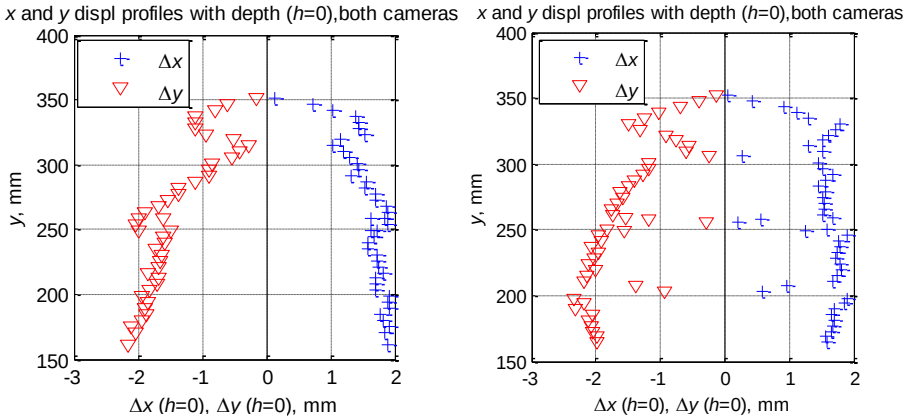

(f) LHS RHS

Figure 4.5: Comparison of data from left hand side (LHS) and right hand side (RHS) of probe in camera 2, test 2C.

4.2.3 Variation of displacement with radial position

The data in Figures 4.6 to 4.11 compares 6 different 'columns' of patches, whose initial horizontal locations from the centreline of the probe are 1.5*R*, 2.3*R*, 3.2*R*, 5.0*R*, 7.0*R*, and 10.3*R*. All Data are from camera 2 because the displacements show relatively little variation with depth, and appear to have reached a steady state.

As can be seen from Figure 4.6, movements are again predominantly initially downward and then outward during the test for all horizontal locations. At 5.0*R* to 10.3*R* the plots indicate some initial inward movement towards the probe. However this movement is very small, about 0.01 mm, which is less than can reliably be measured in the test. The magnitude of the displacements drops quickly as the radius increases. When $h = 0$, as denoted by the red cross ('+'), the relative proportion of horizontal to vertical displacement is approximately equal across all horizontal locations.

Figure 4.7 shows that after the probe passes the movements are predominantly downward, with relatively little horizontal movement. The soil again appears to be 'dragged' behind the probe after it has passed. The movements after the probe passes are very small. The horizontal values are approximately 0.03 mm, while the vertical values are approximately 0.07 mm. Theses values are only about 1 % of the probe radius.

Figure 4.8 reveals that there is little systematic variation with depth of movement when $h = 0$. However, there is a slight tendency for vertical movement to increase with depth, particularly at larger values of *R*.

In Figure 4.9, the amount of vertical movement after the probe has passed tends to reduce with depth, as observed in Sections 4.2.1 and 4.2.2 (again reflecting the lower

value of *h* at the end of the test for deeper patches), but movement is very small. There is very little horizontal movement after the probe passes.

Figure 4.10 shows that significant vertical movement is observed at about 10 diameters for the column at *x/R* = 2.3. The movements begin earlier as the distance from the probe increases, but at large *x/R* the displacement is very small and occurs at a virtually constant rate irrespective of *h*. At *x/R* = 10.3 the gradient is about 0.001 – ie. the soil settles 0.001 mm for every 1 mm that the probe advances. Significant horizontal movement begins at about 5 diameters for the column at *x/R* = 2.3. This movement also starts slightly earlier as *x* increases. There is little horizontal movement after the probe passes at all horizontal locations.

From Figure 4.11, it is found that near the probe there is a significant tendency for displacement to increase to *y* = 250 mm, and displacement increases relatively little below this depth. At the largest radius considered displacements are much smaller, but continue to increase at a fairly constant rate throughout all the depth (particularly for vertical displacement). Again the data shows reasonable consistency for the lowest data from camera 1 and the highest data from camera 2.

Summary

1 Displacements are again predominantly initially downward and then outward during the test.

2 The displacements after the probe passes are very small. Soil appears to be dragged behind the probe after it has passed.

3 The vertical displacement starts earlier as the radial position from the probe is increased.

4 The magnitude of displacements drops quickly as the radial position increases.

5 There is little movement after the probe passes for columns at x/R = 2.3 and 3.2. For the column at x/R=10.3, no increase in rate of increase in vertical displacement with h is observed as the probe approaches, and the vertical displacement still increases at the same rate when $h > 0$.

6 Generally the behaviours to a horizontal distance of 5.0R are very similar to the near field behaviour. For radii in excess of 7.0R, the displacements have different behaviour, thus can be considered as 'far field'. Between the 5.0R to 7.0R, the movements show a gradual transition.

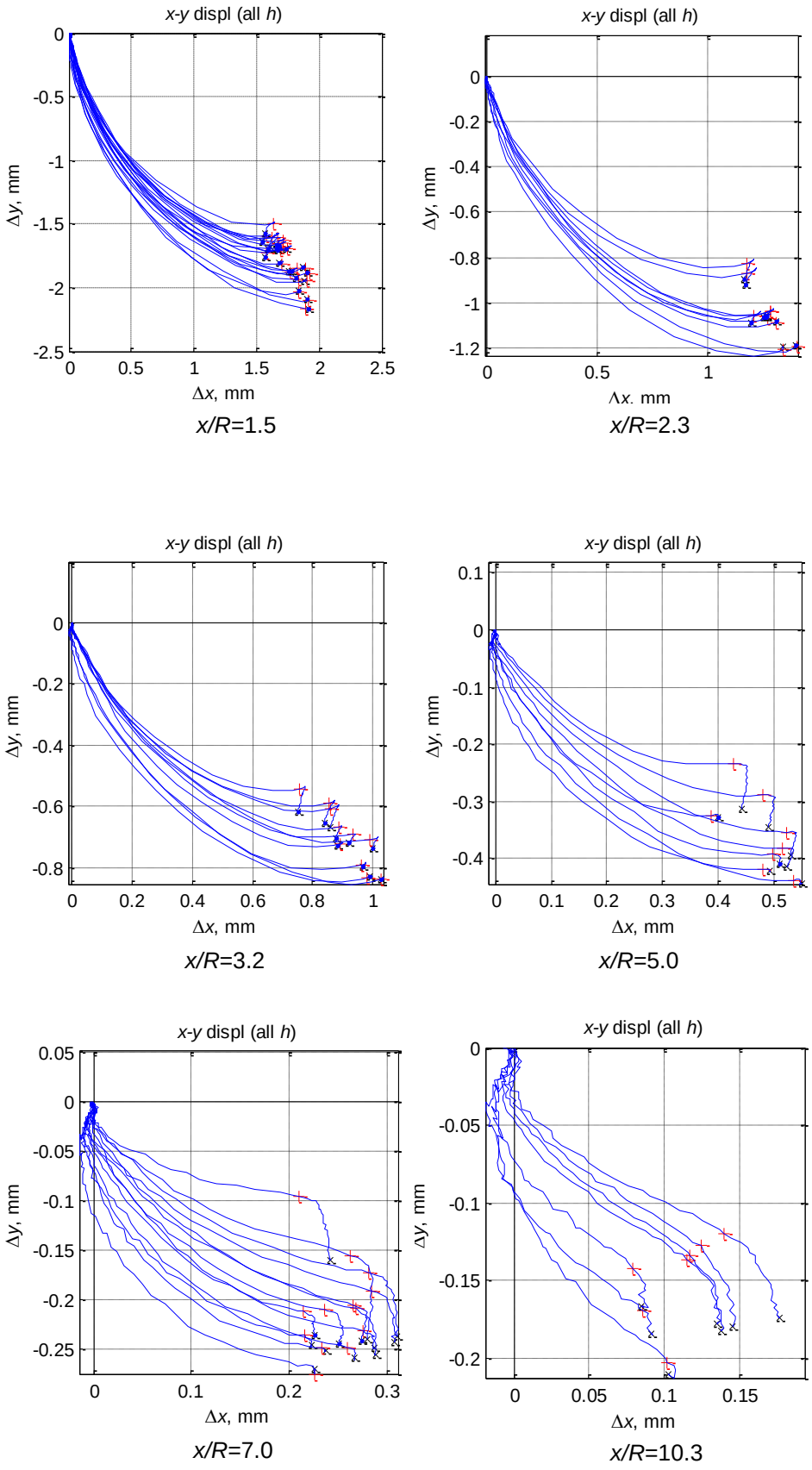

Figure 4.6: Variation of displacement trajectory with radial position in camera 2, test 2C.

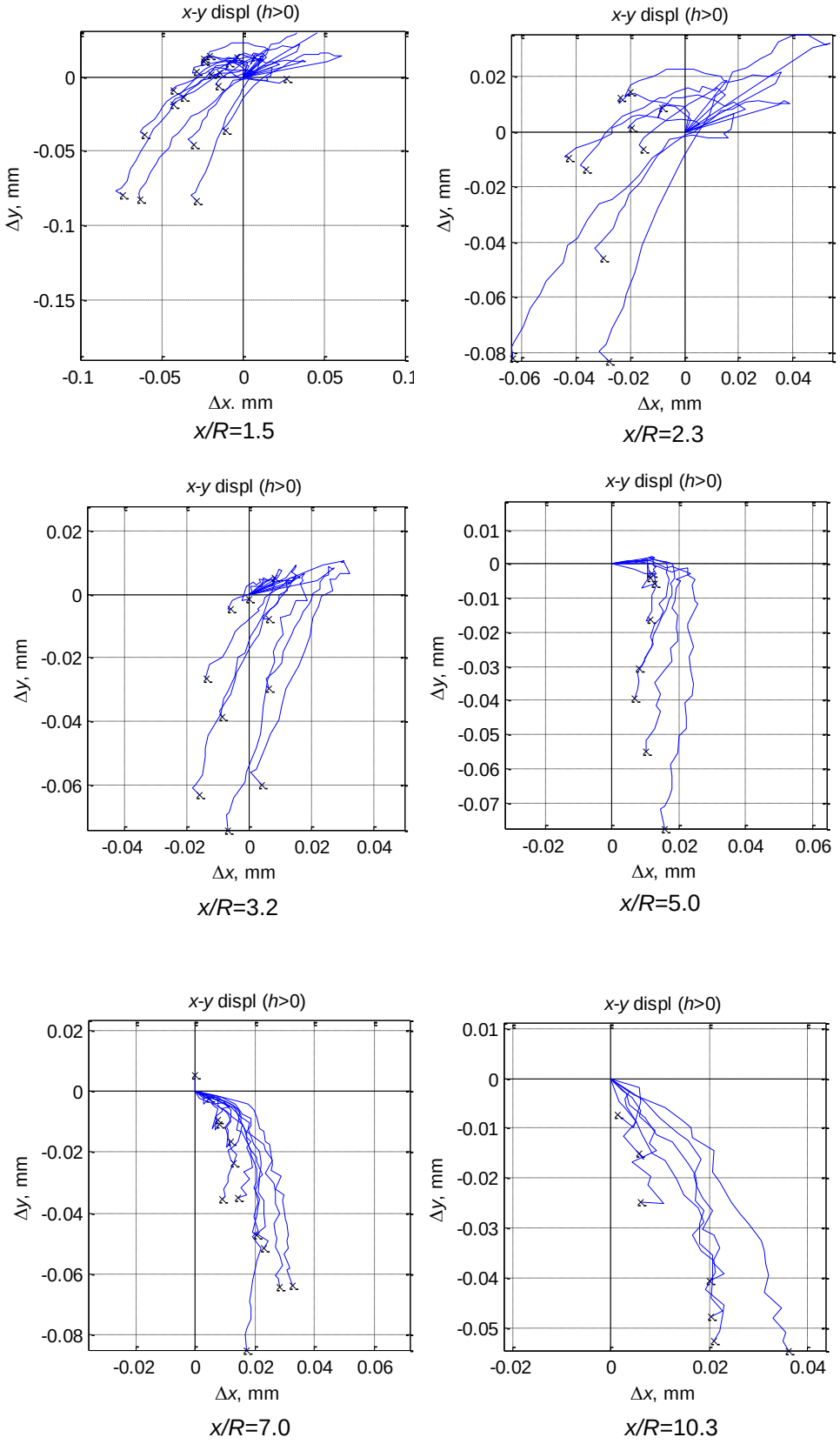

Figure 4.7: Variation of displacement trajectory for h>0 with radial position in camera 2, test 2C.

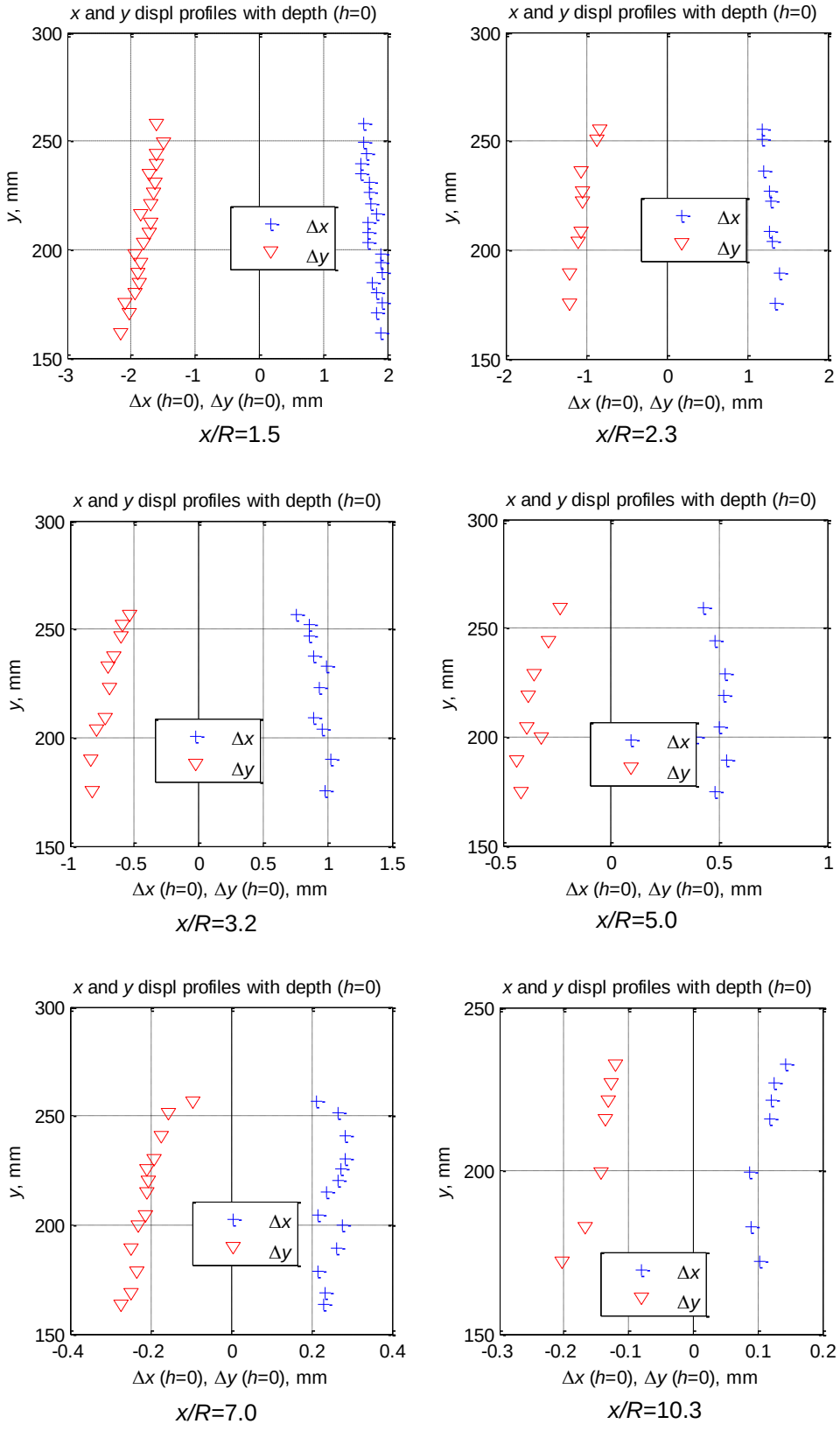

Figure 4.8: Variation of x and y displacement at h = 0 as profiles with depth in camera 2, test 2C.

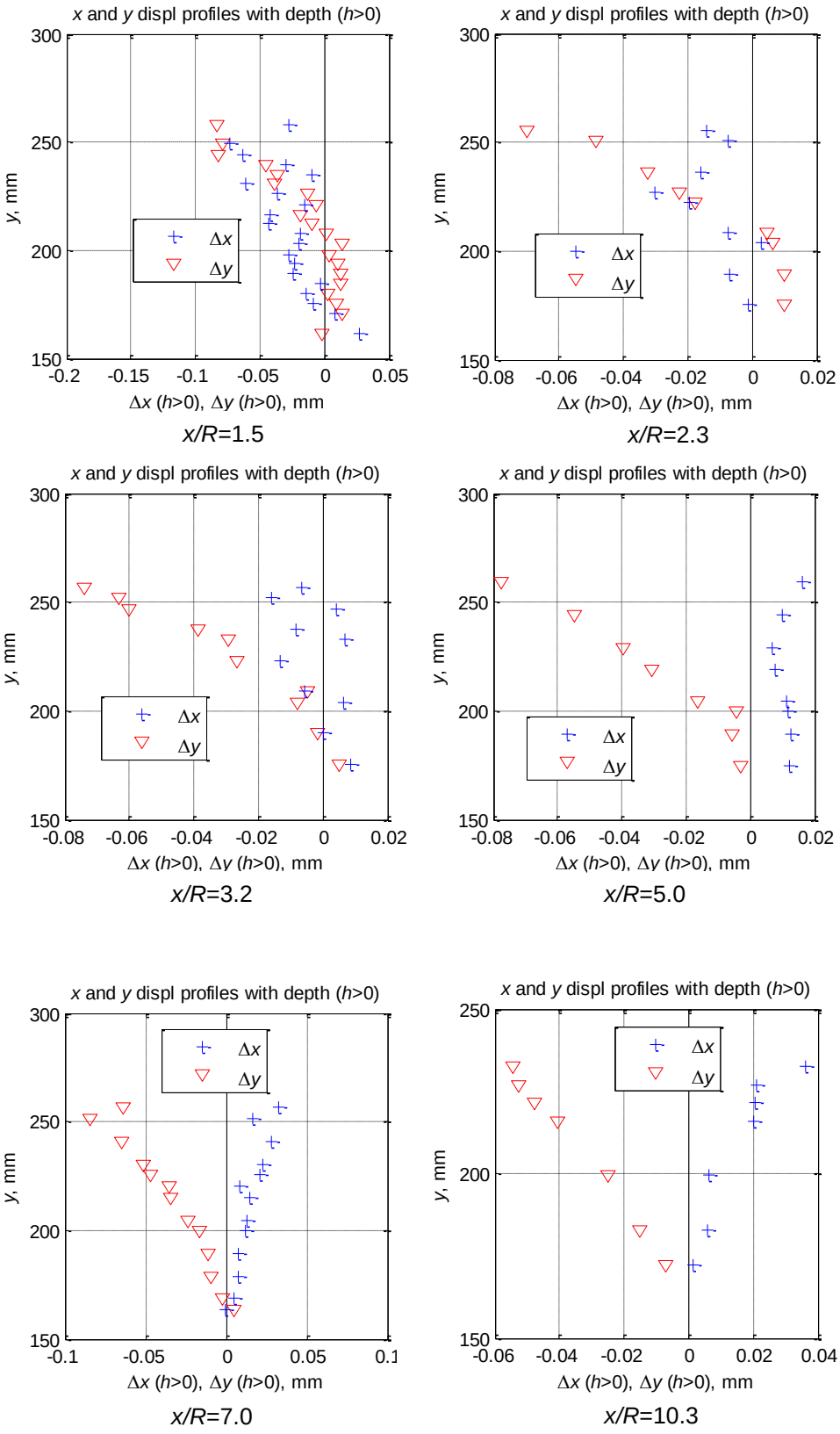

Figure 4.9: Variation of x and y displacement for $h > 0$ as profiles with depth in camera 2, test 2C.

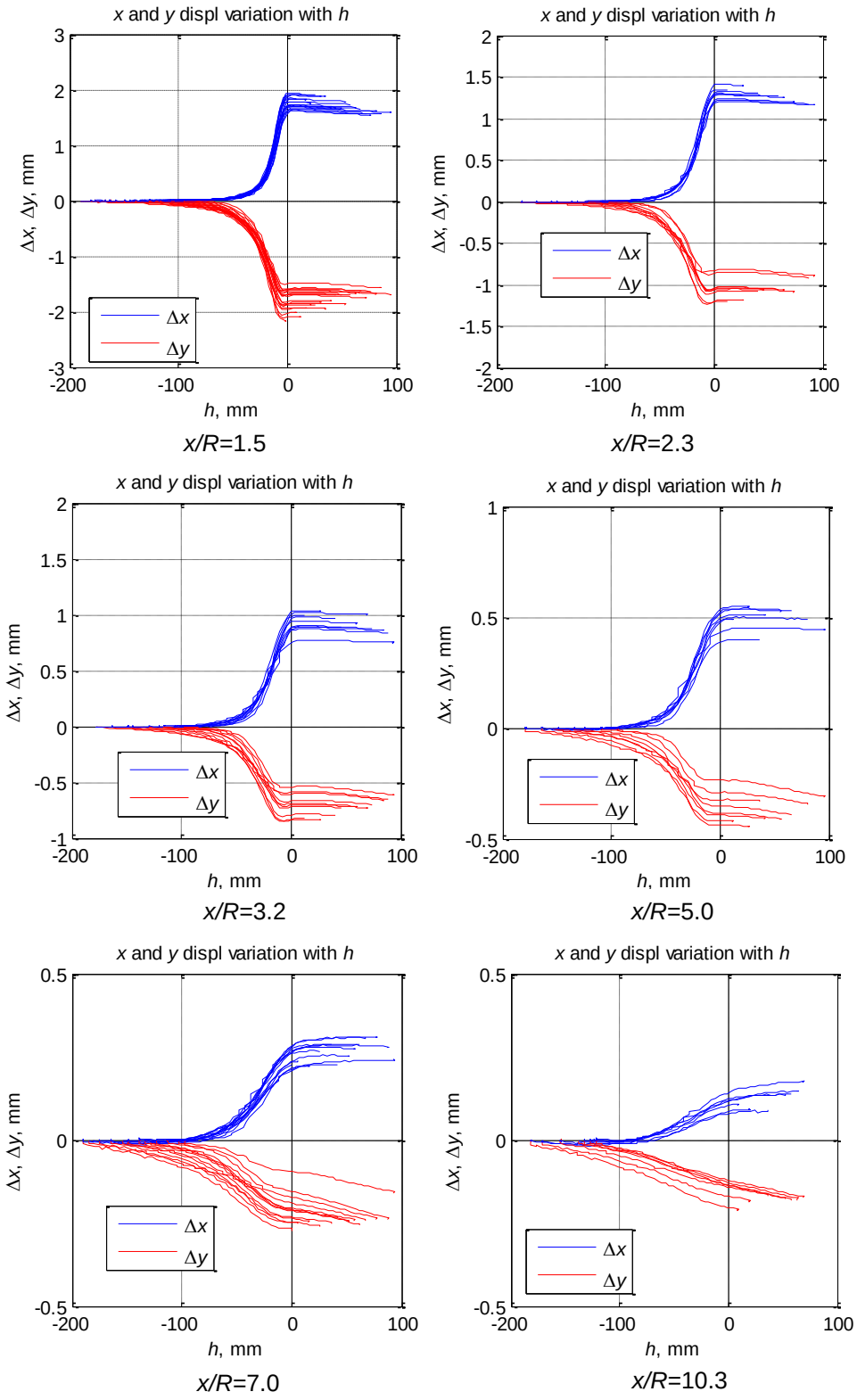

Figure 4.10: Variation of the *x* and *y* displacement with *h* in camera 2, test 2C.

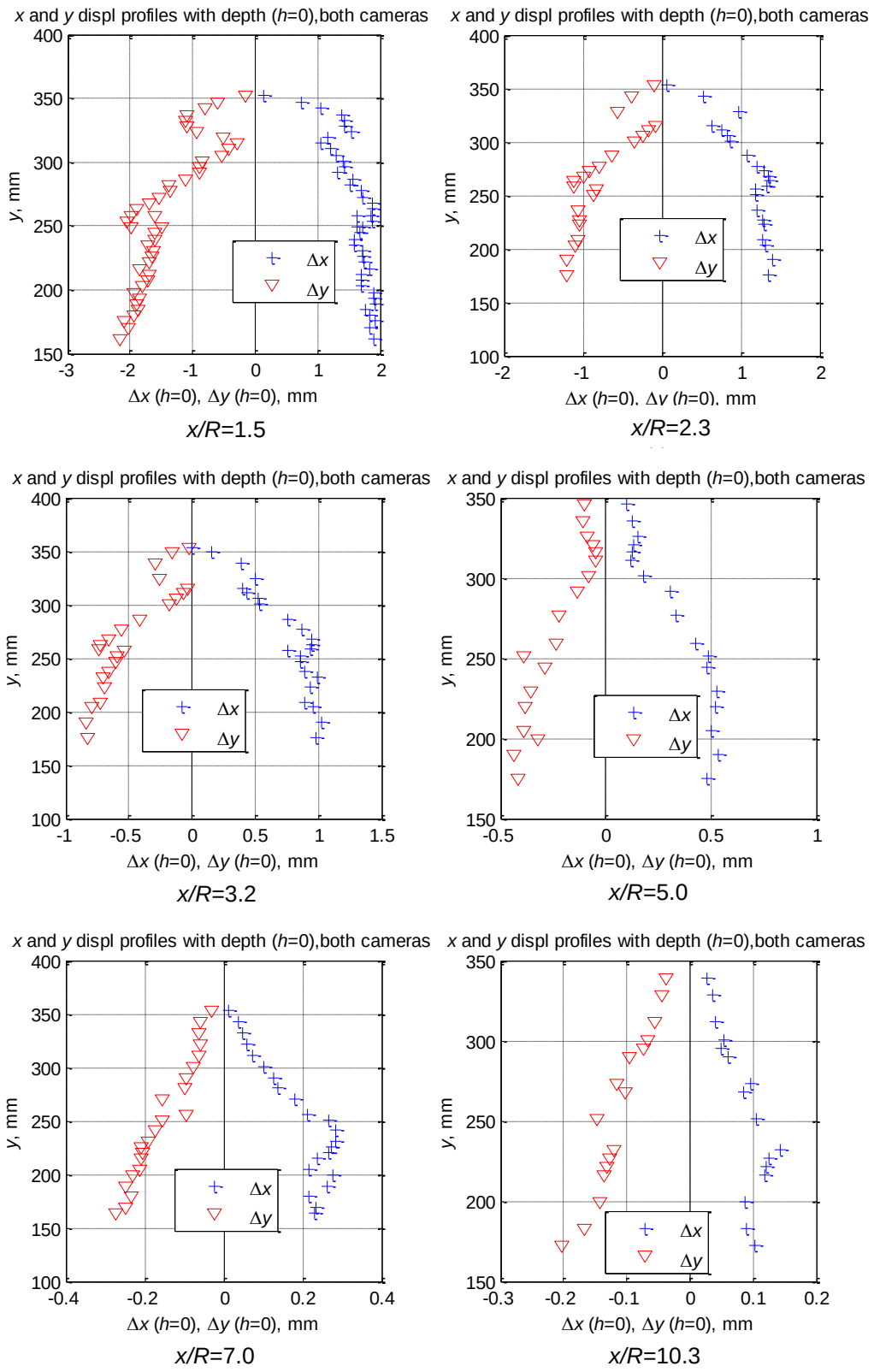

Figure 4.11: Variation of x and y displacement for $h > 0$ as profiles with depth in both cameras, test 2C.

4.2.4 Summary of displacement and strains patterns

Introduction to summary plots

Data for individual PIV patches as presented so far can suffer from anomalies making interpretation more difficult. Before looking at patterns in more detail a methodology of 'averaging' the data is introduced.

Five rows of patches near mid height of the image (y ≈ 200 to 220 mm) were used for more detailed analysis to complement the previous sections. Figure 4.12 shows the patches which have been used. Each column of patches has a virtually constant x-location (like the figures in Section 4.2.3). Each row of patches has a y-location which differs slightly with distance from the probe (Figure 4.1). However, there is little systematic variation in displacement over this range of *y* as shown earlier by Figure 4.3, so the variation with *h* should be nominally the same for all patches in one column. Thus when expressed in terms of *h* the data can be 'averaged' for 5 patches in one column.

The initial data for different patches exists at intervals of *h* ≈ 5 mm with precise values which depend on the probe location relative to the initial location of the patch when an image was taken. Thus the data must be 'standardised' with respect to variation with *h* before it can be averaged.

A standard data set for each patch was formed with values of *x* and *y* displacement at integer values of *h* at 1 mm intervals (i.e. *h* = -150 mm, -149 mm etc). The *x* and *y* displacement for each value of *h* was derived by linear interpolation between the original data points.

The values of *x* and *y* displacement for the 5 patches for a given value of *h* were then averaged. This had the effect of reducing the effect of any random variations in response for individual patches, and gave relatively smooth variation with *h*.

Vertical strain was derived as -d(Δy)/dh, since all points with the same initial x are assumed to follow the same variation of Δy with h, but h is also the vertical separation of points in the soil. This gradient could be easily derived numerically from the averaged Δy response as it varied with h. Figure 4.12 illuminates how the vertical strain was deduced.

Horizontal strain for a given value of h was derived from the difference in averaged Δx response for adjacent columns divided by the original nominal separation of the columns. The resulting data was then plotted at the midpoint between the two column locations. This approach neglected a relatively small second order term in a full axisymmetric formulation (eg. Gupta, 1991):

$$\varepsilon_{rr} = \frac{\delta u}{\delta r} - \frac{1}{2}\left(\frac{\delta u}{\delta r}\right)^2 \qquad (4.1)$$

However this term has relatively little significance for strains less than 10 %.

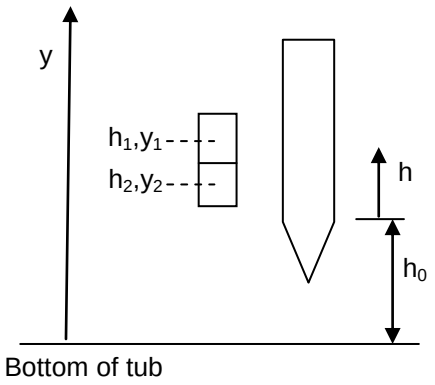

For the tip at $y=h_0$,

$h_1=h_0+y_1$

$h_2=h_0+y_2$

$y_1-y_2= h_1-h_2$

$\varepsilon_v=(\Delta y_1-\Delta y_2)/(y_1-y_2) =(\Delta y_1-\Delta y_2)/(h_1-h_2)$

Figure 4.12: Vertical strain calculation

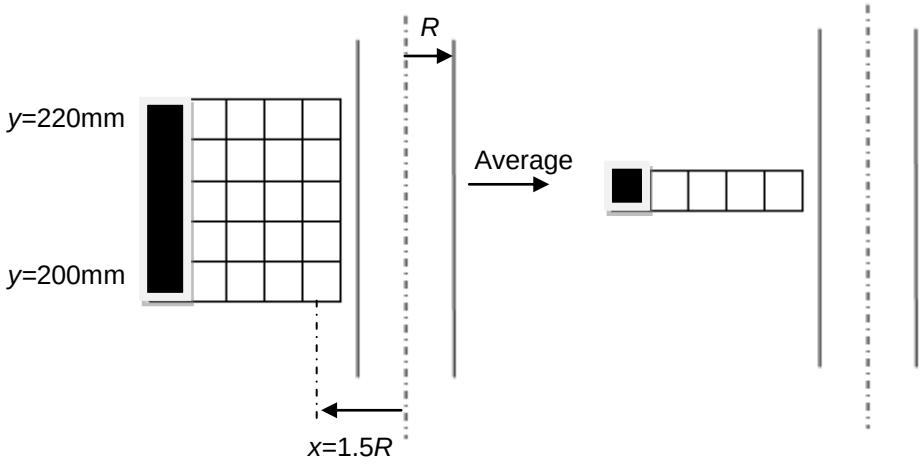

Figure 4.13: Averaging of results from 5 patches in a column

Figure 4.14 shows normalised displacements and strains in relation to probe position. In the top row (subplots (a), (b) and (c)) vertical position of the probe is represented by the vertical axis with the horizontal axis representing displacements or strain in both *x* and *y* directions.

The bottom row (subplots (d), (e) and (f)) represents displacements and strain distributions in the horizontal direction when $h = 0$. The axes are reversed so that horizontal (radial) position is represented on the horizontal axis and displacement or strain value on the vertical axis as in this form it imitates the actual geometric distribution. The horizontal distributions also reduce to a single line. This series of graphs represents a useful summary of probe behaviour and will be discussed in detail.

Subplots (a) and (d)

Subplot (a) is equivalent to Figure 4.3(e) etc rotated through 90^{o} (and taking a mirror image), and summarising averaged data for a range of values of *x/R* in one test along y=200 to 220mm. The data has also been normalised by the probe radius (*R*) in the case of displacements, and the probe diameter *D* for *h*.

Vertical displacement, Δy is always negative and thus plots on the LHS, while horizontal displacement, Δx, is always positive and thus plots on the RHS. As anticipated, Δx begins somewhat later than Δy as the probe approaches. In fact, if the probe is imaged to be stationary as the soil 'flows' upwards past it, then, the profiles represents 'flow lines' relative to the original x-location.

The various lines are not labelled. However, subplot (d) shows variation of Δx and Δy when $h = 0$, and thus the values of x/R for a given line can be established as required. In general both Δx and Δy reduce as x/R increases. Δx and Δy are approximately equal when $h = 0$.

Subplot (d) also shows a line $(\Delta x/R) = (R/2x)$, which is based on cylindrical cavity expansion theory (see Section 4.2.5 below). The data show excellent agreement with this close to the probe, but displacement is somewhat less than that predicted at a larger radius.

Subplots (b) and (e)

As anticipated there is some 'random noise' on the strain data since differentiation tends to 'amplify' the effect of any noise on the original data. However, the overall trends of behaviour are clear.

Vertical strain in subplot (b) is essentially the gradient of the Δy profiles on plot (a). Again the various lines are not labelled. However, subplot (e) shows the maximum (compressive) strain for all h, which again tends to reduce with x. The minimum value is also shown, and is sometimes negative, indicating tensile strain.

It can be seen that compressive strain first develops when $h/D \approx -8$, and rises to a maximum at $h/D \approx -2$ when $x/R = 1.5$. The maximum occurs somewhat earlier as x/R

increases. For x/R < 4 there is some evidence of tension when $h/R \approx 0$. After the probe passes the vertical strain returns to zero.

Subplot (b) also shows a line $\varepsilon_v = 0.5(R/h)^2$, corresponding to spherical cavity expansion directly (vertically) ahead of the probe (see Section 4.2.5 below). It can be seen that initially the test data indicate vertical strains somewhat in excess of this prediction up to the point of maximum strain.

Subplot (c) and (f).

The format of the plots is the same as (b) and (e), but showing horizontal rather than vertical strain. For x/R less than about 3, the initial strain is tensile (negative) from $h/D \approx -5$. The strain then returns to zero, corresponding to the point where the Δx data for adjacent columns in subplot (a) crosses. The maximum compressive strain then occurs at $h = 0$, and is approximately constant after the probe passes.

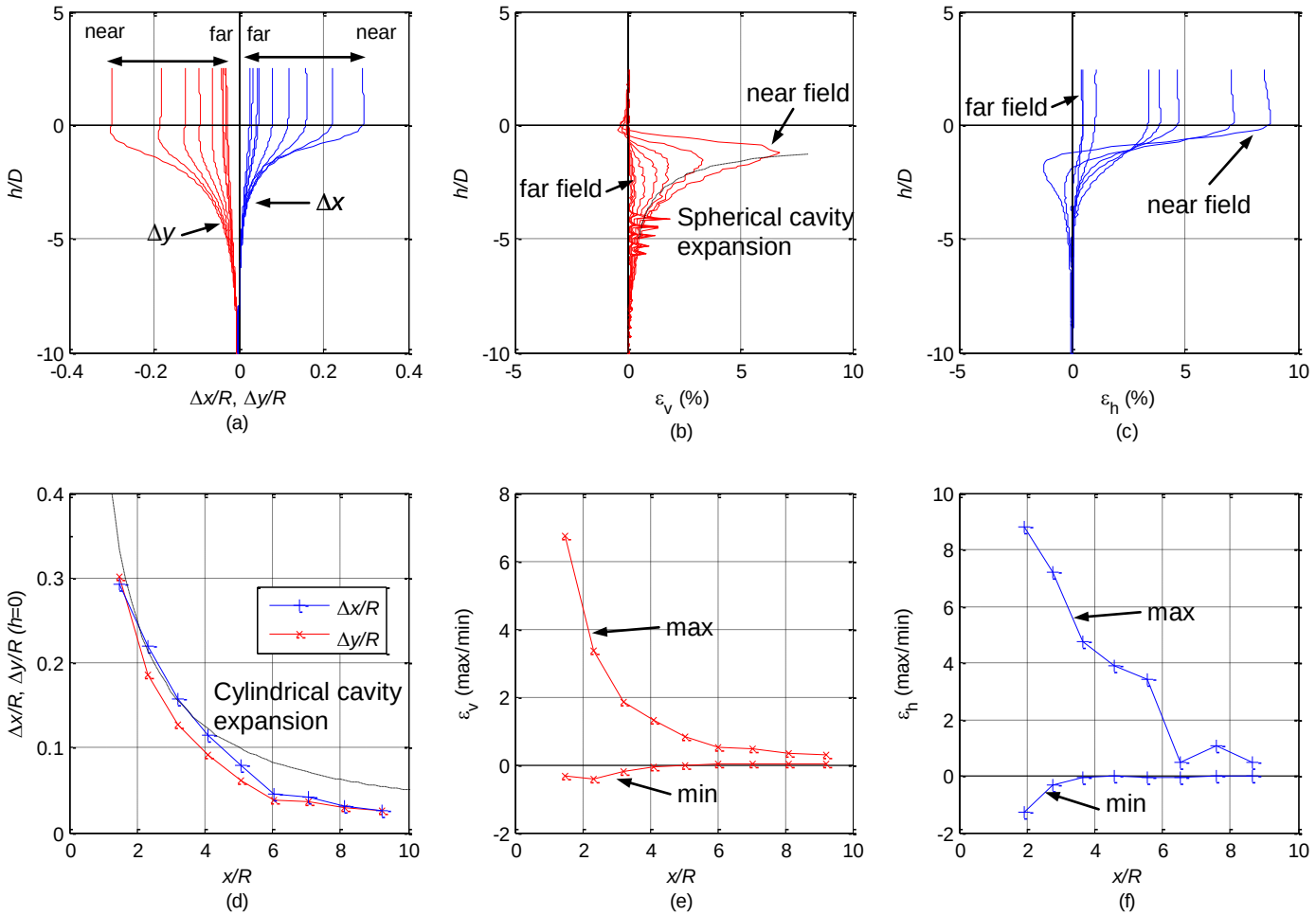

Figure 4.14: Summary of displacement and strains, camera 2, test 2C

4.2.5 Explanation of the trend lines added to figure 4.13

Circular (cylindrical) cavity expansion (subplot (d)):

Figure 4.15 shows circular cavity expansion.

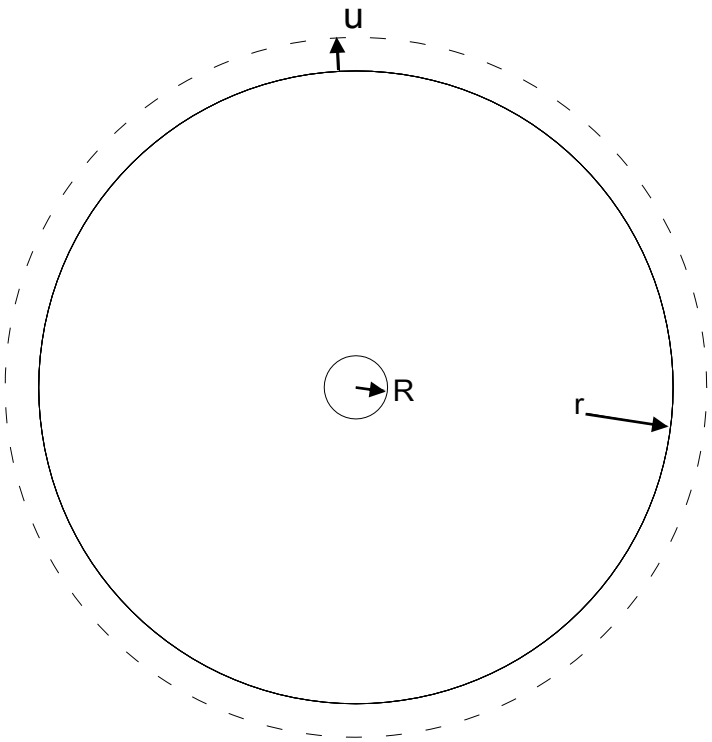

Figure 4.15: Illustration of soil displacement (plan view).

As the probe passes (h = 0), the soil which was in the probe area is now assumed to move outward. Assuming that the soil is incompressible, the original soil area should be equal to the post installation soil area. The new radius of the soil is r+u.

So the change of area = expansion of circle in plan = area displaced by probe

$$\delta A = 2\pi r u = \pi R^2 \tag{4.2}$$

$$\frac{u}{R} = \frac{R}{2r} \tag{4.3}$$

Spherical cavity expansion (labelled in subplot (b)):

The radius of the probe is *R,* while the radius of the soil deformation area is *r*. As the probe passes through (moving a distance δh), the soil which was in the probe area

goes outward and downwards a distance δu assuming expansion of a hemisphere. Assuming the soil is incompressible; the original soil volume should be equal to the post installation soil volume (i.e. expansion of hemisphere = volume displaced by advancing probe).

$$2\pi r^2 \delta u = \pi R^2 \delta h \tag{4.4}$$

$$\frac{\delta u}{\delta h} = \frac{1}{2}\left(\frac{R}{r}\right)^2 \tag{4.5}$$

which directly ahead of the probe can be written as

$$\frac{\delta(\Delta y)}{\delta h} = \frac{1}{2}\left(\frac{R}{h}\right)^2 = \frac{1}{8}\left(\frac{D}{h}\right)^2 \tag{4.6}$$

As described above, this expression is equivalent to the vertical strain in the soil.

4.2.6 Further supporting test results

Figure 4.14 is an efficient format for presenting results. Other test results are now presented in the same format. Tests 1, 2A, 2B and 2C were all run at 50g, with dense soil samples (refer to table 3.3 for the precise densities). A glass window was used in test 2A, 2B and 2C, whilst Perspex was used for test 1. Again 5 rows of patches near mid height of the image ($y \approx$ 200 to 220 mm) are shown in Figures 4.16, 16 & 16.

Figure 4.16 compares the displacement for tests 1, 2A, 2B and 2C. Again Δx begins later than Δy as the probe approaches. Δx reaches an ultimate value at $h = 0$, which is also slightly later than Δy (achieved at $h < 0$). Δx is generally similar to Δy at $h = 0$.

The data again show good agreement with the circular cavity expansion line. However, in test 2B Δx somewhat exceeds the cavity expansion prediction. Test 2C gives unusually low values for large *x/R*. Overall, the differences in displacement and

strain data between tests using Perspex (Test 1) and glass (all other tests) are negligible.

Figure 4.17 compares the vertical strains for the tests. Again the compressive strain develops when $h/D \approx -8$ and then rises to a peak while h is still negative. The maximum is smaller and occurs earlier as x/R increases. The maximum (compressive) strain for all h again tends to reduce with x/R, and is reasonably consistent for the various tests. The minimum value is again negative, indicating tensile strain close to the probe when $h/R \approx 0$. However, the magnitude of this value shows some variation between the tests. Initially the vertical strains are again somewhat in excess of the spherical cavity expansion prediction up to the point of maximum strain.

Figure 4.18 compares the horizontal strain for the tests. The maximum compressive strain again occurs at $h = 0$. Its value again tends to reduce with x/R although there can be some fluctuation in the results at larger x/R. In general the results are reasonably consistent for the various tests.

Again there is some tension from $h/D \approx -5$ for x/R less than about 4. The strain then returns to zero, before becoming significantly compressive. The amount of tensile strain does tend to vary somewhat, and, for instance, is quite small in test 1, potentially implying some effect of the use of Perspex rather than glass.

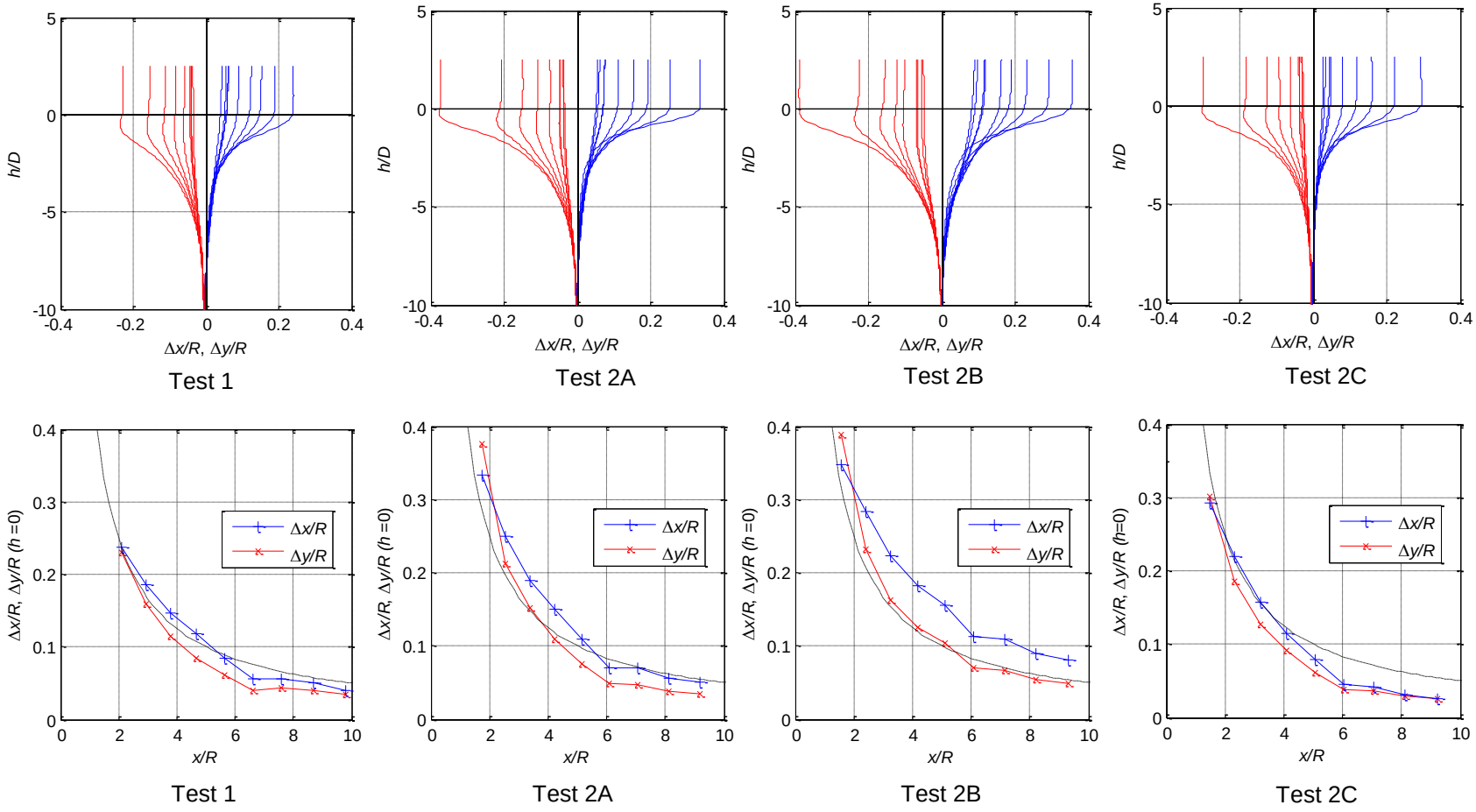

Figure 4.16: Summary of displacement (tests 1, 2A, 2B and 2C).

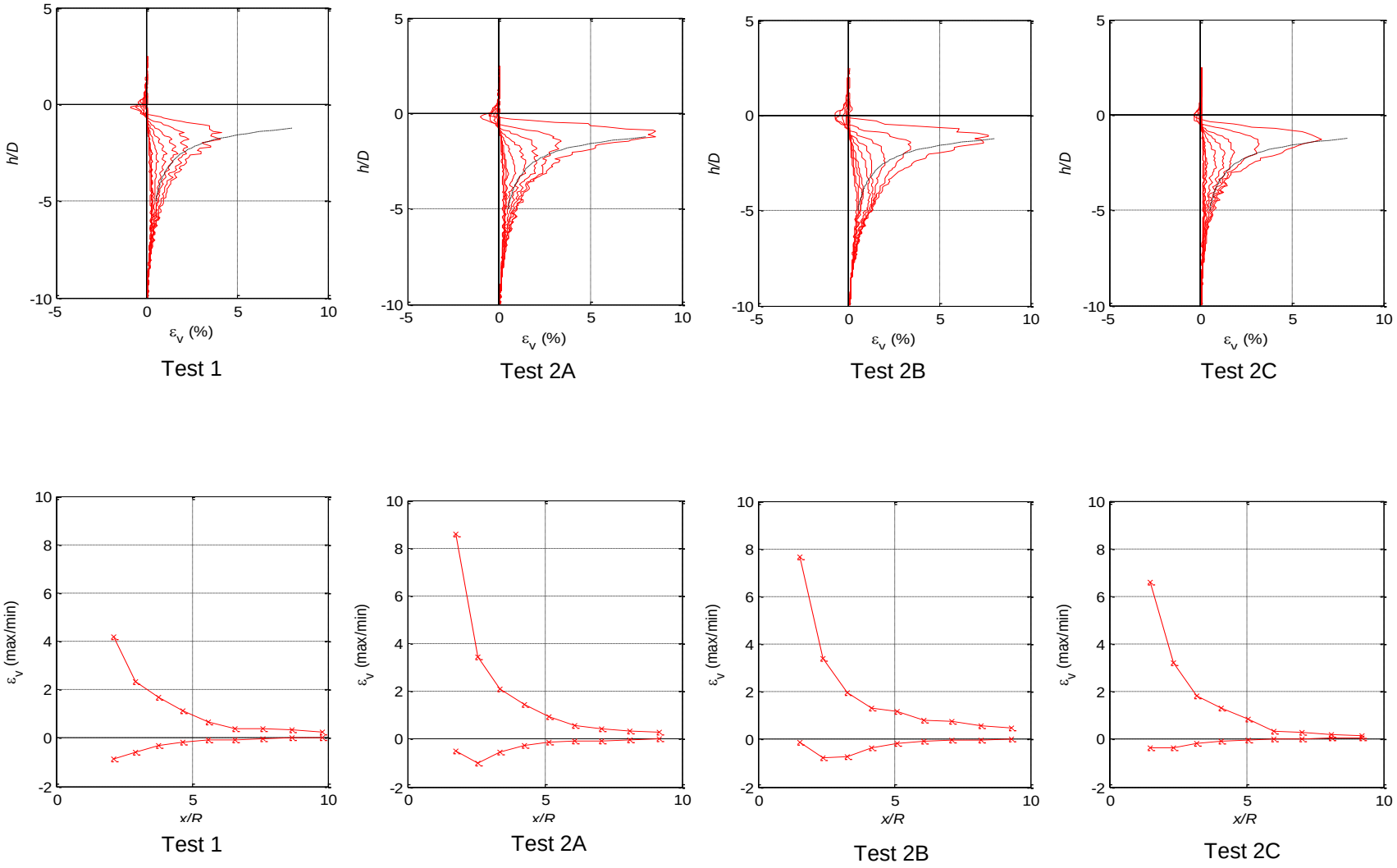

Figure 4.17: Summary of vertical strains (tests 1, 2A, 2B and 2C).

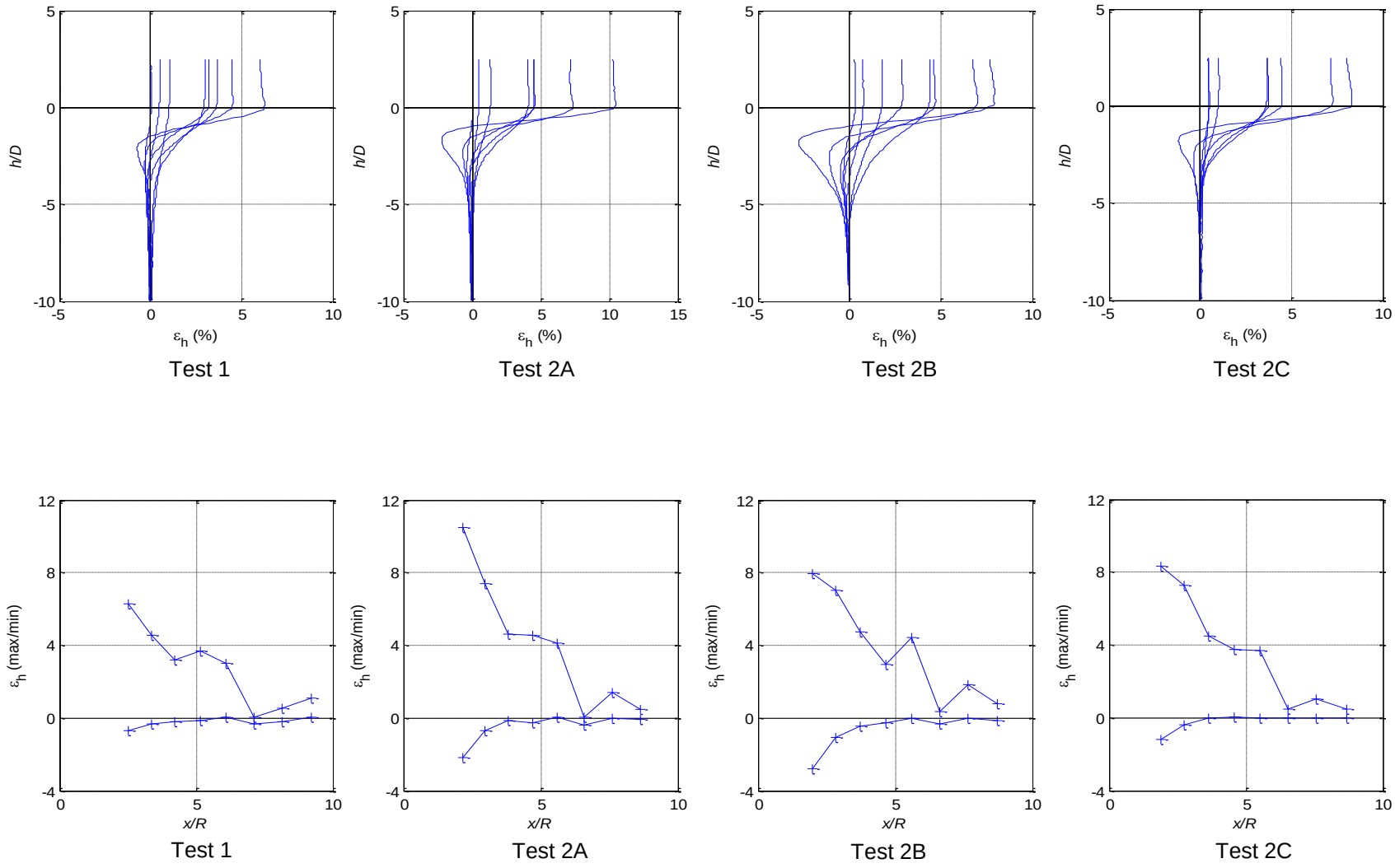

Figure 4.18: Summary of horizontal displacement (tests 1, 2A, 2B and 2C).

4.3 Chapter summary

1 Displacement is initially downwards tending to become outwards as the probe arrives and h reaches zero, ultimately giving similar vertical and horizontal (radial) movement. These displacements show reasonable correspondence with circular (cylindrical) cavity expansion, as could be anticipated for the horizontal displacement.

2 The amount of displacement generally increases with depth in camera 1. However, after about 8 to 10 diameters penetration (camera 2) the amount of movement does not vary significantly with depth.

3 After the probe passes there is little systematic movement, although near the surface of the soil the highest patches initially heave upwards and are later dragged down as the probe advances. For the columns at large radial distance, particularly the vertical movement increases at the same small rate as for $h < 0$.

4 The magnitude of displacements drops quickly as the radial position increases. The displacement variation with radius shows excellent agreement with circular cavity expansion theory $(\Delta x/R) = (R/2x)$ close to the probe, but can be somewhat less than that predicted at a larger radius.

5 Generally the behaviour inside a radius of $5.0R$ can be classified as the near field behaviour. For larger radii the movements have different behaviour, which can be considered as 'far field', particularly beyond $7.0R$.

6 Comparison of near-field data from both sides of the probe confirms that the behaviour on the right side of the model (which is obscured at larger radius) shows reasonable symmetry with results from the left hand side which are more generally reported.

7 Initially the test data indicate vertical strains at small radius somewhat in excess of a spherical cavity expansion prediction. The maximum (compressive) vertical strain occurs somewhat before the probe arrives at a

particular point in the soil and occurs earlier but is smaller as x/R increases. At small radius a much smaller tensile vertical strain is observed just as the probe passes.

8 Significant horizontal strains are observed later than the vertical strains. At small radius they are initially tensile. However, as the probe passes, larger compressive strains are observed, with magnitude reducing with x/R.

9 The results from the repeat tests show reasonable consistency. Overall negligible difference between Perspex and glass windows was observed.

CHAPTER 5 - RE-DRIVEN TEST RESULTS

5.1 Soil displacement

After Test 2C, the centrifuge was stopped (returning the model to 1g), the probe was withdrawn and then the model was accelerated to 50g again and the probe was 're-driven' as test 2D. Test 2D used exactly the same sample as test 2C, but run a second time, driving the probe into the soil which had been significantly disturbed by the initial insertion and withdrawal.

Figure 5.1 shows results from the same 'column' of patches near the probe, whose initial location is a horizontal distance 1.5*R* from the centreline of the probe (on the left), and whose y-location varies. The results can be compared with Figure 4.3 for test 2C for camera 2.

As shown in Figure 5.1(a), movement is again predominantly initially downward and then outward during the test. Final horizontal and vertical movements are again approximately equal. According to Figure 5.1(b) and (d), again there is little movement after the probe passes, and the magnitude is only about 1% of the probe radius. Figure 5.1(c) reveals that there is a slight tendency for movement to increase with depth, which is also indicated in Figure 5.1(f). From Figure 5.1(e), again significant vertical movement is observed at about 8 diameters, whereas significant horizontal movement again begins at about 4 diameters.

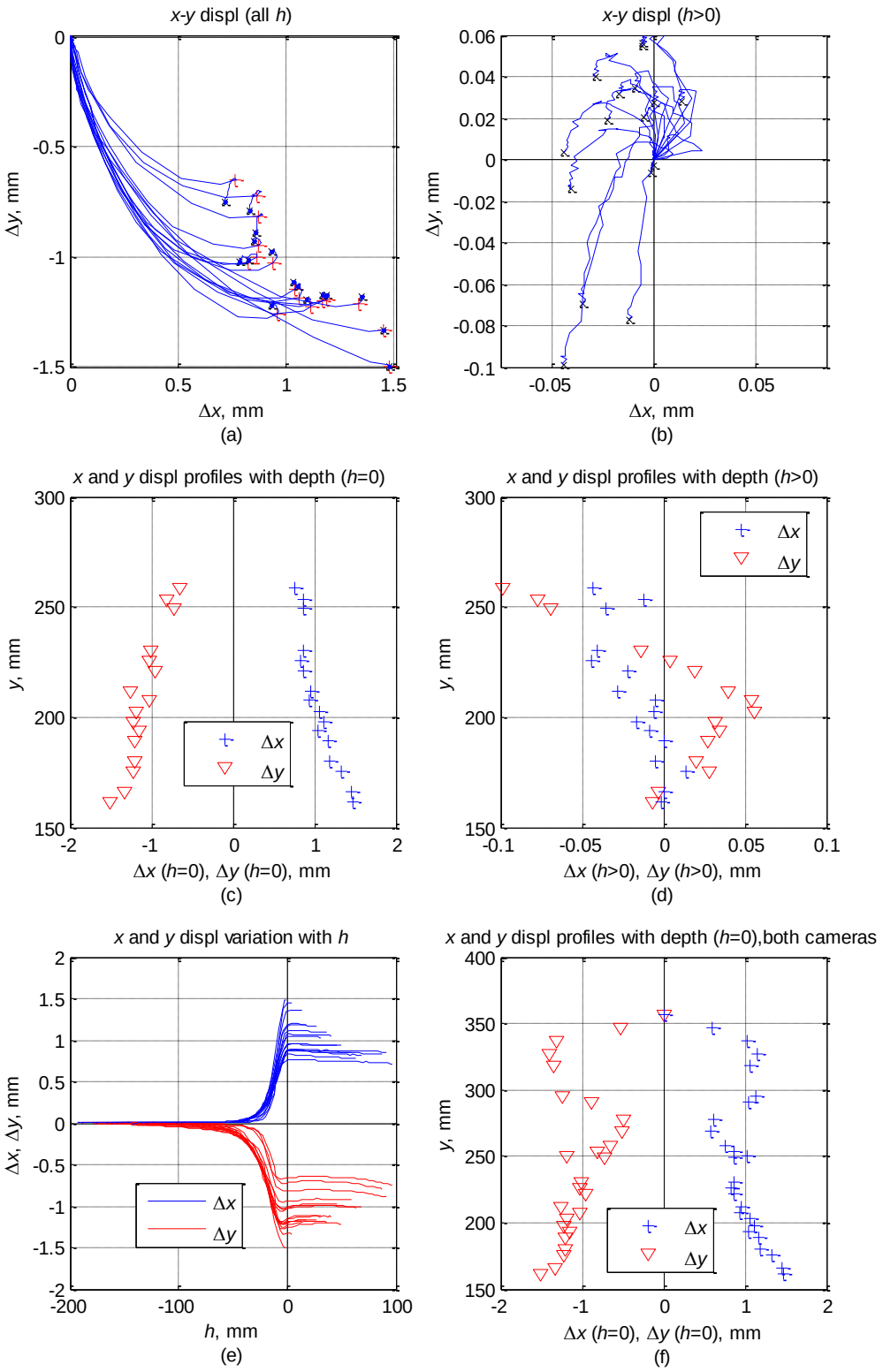

Figure 5.1: Displacement at x/R = 1.5 in camera 2, test 2D

5.2 Soil strains

In Figure 5.2, 5 rows of patches near mid height of the image ($y \approx 200$ to 220 mm) were again analysed here, and can be compared with Figure 4.13 for test 2C.

Subplots (a) and (d)

Again Δx begins later than Δy as the probe approaches. Δx achieves its ultimate value at $h = 0$, which is also later than Δy (achieved at $h < 0$). Δx is slightly larger than Δy at $h = 0$.

In contrast to test 2C, both Δx and Δy are quite significantly less than the circular cavity expansion prediction. The value is about half the circular cavity expansion prediction at small x, and even less at large x. This is probably due to the fact that the soil around where the probe had been inserted and withdrawn was loose.

Subplots (b) and (e)

Compressive vertical strain develops when $h/D \approx -7$, which is slightly later than test 2C. The strain then rises to a peak while h is still negative. Again the maximum is smaller and occurs earlier as x/R increases. The minimum value is again sometimes negative, indicating tensile strain close to the probe when $h/D \approx 0$.

In contrast to test 2C, the vertical strains agree well with the spherical cavity expansion prediction up to the point of maximum strain for $x/R = 1.5$. The value of the vertical strain in test 2D is less than test 2C, corresponding to the reduced displacement.

Subplots (c) and (f)

The maximum horizontal (radial) compressive strain again occurs at $h = 0$. Its value again tends to reduce with x. In contrast to test 2C, there is no tensile horizontal strain prior to the compressive strain. The maximum value is slightly less than test 2C.

The difference is not as significant as the displacement, but the strain does tend to reduce more rapidly as the radius increases.

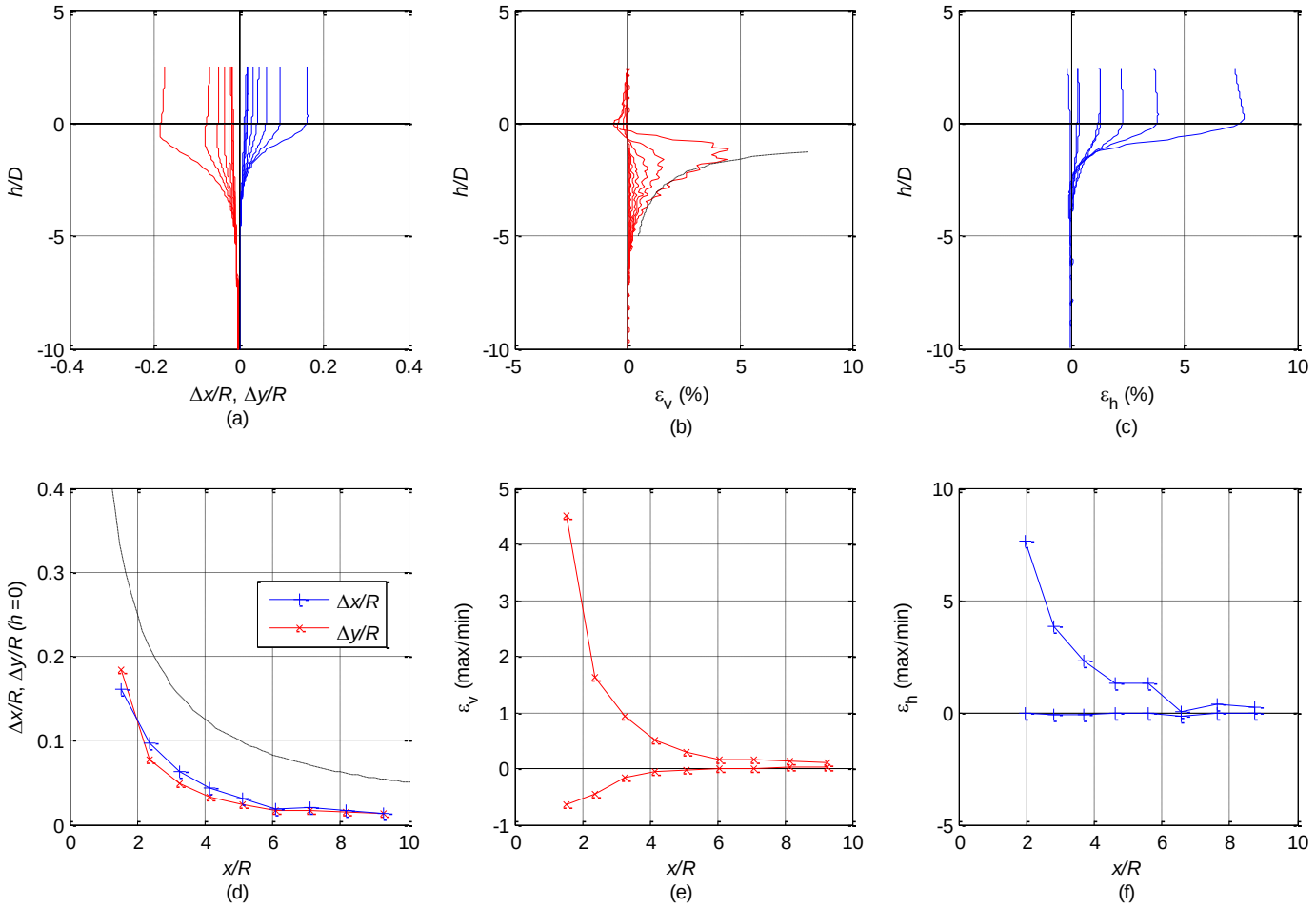

Figure 5.2: Summary of displacement and strains in camera 2, test 2D

5.3 Chapter summary

1 Both Δx and Δy are much less than the circular cavity expansion prediction. The value is about half the circular cavity expansion prediction at small *x*, and even less at large *x*.

2 Compressive vertical strain develops when $h/D \approx -7$, which is slightly later than test 2C. The strain then rises to a peak while *h* is still negative. Again the maximum is smaller and occurs earlier as *x/R* increases. In contrast to the test 2C, the vertical strains agree well with the spherical cavity expansion prediction for $x/R = 1.5$ and are less than test 2C.

3 Again tensile vertical strain is observed as the probe passes.

4 In contrast to test 2C, there is no initial tensile horizontal strain as the probe approaches.

5 The maximum value of horizontal strain is slightly less than for test 2C, since although horizontal displacements at small *x* are much smaller, reduction with *x* is rapid.

CHAPTER 6 - EFFECT OF SOIL DENSITY

6.1 Introduction

Bolton & Gui (1993) found that the tip resistance is significantly affected by the relative density. Soil with higher density would be associated with higher tip resistance. Tests with different density were run to investigate the effect on displacement and strain.

6.2 Loose sample results

6.2.1 Displacement in loose sample

Test 3A was run at 50g with a loose soil sample (ρ =1.57 g/mm^3). The void ratio was 0.68, with relative density 49 %.

When initially examining the results it was found that there were several wild or random vectors near the probe. Therefore a 'column' of patches was chosen whose initial location was a horizontal distance 2.5*R* from the centreline of the probe (compared to 1.5*R* for tests 2), and whose y-location varies. Figures 6.1 and 6.2 show data for cameras 1 and 2, and can be compared with Figures 4.2 and 4.3 for dense sand.

As shown in subplot (a), movement is again predominantly initially downward and then outward during the test. The final Δx is slightly larger than Δy in camera 1, while the final Δx is slightly smaller than Δy in camera 2.

Subplot (b) reveals that again the soil appears to be 'dragged' behind the probe after it has passed in camera 1. Again there is little movement after the probe passes in camera 2.

Subplot (c) shows that again the amount of movement when $h = 0$ increases steadily with depth in camera 1. The movement when $h = 0$ increases slightly with depth in camera 2.

According to subplot (d), again the amount of vertical movement after the probe has passed tends to reduce with depth in camera 1.

Subplot (f) in Figure 6.2 again shows reasonable consistency for the lowest data from camera 1 and the highest data for camera 2.

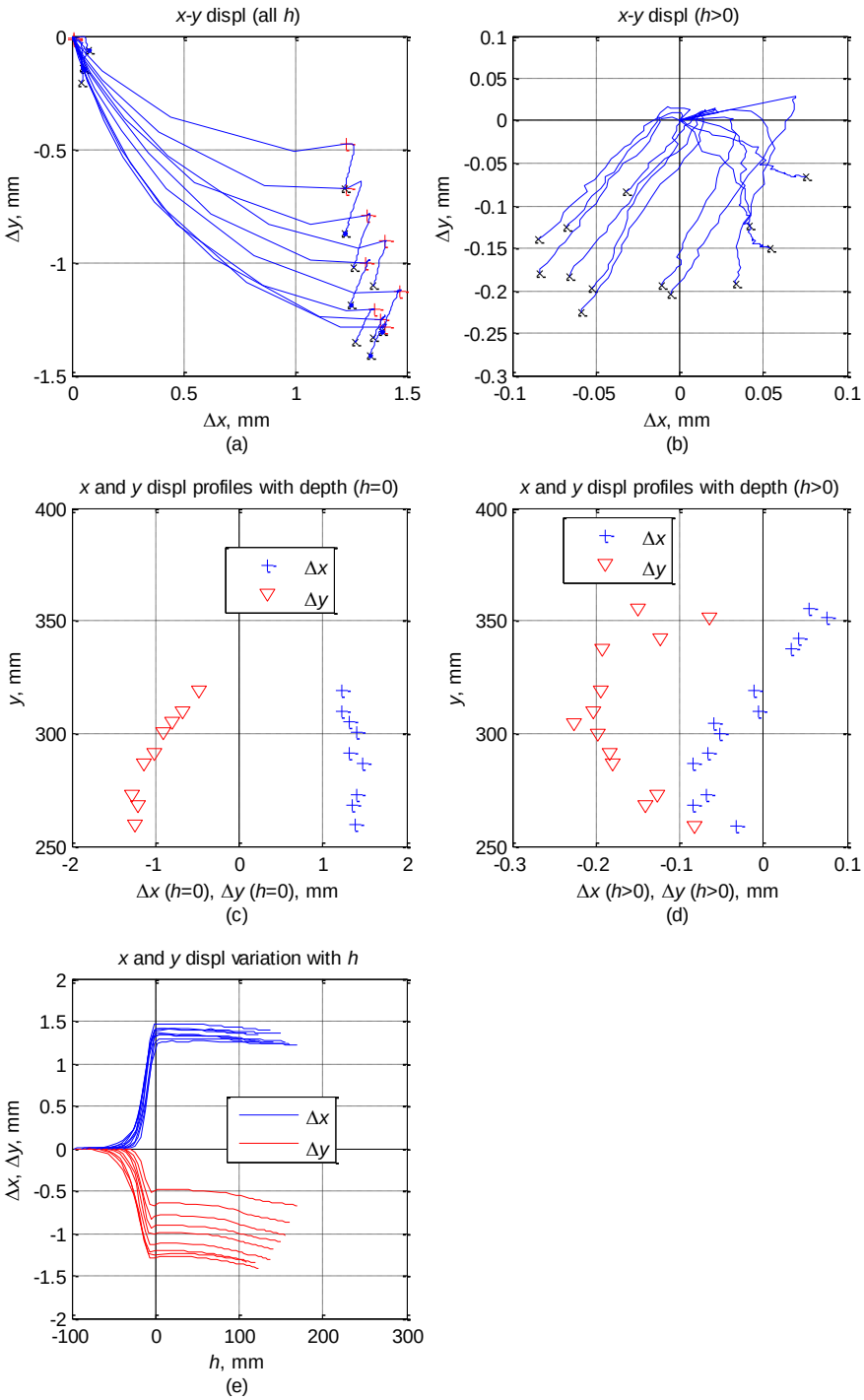

Figure 6.1: Displacement at x/R = 2.5 in camera 1, test 3A.

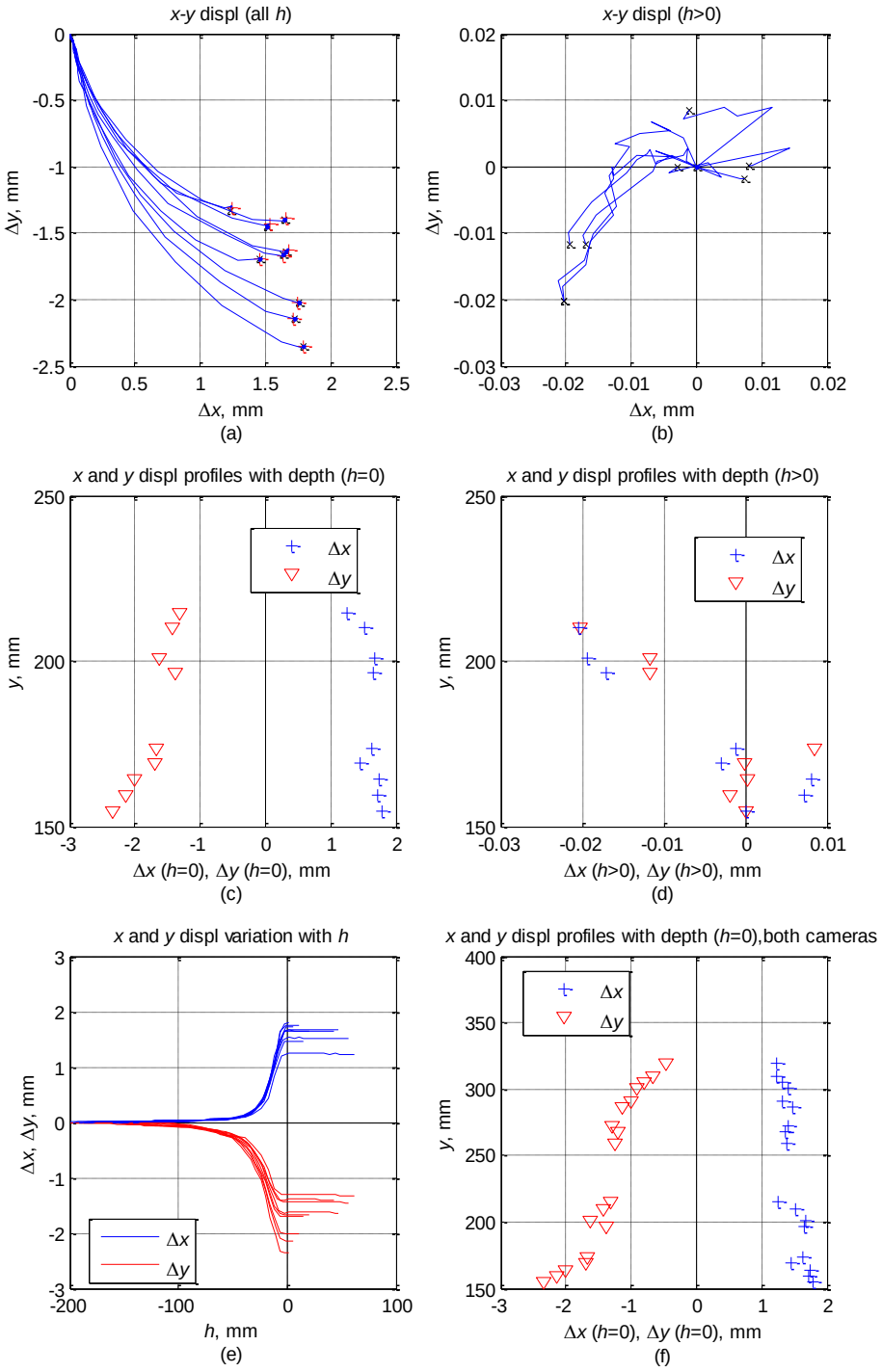

Figure 6.2: Displacement at x/R = 2.5 in camera 2, test 3A.

6.2.2 Summary of strains in loose soil

For Figure 6.3 five rows of patches near mid height of the image ($y \approx 190$ to 210 mm) were analysed again. As mentioned before, the first column starts from $x/R = 2.5$.

Subplots (a) and (d)

Again Δx begins later than Δy as the probe approaches. Δx is slightly larger than Δy at $h = 0$. The data from subplot (d) shows excellent agreement with the cavity expansion prediction close to the probe, but is somewhat less than the prediction at a larger radius.

Subplots (b) and (e)

The vertical strain rises to a peak while h is still negative. Again the maximum is smaller and occurs earlier as x/R increases. There is some evidence that the minimum value is again negative, indicating tensile strain close to the probe when $h/R \approx 0$. However, the tendency for this is limited, possibly since there is no data for small x/R.

The vertical strain for $x/R = 2.5$ is slightly in excess of the spherical cavity expansion prediction up to the point of maximum strain. However, there is not much difference in test 3A compared to the test 2 series (dense soil sample).

Subplots (c) and (f)

The maximum compressive horizontal (radial) strain again occurs at $h = 0$. Its value again tends to reduce with x. The maximum value is similar to the test 2 series (dense sample). Again there is some evidence of initial tensile strain but the tendency for this is limited, possibly since there is no data for small x/R.

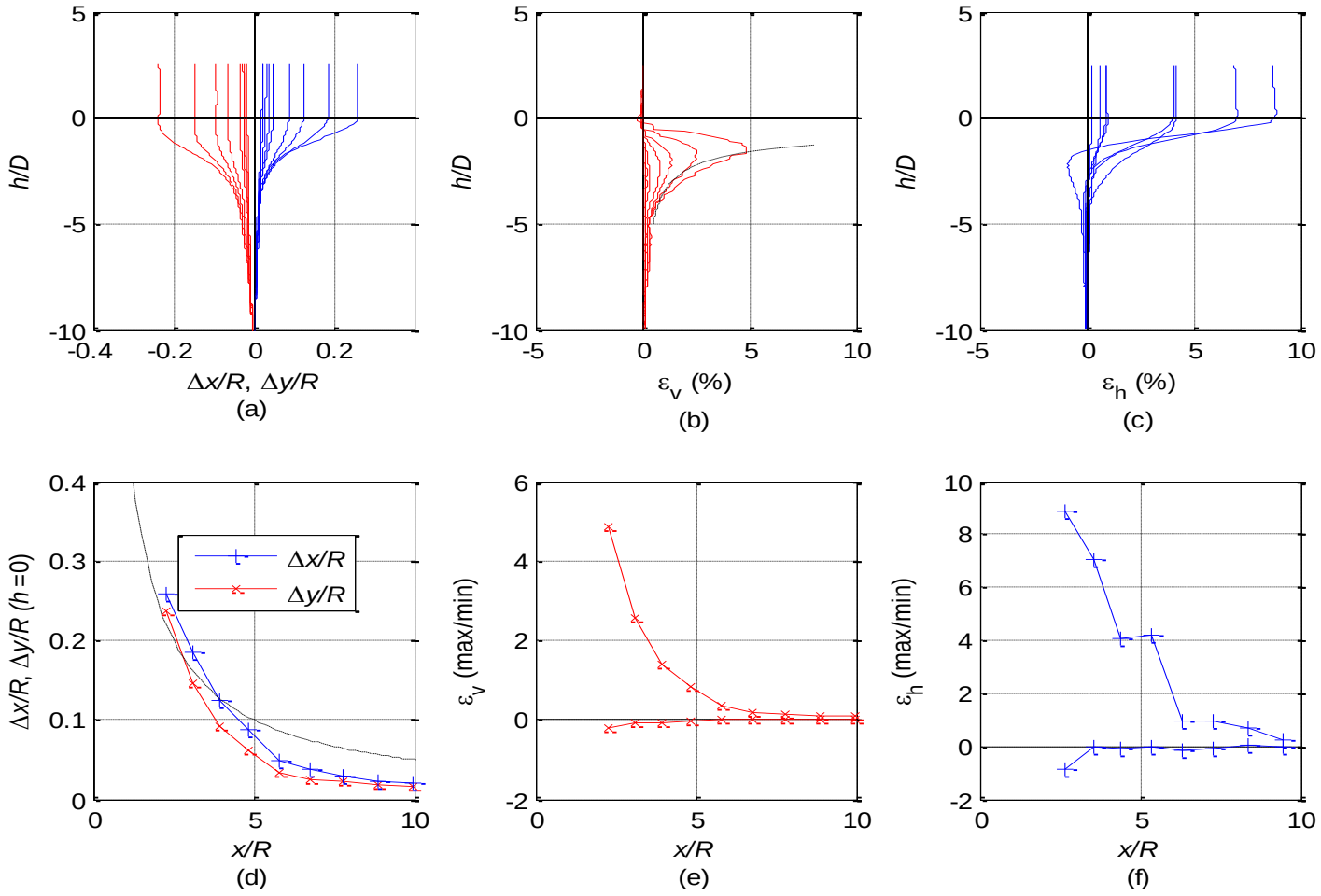

Figure 6.3: Summary of displacement and strains, camera 2, test 3A.

6.3 Loose over dense sand results

The sample for test 3B was loose over dense sand. From the bottom of the sample to y = 250 mm is a dense sample with density of 1.67 g/mm^3, void ratio 0.58, and relative density 89 %. From 250 mm to the top is a loose sample with density of 1.59 g/mm^3, void ratio 0.67, and relative density 53 %. This means that both layer thickness are over 5D and can fully develop the absolute value in the layer (Gui et al, 1998).

6.3.1 Displacement in loose over dense soil

Figures 6.4 and 6.5:

A similar 'column' of patches was used as in test 3A, whose initial location is a horizontal distance 2.5*R* from the centreline of the probe, and whose y-location varies.

As for test 3A (Figures 6.1 and 6.2), subplot (a) shows that final Δx is slightly larger than Δy in camera 1, while the final Δx is slightly smaller than Δy in camera 2. As shown in subplot (b), there is not much difference compared to test 3A for the soil's movement after probe passes in both cameras.

Subplot (c) reveals that again the amount of movement when h = 0 increases steadily with depth in camera 1. As for the dense sample, the values of the movement when h = 0 varies little in camera 2. The value is approximately the same as test 3A (loose sample) at the top, but is slightly less than test 3A at the end. Subplot (d) shows that again the amount of vertical movement after the probe has passed tends to reduce with depth in camera 1.

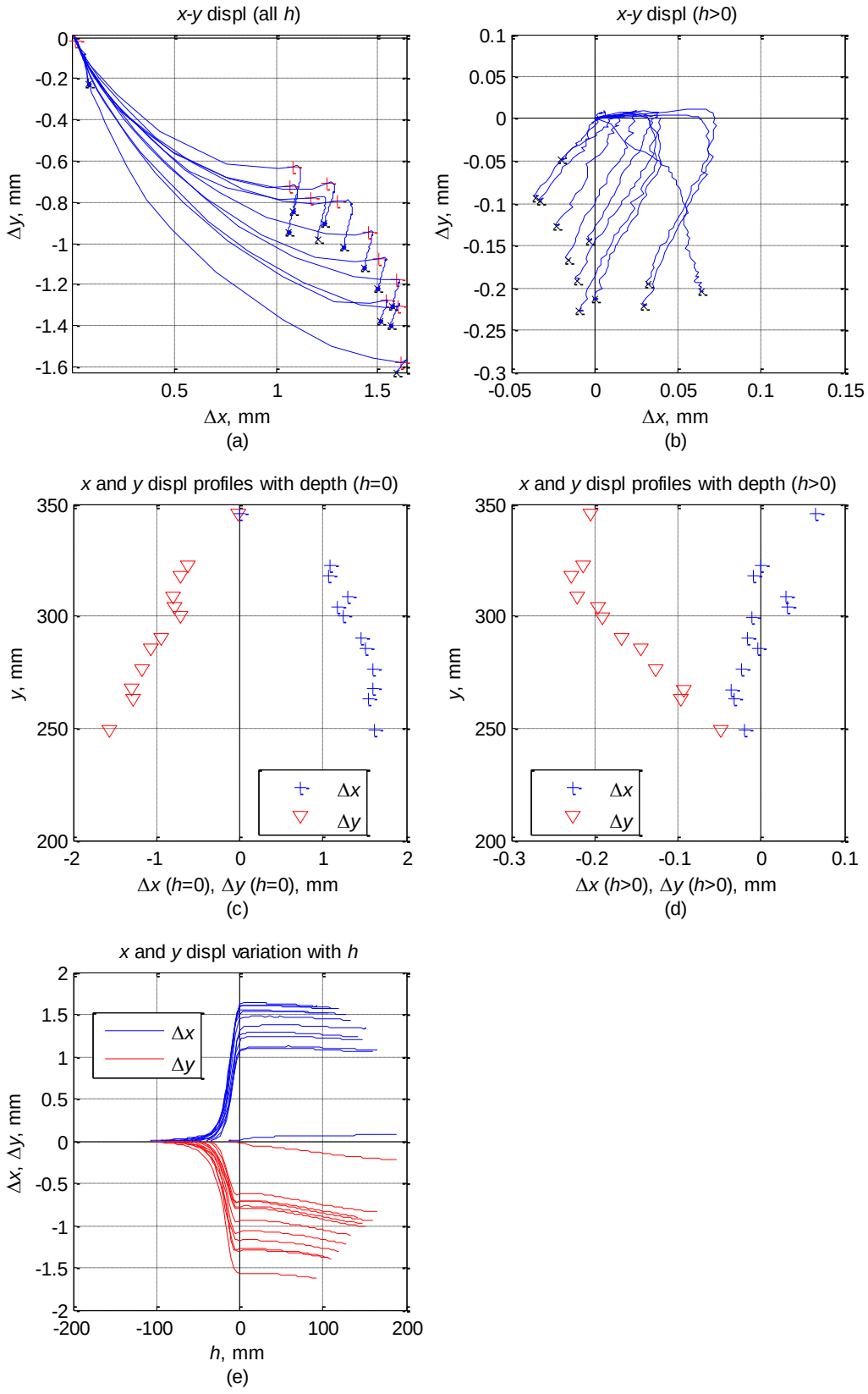

Figure 6.4: Displacement at x/R = 2.5 in camera 1, test 3B.

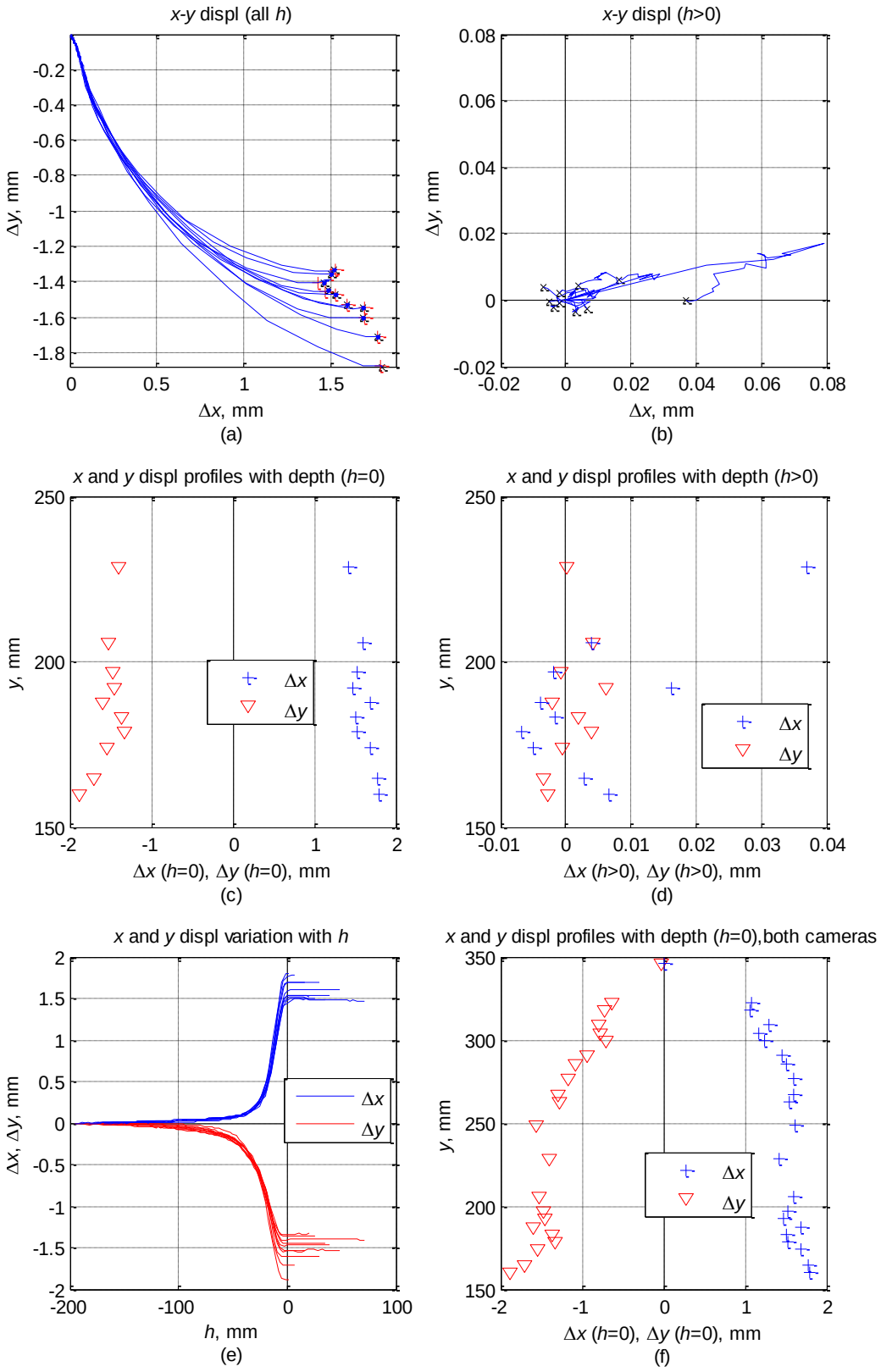

Figure 6.5: Displacement at x/R = 2.5 in camera 2, test 3B.

6.3.2 Summary of strains in loose over dense soil:

Again 5 rows of patches near mid height of the image ($y \approx 195$ to 215 mm, about 50 mm below the loose/ dense interface) were analysed and the results are plotted in Figure 6.6. As mentioned before, the first column starts from $x/R = 2.5$.

Subplot (a) and (d)

The movement at $h = 0$ is slightly in excess of the cavity expansion prediction close to the probe, but is somewhat less than the prediction at a larger radius.

Subplot (b) and (e)

The vertical strain rises to a peak while h is still negative. Again the maximum is smaller and occurs earlier as x/R increases. The minimum value is again sometimes negative, indicating tensile strain close to the probe when $h/D \approx 0$. However, the tendency for this is limited, possibly since there is no data for small x/R. The vertical strain for $x/R = 2.5$ agrees well with spherical cavity expansion prediction up to the point of maximum strain. The maximum value of the vertical strain in test 3B is very similar to the value from test 3A (loose sample).

Subplot (c) and (f)

The maximum horizontal (radial) compressive strain again occurs at $h = 0$. Its value again tends to reduce with x. The maximum value is slightly less than the test 2 series (dense sample), and is very close to the value from test 3A (loose sample).

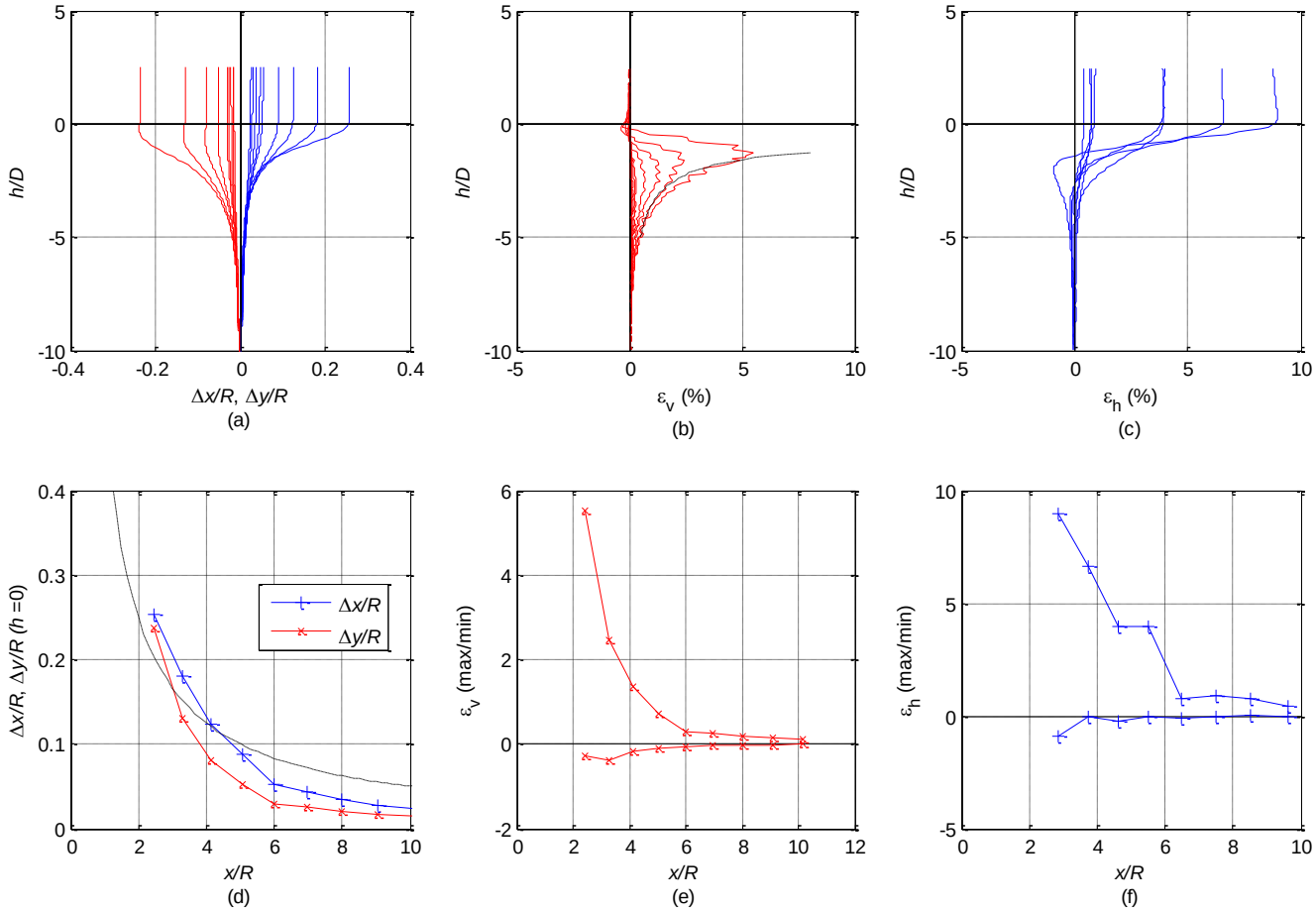

Figure 6.6: Summary of displacement and strains, camera 2, test 3B.

6.4 Effect of density

Figure 6.7 and 6.8 show a summary of variation of displacements and strains with different density with y location about 200 to 220mm. It is found that there are no significant deviations.

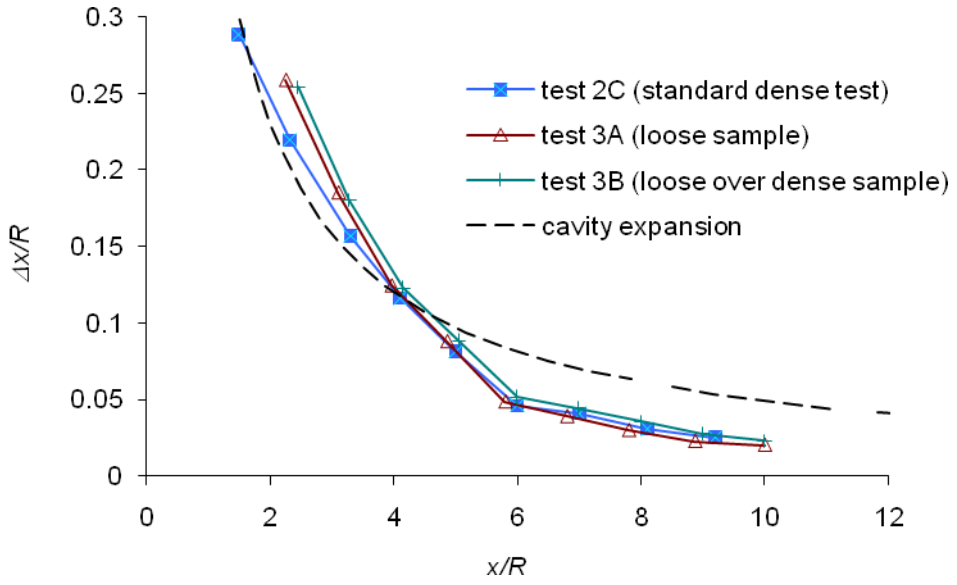

(a)

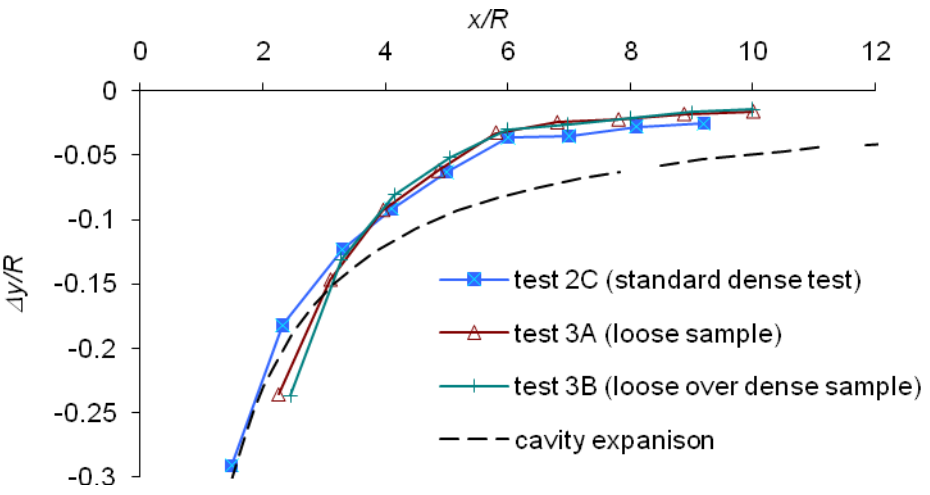

(b)

Figure 6.7: Effect of density on displacement: (a) horizontal displacement (b) vertical displacement

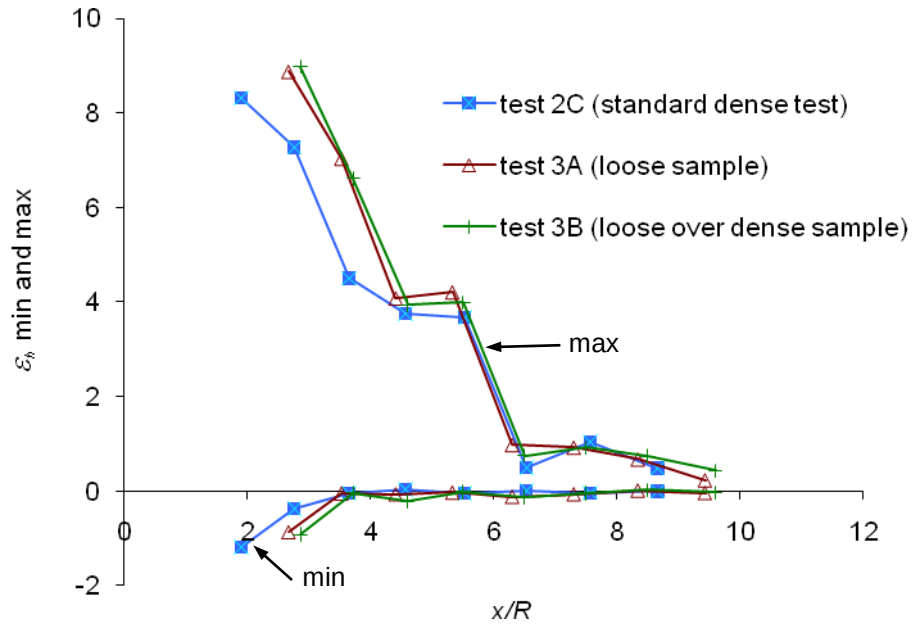

(a)

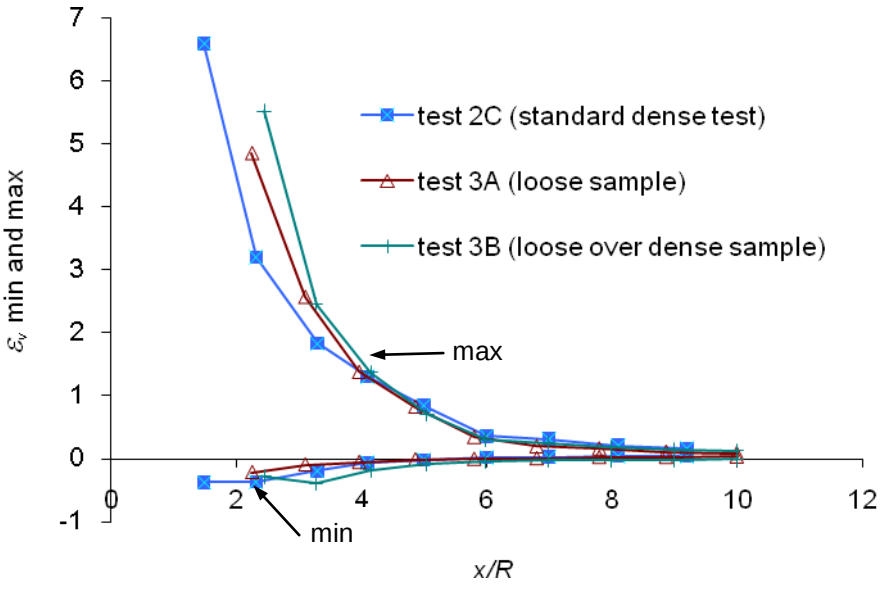

(b)

Figure 6.8: Effect of density on strain: (a) horizontal strain (b) vertical strain

6.5 Chapter summary

1 Movement is again initially downwards tending to become outwards as *h* reaches zero, ultimately giving similar vertical and horizontal movement.

2 The amount of movement when *h* = 0 increases steadily with depth in camera 1, while the values varies little in camera 2.

3 It is found that there is no significant deviation in displacement and strains for different density. This may be because the 'loose' soil does not have a very low relative density. Furthermore, this density was measured before the model was loaded onto the centrifuge, and it is possible that the density for the 'loose' samples could have increased prior to the actual test due to densification as the model was moved and lifted onto the centrifuge.

CHAPTER 7 - EFFECT OF CENTRIFUGE ACCELERATION

By varying the centrifuge acceleration, the stress field in the soil is changed. Gui et al (1998) found that a larger in situ stress level corresponded to a smaller bearing factor (N_q). A series of tests under different g-levels were undertaken to investigate the effect of stress level on displacement of the soil as the probe advanced.

7.1 100g test results

Test 4 was run at 100g with a dense soil sample, compared with 50g for the other tests reported so far. The soil density was 1.68g/mm^3, void ratio was 0.58, and the relative density was 90%, and thus the results can be compared with test series 2.

7.1.1 Displacement in 100g test

The data in Figure 7.1 is from a 'column' of patches (for camera 2), whose initial location is a horizontal distance 2.0*R* from the centreline of the probe, and whose y-location varies.

As shown in subplot (a), Δx is slightly smaller than Δy. Subplots (b) & (d) show that again there is little movement after the probe passes. Subplot (c) reveals that again the values of movement when $h = 0$ vary little with depth for camera 2. From Subplot (e) significant vertical movement is observed at about 6 diameters, whereas significant horizontal movement again begins at about 4 diameters. Subplot (f) again shows reasonable consistency for the lowest data from camera 1 and the highest data for camera 2. It appears that again co-incidentally the increase in displacement with depth is substantially complete at the interface of the images from the two cameras, corresponding to an embedment of about 8 or 10 diameters.

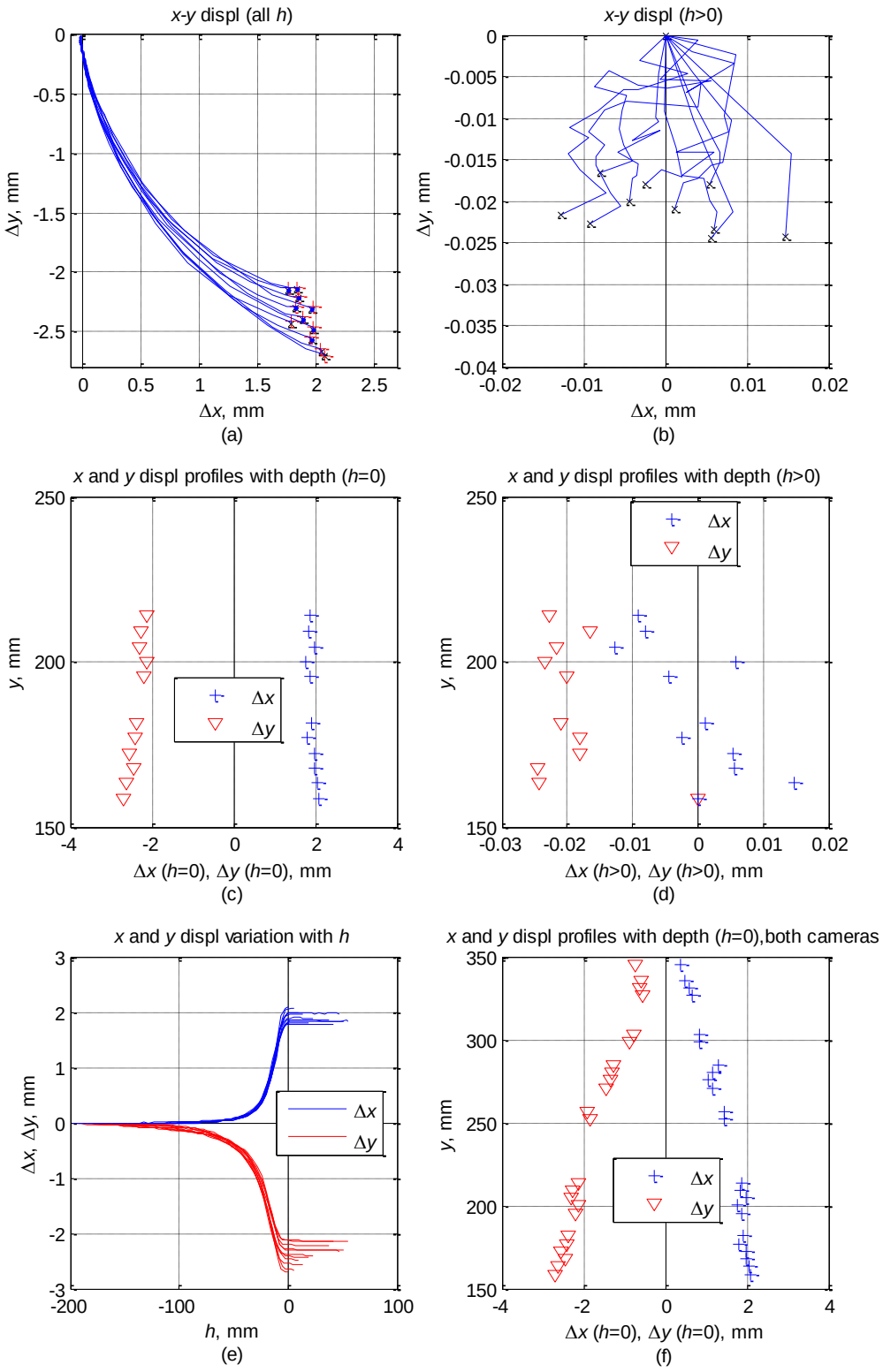

Figure 7.1: Displacement at *x/R* = 2.0 in camera 2, test 4.

7.1.2 Summary of strains and displacement in 100g test

Again 5 rows of patches near to the mid height of the image ($y \approx 190$ to 210 mm) were analysed and the results are plotted in Figure 7.2. As mentioned before, the first column starts from x/R = 2.0.

Subplots (a) and (d)

Again Δx begins later than Δy as the probe approaches. The movement at h = 0 is slightly in excess of the cavity expansion prediction close to the probe, but is somewhat less than the prediction at a larger radius.

Subplots (b) and (e)

Again the vertical strains reach a maximum compressive value before the probe arrives. No significant tensile strains are observed as the probe passes, compared with results from test series 2 (50g) where there was some evidence of this effect. The vertical strains are slightly in excess of the spherical cavity expansion prediction up to the point of maximum strain.

Subplots (c) and (f)

The maximum horizontal (radial) compressive strain again occurs at h = 0. Its value again tends to reduce with x. Again there is some initial tension from $h/D \approx -5$ for x/R less than about 4, but this effect is somewhat less than in test series 2.

In conclusion in general there is not conspicuous difference compared to the corresponding 50g test series, except that there is less evidence of horizontal tensile strain as the probe approaches and less evidence of vertical tensile strain as the probe passes.

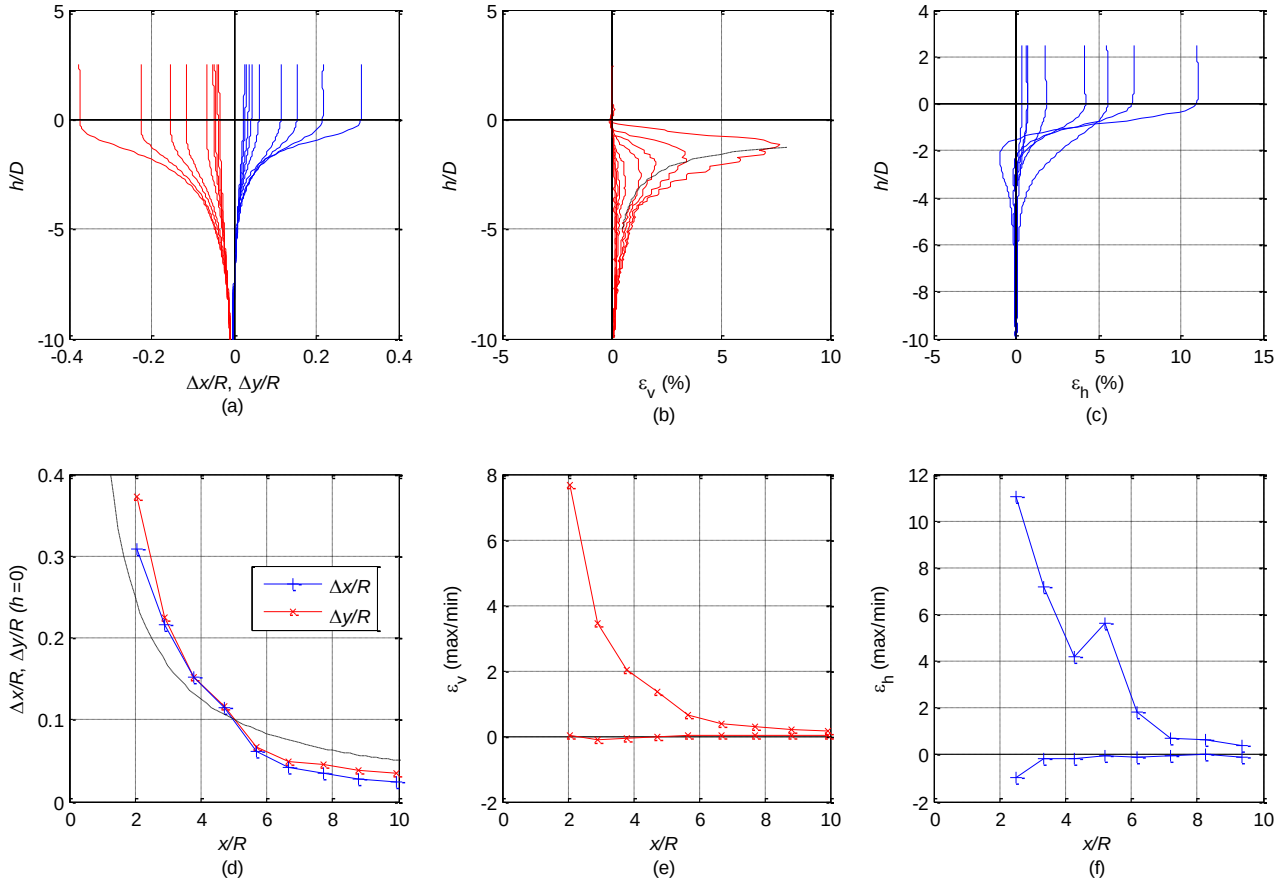

Figure 7.2: Summary of displacement and strains, test 4.

7.2 1g test results

Test 6 was carried out at 1g with a dense soil sample, using the normal centrifuge model. The soil density was 1.67 g/mm^3, corresponding to a void ratio of 0.59, and relative density of 86 %.

7.2.1 Displacement in 1g test

Data in Figure 7.3 is from a 'column' of patches (for camera 2) whose initial location is a horizontal distance 1.8*R* from the centreline of the probe, and whose y-location varies.

The displacement is quite similar to the 50g or 100g tests on dense soil. As show in subplot (a), movement is again predominantly initially downward and then outward during the test. According to subplots (b) and (d), again there is little movement after the probe passes. Again the values of the movement when $h = 0$ vary little with depth for camera 2 (subplot (c)).

However, subplot (e) indicates that the displacement of 1g test appears slightly later than the 50g or 100g tests – this will be discussed further below based on the strain results.

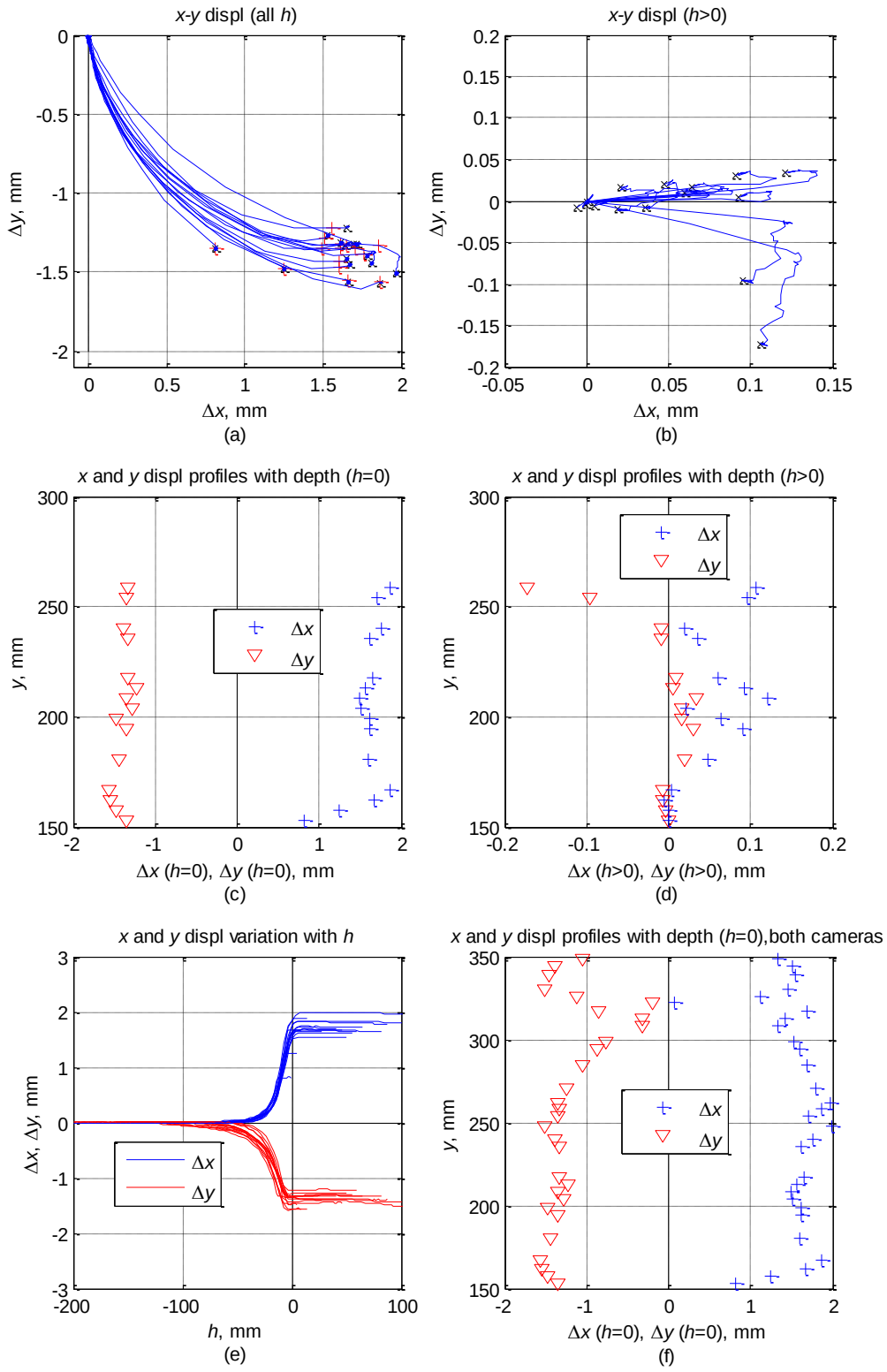

Figure 7.3: Displacement at *x/R* = 1.8 in camera 2, test 6.

7.2.2 Summary of strains and displacement in 1g test

In Figure 7.4, 5 rows of patches near mid height of the image ($y \approx 200$ to 220 mm) were again analysed.

Subplots (a) and (d)

The vertical displacement in the 1g test appears at $h/D \approx -5$, which is slightly later than the 50g or 100g test. The value of Δx is generally larger than Δy at $h = 0$. Δx shows good agreement with the circular cavity expansion line near the probe, but is somewhat less than the cavity expansion prediction for larger x. However, Δy gives unusually low values compare to the other tests.

Subplots (b) and (e)

Again vertical compressive strain develops when $h/D \approx -6$, and then rises to a peak while h is still negative. The maximum is smaller and occurs earlier as x/R increases. The minimum value is again sometimes negative, indicating tensile strain close to the probe when $h/R \approx 0$. Initially the vertical strains show good agreement with the spherical cavity expansion prediction up to the point of maximum strain.

Subplots (c) and (f)

The maximum compressive strain again occurs at $h = 0$. Its value again tends to reduce with x although there can be some fluctuation in the results at larger x. Again there is some tension from $h/D \approx -5$ for x/R less than about 4. The strain then returns to zero, before becoming significantly compressive.

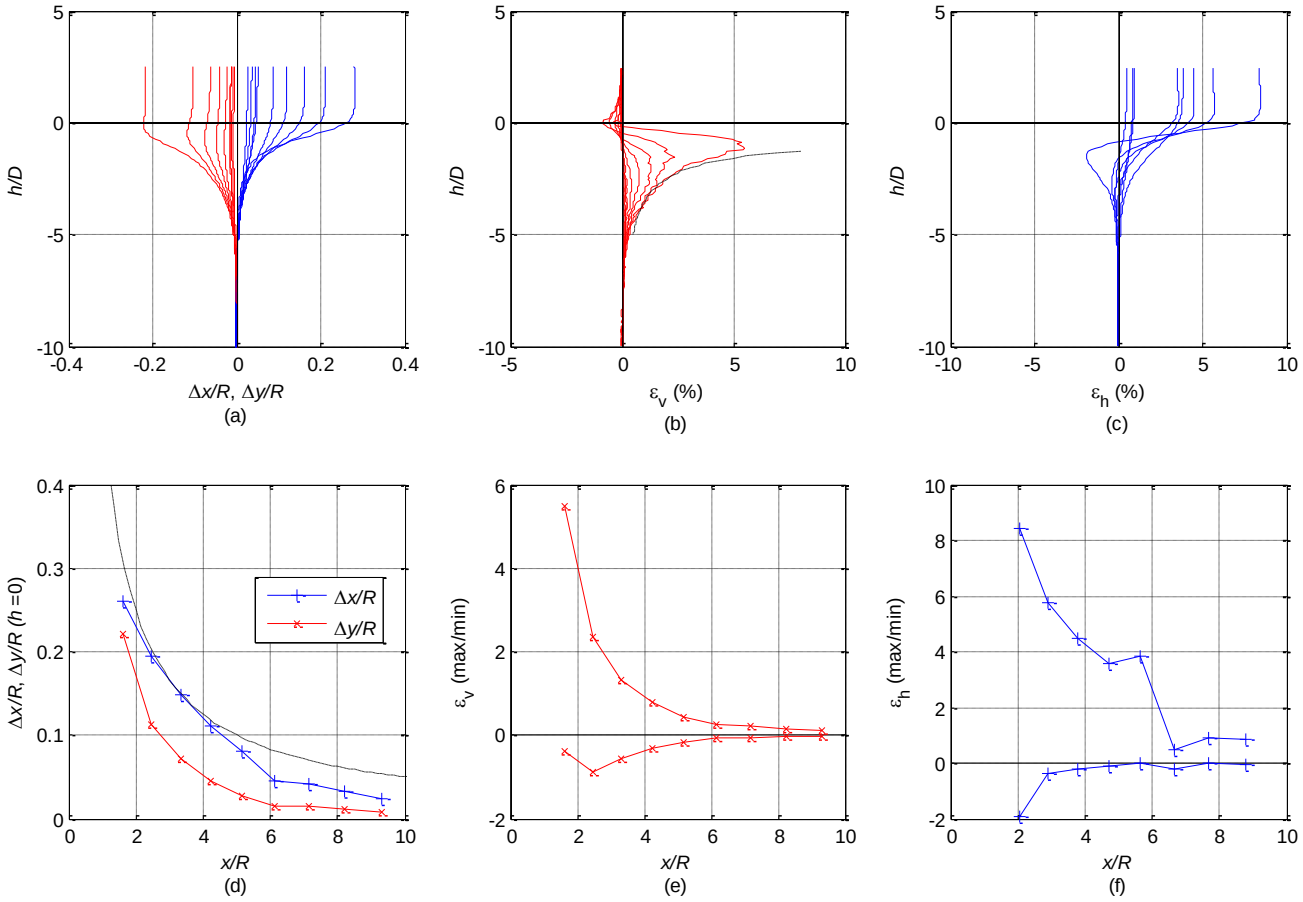

Figure 7.4: Summary of displacement and strains, test 6.

7.3 Discussion of the effect of acceleration

Figure 7.5 shows a summary of vertical and horizontal displacement for different g-levels. The horizontal displacement shows slight difference close to probe, but is very similar at large radius. The vertical displacement varies more, and increases with g-level.

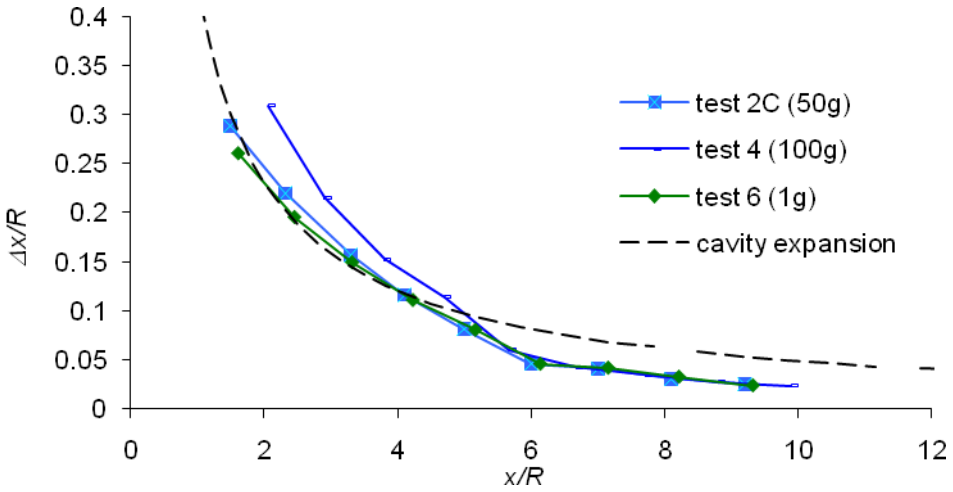

(a)

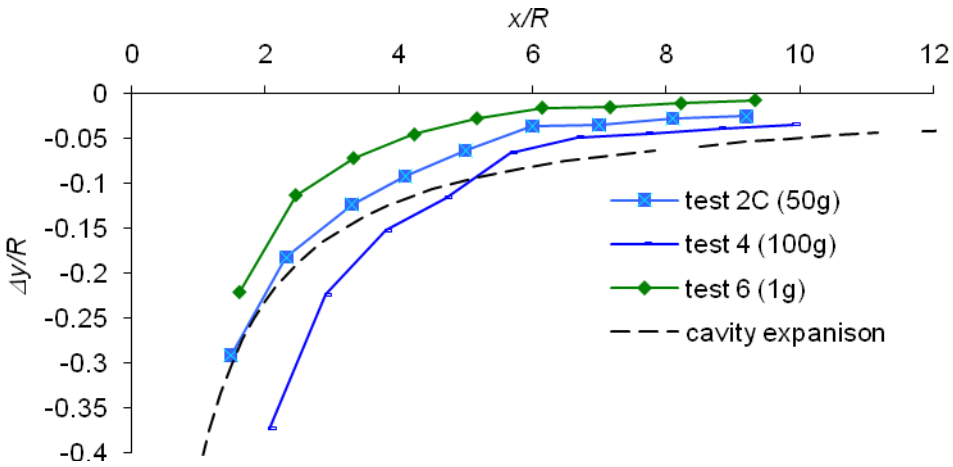

(b)

Figure 7.5: Summary of displacement under different g-level: (a) horizontal displacement. (b) vertical displacement.

Figure 7.6 shows a summary of maximum and minimum vertical and horizontal strain for different g-levels. Similar to the displacement, it is found that the higher g-level corresponds to a higher maximum vertical strain. As the acceleration increased to N

times gravity, the corresponding vertical stress would be increased to N times. According to Hardin & Drnevich (1972), the Young's modulus E is proportional to the square root of the vertical stress; therefore the strain should be proportional to the square root of the N (equation 7.1-7.3). This explains why the higher g-level corresponds to a higher vertical strain.

$$\sigma_v \propto N \tag{7.1}$$

$$E \propto \sqrt{\sigma_v} \propto \sqrt{N} \tag{7.2}$$

$$\varepsilon_v = \sigma_v / E \propto \sqrt{N} \tag{7.3}$$

For horizontal strain, the maximum strain in the 100g test is slightly higher than the others close to the probe. The small tensile vertical strain as the probe passes tends to reduce as g-level increases.

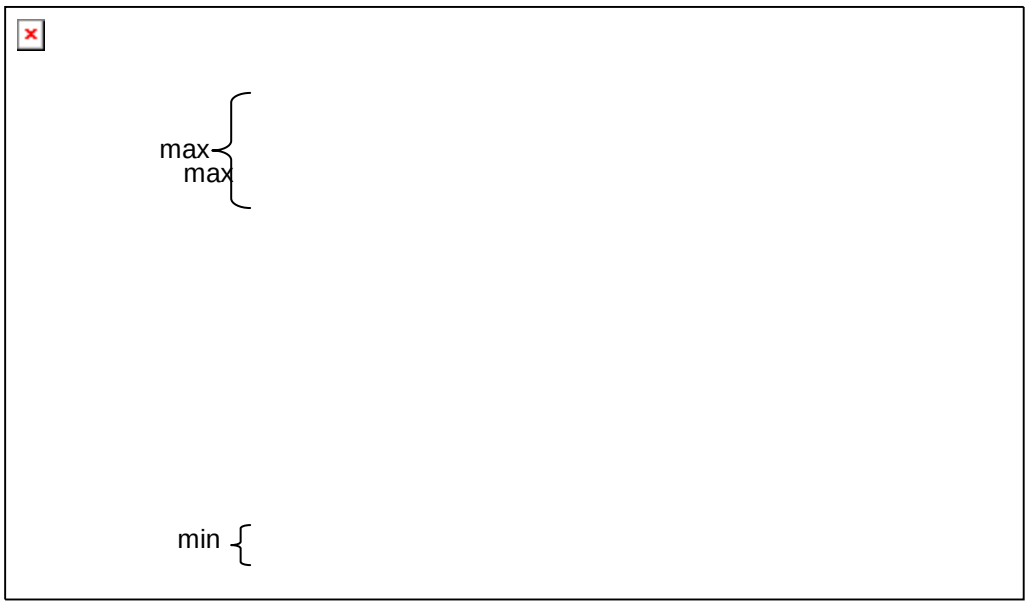

(a)

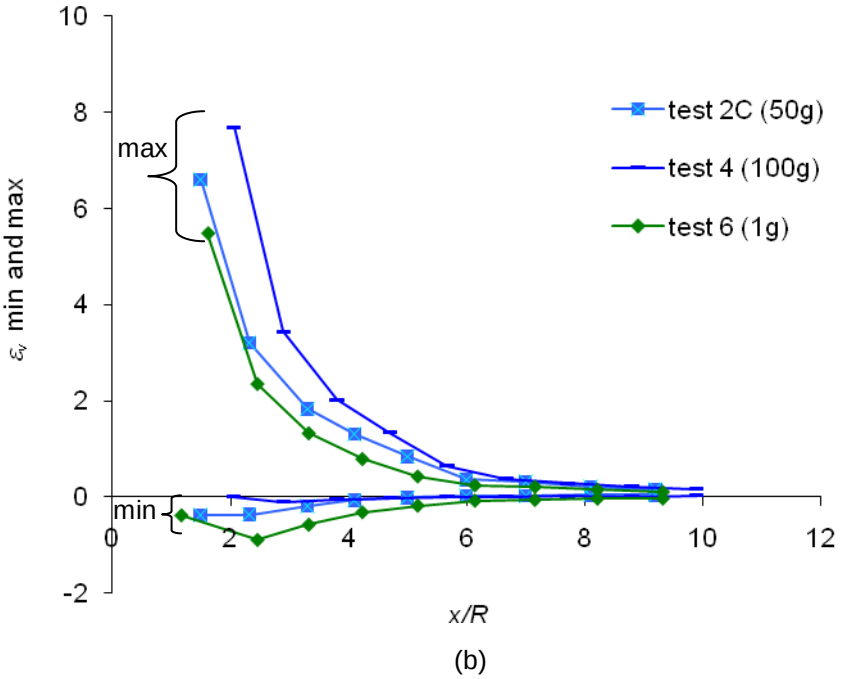

(b)

Figure 7.6: Summary of strain under different acceleration: (a) max and min horizontal strain. (b) max and min vertical strain.

7.4 Chapter summary

1 The vertical displacement varies quite significantly with the centrifuge acceleration level, and tends to increase with g-level. Correspondingly the maximum vertical strain also exhibits this trend. Conversely, the small tensile vertical strain as the probe passes tends to reduce as g-level increases. Horizontal strain and displacement exhibit less dependency on g-level.

2 Significant displacement for the 1g test begins at $h/D \approx -5$, which is slightly later than the 50g or 100g tests.

CHAPTER 8 - BLUNT PROBE TEST RESULTS

A 60^{o} cone tip has been used in this project (eg. corresponding to the cone penetration test). However, piles used in the field are likely to have a blunt tip (or may be hollow). To investigate the effect of tip shape on soil displacement, a 'blunt' (flat tip) probe test was undertaken to compare results with the cone tip.

8.1 Visual observations

Test 5 used a blunt probe at 50g with a dense soil sample. The density is 1.64 g/mm^3, void ratio is 0.61, and the relative density is 76.8%.

Figure 8.1 shows 3 images when the probe was stopped at different *y* locations during the test. Digital camera images are generally obtained on the Nottingham centrifuge using a small aperture to maximise depth of focus, and reduce potential problems with poor focus in general. However, this leads to long exposure times of typically about 1 second. Therefore it was necessary to stop the probe to avoid potential blurring of the image near the probe tip, where movement during the exposure would have been significant.

As shown in Figure 8.1, a triangle or cone of crushed soil appeared to form immediately in front of the probe as it penetrated. There is also some evidence from the photos that this material along the shaft as the probe penetrated, an effect noted by White el al (2004) during plane strain tests.

Figure 8.2 also shows a similar effect for the conical tip, but with crushed material appearing to be generated only at the edge of the cone; again there is also some evidence that this material went along the shaft as the probe penetrated. It can also be seen that (as described in Chapter 3) some sand had become trapped between the shaft of the penetrometer and the window behind the tip.

(a)

(b)

(c)

Figure 8.1: Images during test 5 (blunt probe)

(a) Tip at y = 248 mm

(b) Tip at y = 188 mm

(c) Tip at y = 153 mm

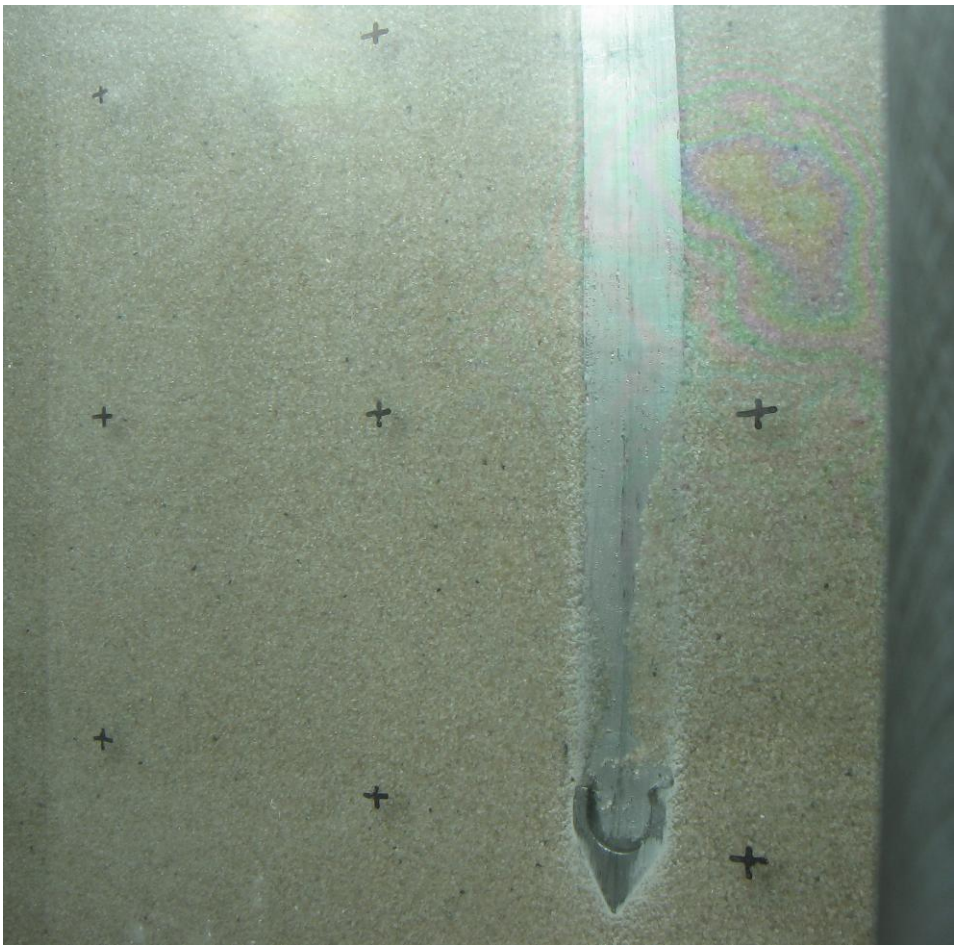

Figure 8.2: Image for conical tip in test 2A (tip at y = 150mm)

8.2 Soil displacements for blunt probe test

Figure 8.3 shows standard displacement plots for data from camera 2 in test 5 which can be compared with test 2C, Figure 4.3, for the probe with a conical tip. A column of patches at x/R = 1.9 was used.

Subplot (a) shows that movement is again predominantly initially downward and then outward during the test. At the end of the test Δx and Δy are approximately equal. Subplots (b) & (d) reveal that the movement after the probe passes is very small, again to the point where it has possibly not been reliably determined.

As shown in subplot (c) again the values of the movement when h = 0 vary little with depth for camera 2. Subplot (f) indicates that again co-incidentally the increase in displacement with depth is substantially complete at the interface of the images from cameras 1 and 2, corresponding to an embedment of about 8 or 10 diameters.

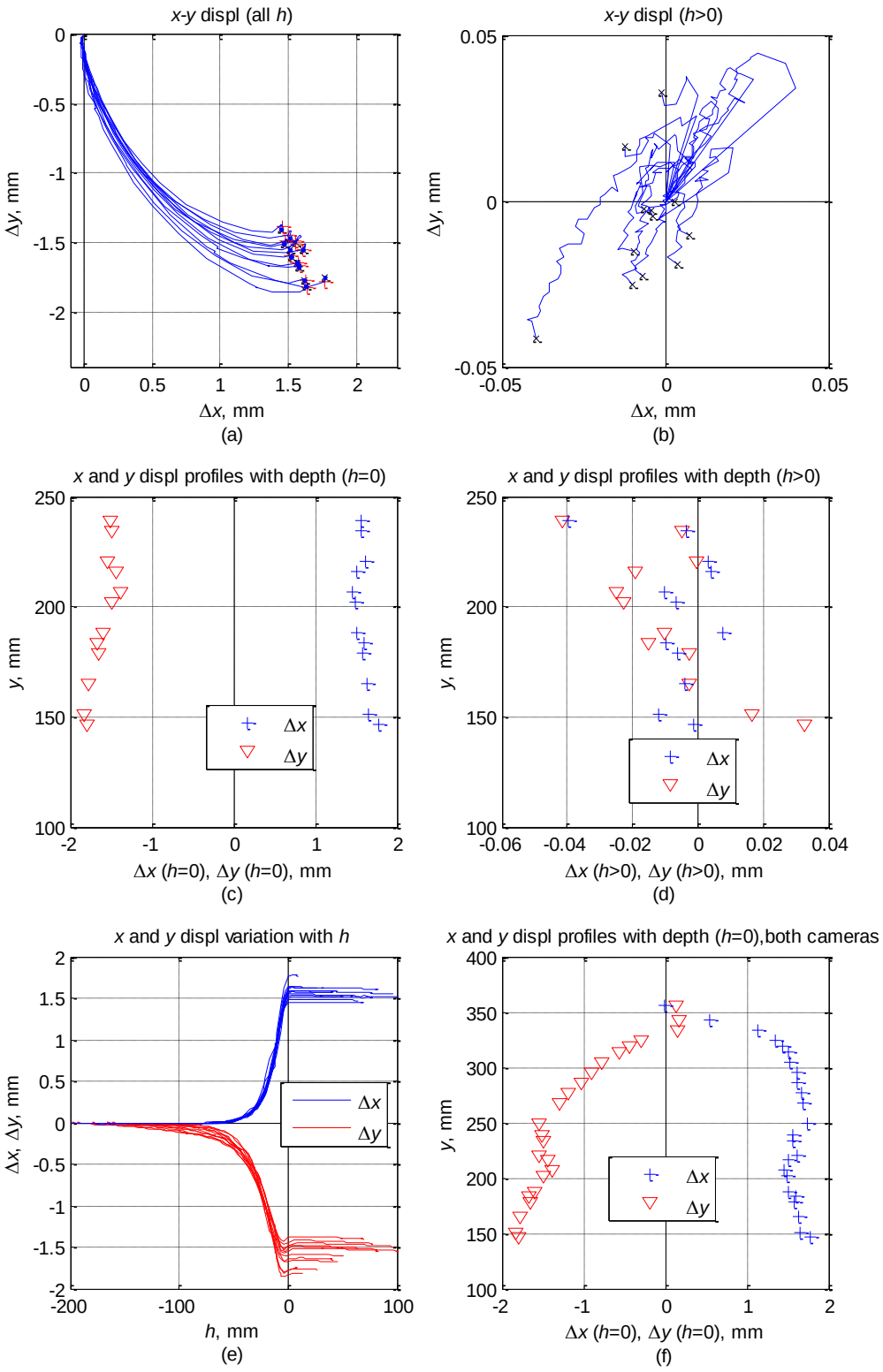

Figure 8.3: Displacement at *x/R* = 1.9 in camera 2, test 5

8.3 Summary of strains and displacement

Again 5 rows of patches near mid height of the image ($y \approx 200$ to 220 mm) were analysed, and the results are presented in Figure 8.4. As mentioned before, the first column starts from $x/R = 1.9$. The results can be compared with Figure 4.13 for test 2C with a conical tip.

Subplots (a) and (d)

Again Δx begins later than Δy as the probe approaches. The movement at $h = 0$ agrees well with cavity expansion prediction close to the probe, but is somewhat less than the prediction at a larger radius.

Subplots (b) and (e)

There is some 'noise' for the vertical strain, which might be due to the pauses in probe installation during the test (which enabled photos to be taken). The maximum compressive vertical strain for all *h* again tends to reduce with *x.* The minimum value is negative, indicating tensile strains at small x as the probe passes. The vertical strains are slightly in excess of the spherical cavity expansion prediction up to the point of maximum strain.

Subplots (c) and (f)

The maximum compressive strain again occurs at $h = 0$. Its value again tends to reduce with *x*. Again there is some negative horizontal strain, indicating initial tensile strain at small *x* for *h/D* less than 4.

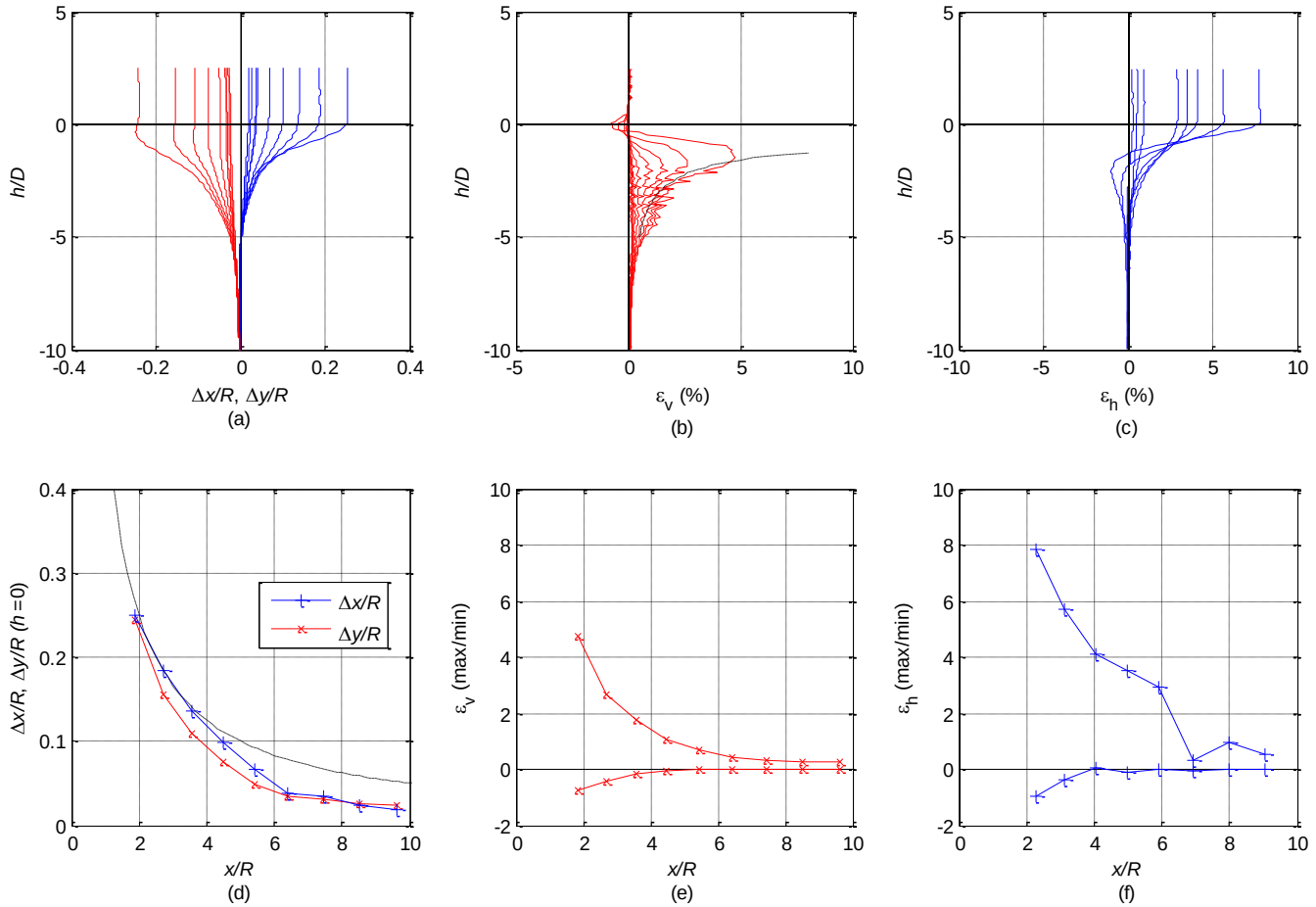

Figure 8.4: Summary of displacement and strains, test 5

8.4 Chapter summary

The soil displacement results for the blunt probe are very similar to the cone probe. For the blunt probe a zone of crushed material could be seen immediately ahead of the probe. Following subsequent penetration this appeared to result in the presence of crushed material along the pile shaft as reported by White & Bolton (2004) when using a blunt probe in plane strain tests. However, within the reliable resolution of the measurements there was no significant evidence of systematic movement after the probe passed as reported by White & Bolton, which they linked to the presence of the layer of crushed material.

Comparing these images with a probe with a cone at the tip, it also appeared that some crushed material could be observed at the edge of the cone, and that this also along the shaft. In the tests with a cone there was also no significant evidence of systematic movement after the probe passed.

CHAPTER 9 - AXISYMMETRIC MODEL COMPARED WITH PLANE STRAIN MODEL

White & Bolton (2004) report observations of the mechanisms of soil displacement around a plane strain model pile under confining stress in a calibration chamber. This chapter compares the results from the axisymmetric tests reported in this thesis (referred to as 'AX') with the plane strain results (referred to as 'PS').

The ratio of probe diameter to soil particle size and boundary location are comparable in both studies, although as noted by White & Bolton 'plane-strain geometry requires a more conservative ratio of chamber to pile size'. White & Bolton consider a calibration chamber test rather than centrifuge test. However, both studies consider 'steady state' response. In the calibration test a nominal overburden stress of 50 kN/m^2 was used. In the centrifuge tests the maximum penetration of 200 mm corresponded to 10 m and a stress of up to 165 kN/m^2 for a nominal unit weight of 16.5 kN/m^3. Other differences are a lower relative density (at least compared to the dense samples reported here) and 'blunt' pile tip in the tests reported by White & Bolton. Nevertheless, the most immediate difference is the comparison of axisymmetry with plane strain.

9.1 Summary of vertical and horizontal displacement from axisymmetric model

Figures 9.1 and 9.2 show a summary of vertical and horizontal displacement for all the tests reported in this thesis. For most of the tests, both vertical and horizontal displacements agree well with the cavity expansion prediction close to the probe, but are somewhat less than the prediction at a larger radius. However, there are some exceptions:

- Test 2D (the 're-driven' test) gives relatively low horizontal and vertical displacements
- Test 6 (the 1g test) gives relatively low vertical displacement
- Test 4 (the 100g test) gives relatively high vertical displacement
- Test 2B gives relatively high horizontal displacement (particularly at large x). However, this was a 'standard' test (dense soil at 50g), and thus this result is rather anomalous.

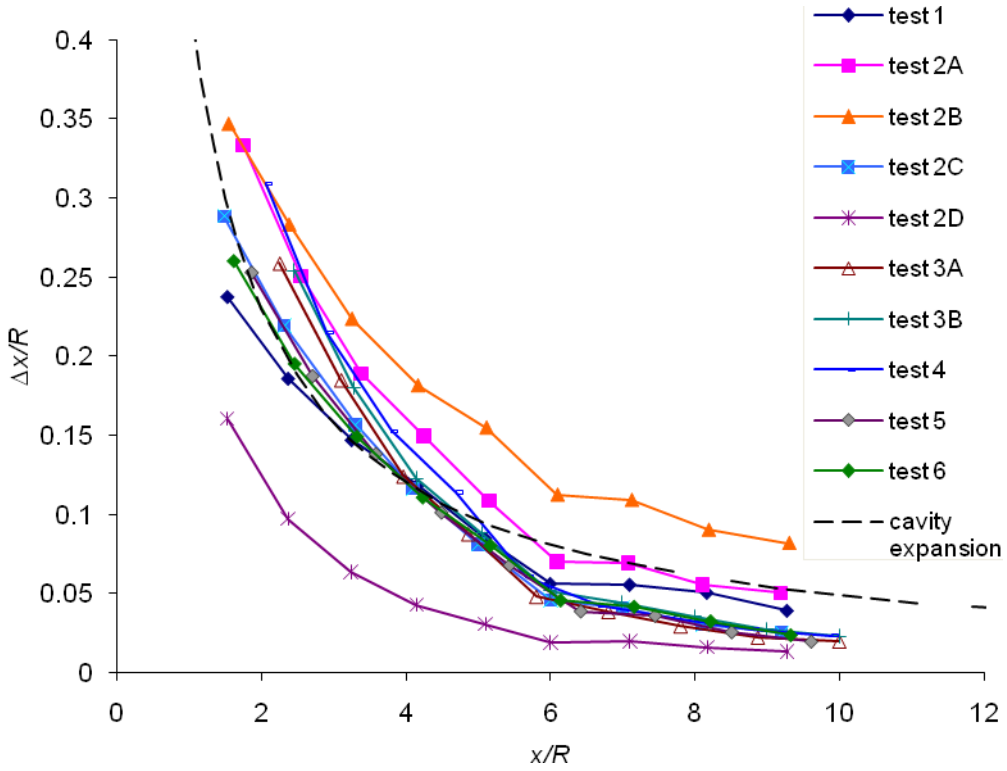

Figure 9.1: Summary of horizontal displacement data in AX tests

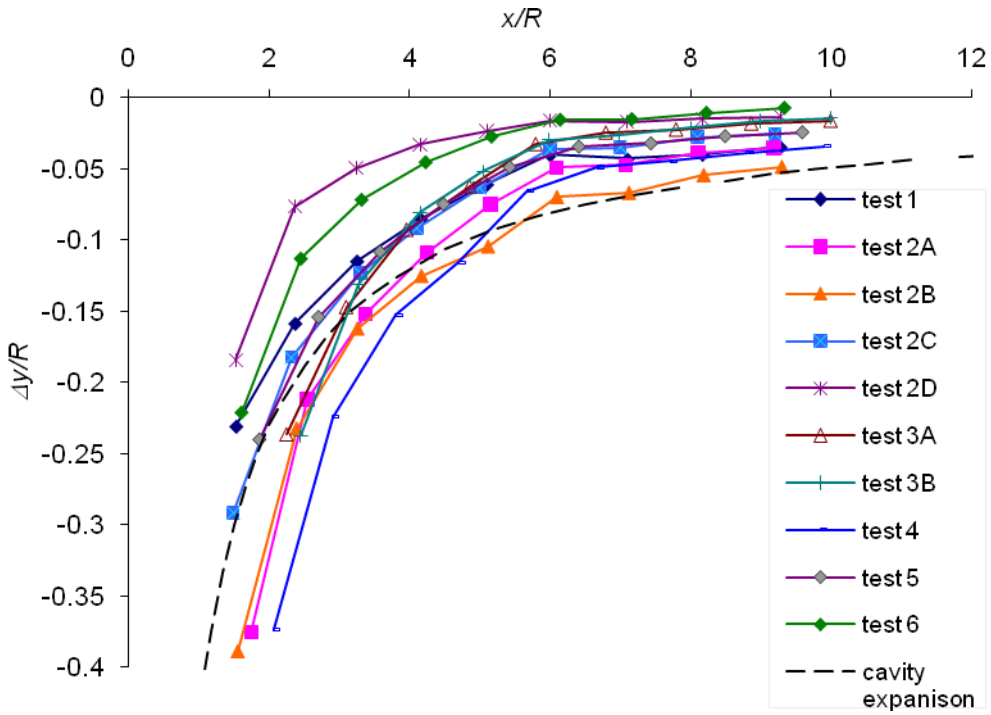

Figure 9.2: Summary of vertical displacement data in AX tests

9.2 Vertical and horizontal strain profiles with *h* compared to the plane strain tests

Figure 9.3 shows vertical, horizontal and principal strains from the plane strain (PS) tests using loose (I_d = 0.34) Leighton Buzzard sand reported by White & Bolton (2004). Since the plane strain probe width was *B*, the value 2*h*/*B* plotted on the x-axis is equivalent to *h*/*R*. Throughout this thesis *h*/*D* has been used, which would be equivalent to *h*/*B* = (2*h*/*B*)/2. Normalised values of x_0 and x_f are stated for each plot, corresponding to the initial and final horizontal offset from the probe centreline. Similarly, 2*x*/*B* is equivalent to *x*/*R* used in this thesis.

In the near field, the compressive (positive) ε_v in the PS test starts from 2*h*/*B* ≈ -20 (*h*/*B* ≈ -10), which is similar to *h*/*D* ≈ -10 (or perhaps slightly less) in the axisymmetric (AX) test reported in this thesis. The near field compressive strain rises to a maximum value at 2*h*/*B* ≈ -5 (*h*/*B* ≈ -2.5) in the PS tests. This again shows reasonable correspondence with *h*/*B* ≈ -2 in the AX tests. As the probe passes (*h* = 0) the AX tests indicate tensile vertical strain for small *x*, and this is also observed in the PS tests except at very small *x*.

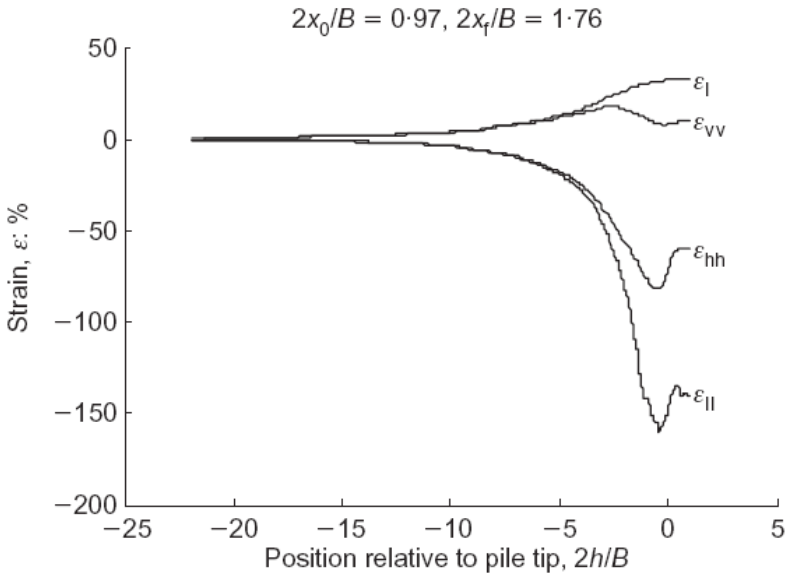

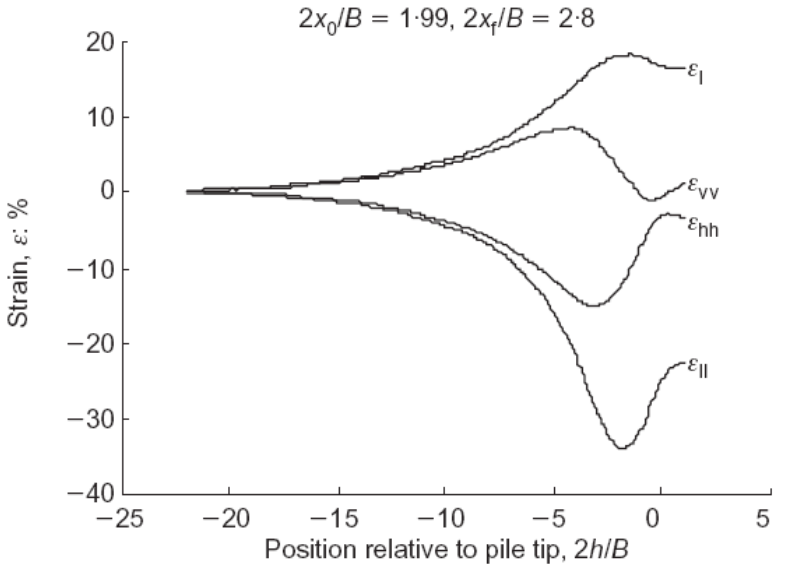

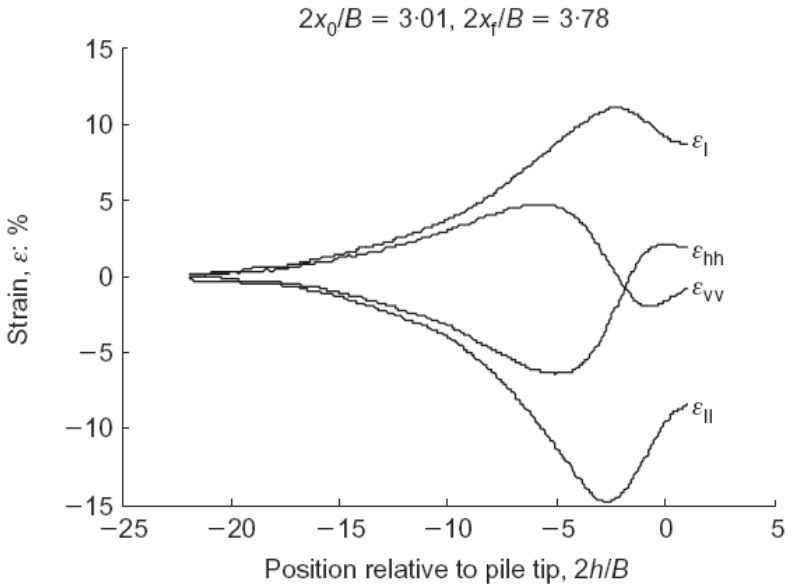

(Figure 9.3 cont' on next page)

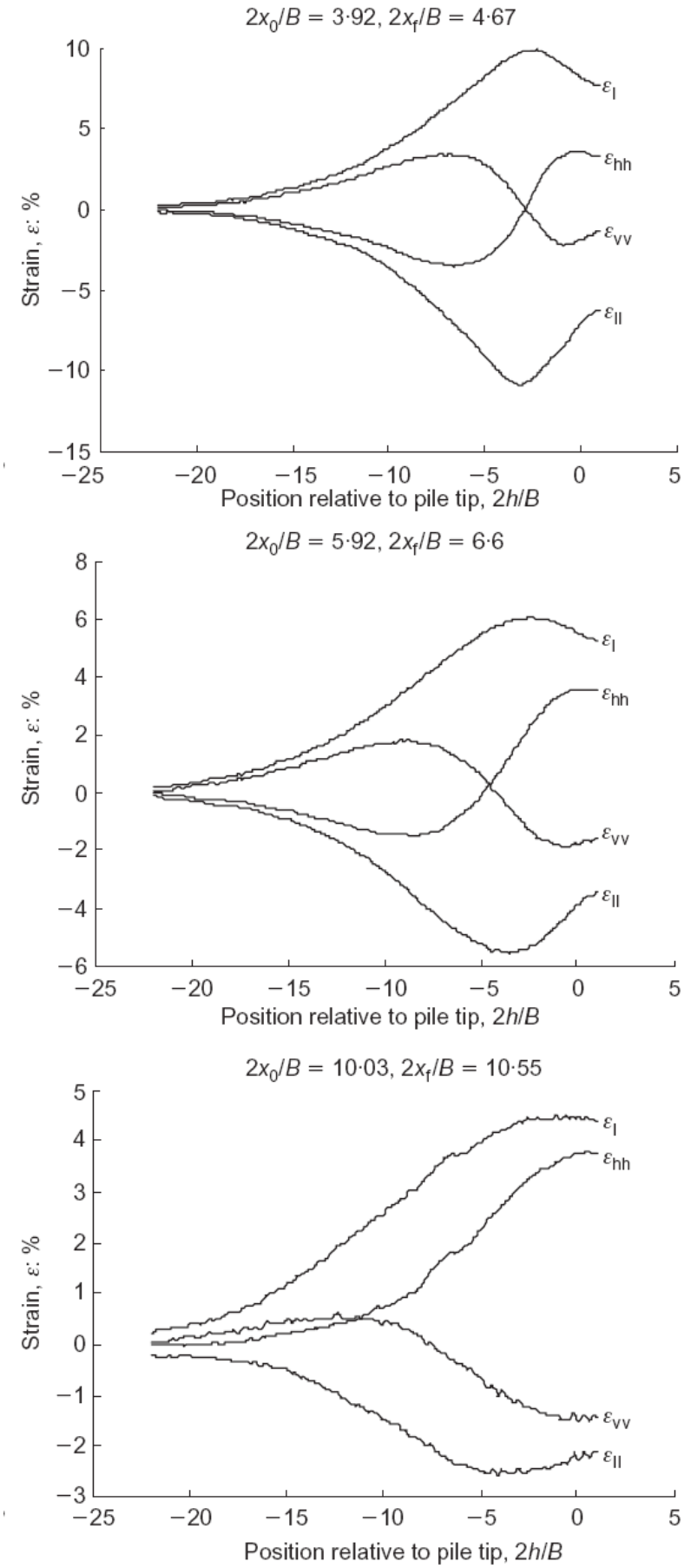

Figure 9.3: Strains in PS tests (White & Bolton, 2004).

Figure 9.4 shows comparison of vertical strain for AX (test 2C) and PS test in the near field (a), middle field (b) and far field (c). In the near field ($x/R = 2x_0/B \approx 2$), the shape of the strain path is similar for both kinds of test. The maximum and minimum vertical strain happens at similar h for both tests. The vertical strain starts from around h/D = -10, then increases as the probe approaches. The maximum compressive strain occurs at around h/D = -2. After that the vertical strain drops dramatically and achieves a minimum (maximum tensile) value at around h/D = 0. Although the general shapes of the strains for both tests are alike, the magnitude of the strain for PS test is much larger than the AX test.

In the middle field ($x/R \approx 4$), the absolute value of strains for both tests are smaller than the near field. Compared with the PS test, the maximum compressive strain is smaller and occurs later in the AX test. The change in direction of strain rate from compression to tension also occurs later in the AX test. The minimum (maximum tensile) vertical strain occurs at similar h ($h/D \approx 0$) position for both tests. However, in the PS test the maximum tensile value is approximately equal in magnitude to the maximum compressive value, whereas in the AX test there is very little tensile strain as the probe passes.

In the far field ($x/R \approx 10$), the vertical strain for the AX test is very small and doesn't show significant variation. The strain for the PS test is much larger (confirming that the influence of the AX probe dissipates more rapidly with distance), and remains initially compressive as the probe approaches and then tensile as the probe passes.

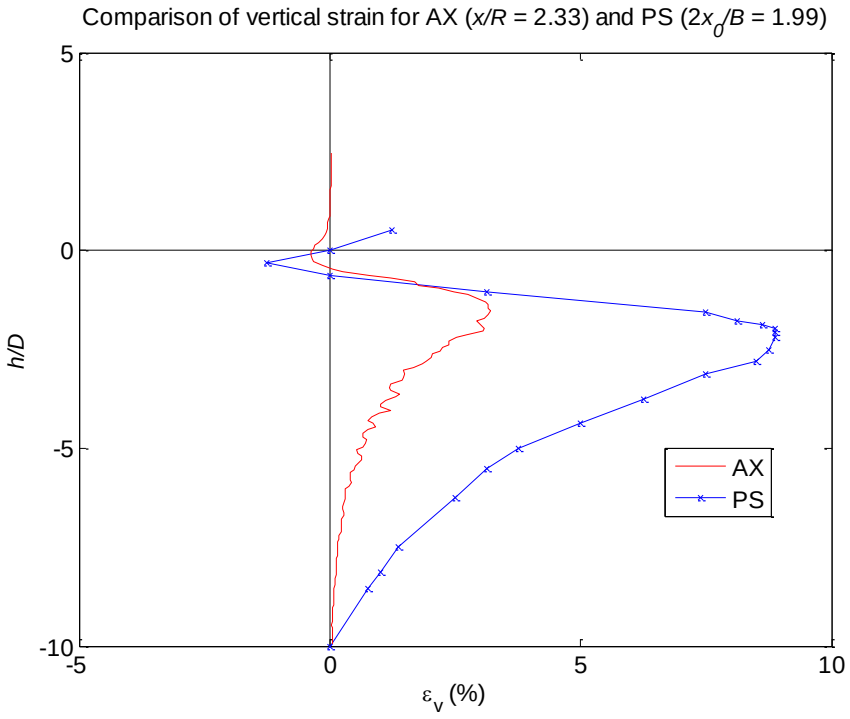

(a)

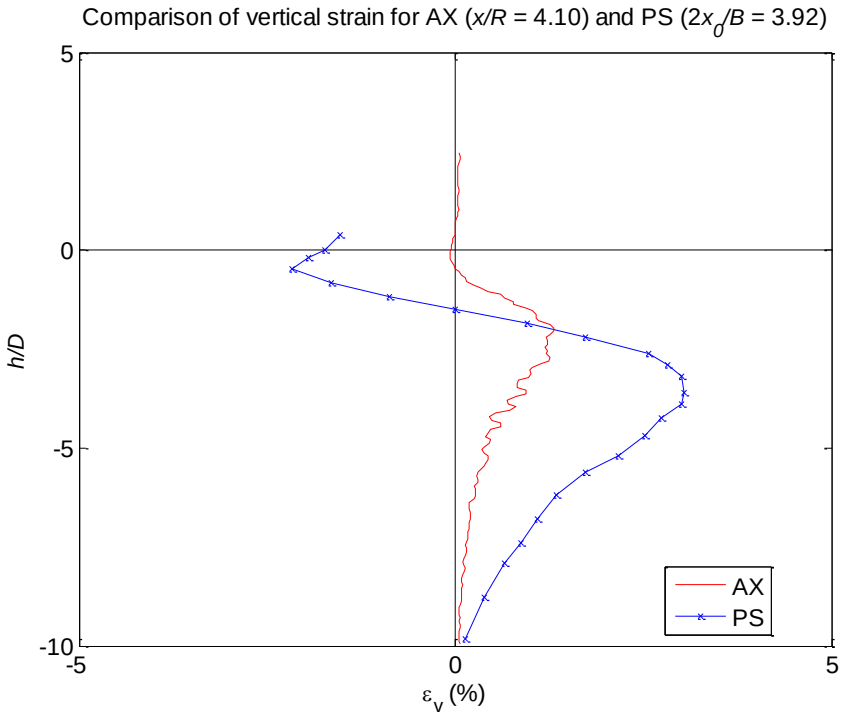

(b)

(Fig 9.4 cont' on next page)

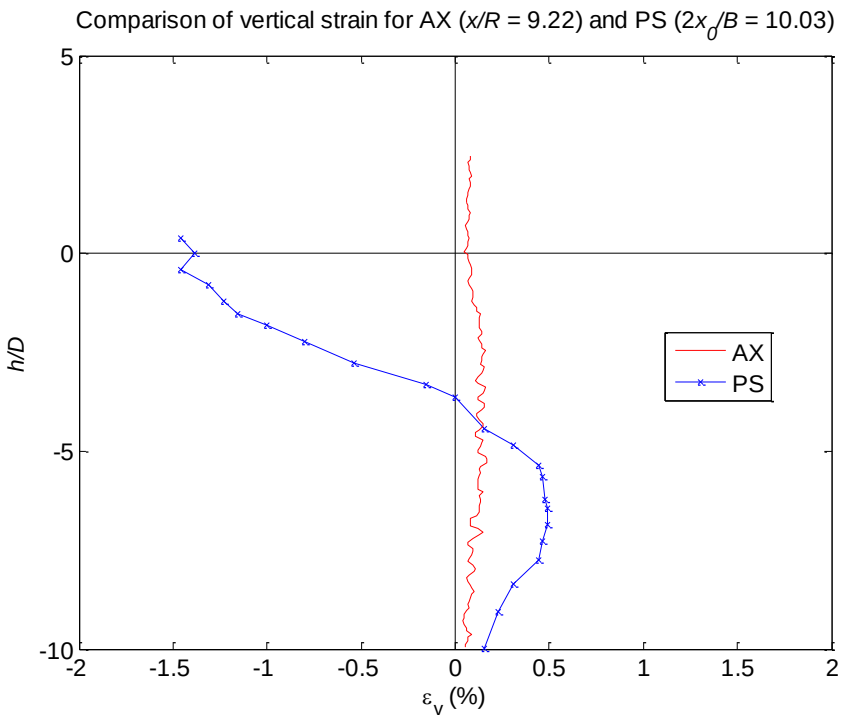

Figure 9.4: Comparison of vertical strain for AX (axisymmetric) and PS (plane strain) tests.

Figure 9.5 shows comparison of horizontal strain for the AX (test 2C) and PS tests in the near field (a), middle field (b) and far field (c). In the near field ($x/R \approx 2$), the shape of the results is similar in a sense. The PS test shows significantly more tendency for initially tensile (negative) strain, which reduces as the probe approaches, dropping to a value close to zero. The AX test shows much less tendency for initial tensile strain, and then develops significant compressive strain as the probe approaches. Nevertheless, the peak tensile strain is observed at roughly the same value of $h/D \approx -2$, and both profiles show a rapid increment of compressive strain after this up to the point where the probe passes.

In a way this pattern is repeated in the middle field ($x/R \approx 4$), with reduced tendency for tensile strain. In the PS test, the initial horizontal extension is followed by compression of approximately equal magnitude as the probe passes. While in the AX test the horizontal strain increases monotonically in compression up to a maximum value as the probe passes.

In the far field ($x/R \approx 4$), the absolute value for PS is much larger than in AX (again confirming that the influence of the AX probe dissipates more rapidly with distance). However, the horizontal strain now increases monotonically in compression for both tests.

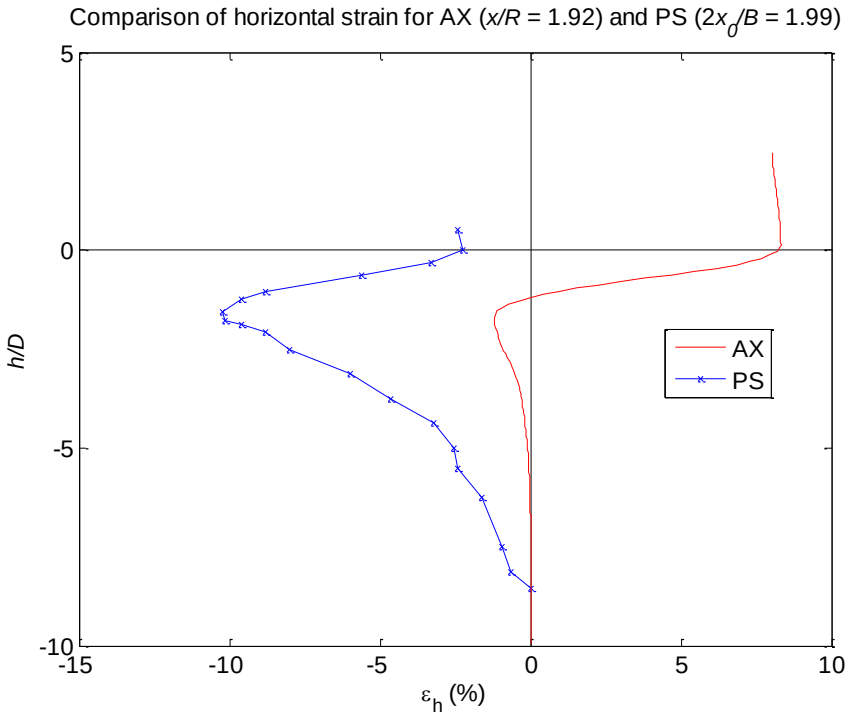

(a)

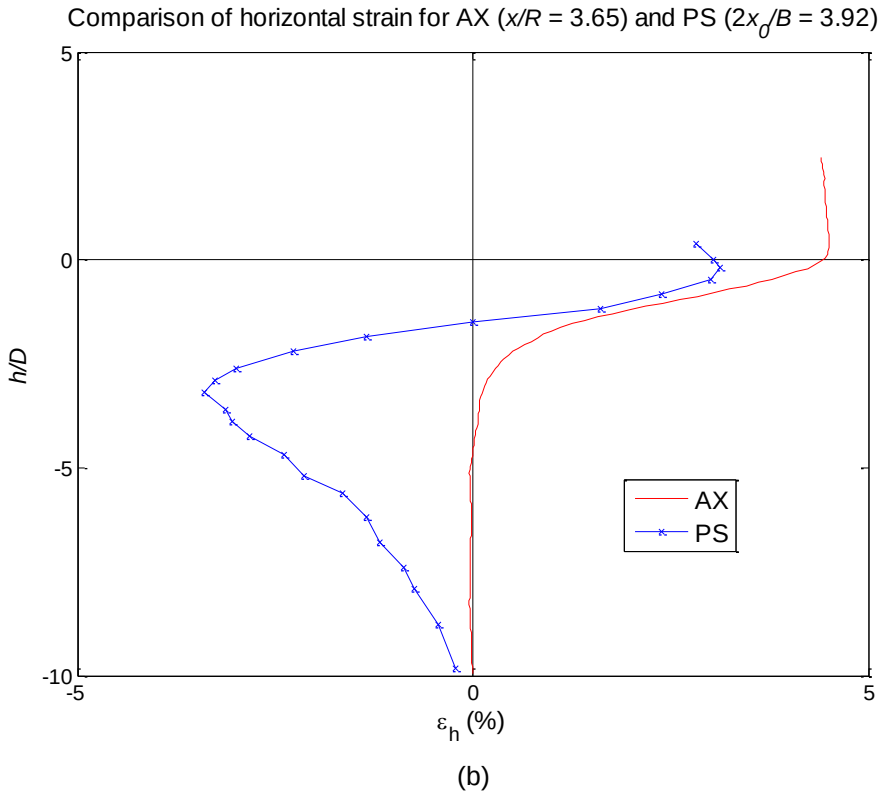

(b)

(Fig 9.5 cont' on next page)

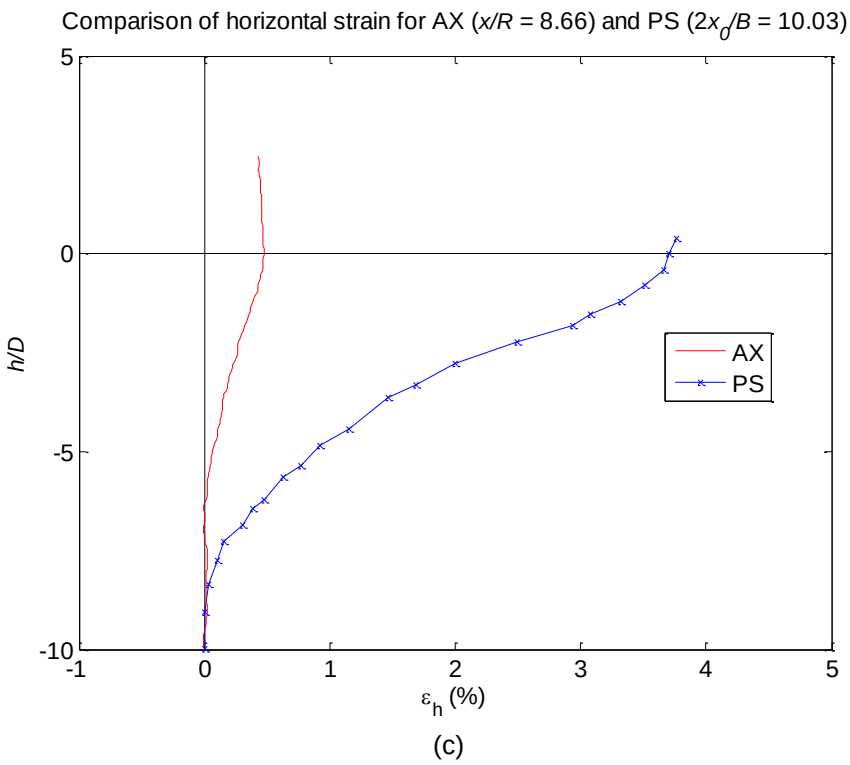

Figure 9.5: Comparison of horizontal strain for AX (axisymmetric) and PS (plane strain) tests.

9.3 Summary of vertical strains compared to the plane strain tests

Figures 9.6 and 9.7 summarise the maximum (compressive) and minimum (maximum tensile) vertical strains for all *h*, plotted against *x*/*R* (which is analogous to 2*x*/*B*), in the AX and PS (using $x = x_0$ – the initial value) tests respectively.

As expected, the maximum compressive vertical strain decreases as *x* increases in both cases. The value of vertical strain is larger (typically double) for the PS tests than the AX tests. In the AX tests the tensile strains (*h* = 0) reduce to zero for large *x*, but in the PS tests there is evidence of tensile strain in the far field with magnitude similar to the near field.

Figures 9.8 and 9.9 summarise the value of *h* (as *h*/*D* or *h*/*B*) when the maximum compressive ε_v is observed for the AX and PS tests respectively, showing variation with *x*/*R* or 2*x*/*B*.

As anticipated, the maximum vertical strain occurs earlier as *x* increases for both tests. The AX data shows some scatter as *x* increases, and this can be attributed to the small vertical strain at large *x*. Nevertheless, the trend of the data is clear. Furthermore the relationship between the normalised *h* and *x* is similar. In both cases the data lie on a line where $h \approx x$, ie. a line at 45^o to the vertical ahead of the probe in the soil (refer to Figure 9.14).

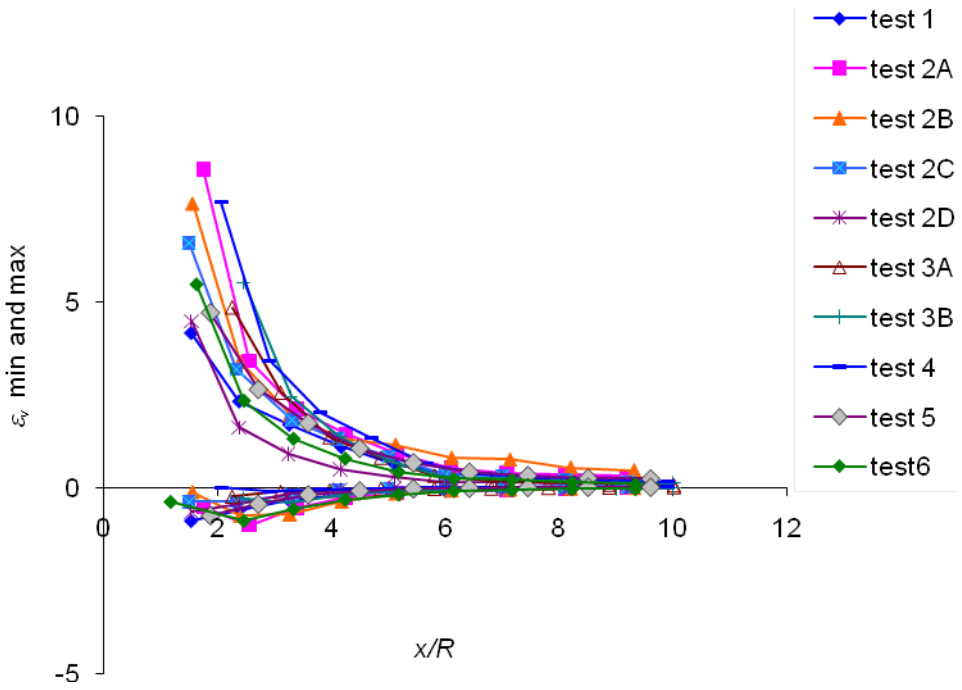

Figure 9.6: Summary of the maximum and minimum vertical strains showing variation with *x/R* in AX tests

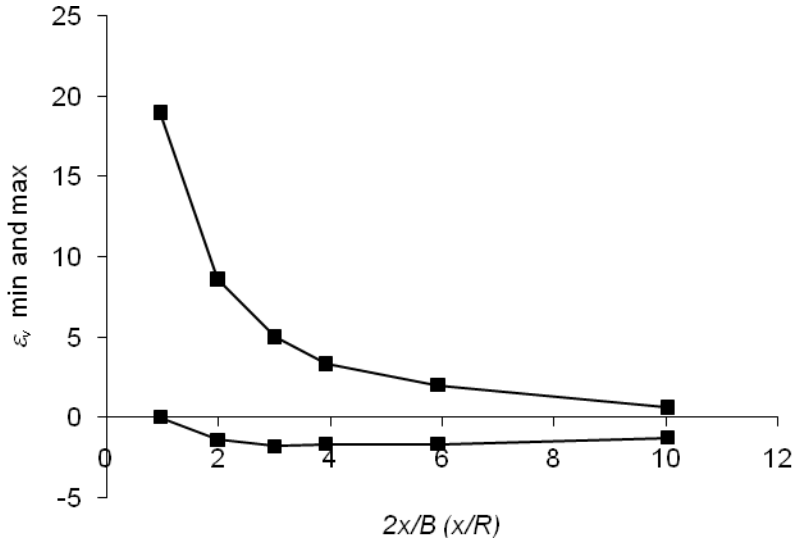

Figure 9.7: Summary of the maximum and minimum vertical strains showing variation with *x/R* in PS tests

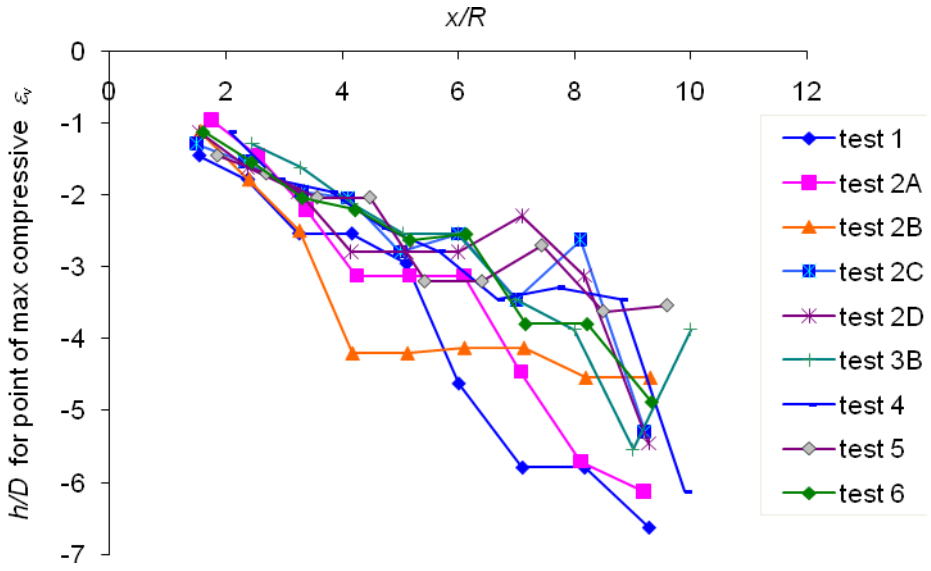

Figure 9.8: *h/D* for the point of maximum ε_v showing variation with *x/R* in AX tests

`

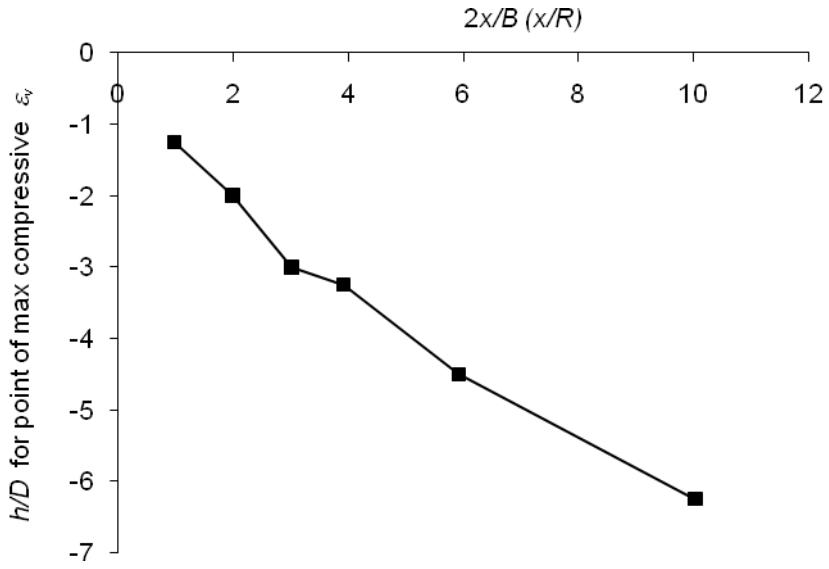

Figure 9.9: *h/D* for the point of maximum ε_v showing variation with *x/R* in PS tests

9.4 Summary of horizontal strains compared to the plane strain tests

Figures 9.10 and 9.11 summarise the maximum (compressive) and minimum (maximum tensile) horizontal strains plotted against *x/R* and 2*x*/B in the AX and PS tests respectively.

In the AX tests, the value of maximum compressive ε_h (which occurred when $h \approx 0$) reduces as x/R increases, as anticipated based on the good correspondence of horizontal displacement with circular cavity expansion. Like in the AX tests the maximum compressive ε_h in the PS tests occurs when $h \approx 0$. The maximum compressive strain does not vary significantly with *x*, indicating uniform compression of the soil from the probe location to the model boundary. However, it is surprising that there is no compressive strain at very small *x*.

In both situations tensile horizontal strains precede the compressive strains when *x*/*R* is less than about 4 (AX tests) or 2*x*/*B* is less than about 6 (PS tests). The magnitude of these strains is highest for small *x*, but reaches a much higher value near the probe in the PS tests.

Figures 9.12 and 9.13 shows *h/D* or *h/B* when the maximum value of tensile ε_h is observed, showing variation with *x/R* or 2*x*/*B* (up to the maximum values of *x* where tensile strain was observed as referred to above) in the AX and PS tests. The results from both types of test are quite similar. In this case $h \approx 2x$, ie at about 30° to the vertical ahead of the probe (see Figure 9.14).

Figure 9.14 illustrates the main differences of the strain fields between the AX and PS cases.

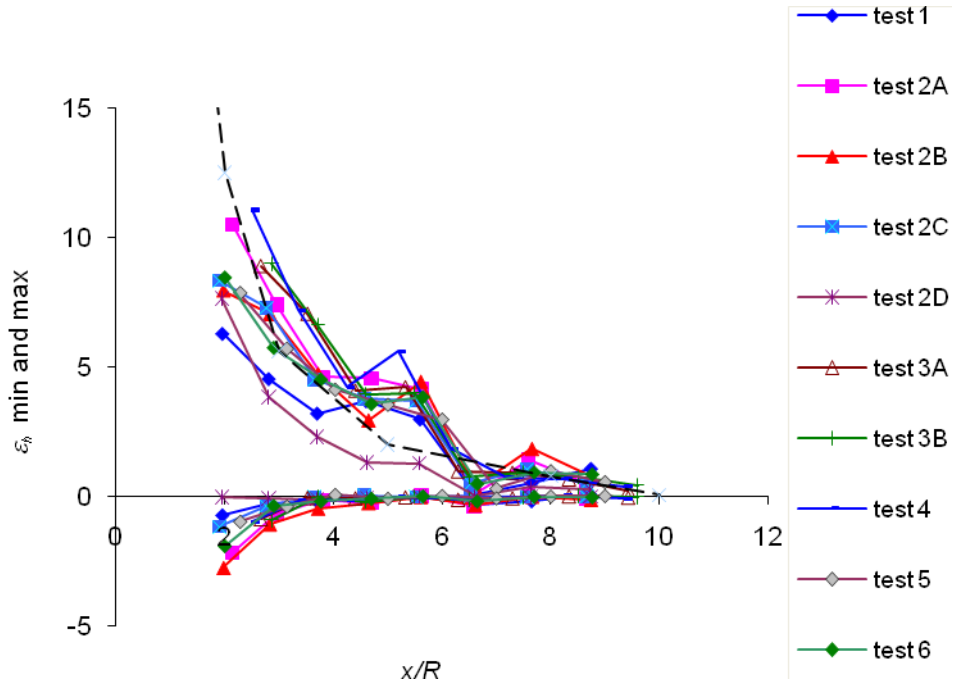

Figure 9.10: Summary of the maximum and minimum horizontal strains showing variations with *x/R* in AX tests

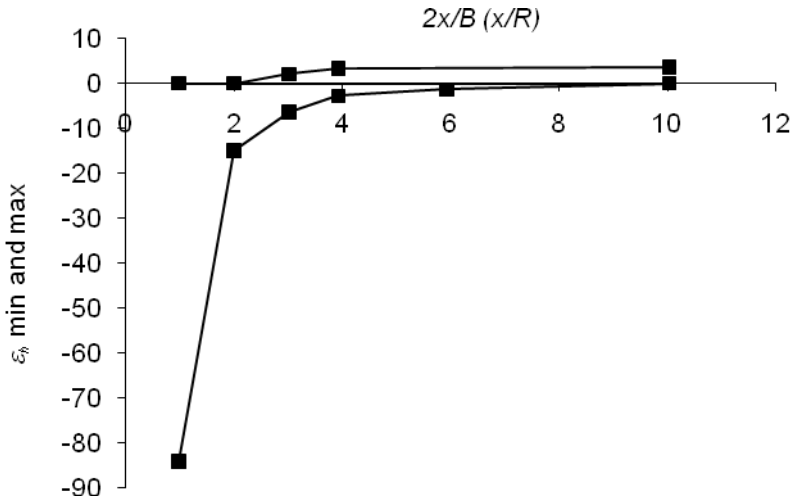

Figure 9.11: Summary of the maximum and minimum horizontal strains showing variations with *x/R* in PS test

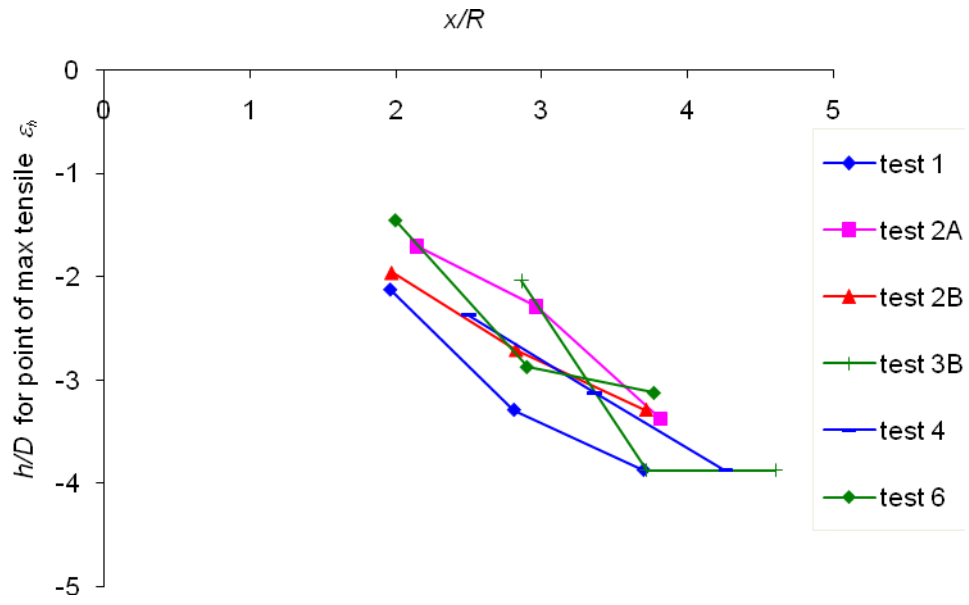

Figure 9.12: *h/D* for the point of maximum ε_h showing variation with *x/R* in AX tests

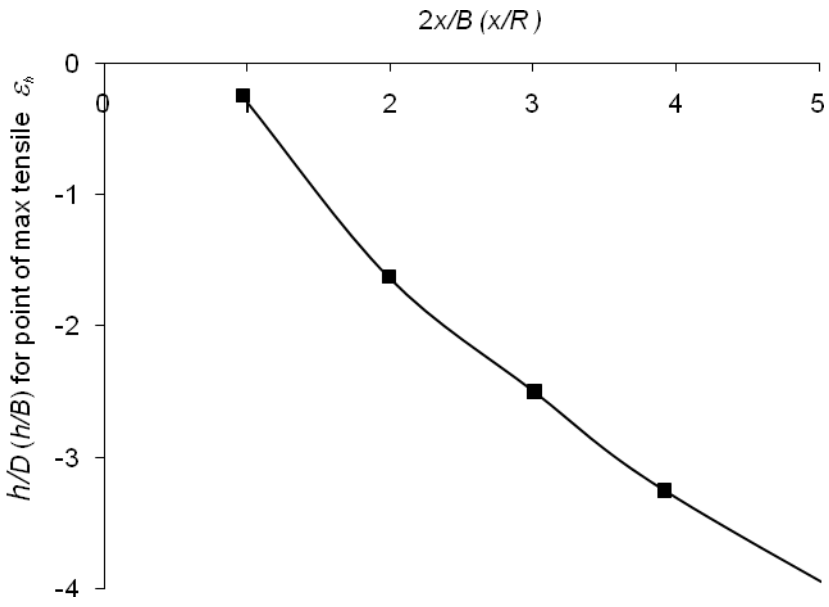

Figure 9.13: *h/D* for the point of maximum ε_h showing variation with *x/R* in PS test

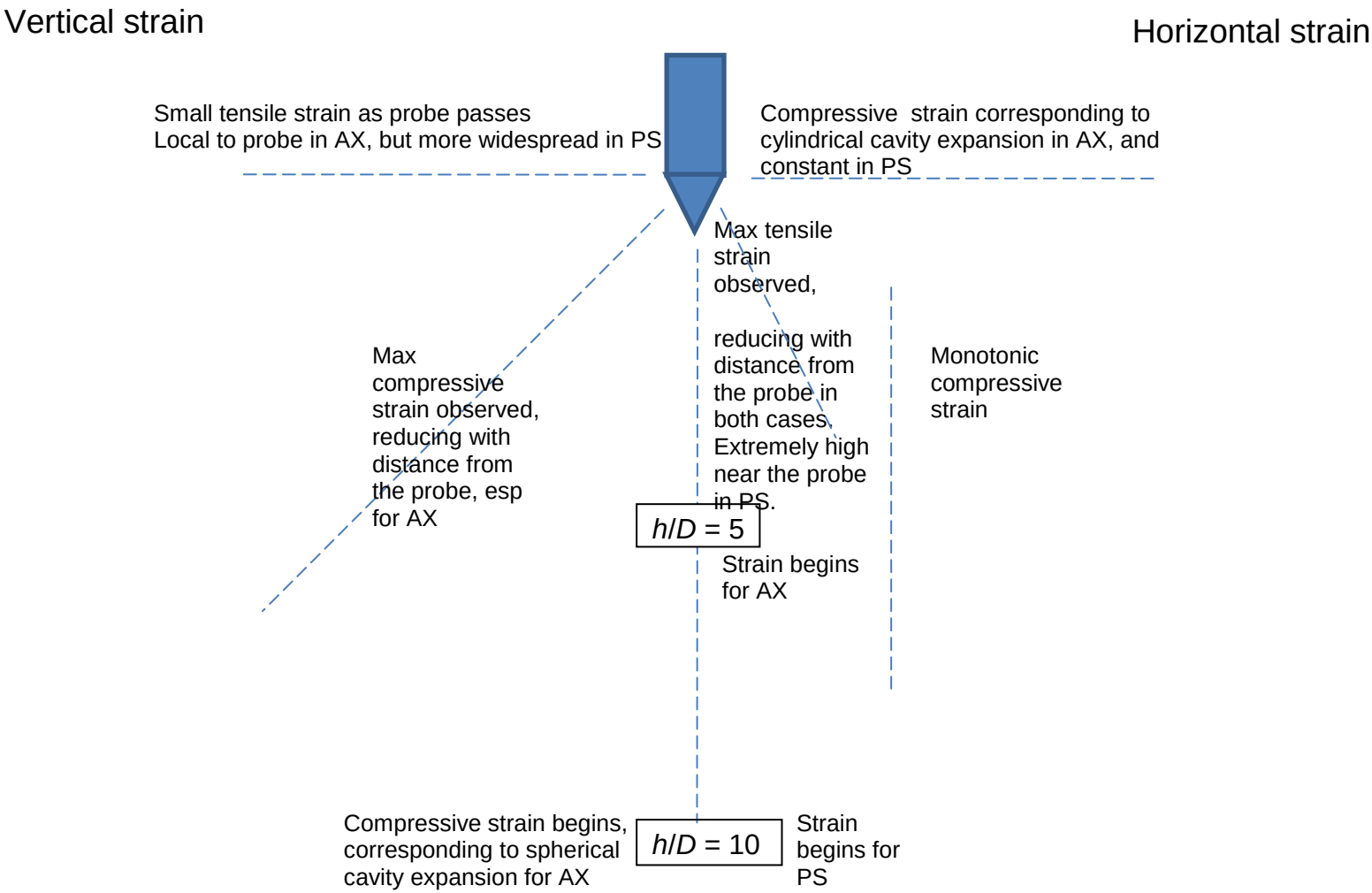

Figure 9.14 Summary of vertical and horizontal strain for AX and PS tests

9.5 Chapter summary

1 In the near field, the initial compressive ε_v in the AX tests starts later. The value of vertical strain in the PS test is larger than the AX tests at a given horizontal location. In the far field, when $x/R > 6$, there is no significant tensile strain in the AX tests, while in the PS test the tensile strains still can be observed for large x/R.

2 The maximum vertical strain is observed slightly earlier as x/R increases for both the AX and PS tests. The maximum vertical strain occurs slightly earlier in the PS test than the AX tests. The point of maximum vertical strain is observed on a line at about 45^o to the vertical ahead of the probe tip.

3 In the near field ($x/R < 4$), there are compressive and tensile values of ε_h in the AX tests, while there are more tensile values in the PS test. In the far field, there is only compressive strain in both tests. However, as anticipated the AX test shows considerably more tendency for reduction of strain with distance from the probe.

4 In the near field, the value of h/D for the point of maximum tensile ε_h is earlier in both tests. The point of maximum vertical strain is observed on a line at about 30^o to the vertical ahead of the probe tip.

CHAPTER 10 - LOAD ALONG THE PROBE

10.1 Introduction

Five strain gauges were fixed along the shaft of the probe (refer to section 3.4.4*)*, and calibrated to measure axial load. They were located at the following distances behind the shoulder of the probe:

*Q*1: 12 mm

*Q*2: 37 mm

*Q*3: 62 mm

*Q*4: 87 mm

*Q*5: 295 mm

ie. at 25 mm intervals *Q*1-*Q*4, with *Q*5 at the 'top' of the probe near the actuator.

10.2 Load in *Q*1-*Q*5

Figure 10.1 shows variation of *Q*1 (practically at the tip) with depth of the shoulder in the soil, *Y*, which is initially 20 mm since the probe was 'buried' by this amount at the start of the test. In the 1*g* tests the load was too small to be reliably determined, and in the blunt probe was not instrumented. The data is not available for tests 2C, 2D or 3A due to malfunction.

Lines for N_q = 100 (50g) and N_q = 200 (50g) are shown on the figure to compare with other researchers' results based on the tip capacity.

$$Q = qA = N_q \sigma_v A = N_q \rho NgAz$$

when N_q = 100 at 50g,

$$Q = 100 \times 1.68 \times (50 \times 9.8) \times 57 \times 10^{-6} \times z \text{ ,}$$

so *Q/z* = 4.69 (kN/m) or (N/mm)

when N_q = 200 at 50g or N_q = 100 at 100g,

Q/z = 9.38

As can be seen, test 3B (loose over dense sample) shows good agreement with the N_q = 100 (50g) line. At Y = 100 mm the probe would have passed from the loose to the dense sample, and thus it is surprising that there is not more tendency for the bearing resistance to increase below this depth.

Tests 2A and 2B (dense sample) are close to the N_q = 200 (50g) line. However, Test 1 (dense sample with Perspex window) and Test 3B (loose soil) are somewhat lower. Test 4 (dense sample at 100g) gives the highest load, but since the g-level has been doubled compared to the other tests this only represents an N_q value slightly in excess of 100. In general these results show reasonable comparison with previous centrifuge studies (eg. Gui et al 1998). $Q1$ increases as the depth increases, but at a slightly deceasing rate after about 100 mm (8 diameters) penetration. This is also mentioned by Randolph et al (1994).

Figure 10.2-10.4 show variation of $Q2$-$Q4$ with Y for the shoulder. As expected, the load value increases up the shaft (eg. Q2 > Q1, etc) since extra load results from shaft resistance once the point where load is measured enters the soil. Again the load increases as the depth increases, but at a slightly decreasing rate after about 100 mm penetration. The test 3A load value seems have the decreasing rate earlier than the others. It is also found that the loose soil sample and re-drive test correspond to a lower load value. White & Lehane (2004) also observed a similar result during their 'pseudo-dynamic' installation test. In principle the aim of these measurements had been to deduce the average shaft resistance between $Q1$ and $Q2$ from ($Q2$-$Q1$) and so on. However, this approach was not successful, since the difference was too small to be reliably determined.

Figure 10.5 shows variation of $Q5$ with Y. The probe penetrates approximately 200 mm in most of the tests, while strain gauge $Q5$ is 295 mm behind the shoulder, and so is always above the soil surface. As Y increases the results are less than $Q1$-$Q4$, indicating a problem with the results. This is almost certainly

due to bending of the probe, which would have affected the measurement of axial strain by a single gauge (refer to section 3.4.4). The probe was effectively cantilevered from the connection to the actuator (where there was restraint against rotation). The probe was specifically designed to reduce the contact force against the window on the shaft (refer to section 3.4.4) whilst maintaining contact of the tip with the window. Hence the cantilever would have been mainly subject to a point load at the tip, and bending moment would have increased from zero at the tip to a maximum at the point of connection to the actuator. It is thus likely that results from *Q*2-*Q*4 were also affected by bending, which may have contributed to the difficultly in interpreting this data to reliably estimate shaft friction.

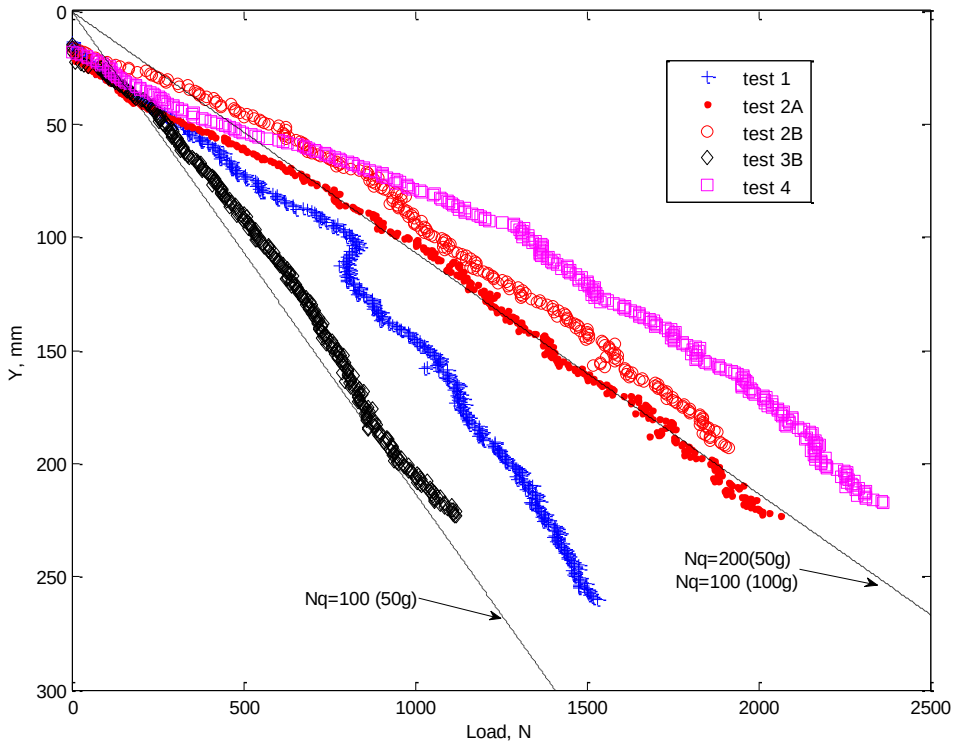

Figure 10.1: Variation of *Q*1 with depth of the shoulder in the soil (*Y*)

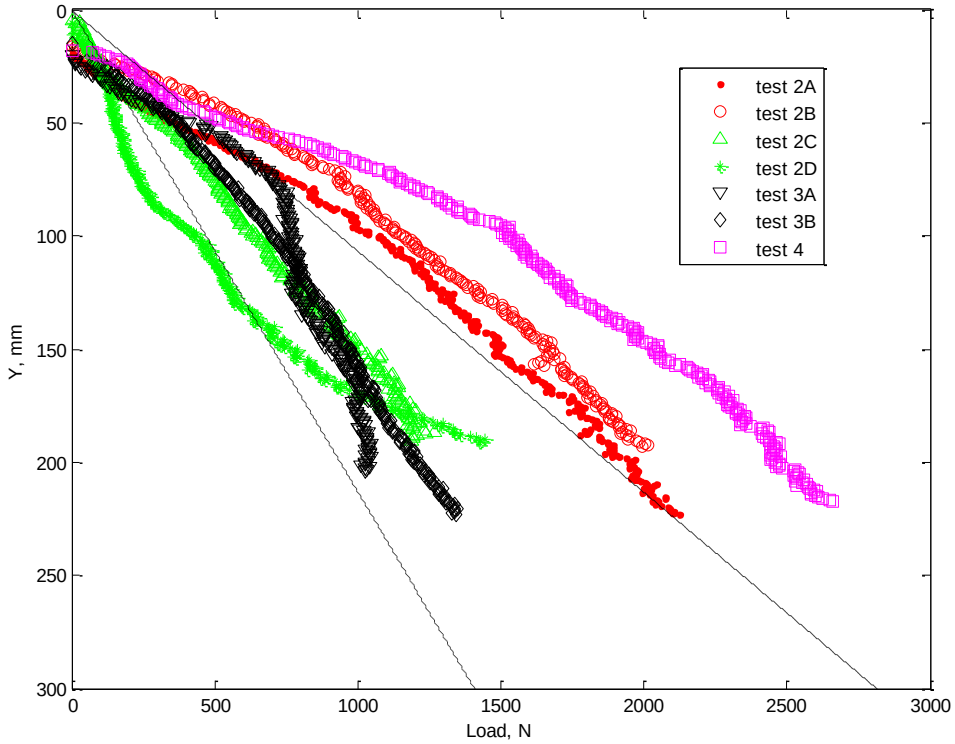

Figure 10.2: Variation of *Q*2 with depth of the shoulder in the soil (*Y*)

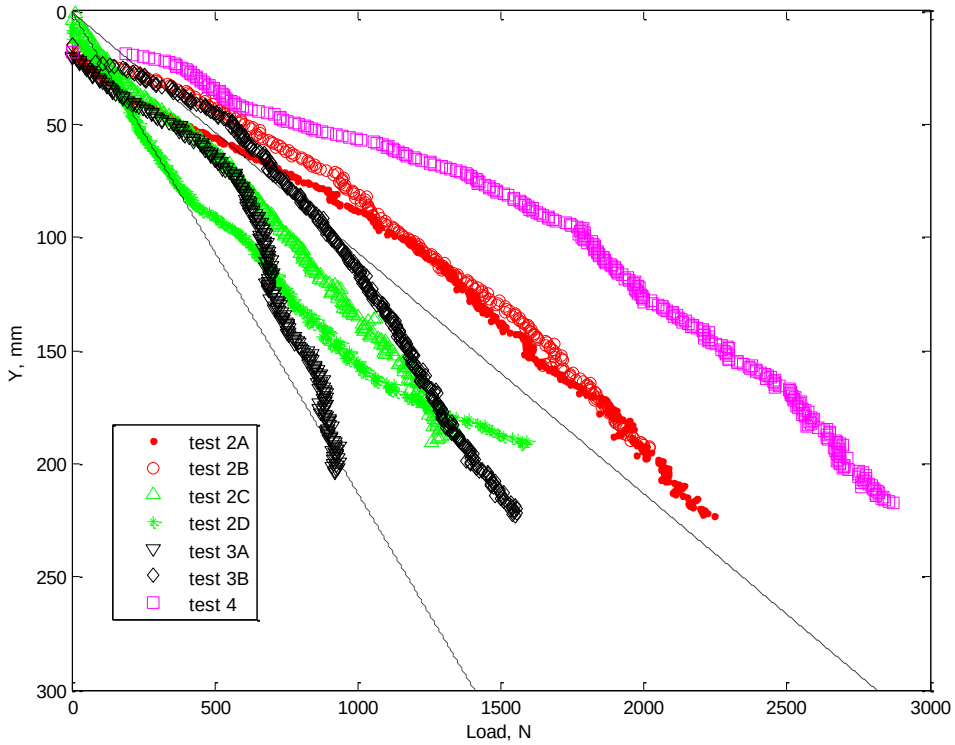

Figure 10.3: Variation of *Q*3 with depth of the shoulder in the soil (*Y*)

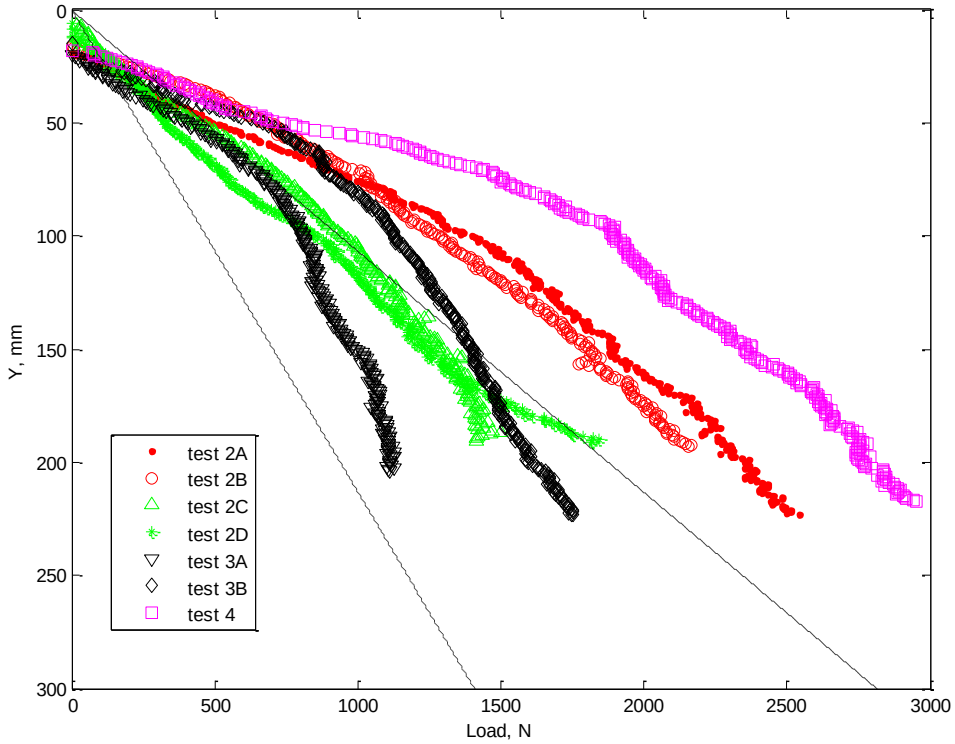

Figure 10.4: Variation of *Q*4 with depth of the shoulder in the soil (*Y*)

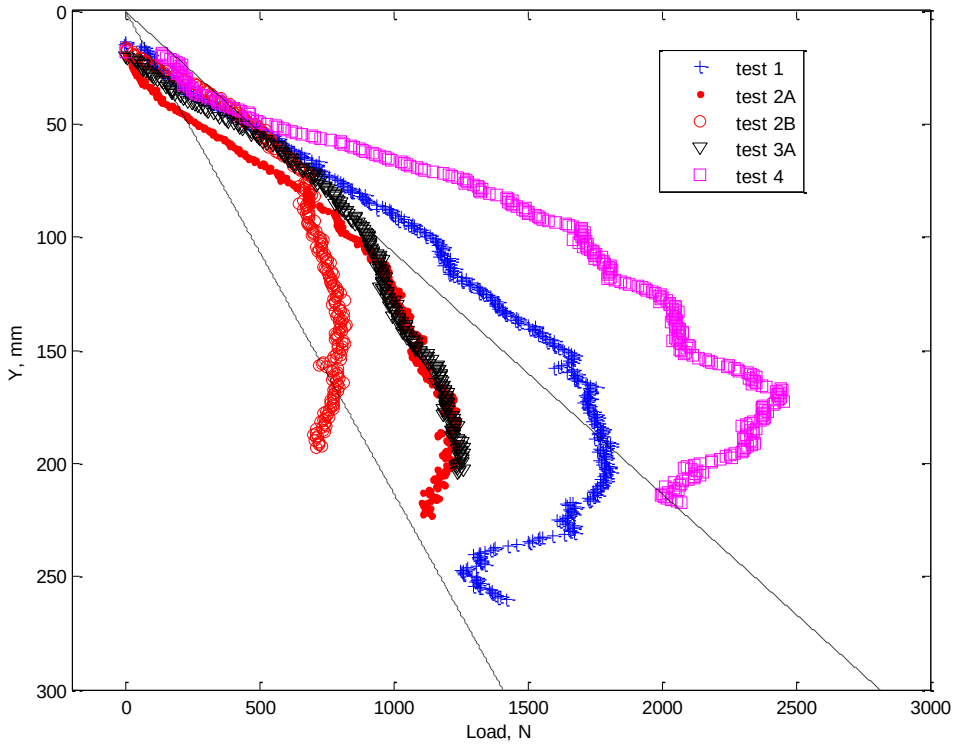

Figure 10.5: Variation of *Q*5 with depth of the shoulder in the soil (*Y*)

10.3 Chapter summary

1 The results are broadly sensible compared to the other researchers in terms of the tip stress (e.g. Gui et al 1998).

2 The stress increases as the depth increases, but at a slightly deceasing rate after about 100 mm (8 diameters) penetration.

3 As expected, the load value increases with distance up the probe. However, the data could not be used to reliably determine the distribution of shaft load. Load measured at the top of the probe (above the soil) appeared to have been significantly affected by bending of the probe.

CHAPTER 11 – DISCUSSION

11.1 Comparison with strain path method

Figure 11.1 compares the soil element trajectories from the experimental work and strain path method (SPM) predictions by Baligh (1985). The SPM prediction is based on incompressible behaviour.

From the experimental results, the soil moves downwards and then outwards as the probe approaches, but does not move significantly after the probe passes. In contrast the strain path method result implies that the soil moves back upwards after the probe passes.

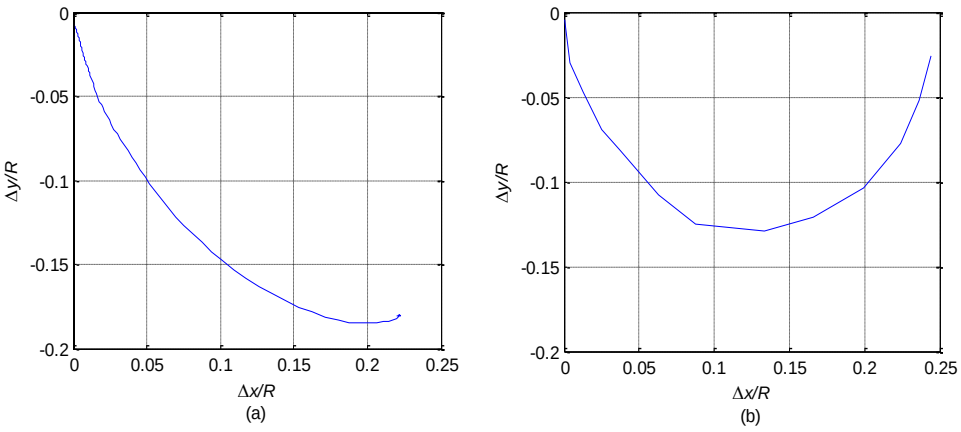

Figure 11.1: Comparison of soil element trajectory. (a) experimental result (test 2C, standard test) at *x/R*=2.3. (b) strain path method result at *x/R*=2 (Baligh, 1985).

Figure 11.2(a) shows data reproduced from Figure 4.13(a). Figure 11.2(b) shows equivalent data from the strain path method for similar values of x/R. The experimental results indicate that movement starts further ahead of the probe than predicted by the strain path method.

The ultimate horizontal displacement from the strain path method agrees well with the experimental result. However, the experimental results show very little movement after the probe has passed, whereas the SPM predicts ongoing movement until $h/D > 1$.

The strain path method correctly predicts rapid increase in downward soil movement as the probe approaches. However, the downward movement as the probe passes is under predicted. Furthermore (as noted from the trajectory), the strain path method predicts upward movement after the probe tip passes which was not observed in the experimental results.

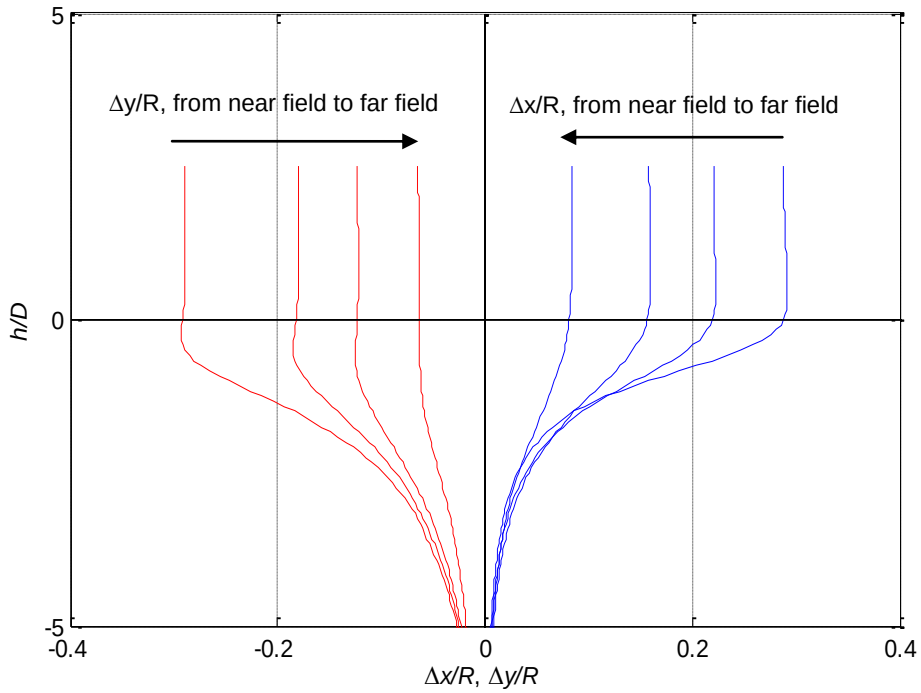

(a)

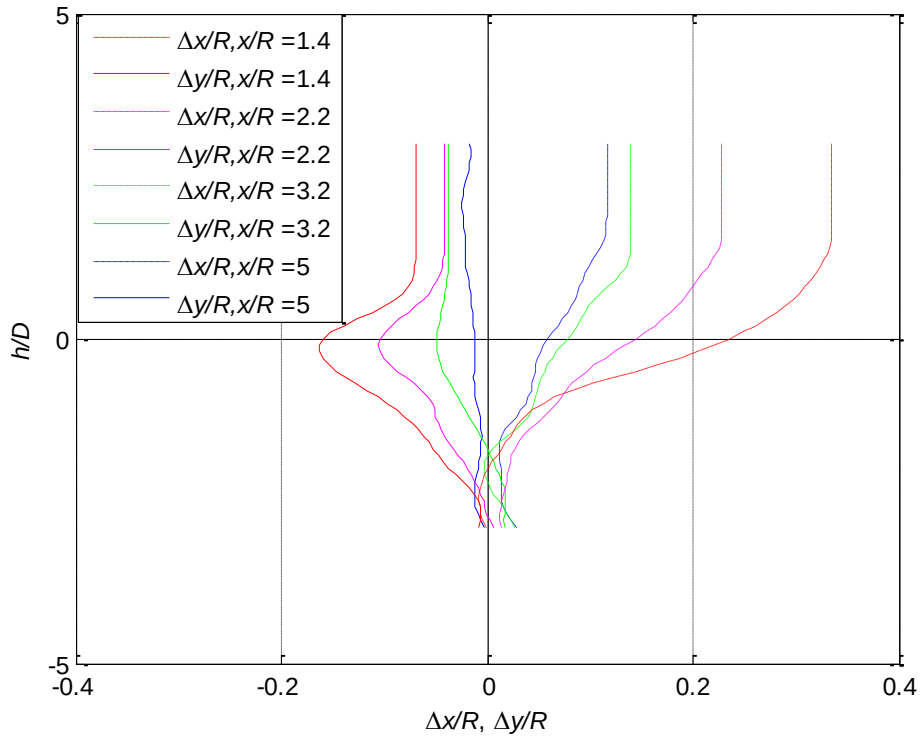

(b)

Figure 11.2: Comparison of displacement variation with *h.* (a) experimental result (b) strain path method result (Baligh, 1985).

Figure 11.3 shows comparisons of SPM displacement for *h/D* = 0 and 1 with equation 4.3 (based on cavity expansion which, like the strain path method, is based on incompressible behaviour), and experimental results for *h/D* = 0. Variation with *x* is shown.

Figure 11.3 (a) indicates that the displacement after probe passed (*h/D* =1) is much lower than *h/D* =0. The ultimate radial displacement (*h/D* =1) predicted by the SPM shows good correspondence with the experimental data. Figure 11.3 (b) indicates that the displacement at *h/D* =0 in SPM prediction is lower than both cavity expansion prediction and experimental results.

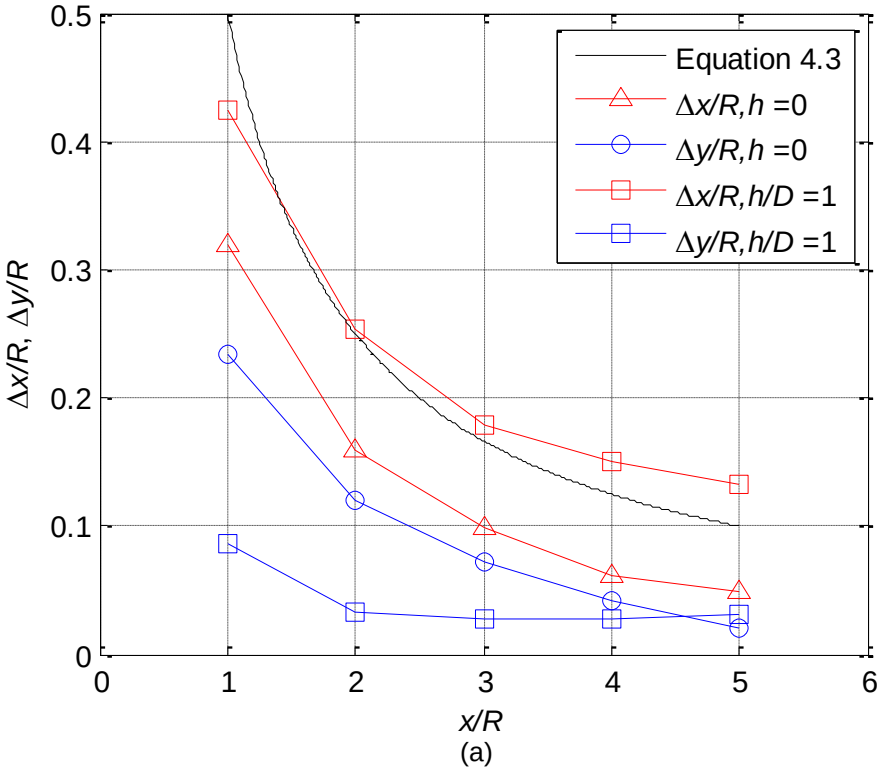

(a)

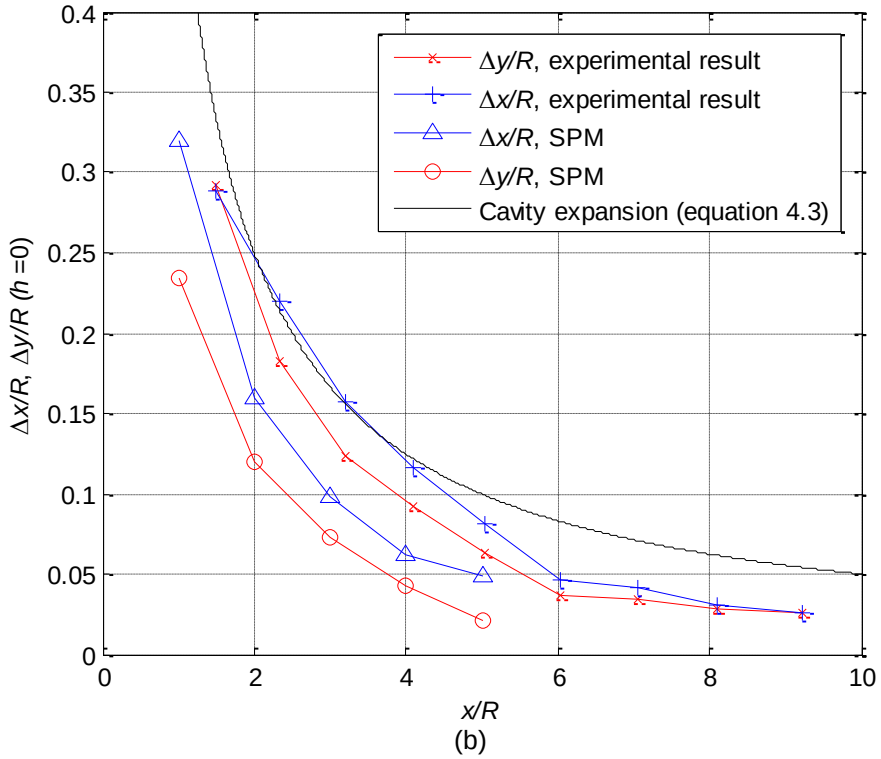

(b)

Figure 11.3: SPM data showing variation with *x:* (a) comparison with Equation 4.3 (*h/D* = 0 and 1) (b) comparison with equation 4.3 and experimental data (*h/D* = 0).

Summary

The experimental results indicate that displacement starts further ahead of the probe than predicted by the SPM.

The ultimate radial displacement predicted by the SPM shows good correspondence with the experimental data. However, the experimental results indicate that this displacement occurs only up to $h = 0$ whereas the SPM predicts ongoing displacement to $h \approx 1$.

Predictions of vertical displacement in the near field are similar as the probe approaches. However, the SPM predicts upward movement after the probe passes, which was not observed in the physical model.

11.2 Comparison with bearing capacity theory

Figure 11.4 shows contours of magnitude of soil displacement around the probe tip for test 2C (the 'standard test'). The *z* axis is depth from the soil surface and the *x* axis is horizontal location from the probe centreline. Both are divided by *R*. The probe shoulder is at about 31*R* (15.5 *D*) penetration.

The contours of displacement under the probe are circular, while the bearing capacity method assumption for failure line is not a circle, and ignore the expansion under the tip (Figure 2.1).

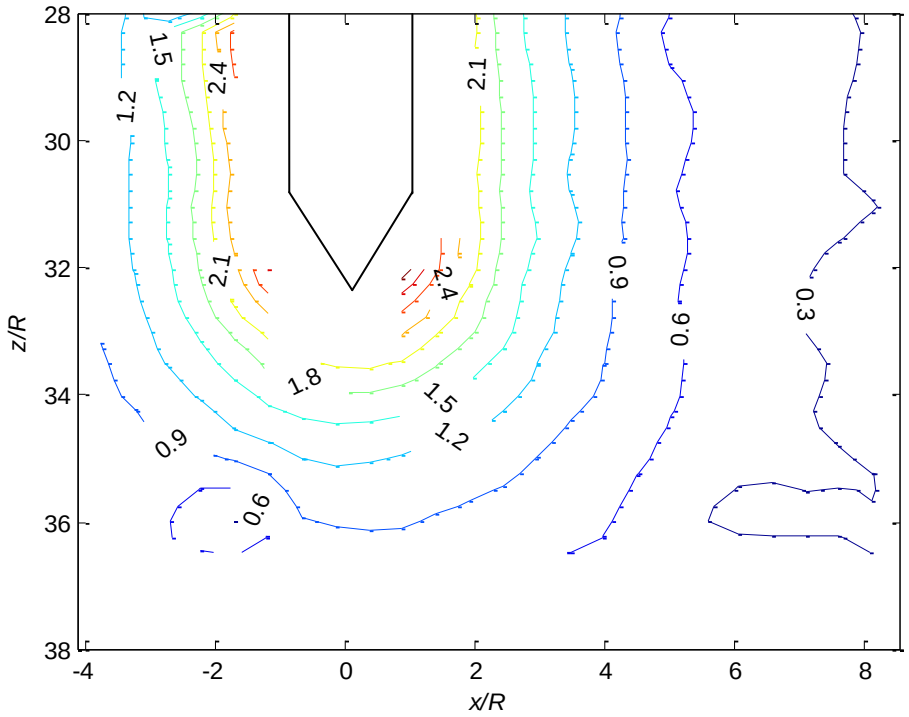

Figure 11.4: Contours of displacement (in mm) around the probe tip

Like the SPM, bearing capacity theory predicts that the movement will become upwards as the pile passes (Figure 2.1 (b)). However, Fig 11.1(a) clearly shows that there is no upward movement once 'steady state' penetration is reached. Fig 4.2(a) shows that there is more evidence of a bearing capacity type mechanism for smaller penetration.

White & Bolton (2004) also note that "There is no evidence of a bearing capacity-type mechanism in which the soil flows along streamlines curving from below the pile tip around to the upward direction on either side of the shaft."

Summary

The bearing capacity assumption doesn't reflect the failure mechanism observed in the centrifuge tests.

11.3 Comparison with circular cavity expansion theory

Figure 11.5 shows variation of normalised horizontal displacement when h = 0 with normalised radial distance from the probe. The test results are from test 2C (the standard test). The black line is from the simple equation 4.3 based on circular cavity expansion in an incompressible soil.

The remaining pink line ('standard') is from the equation deduced by Yu & Houlsby (1991) for circular cavity expansion. The parameters used for the standard line (Yu & Houlsby) are as follows: v=0.2, Φ=32^o, Ψ=0^o, E_s = 10 MN/m^2 and p_{0s} = 100 kN/m^2.

The standard line is quite similar to the simple equation 4.3 based on a constant volume approach. As anticipated the reduced Poisson's ratio reduces displacement in the far field, and this agrees well with the experimental results.

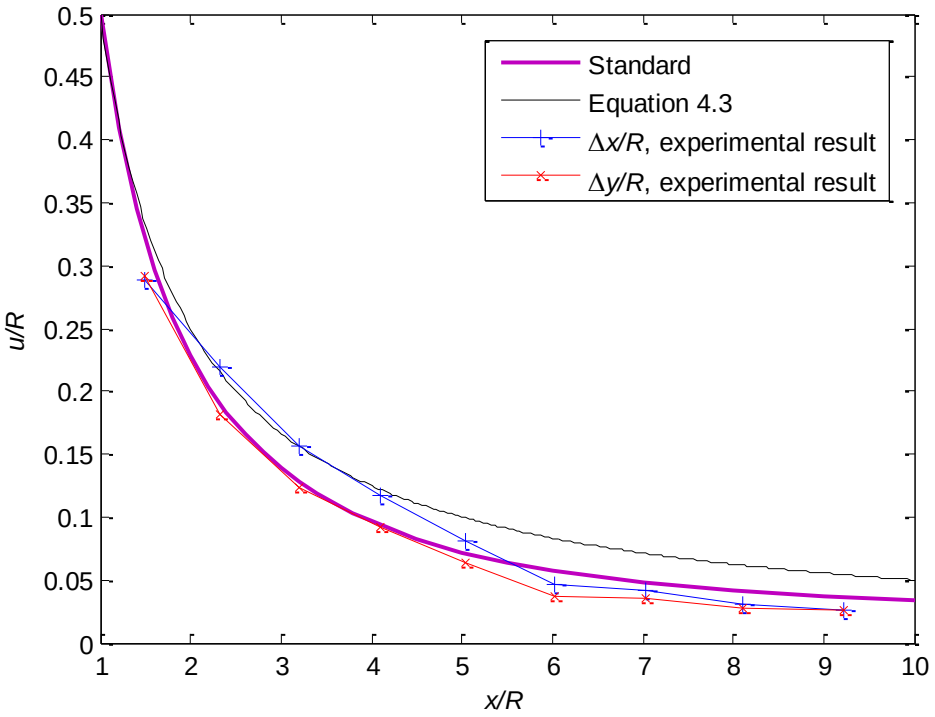

Figure 11.5: Experimental result compared to circular cavity expansion method results.

Figure 11.6(a) shows the effect of varying (doubling or halving) E or p_0 (compared to the standard values) for the equation deduced by Yu & Hously. In fact the dependency of the equation is on (E/p_0) and thus halving E has the same effect as doubling p_0 and vice versa. As shown, the displacement increases slightly when E_0 increases or p_0 decreases, but the effect is not that significant.

As shown in figure 11.6(b), the displacement increases with higher Poison's ratio. When *v*=0.49, the result matches with equation 4.3, which assumed that the sand is incompressible. In the far field, the standard line (*v* =0.2) agrees better with measured result than the v=0.49.

Also shown on Figure 11.6(b) displacement increases with a higher dilation angle (which implies volumetric expansion). However, this does not reflect the experimental results since dilation is a transient effect. The displacement decreases slightly with higher friction angle, due to reduction of yield and associated plastic displacement.

Summary

The circular cavity expansion theory agrees well with the measured result when *h/D* = 0 by choosing the sensible parameters. Particularly, use of Poisson's ratio less than 0.5 improves agreement in the far field.

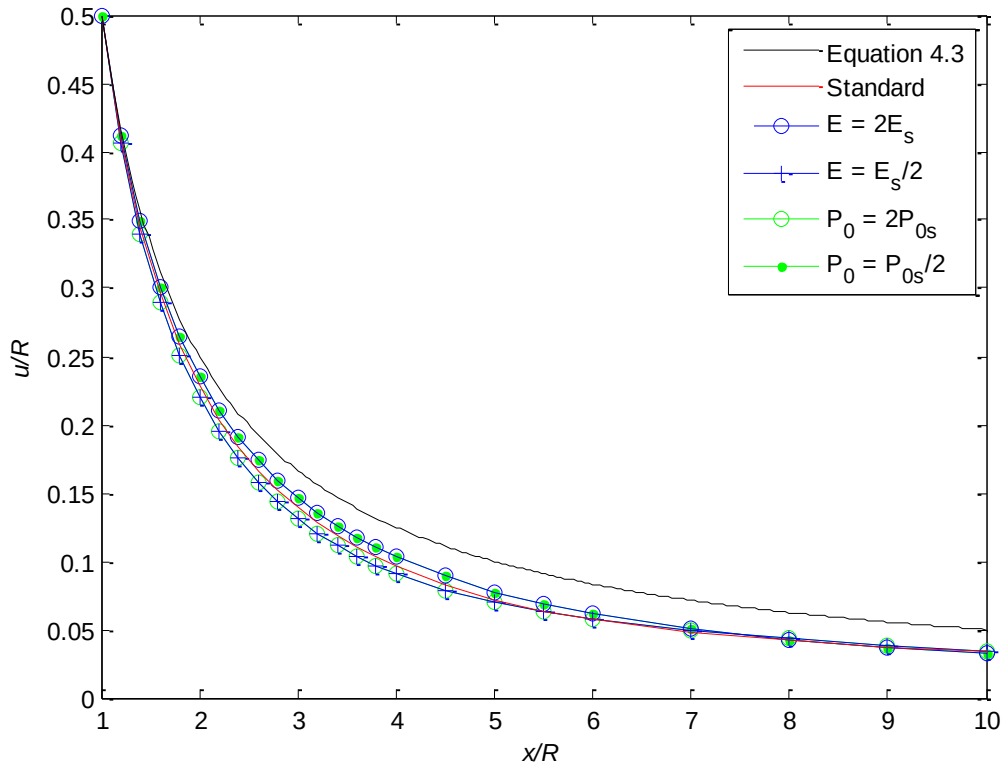

(a) Effect of changing stiffness and ambient stress

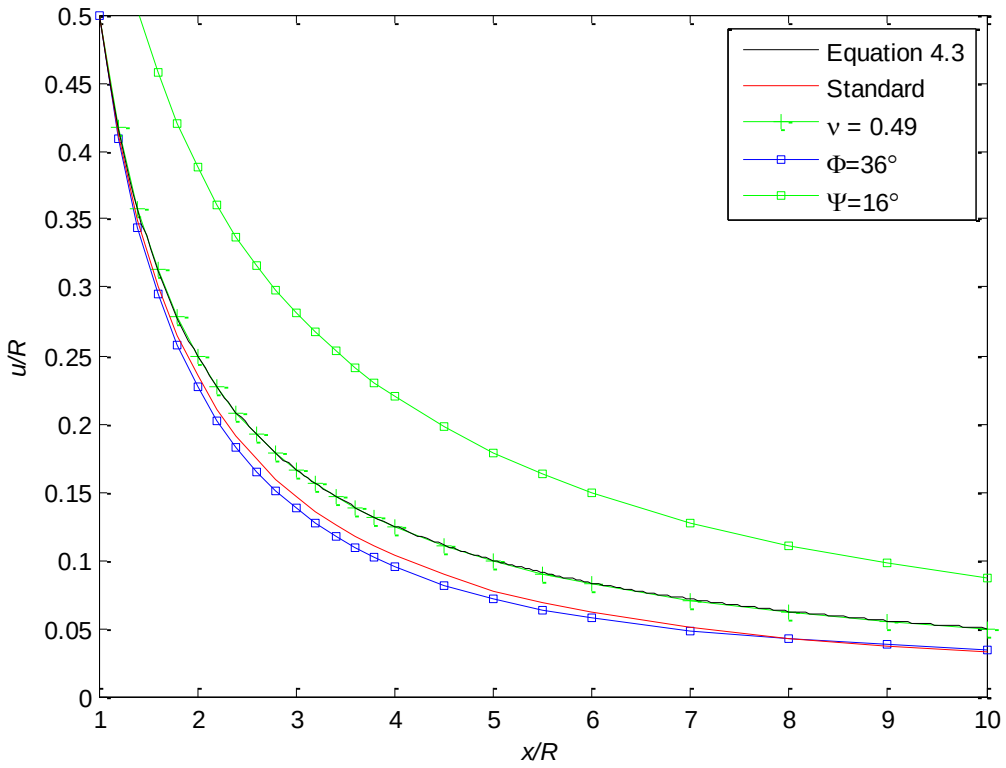

(b) Effect of Poisson's ratio, friction angle, and dilation

Figure 11.6: Parametric variation for Yu & Houlsby's method

11.4 Implications of research

As a pile is driven, it induces deformation in the soil nearby, which may adversely affect nearby buried structures. The soil movement may induce extra tensile forces which may cause tensile cracks or joint separation within an adjacent pipe, for example. As a design engineer, it is important to assess the effect of pile driving on nearby structures. Here, the effect of driving pile on a pipeline is presented as an example.

The pipe considered here is perfectly flexible pipe, which is the 'worst case'. For a flexible pipeline, the pipeline movement could be deduced by the soil displacement. Figure 11.7 shows the pipeline movement due to the pile penetration.

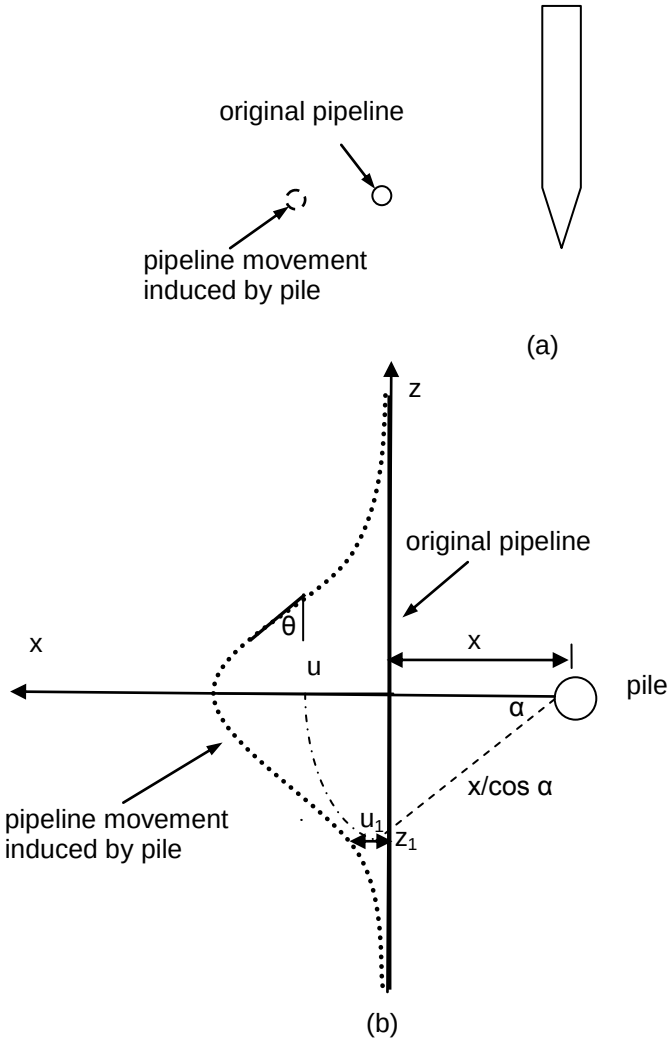

Figure 11.7 pipeline movements induced by pile installation

Calculation procedure

- In axisymmetric model, the radial displacement is same for every direction, and is a function of the distance to the pile: $u_x=f(x)$. The relationship between displacement u and distance x/R is known from experiment result (see Figure 4.14 (d) – centrifuge test 2C).
- At point z_1, the distance to the pile is x/cos α. The displacement u_{x1}= f(x/cos α) (see Figure 11.7 (b)).
- Do the same procedure for vertical displacement u_{y1} .
- $u=\sqrt{u_x^2+u_y^2}$, the displacement at point z_1 can be deduced. By varying α, the displacement of the whole pipeline could be calculated.
- tan θ=du/dz. θ is the rotation of the pipe joint. The maximum θ at each x location is shown in Figure 11.8 (a).
- Maximum u occurs at α=0. The maximum u at each x location is shown in Figure 11.8 (b)

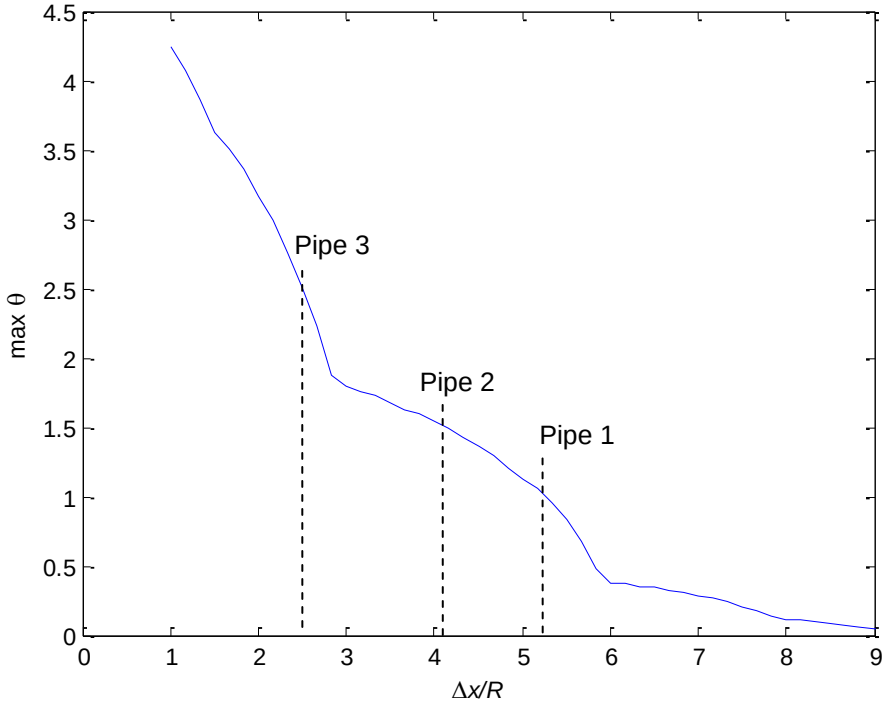

(a)

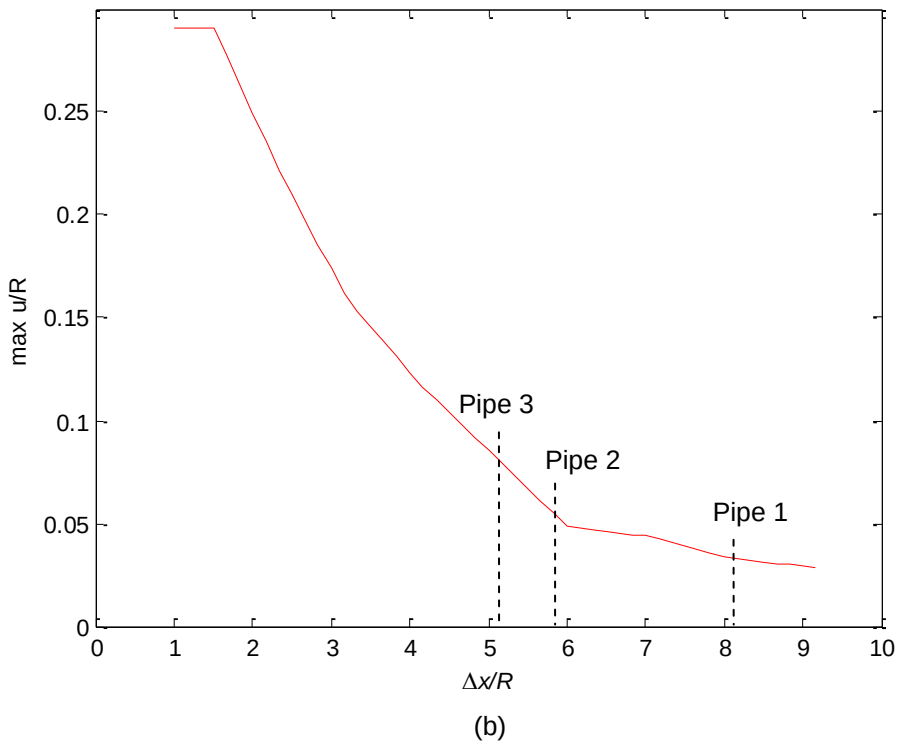

(b)

Note: Pipe 1: Lead-yarn joint in sound gas main

Pipe 2: Lead-yarn joint in water mains

Pipe 3: Rubber gasket joint in gas or water mains

Figure 11.8: Effect of piling based on centrifuge test 2C: (a) maximum θ varies with x/R. (b) maximum displacement varies with x/R

The critical distance between pile and pipeline is given in table 11.2. As can be seen from the table, the pull out criterion is more critical than the rotation. The critical distance with pile for ' lead-yarn joint in sound gas main' pipe is 8.1 R, 5.8R for 'lead-yarn joint in water mains' pipe, and 5.1R for 'rubber gasket joint in gas or water mains' pipe. For 'lead-yarn joint in gas main with history of leaks' pipe, the pile is not allowed to be driven anywhere near it.

Description	Rotation, θ, (degrees)	Pull-out, R, (mm)
lead-yarn joint in gas main with history of leaks	none	none
lead-yarn joint in sound gas main	1.0	10
lead-yarn joint in water mains	1.5	15
rubber gasket joint in gas or water mains	2.5	25

Table 11.1: Allowable joint rotation and pull-out (Attewell et al., 1986).

Description	Critical x/R for rotation	Critical x/R for pull out	Critical x/R
Lead-yarn joint in gas main with history of leaks	Not allowed	Not allowed	Not allowed
Lead-yarn joint in sound gas main	5.2R	8.1R	8.1R
Lead-yarn joint in water mains	4.1R	5.8R	5.8R
Rubber gasket joint in gas or water mains	2.5R	5.1R	5.1R

Table 11.2: Critical distance from pile – based on centrifuge test 2C.

11.5 Chapter summary

The experimental results indicate that displacement starts further ahead of the probe than predicted by the SPM. The ultimate radial displacement predicted by the SPM shows good correspondence with the experimental data. However, the experimental results indicate that this displacement occurs only up to $h = 0$ whereas the SPM predicts ongoing displacement to $h \approx 1$. Predictions of vertical displacement in the near field are similar as the probe approaches. However, the SPM predicts upward movement after the probe passes, which was not observed in the physical model.

The bearing capacity assumption doesn't reflect the failure mechanism observed in the centrifuge tests

The circular cavity expansion theory agrees well with the measured result when $h/D = 0$ by choosing sensible parameters. Particularly, use of Poisson's ratio less than 0.5 improves agreement in the far field.

As a pile is driven, it induces deformation in the soil nearby, which may adversely affect nearby buried structures, such as pipelines. The critical distance for 'lead-yarn joint in sound gas main' is 8.1 R, and 5.8R for 'lead-yarn joint in water mains', 5.1R for 'rubber gasket joint in gas or water mains' pipe. For 'lead-yarn joint in gas main with history of leaks' pipe, the pile is not allowed to be driven anywhere near it.

CHAPTER 12 - CONCLUSIONS

12.1 The work presented

Geotechnical centrifuge modelling is widely recognised to approximately replicate a stress regime corresponding to an equivalent full-scale prototype in a laboratory simulation.

A 180^{o} axisymmetric model was developed, which allowed viewing of soil movement as a half-cylindrical penetrometer advanced into the soil. The basis of the package was a 500 mm internal diameter 'tub', with height 500 mm. A 50 mm thick piece of Perspex was mounted 'across' the tub, and a 3 mm thick piece of glass was used between the Perspex and soil to reduce friction at this interface.

Two cameras were mounted on a gantry in the side of the tub not occupied by soil, thus viewing the window. The cameras were controlled in real-time via a PC 'onboard' the centrifuge. GeoPIV (White et al, 2003) was used to 'track' the movement of soil 'patches' through a series of images, and this data was then converted to actual movement in the model using the known location of control points.

A 10 kN lead screw actuator was developed specifically for these tests, and was mounted on top of the tub. The displacement was measured by a linear potentiometer and controlled in real-time from the centrifuge control room via the slip rings.

A half cylindrical probe with a 60^{o} tip was developed for the tests. The probe was required to stay 'against' the window as it slid down it, but this did prove to be problematic. Initial trials indicated that the inclusion of a compressible element along the shaft of the probe improved the probability that the tip would remain in contact. This was the most important consideration since once the tip lost contact

no useful data could be obtained. Chapter 3 reported the development of the probe which included a compressible foam element over the length of the shaft.

The soil used in the tests was Leighton Buzzard Fraction C sand, with particle size in the range 0.3 to 0.6 mm.

A series of 10 centrifuge tests have been reported. The most important features of the results are summarised below.

Standard tests (50g, dense soil sample)

1 Displacement of the soil ahead of the probe is initially downwards tending to become outwards as the probe arrives and *h* (the distance behind the shoulder of the probe) reaches zero, ultimately giving similar vertical and horizontal (radial) movement. These displacements show reasonable correspondence with circular (cylindrical) cavity expansion, as could be anticipated for the horizontal displacement.

2 The amount of displacement initially increases with depth. However, after about 8 to 10 diameters penetration the amount of movement does not vary significantly with depth.

3 After the probe passes there is little systematic movement, although near the surface of the soil the highest patches initially heave upwards and are later dragged down as the probe advances.

4 The magnitude of displacements drops quickly as the radial position increases. The displacement variation with radius shows excellent agreement with circular cavity expansion theory close to the probe, but can be somewhat less than that predicted at a larger radius, presumably due to compressibility of the soil.

5 Initially the test data indicate vertical strains at small radius somewhat in excess of a spherical cavity expansion prediction immediately ‘ahead’ of

the probe. The ‘arrival’ of the probe was first ‘sensed’ about 10 diameters ahead of it. The maximum (compressive) vertical strain occurs somewhat before the probe arrives at a particular point in the soil and occurs earlier but is smaller as x/R (normalised radial distance from the probe) increases. At small radius a much smaller tensile vertical strain is observed just as the probe passes.

6 Significant horizontal strains are observed later than the vertical strains (about 5 diameters ‘ahead’ of the probe). At small radius they are initially tensile, but as the probe passes larger compressive strains are observed, with magnitude reducing with x/R.

7 The results from the repeat tests show reasonable consistency. Overall relatively little difference between Perspex and glass windows in contact with the soil was observed, although there was some evidence that strains in the soil were lower for the Perspex window, as might be anticipated.

Effect of ‘re-driving’ a probe

A test was carried out where the probe was driven into the soil, withdrawn to the top of the soil, and then ‘re-driven’ into the disturbed soil sample. The main effect was that both vertical and horizontal movement of the soil as the probe approached and passed were quite significantly reduced. It seems likely that the disturbed soil had been significantly loosened (particularly close to the probe) and was therefore more compressible.

Effect of density

It is found that there is no significant deviation in displacement and strains for different density of the soil. Using air pluviation it was not possible to form a particularly loose sample. Since density was measured before the model was

loaded onto the centrifuge it is also possible that the 'loose' soil was further densified prior to the actual test.

Effect of acceleration

1g and 100g tests were undertaken for comparison with the 50g 'standard' tests. The most significant observation was that the amount of vertical displacement in the soil tended to increase with g-level. It seems likely that the amount of horizontal displacement as the probe passes is fundamentally linked to the cavity expansion analogy, and is independent of the g-level. The increase of vertical displacement with g-level could be linked to increased stiffness of the soil.

Effect of probe tip

The majority of tests were carried out using a probe with a 60^{o} tip. However, a 'blunt' (flat) tip was also considered. As previously noted by White & Bolton (2004) in plane strain tests, the blunt probe generated a 'cone' of crushed soil immediately ahead of the probe. In tests with a 60^{o} tip there was also evidence that crushed soil was generated at the edge of the tip.

White & Bolton (2004) place significant emphasis on the effect of the crushed material at the tip 'coating' the shaft of the probe as penetration continues. In these tests there was also some evidence that this occurred. White and Bolton observed horizontal movement in the soil of the order of 1 % of the probe width towards the probe after the tip had passed.

In these tests, 1 % of the probe diameter = 0.12 mm. Horizontal movements observed in the soil after the probe had passed were typically less than half this value, and were probably at the limit of the resolution of the optical measurement system.

Comparison with White & Bolton (2004)

White & Bolton (2004) presented results of calibration chamber tests on a plane strain (PS) probe which can be compared with the axisymmetric (AX) results reported here.

In terms of vertical strains, compressive strain is observed slightly further ahead of the probe in the PS tests. In both tests this reaches at maximum on a line projected at about 45^o to the vertical into the soil ahead of the probe. The maximum strain is smaller in the AX test, and strain dissipates with distance from the probe in both tests. As the probe passes some tensile strain is observed, but this is more significant and widespread for the PS test.

In terms of horizontal strains, near the probe the initial strain is tensile for both types of tests, but is observed further from the probe for the PS test. This tensile strain reaches a maximum on a line projected at about 30^o to the vertical into the soil ahead of the probe, and is larger in the PS tests. Further from the probe no tensile strain is observed, and compressive strain increases monotonically.

As the probe passes, compressive horizontal strain is observed at all locations. For the AX test the displacement (and hence strain) show good correspondence with cylindrical cavity expansion, reducing rapidly with distance from the probe. In the PS test the strain is virtually constant with radius.

Stress along the probe

Measurement of the axial load near the probe tip was largely successful in confirming that the probe tip resistance had a typical value for dense sand. However, it did not prove possible to determine the distribution of load up the shaft to infer the shaft stress. This would rely upon accurate assessment of relatively small changes of load, and this was not achieved. It is thought that

bending of the probe along the compressible shaft between the actuator and tip had a significantly detrimental effect of measurement of axial load. However, it is possible that improvements could be made in this respect.

Comparison with other theories

The experimental results indicate that displacement starts further ahead of the probe than predicted by the SPM. The ultimate radial displacement predicted by the SPM shows good correspondence with the experimental data. However, the experimental results indicate that this displacement occurs only up to $h = 0$ whereas the SPM predicts ongoing displacement to $h \approx 1$. Predictions of vertical displacement in the near field are similar as the probe approaches. However, the SPM predicts upward movement after the probe passes, which was not observed in the physical model.

The bearing capacity assumption doesn't reflect the failure mechanism observed in the centrifuge tests

The circular cavity expansion theory agrees well with the measured result when $h/D = 0$ by choosing sensible parameters. Particularly, use of Poisson's ratio less than 0.5 improves agreement in the far field.

Pile driving effects on pipelines

The critical distance for 'lead-yarn joint in sound gas main' is 8.1 R, and 5.8R for 'lead-yarn joint in water mains', 5.1R for 'rubber gasket joint in gas or water mains' pipe. For 'lead-yarn joint in gas main with history of leaks' pipe, the pile is not allowed to be driven anywhere near it.

12.2 Recommendation for future research interests

This thesis has demonstrated the practicality and presented the results of an experimental study on the soil movement as an axisymmetric penetrometer advances into soil. Building on this there are several areas where further work could be undertaken.

Design of the probe

The design of the probe with a compressible element in the shaft was generally successful in maintaining contact of the probe tip with the window. However, it sometimes resulted in sand locally becoming trapped between the probe shaft and the window (see photos Appendix A). It would be preferable that this was avoided, but in this work any effort to reduce this problem (by making the shaft less compressible) resulted in a significant increase in the probability of the probe tip separating from the window, which was considerably more undesirable. However, it is possible that an improved probe (and/or actuator) design could overcome this problem.

The probe was nominally 'smooth'. The effect of a 'rough' probe shaft could be considered. However, this would again be complicated by the 'compressible' shaft, where an aluminium strip was used directly against the window. The edges of this would need to be roughened, and the effect of the adjacent foam considered at the probe-soil interface.

As described above, it was not possible to determine the distribution of shaft stress, and improvements in this respect could be considered.

The soil model

Attempts to compare the response of dense and loose soil samples indicated little difference. It was not possible to produce a sample which was initially that loose, and this was probably compounded by subsequent densification as the model

was moved and loaded onto the centrifuge. This issue could potentially be addressed by a different model preparation technique; or models using different soil could be considered.

REFERENCES

Al-Douri, R. H. & Poulos, H. G. (1991). Static and direct shear tests on carbonate sands. *ASTM Geotechnical. Test. Journal.* Vol. **15**, No. 2, pp.138–157.

Allersma, H. G. B. (1988). Photoelastic investigation of the stress distribution during penetration. *Proc. 2nd Eur. Symp. Penetration Testing,* Amsterdam, pp. 411–418.

API (2000). *Recommended practice of planning, designing and constructing fixed offshore platforms: working stress design*, RP2A, 20th edn. Washington: American Petroleum Institute

Astedt, B., Weiner, L. & Holm, G. (1992). Increase in bearing capacity with time for friction piles in silt and sand. *Proc.Nordic Geotech. Meeting*, pp. 411–416.

Axelsson, G. (2000). *Long term set-up of driven piles in sand*. PhD thesis, Royal Institute of Technology, Stockholm, Sweden.

Barligh, M. M. (1985). Strain path method. *Journal of the Soil Mechanics and Foundation Division, ASCE*, Vol. **111**, No. 9, pp. 1108-1136.

Berezantzev, V. C., Kristoforov, V. & Golubkov, V. (1961). Loadbearing capacity and deformation of piled foundations. *Proc. 5th Int. Conf. Soil Mech. Fdn. Engng, Paris* 2, pp. 11–12.

Borghi, X., White, D. J., Bolton, M. D. & Springman, S. M. (2001). Empirical pile design based on CPT results: an explanation for the reduction of unit base resistance between CPTs and piles. *Proc. 5th Int. Conf. on Deep Foundation Practice*, *Singapore*, pp. 125–132.

Bolton, M. D. & Gui, M. W. (1993). The study of relative density and boundary effects
for cone penetration tests in centrifuge. *Technical Report No. CUED/D-SOILS/TR256.* University of Cambridge, UK.

Bowman, E. T. (2002). *The ageing and creep of dense granular materials*. PhD thesis, University of Cambridge.

Bullock, P. J., Schmertmann, J. H., McVay, M. C. & Townsend, F. C. (2005). Side shear setup. II: Results from Florida test piles. *Journal of Geotechnical and Geoenvironmental Engineering, ASCE*, Vol. **131**, No. 3, pp. 301–310.

Butterfield, R., Harkness. R. M. & Andrawes, K. Z. (1970). A stereo-photogrammetric method for measuring displacement fields. .*Géotechnique,* Vol. **20**, No. 3, pp. 308-314.

Carter, J. P, Booker, J. R., & Yeung, S. K. (1986). Cavity expansion in cohesive frictional soils. *Géotechnique,* Vol. **36**, No. 3, pp. 349-353.

Chen, J. W.& Juang, C. H. (1996). Determination of drained friction angle of sands from CPT. *Journal of Geotechnical Engineering*, *ASCE*, Vol. **122**, No.5, pp. 374-381.

Chong, F. (1988). Density changes of sand on cone penetration resistance. *Proc. 1st Symp. Penetration Testing,* ISOPT-1, 2, pp. 707–714. Rotterdam: Balkema.

Chow, F. C. (1997). *Investigations into displacement pile behavior for offshore foundations.* PhD thesis, University of London (Imperial College).

Chow, F. C., Jardine, R. J., Brucy, F. & Nauroy, J. F. (1997). Time related increases in the shaft capacities of driven piles in sand. *Géotechnique ,* Vol. **47**, No. 2, pp. 353–361.

Cividini, A., & Gioda, G. (1998). A simplified analysis of pile penetration. *Proc, 6th Int. Conf. Numer, Methods in Geomech.,* A. A. Balkema, Rotterdam, The Netherlands, pp. 1043-1049.

Coop, M. R. (1990). The mechanics of uncemented carbonate sands. *Géotechnique,* Vol. **40**, No. 4, pp. 607–626.

Coop, M. R., Klotz, E. U. & Clinton, L. (2005). The influence of the in situ state of sands on the load-deflection behavior of driven piles. *Géotechnique,* Vol. **55**, No. 10, pp. 721-730.

Cox, C. (2005). The use of Matlab in conjunction with Particle Image Velocimetry (PIV) to monitor the deformations of sand surfaces, *Personal correspondence*.

Davidson, J. L., Mortensen, R. A. & Barreiro, D. (1981). Deformations in sand around a cone penetrometer tip. *Proc. 10th Int. Conf. Soil Mech. Fdn. Engng Stockholm ,* Vol. **2**, pp. 467–470.

DeJong, J., Randolph, M. F. & White, D. J. (2003). Interface load transfer degradation during cyclic loading: a microscale investigation. *Soil and Foundations.* Vol. **43**, No. 4, 81–93.

Dijkstra, J. , Broere, W.& van Tol, A.F. (2006). Experimental Investigation into the Stress and Strain Development around a Displacement Pile. *Piling and Deep Foundations*, DFI, pp. 252-259.

De Borst, R., & Vermeer, P. A. (1982). Finite element analysis of static penetration tests. *Proc., 2nd Eur. Symp. on Penetration Testing,* Vol. **2**, pp. 457-462.

De Pater, C.J. & Nieuwenhuis, J. D. (1986). Method for measuring the deformations of a sand surface. *Géotechnique ,* Vol. **36**, No. 4, pp. 581-585.

Durgunoglu, H. T, & Mitchell, J. K (1975). Static penetration resistance of soils: Analysis. *Proc. ASCE Spec, Conf. on In Situ Measurement of Soil Properties*, *ASCE*, New York, Vol. **1**, pp. 151-171.

Ellis, E.A., Cox, C., Yu, H.S., Ainsworth, A. and Baker, N. (2006). A new geotechnical centrifuge at the University of Nottingham, UK. *6th International Conference of Physical Modelling in Geotechnics: ICPMG'06*. Taylor & Francis Group, London, pp. 129-133.

Fellenius, B. H. (2007). Discussion on 'Behavior of jacked and driven piles in sandy soil' by Yang, J., Tham, L. G., Lee, P. K. K., Chan, S. T., and Yu, F. *Géotechnique ,* Vol. **57**, No. 5, pp. 245-259.

Foray, P., Balachowski, L. and Rault, G. (1998). Scale effect in shaft friction due to the localisation of deformations. *Centrifuge'98.* Balkema, Rotterdam.

Gibson, R. E. (1950). Discussion to "The bearing capacity of screw piles and screwcrete cylinders" by G. Wilson. *Journal of the Institute of Civil Engineers*, Vol. **34**, pp. 382–383.

Gui, M. W., Bolton, M. D., Garnier, J., Corte, J. F., Bagge, G., Laue, J. & Renzi, R. (1998). Guidelines for cone penetration tests in sand. *Proceedings International Conference Centrifuge '98*, Tokyo, Vol. **1**, pp. 155-160.

Gupta, R. C. (1991). Finite strain analysis for deep cone penetration. *Journal of Geotechnical Engineering*. Vol. **117**, No.10, pp 1610-1630.

Hardin B. O. & Drnevich V. P.(1972). Shear modulus and damping in soils: design equations and curves. *Journal of the Soil Mechanics and Foundations Division, ASCE*, Vol **98**, No. SM7, 667–692.

Heerema E. P. (1980). Predicting pile driveability: heather as an illustration of the "friction fatigue" theory. *Journal of Ground Engineering*, Vol. **13**, No. 3. pp. 15-20.

Jardine, R. J. & Chow, F. C. (1996). New design methods for offshore piles, *MTD Publication 96/103*. London: Marine Technology Directorate.

Jardine, R. J., Standing, J. R. & Chow, F. C. (2006). Some observations of the effects of time on the capacity of piles drivenin sand. *Geotechnique,* Vol.**56**, No. 4, pp.227–244

Kraft, L. M. (1990). Computing axial pile capacity in sands for offshore conditions. *Marine Geotech.,* Vol. **9**, pp. 61–72.

Klotz, E. U. & Coop, M. R. (2001). An investigation of the effect of soil states on the capacity of driven piles in sands. *Géotechnique,* Vol. **51**, No. 9, pp. 733-751.

Kobayashi, T. & Fukagawa, R. (2003). Characterization of deformation process of CPT using X-ray TV imaging technique. *Third International Conference on Deformation Characteristics of Geomaterials*, pp. 43-47.

Ladanyi, B. and Johnson, G.H. (1974). Behaviour of circular footings and plate anchors embedded in permafrost, *Canadian Geotechnical Journal*, Vol. **11,** pp. 531–553.

Lee, J. H. & Salgado, R. (1999). Determination of pile base resistance in sands. *Journal of Geotechnical and Geoenvironmental Engineering*, *ASCE,* Vol. **125**, No. 8, pp. 673–683.

Lehane, B. M., Jardine, R. J., Bond, A. J. & Frank, R. (1993).Mechanisms of shaft friction in sand from instrumented pile tests. *Journal of Geotechnical and Geoenvironmental Engineering, ASCE,* Vol. **119**, No. 1, pp. 19–35.

Loukidis, D. and Salgado, R. (2008). Analysis of the Shaft Resistance of Nondisplacement Piles in Sand. *Geotechnique*, Vol. **58**, No. 4, pp. 283–296.

Maiorano, R.M.S., Viggiani, C. and Randolph, M.F. (1996) Residual stress system arising from different methods of pile installation. *The 5th International Conference on the Application of Stress-Wave Theory to Piles*, Rotterdam, Balkema, A.A., 1: pp 518-528

Mikasa, M. & Takada, N. (1973). Significance of centrifugal model tests in soil mechanics. *Proc. 8th Int. Conf. Soil Mech. Fdn. Engng, Moscow*, pp. 273–278.

Ohtomo, K.& Tan A.C. C. (2001). Direct Measurement of Soil Deformation using the Bead-grid Method. *Journal of Agricultural Engineering Research,* Vol. **78**, No. 3, pp. 325-332.

Ovensen (1979), Contribution to Discussion on The Use of Physical Models in design. *Proc. of 7th European Conference on soil Mechanics and Foundation Engineering*, Brighton, pp. 319-323.

Poulos, H. G. (1987) Analysis of Residual Stress Effects in Piles. *Journal of Geotechnical Engineering, ASCE,* Vol. **113**, No. 3. pp.216-229.

Poulos, H. G., Randolph, M. F. & Semple, R. M. (1988). Evaluation of pile friction from conductor tests. *Proc. Int. Conf. Calcareous Sediments,* Perth, Vol. **2**, pp. 599–605.

Randolph, M. F., Dolwin, J. & Beck, R. (1994). Design of driven piles in sand. *Géotechnique*, Vol. **44**, No. 3, pp. 427-448.

Randolph, M. F. (2003). Science and empiricism in pile foundation design. *Géotechnique*, Vol. **53**, No. 10, pp. 847-875.

Reese, L. C., Isenhower, W. M & Wang, S (2006). *Shallow and deep foundations*. Jonh Wiley & Sons, Inc., Hoboken, New Jersey.

Robinksy, E. I. & Morrison, C. F. (1964). Sand Displacement and compaction around model friction piles. *Canadian Geotechnical Journal*, Vol.**1**, No. 2, pp. 81-93.

Sadek S, Iskander M & Liu J. (2003). Accuracy of digital image correlation for measuring deformations in transparent media. *ASCE, Journal of Computing in Civil Engineering*, Vol. **17**, No. 2, pp. 88-89.

Salgado, R. (1993). *Analysis of penetration resistance in sands.* PhD thesis, University of California, Berkeley, California.

Salgado, R., Mitchell, J. K., & Jamiolkowski, M. (1997). Cavity expansion and penetration resistance in sand. *Journal of Geotechnical and Geoenvironmental Engineering, ASCE,* Vol. **123**, No. 4. pp. 344-354.

Schofield, A.N. (1980) Cambridge Geotechnical Centrifuge Operations Twentieth Rankine Lecture. *Géotechnique,* Vol. **30**, No. 3, pp. 227-268.

Takemura. A.A. Balkema, Rotterdam, the Netherlands. Vol. 2, pp. 1047-1055.

Teh, C.I. & Houlsby, G.T.(1991). An Analytical Study of the Cone Penetrometer Test in Clay. *Géotechnique*, Vol. **41**, No. 1, pp. 17-34.

Tejchman, A. & Gwizdala, K. (1979). Analysis of safety factors of bearing capacity for large diameter piles. *Proc. Eur. Conf. Soil Mech. Fdn Engng,* Brighton, Vol. **1**, pp. 293–296.

Taylor, R.N. (1995) *Geotechnical Centrifuge Technology*. Blackie Academic & Professional.

Ueno, K. (1998). Methods for preparation of sand samples. *In Proceedings of the International Conference Centrifuge 98,* Edited by T. Kimura, O. Kusakabe, and J. Takemura. A.A. Balkema, Rotterdam, the Netherlands. Vol. 2, pp. 1047-1055.

Van den Berg, V. (1994). *Analysis of soil penetration*. PhD thesis. Delft University. Delft, The Netherlands.

Vesic, A. S. (1972). Expansion of cavities in infinite soil mass. *Journal of the Soil Mechanics and Foundation Division*, *ASCE* ,Vol. **98**, No. 3, pp. 265-290.

Winterkorn, A. F. & Fang, S. Y. (1975). *Foundation engineering handbook*. New York: Van Nostrand Reinhold.

White, D. J. & Bolton, M. D. (2002). Observing friction fatigue on a jacked pile. *Centrifuge and constitutive modelling: two extremes (ed. S.M. Springman*), Rotterdam: Swets & Zeitlinger, pp. 347-354.

White, D. J., Take, W. A. & Bolton, M. D. (2003). Soil deformation measurement using particle image velocimetry (PIV) and photogammetry. *Géotechnique*, Vol. **53**, No. 7, pp. 619–631.

White, D. J. & Bolton, M. D. (2004). Displacement and strain paths during plane-strain model pile installation in sand. *Géotechnique*, Vol. **54**, No. 6, pp. 375-397.

White, D. J. & Lehane, B. M. (2004). Friction fatigue on displacement piles in sand. *Géotechnique*, Vol. **54**, No. 10, pp. 645-658.

White, D. J. & Bolton, M. D. (2005). Comparing CPT and pile base resistance in sand. *Proc. Instn Civ. Engrs, Geotechnical. Engineering*, Vol. **158**, Issue GEI, pp. 3-14.

Yang, J., Tham, L. G., Lee, P. K. K., Chan, S. T., and Yu, F. (2006). Behaviour of jacked and driven piles in sandy soil. *Géotechnique*, Vol. **56**, No. 4, pp. 245–259.

Yasufuku, N. & Hyde, A. F. L. (1995). Pile end-bearing capacity in crushable sands. *Géotechnique*, Vol. **45**, No. 4, pp. 663–676.

Yetginer, A. G., White, D. J. & Bolton, M. D. (2006). Field measurements of the stiffness of jacked piles and pile groups. *Géotechnique*, Vol. **56**, No. 5, pp. 349–354.

Yoon, B. S. (2008). *Centrifuge modelling of discrete pile rows to stabilise slop*. PhD thesis. University of Nottingham.

Yu, H. S. & Houlsby, G. T. (1991). Finite cavity expansion in dilatant soil: loading analysis. *Géotechnique*, Vol. **41**, No. 2, pp. 173-183.

Yu, H. S., and Mitchell, J. K.(1998). Analysis of cone resistance: review of methods. *Journal of Geotechnical and Geoenvironmental engineering,* Febrauray, pp. 140-149.

Yu, H S; Herrmann, L R & Boulanger, R W (2000). Analysis of steady cone penetration in clay. *Journal of Geotechnical & Geoenvironmental Engineering*, ASCE, 126(7): 594-605.

Yu, H. S. (2000) *Cavity Expansion Methods in Geomenics*, Kluwer Academic Publishers.

APPENDIX A - PHOTOS OF PROBE IN THE TESTS

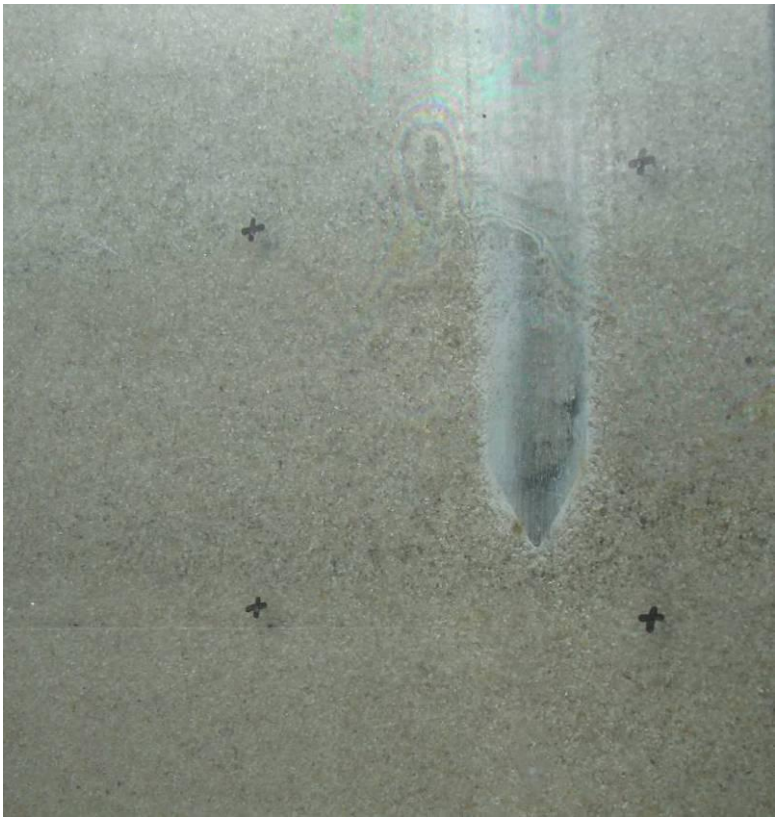

Figure A.1: Image in test 1 (Perspex window, tip at y = 115mm)

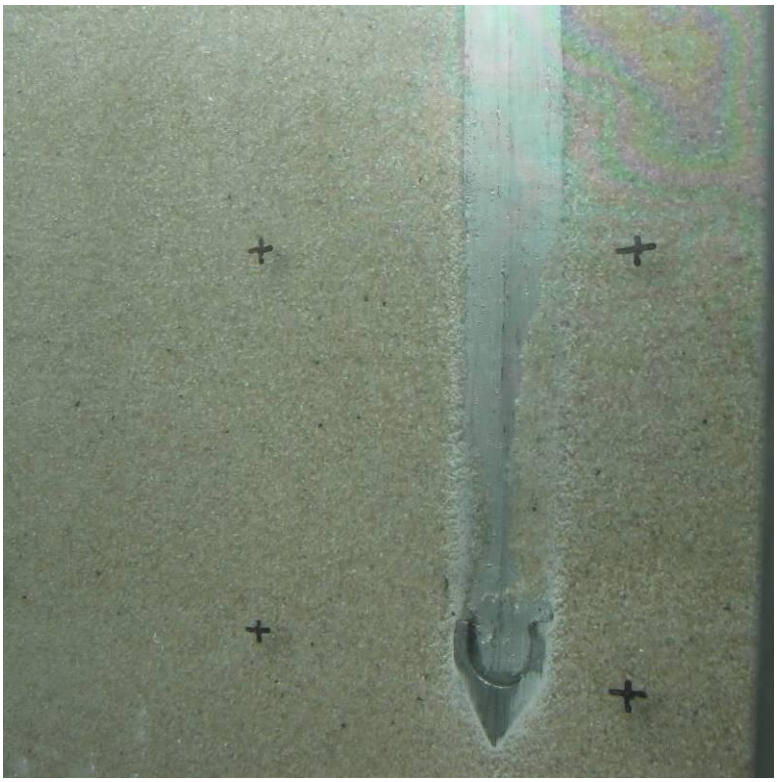

Figure A.2: Image in test 2A (tip at y = 150mm)

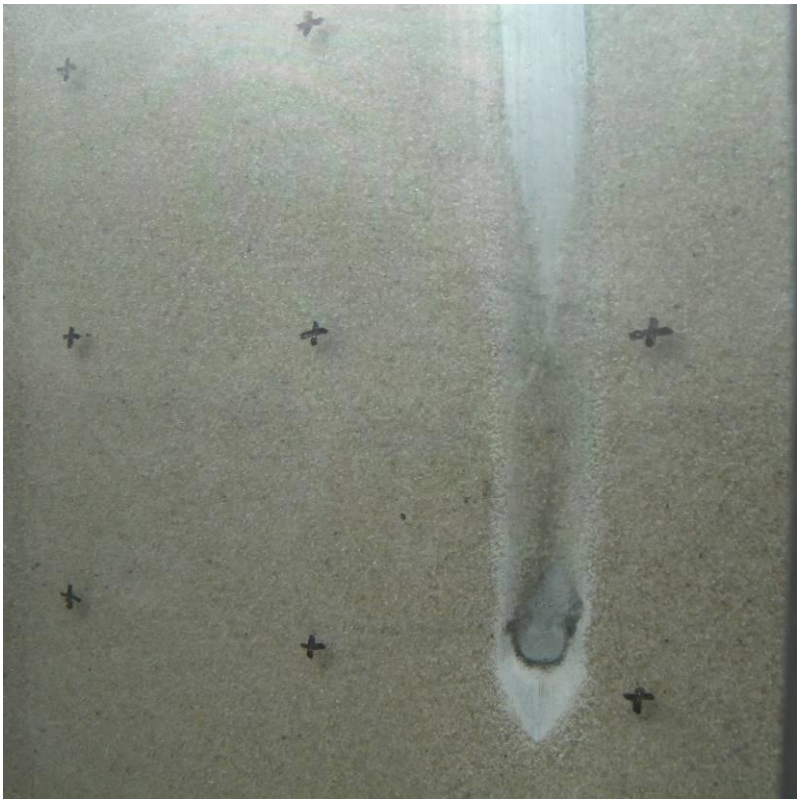

Figure A.3: Image in test 2B (tip at y = 150mm)

Figure A.4: Image for conical tip in test 2C (tip at y = 155mm)

Figure A.5: Image in test 2D (Re-drive test, tip at y = 154mm)

Figure A.6: Image in test 3A (loose sample test, tip at y = 150mm)

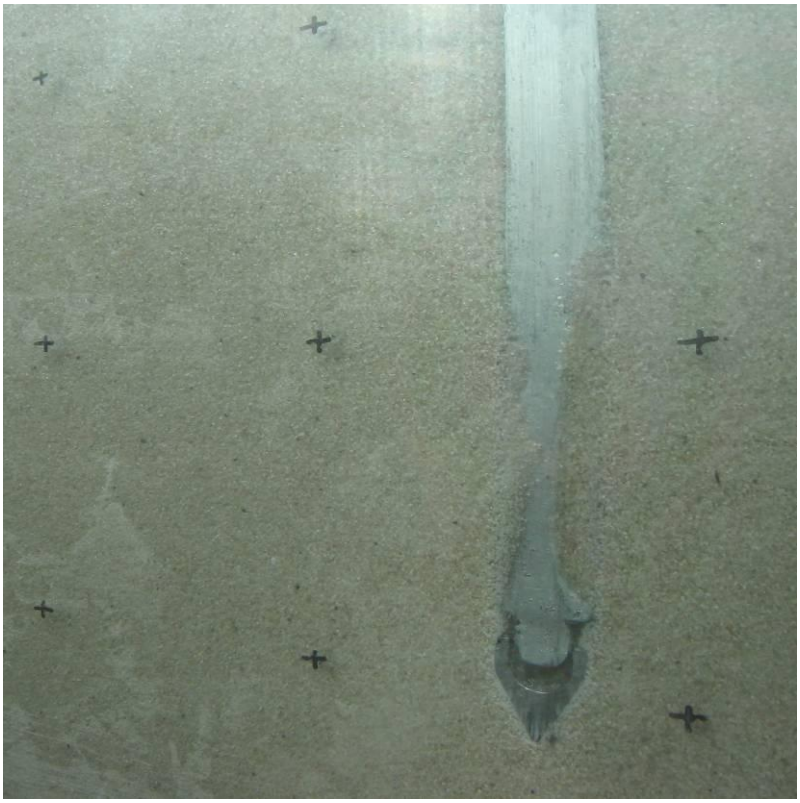

Figure A.7: Image in test 3B (loose over dense sample test, tip at y = 151mm)

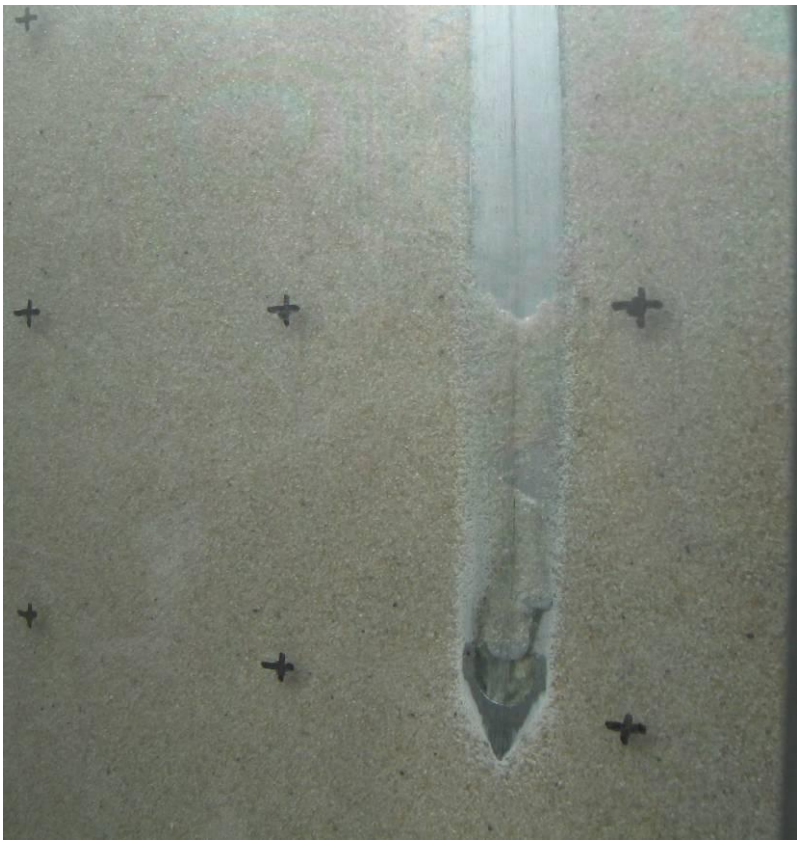

Figure A.8: Image in test 4 (100g test, tip at y = 152mm)

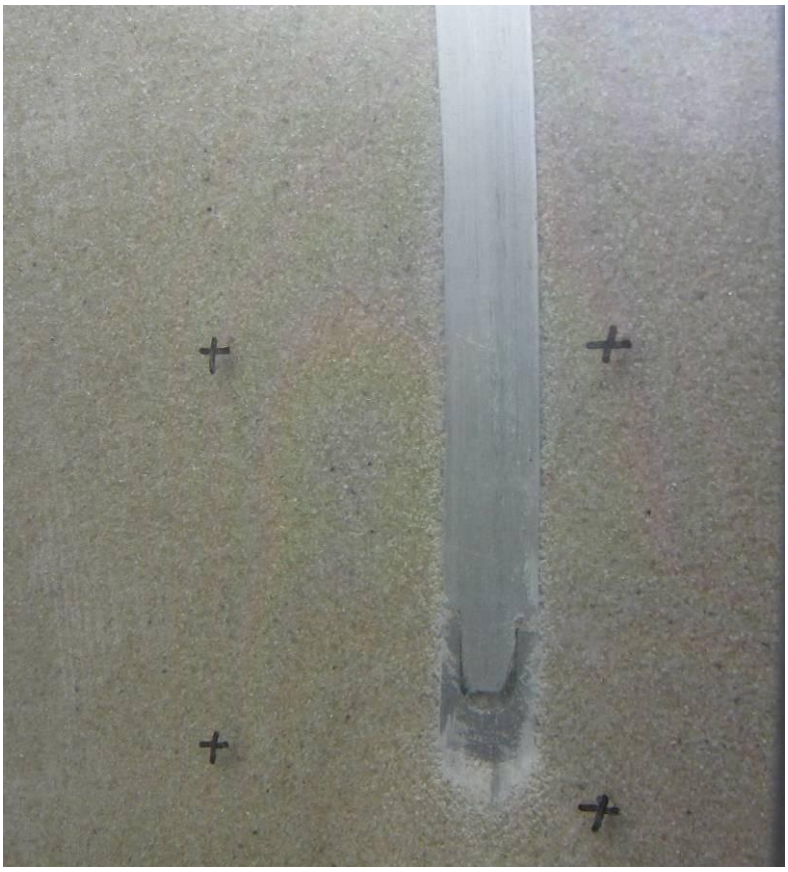

Figure A.9: Image in test 5 (blunt probe, tip at y = 153mm)

Figure A.10: Image in test 6 (1g test, tip at y = 149mm)

Appendix B - EFFECT OF REFRACTION ON IMAGE DATA

When a camera points directly at a Perspex window, it is normally assumed that the image position of control points in the model behind the window can be used to directly 'map' image space to object space using uniform scaling. The effect of refraction is not considered, but is assumed to introduce negligible error.

Here the camera is not pointing directly at the window in a horizontal plane, and the typical error due to refraction will be considered. Initially a vertical plane is considered before proceeding to the horizontal plane.

Vertical plane

In the tests reported here the cameras point nominally horizontally, with a field of view of about 18^{o} above or below the horizontal. As shown in Figure B.1 an actual ray of light with inclination of α_1 to the horizontal will be considered. The actual location of the camera optical centre from the model is y_c, and the window has thickness t. However, neglecting the effects of refraction the 'apparent' location is $y_c' < y_c$.

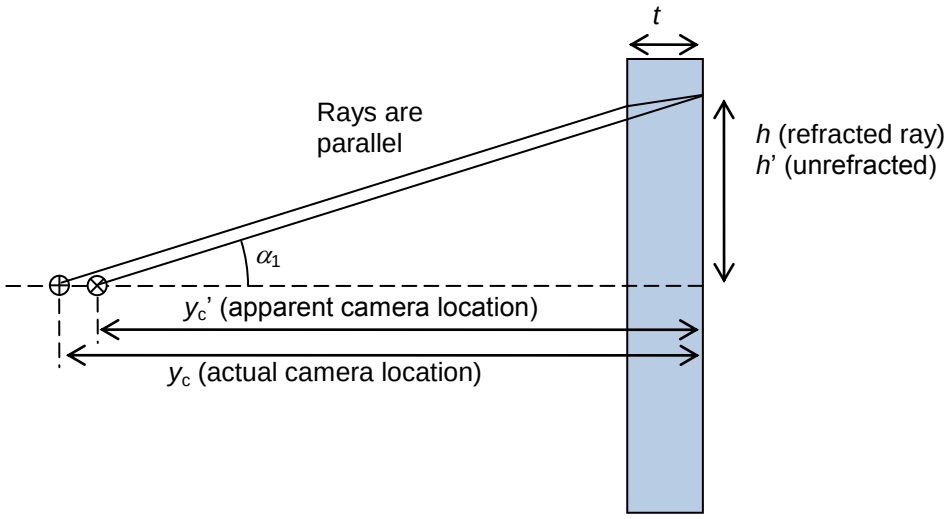

Figure B.1 Schematic of refracted and unrefracted rays in a vertical plane

The height h above the camera location in the model for a refracted ray of light passing through the actual camera location is:

$$h = (y_c - t)\tan\alpha_1 + t\tan\alpha_2 \qquad \text{Equation 1(a)}$$

where the angle of the refracted ray is given by $\sin\alpha_2 = \sin\alpha_1/n$, and n is the refractive index of perspex = 1.5.

For the apparent camera location and ray which is assumed to be unrefracted

$$h' = y_c'\tan\alpha \qquad \text{Equation 1(b)}$$

Since the rays have the same angle (α_1) at the camera they will have the same image position, and (h'-h) is the 'error' in model position from neglect of refraction.

In the tests reported here $y_c \approx 180$ mm, and $t = 50$ mm. A value of y_c' of 162.6 mm will be considered (which has been determined by trial and error to minimise the error). Figure B.2 shows results for α_1 in the range $\pm 18^o$. The error (h'-h) is plotted on the x-axis, with the nominal model position h derived from Eq 1(a) on the y-axis. h varies in the range ±53 mm, corresponding to the nominal vertical field of view of 100 mm.

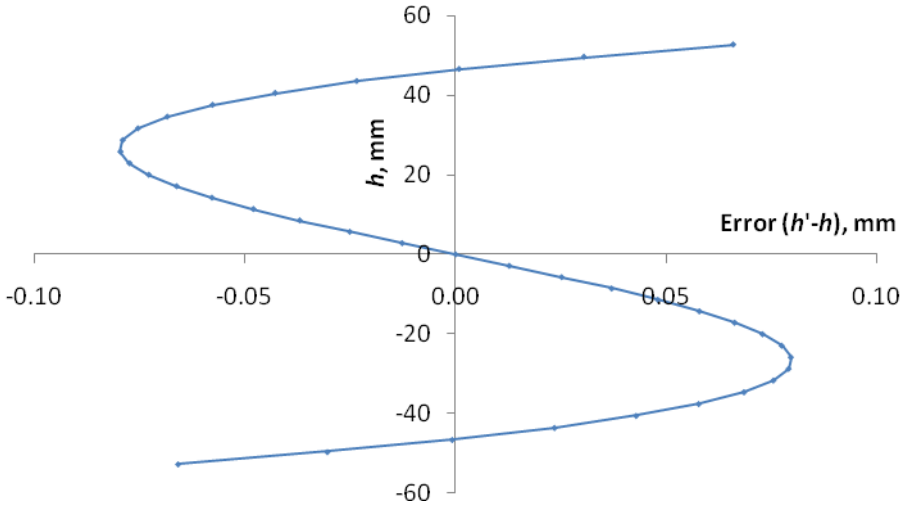

Figure B.2: Error in determination of vertical model position

The 'optimised' y_c' has given approximately equal and opposite positive and negative errors with magnitude 0.08 mm. Unsurprisingly the error is zero when $\alpha_1 = h = 0$ since this ray meets the window perpendicularly and is not refracted. Also the error is symmetrical above and below $h = 0$.

Provided there are sufficient well-dispersed control points a procedure to optimise the 'apparent' camera location y_c' should give similar results, and it can be seen that any error in determination of model position from the neglect of refraction is negligible.

Horizontal plane

Figure B.3 shows a similar approach for rays in a horizontal plane. The x-axis runs along the window/ model interface, and the co-ordinates of the actual camera position are (0, y_c). The apparent camera position is (x_c', y_c').

A ray with angle β_1 anticlockwise from the negative y-axis is considered. The value of y_c' was established above to minimise error in a vertical plane, and will not be changed. For a horizontal plane x_c' can be optimised, and also rotation about a vertical axis. It will be assumed that the 'apparent' rotation of the camera is θ clockwise relative to the actual camera rotation.

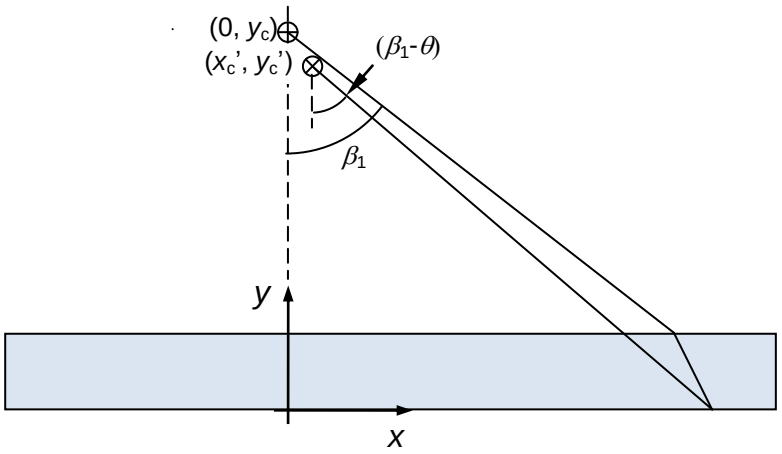

Figure B.3: Schematic of refracted and unrefracted rays in a horizontal plane

The equivalent equation to 1(a) for the refracted ray is:

$$x = (y_c - t)\tan\beta_1 + t\tan\beta_2 \qquad \text{Equation 2(a)}$$

where the β_2 is the angle of the refracted ray.

For the apparent camera location and rotation, and a ray which is assumed to be unrefracted

$$x' = x_c' + y_c'\tan(\beta_1 - \theta) \qquad \text{Equation 2(b)}$$

Again the error in model position is (x'-x)

To remove the complication of optimising for two variables (x_c' and θ) simultaneously it is assumed that θ = atan(x_c'/y_c'). Hence when β_1 = 0, x = x' = 0 and there is no error.

x_c' was optimised by hand to give a value of 7.6 mm (and hence θ = 2.68^o). The approximate range of β_1 for the actual camera position in the model was 0 to 64^o. Figure B.4 shows the resulting error (x'-x), plotted against x which as anticipated gives a field of view of about 300 mm.

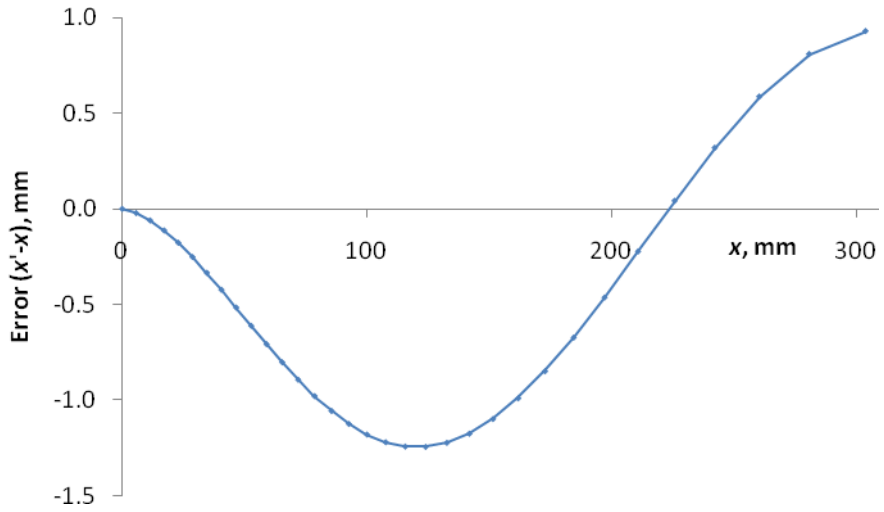

Figure B.4: Error in determination of horizontal model position

The maximum error is -1.2 mm, with somewhat smaller maximum positive error. Thus the camera position and rotation are not optimised in this sense, due to the assumption that $\theta = \text{atan}(x_c'/y_c')$. Indeed, further reduction in the error could have been realised by optimising the values of x_c', y_c' and θ simultaneously.

This is essentially what happened in analysis of the centrifuge image test data. The colinearity equations were used (without consideration of refraction) to determine the 3-d camera position and rotation, optimising these variables simultaneously to match control point locations dispersed throughout the image. The error in matching control point locations was typically about 1 mm, corresponding to the estimate in Figure B.4, and the accuracy with which control points could practically be positioned in the model.

Note that rotations about the two horizontal axes (both nominally zero), and vertical position should not be significantly affected by refraction. The 3 mm thick glass used in most tests would have significantly less effect than the 50 mm Perspex considered here, and would in any case be largely 'removed' by assumption of an apparent camera position in the same way as refraction due to the Perspex as illustrated here.